JUSTUS-LIEBIG-
UNIVERSITÄT
GIESSEN

Mechanistic insights into the regulation of DEAD-box helicases Sub2 and UAP56 by Tho1-family proteins

---

Dissertation

zur Erlangung des Doktorgrades der Naturwissenschaften

– Dr. rer. nat. –

am Fachbereich 08 für Biologie und Chemie

der Justus-Liebig-Universität Gießen

vorgelegt von

Fabienne Becker

Gießen, 2026

Die vorliegende Arbeit wurde am Institut für Biochemie (Fachbereich 08) der Justus-Liebig-Universität Gießen, unter Leitung von Apl. Prof. Dr. Peter Friedhoff, erstellt.

Dissertation eingereicht am: 13.03.2026

Erstgutachter: Apl. Prof. Dr. Peter Friedhoff
Fachbereich 08: Biologie und Chemie
Institut für Biochemie
Justus-Liebig-Universität Gießen

Zweitgutachter: Prof. Dr. John Ziebuhr
Fachbereich 11: Medizin
Institut für Medizinische Virologie
Justus-Liebig-Universität Gießen

Teile dieser Arbeit wurden in dem folgenden Artikel veröffentlicht:

Becker F., Miosga M.B., Mannan M., Bettenworth V., Steinchen W., Sträßer K., Friedhoff P. (2026), Tho1 and MOS11 promote nucleic acid double-strand unwinding by facilitating DEAD-box helicase oligomerisation, *Nucleic Acids Research*, Volume 54, Issue 2, gkaf1512

Table of Contents

Abstract

Eukaryotic mRNA is transcribed, processed, and packaged into messenger ribonucleoprotein particles (mRNPs) in the nucleus before being exported to the cytoplasm for translation. The highly conserved TREX complex plays a central role in coordinating these events. In baker's yeast *Saccharomyces cerevisiae*, defects in the largest TREX subunit, the THO complex, result in hyperrecombination, impaired mRNA export, and growth defects. Notably, these phenotypes can be suppressed by overexpression of the DEAD-box RNA helicase and TREX component Sub2 or its interaction partner Tho1. Despite increasing interest in TREX and its associated factors in the past years, the molecular mechanisms by which Tho1, in particular, fulfils its cellular functions remain unclear. Recent structural studies revealed a 2:1 complex formed by two protomers of the human Sub2 ortholog DDX39B and the C-terminal domain (CTD) of Tho1. However, the functional and physiological relevance of their interaction is not yet understood.

This study provides a comprehensive biochemical characterisation of Tho1 and its *A. thaliana* ortholog MOS11, elucidating the molecular mechanism by which they stimulate unwinding by Sub2 or its *A. thaliana* ortholog UAP56.

Building on the prior identification of a nucleic acid annealing activity of Tho1, the functional contributions of individual Tho1 domains were assessed using quantitative fluorescence-based real-time binding and annealing assays. Importantly, different Tho1 truncation mutants were tested for their ability to suppress a temperature-sensitive growth defect in cells lacking the THO component Hpr1, revealing that the Tho1-CTD alone is sufficient for phenotype suppression. Strikingly, while the Tho1-CTD lacks intrinsic nucleic acid binding and annealing activities, it interacts with and stimulates Sub2's helicase activity.

To dissect the mechanism underlying this helicase stimulation, fluorescence-based real-time unwinding assays were combined with complex modelling and mutational analyses. The Tho1-CTD contains two conserved α-helical motifs, each capable of interacting with one helicase protomer, and both motifs were shown to be crucial for helicase stimulation. Evolutionary conservation of this mechanism was confirmed by demonstrating that the Tho1-CTD stimulates UAP56. Furthermore, crosslinking approaches showed that formation of a 2:1 complex is critical for helicase stimulation. Together, these findings reveal that Tho1 acts as a molecular scaffold promoting helicase oligomerisation and thereby activation. The physiological importance of this

mechanism is underscored by the requirement for two intact helical motifs within the Tho1-CTD to suppress the growth defect in Δ*hpr1* cells.

Further investigation of MOS11, which contains five helical motifs connected by flexible linker regions, provided additional insight into how both the number of motifs and their spatial arrangement influence scaffold function. These structural features define its effective reach, which in turn determines the range of substrates on which helicase stimulation can be observed.

Collectively, this work combines *in vitro* biochemical assays, *in silico* modelling, and *in vivo* studies to provide mechanistic insights into the interaction of Tho1-family proteins and their role as cofactors that facilitate DEAD-box helicase oligomerisation.

Zusammenfassung

In Eukaryoten wird mRNA im Zellkern transkribiert, prozessiert und in Messenger-Ribonukleoproteinpartikel (mRNPs) verpackt, die anschließend für die Translation ins Zytoplasma exportiert werden. Der hochkonservierte TREX-Komplex spielt bei der Koordination dieser Vorgänge eine zentrale Rolle. In der Bäckerhefe *Saccharomyces cerevisiae* führen Defekte in der größten TREX-Untereinheit, dem THO-Komplex, zu Hyperrekombination, beeinträchtigtem mRNA-Export und Wachstumsdefekten. Bemerkenswerterweise lassen sich diese Phänotypen durch die Überexpression der DEAD-box-RNA-Helikase und TREX-Komponente Sub2 oder ihres Interaktionspartners Tho1 unterdrücken. Obwohl das Interesse am TREX-Komplex und seinen assoziierten Faktoren in den letzten Jahren stark zugenommen hat, sind die molekularen Mechanismen, durch die insbesondere Tho1 seine zellulären Funktionen erfüllt, weiterhin weitgehend ungeklärt. Eine aktuelle Studie zeigte die Bildung eines 2:1-Komplexes aus zwei Protomeren des humanen Sub2-Orthologs DDX39B und der C-terminalen Domäne (CTD) von Tho1, dessen funktionelle und physiologische Relevanz jedoch bisher unklar ist.

Die vorliegende Arbeit liefert eine umfassende biochemische Charakterisierung von Tho1 und seinem *A. thaliana*-Ortholog MOS11 und deckt einen molekularen Mechanismus auf, durch den sie die Helikase-Aktivität von Sub2 beziehungsweise von UAP56 aus *A. thaliana* stimulieren.

Aufbauend auf der zuvor beschriebenen Nukleinsäure-Annealing-Aktivität von Tho1 wurde die funktionelle Relevanz einzelner Tho1-Domänen mittels quantitativer fluoreszenzbasierter Bindungs- und Annealing-Experimente untersucht. Zudem wurden verschiedene Tho1-Mutanten auf ihre Fähigkeit getestet, einen temperaturinduzierten Wachstumsdefekt in Hefezellen zu unterdrücken, denen die THO-Komponente Hpr1 fehlt. Dabei zeigte sich, dass die Tho1-CTD allein für die Unterdrückung des Phänotyps ausreicht. Interessanterweise besitzt die Tho1-CTD selbst keine Nukleinsäure-Bindungs- oder Annealing-Aktivität, interagiert jedoch mit Sub2 und stimuliert dessen Helikase-Aktivität.

Zur Aufklärung des Mechanismus dieser Helikase-Stimulierung wurden fluoreszenzbasierte Entwindungsassays mit computergestützter Modellierung von Komplexen und Mutationsanalysen kombiniert. Die Tho1-CTD enthält zwei konservierte α-helikale Motive, die jeweils mit einem Helikase-Protomer interagieren können, und beide dieser Motive wurden als essenziell für die Helikase-Stimulierung

erwiesen. Die evolutionäre Konservierung dieses Effekts wurde durch die Stimulierung von UAP56 durch die Tho1-CTD bestätigt. Darüber hinaus zeigten Crosslinking-Experimente, dass die Bildung eines 2:1 Komplexes entscheidend für die Helikase-Stimulierung ist. Zusammenfassend zeigten diese Ergebnisse, dass Tho1 als molekulares Gerüst fungiert, welches die Oligomerisierung und damit die Aktivierung der Helikasen ermöglicht. Die physiologische Bedeutung dieses Mechanismus wurde durch die Notwendigkeit zweier intakter helikaler Motive innerhalb der Tho1-CTD zur Unterdrückung des Wachstumsdefekts in ∆*hpr1*-Zellen unterstrichen.

Weitere Untersuchungen von MOS11, das fünf flexibel angeordnete helikale Motive besitzt, lieferten zusätzliche Einblicke, wie sowohl die Anzahl als auch die räumliche Anordnung der Motive die Gerüstfunktion des Proteins beeinflussen. Diese strukturellen Eigenschaften definieren die effektive Reichweite des Proteins und bestimmen somit das Substratspektrum für die Helikase-Stimulierung.

Zusammenfassend kombiniert diese Arbeit *in vitro*-biochemische Assays, *in silico*-Modellierung und *in vivo*-Studien, um mechanistische Einblicke in die Interaktion von Proteinen der Tho1-Familie und ihre Rolle als Cofaktoren bei der Oligomerisierung von DEAD-box Helikasen zu liefern.

List of Figures

List of Tables

List of Abbreviations

Δ	deletion
Amp	ampicillin
ADP	adenosine diphosphate
AMPPNP	adenylyl-imidodiphosphate
ATP	adenosine triphosphate
bp	base pairs
CTD	carboxy-terminal-domain
C-terminal	carboxy-terminal
CTE	carboxy-terminal-extension
dATP	deoxyadenosine triphosphate
dCTP	deoxycytidine triphosphate
DEAD	Asp-Glu-Ala-Asp-box
DECD	Asp-Glu-Cys-Asp-box
dGTP	deoxyguanosine triphosphate
DNA	deoxyribonucleic acid
ds	double-stranded
DTT	dithiothreitol
dTTP	deoxythymidine triphosphate
EDTA	ethylenediaminetetraacetic acid
EM	electron microscopy
HDX	hydrogen/deuterium exchange mass spectrometry
His_6	6x histidine-tag
IPTG	isopropyl β-D-1-thiogalactopyranoside
KanR	kanamycin resistance
kDa	kilodalton
LB	Luria-Bertani medium
LC-MS	liquid chromatography-mass spectrometry
LEU	leucine
m7G	7-methylguanosine
mRNP	messenger ribonucleoprotein
N-terminal	amino-terminal
NAD^+	β-nicotinamide adenine dinucleotide
NPC	nuclear pore complex
nt	nucleotides

NTM	N-terminal motif
OD	optical density
OH	overhang
ORF	open reading frame
ori	origin of replication
PAGE	polyacrylamide gel electrophoresis
PAS	polyadenylation signal
PBS	phosphate buffered saline
PCR	polymerase chain reaction
PEG	polyethylene glycol
PMSF	phenylmethylsulfonyl fluoride
poly(A)	polyadenosine
(pre-)mRNA	(precursor) messenger ribonucleic acid
RNA	ribonucleic acid
Pol II	RNA polymerase II
SAP	SAF-A/B, Acinus, and PIAS
SOB	super optimal broth
SOC	super optimal broth with catabolite repression
SR	serine–arginine-rich
ss	single-stranded
STE	sodium chloride-Tris-EDTA buffer
TAE	Tris-acetate-EDTA buffer
TCA	trichloroacetic acid
TCEP	tris(2-carboxyethyl) phosphine
TEMED	tetramethylethylenediamine
TEV	tobacco etch virus
TREX	transcription/export
Trp	tryptophan
wt	wild-type
YPD	yeast peptone dextrose
YPG	yeast peptone galactose

1. Introduction

1.1. Steps of mRNA Biogenesis

A fundamental characteristic of eukaryotic cells is the compartmentalisation into membrane-bound, specialised organelles (Gabaldón & Pittis 2015; Satori *et al.* 2013). One example of such an organelle is the nucleus, which houses genetic information in the form of DNA (Mekhail & Moazed 2010). Whereas DNA is replicated and transcribed into messenger RNA (mRNA) in the nucleus, the subsequent translation of mRNA into proteins occurs in the cytoplasm, requiring the nuclear export of mRNAs (Clancy & Brown 2008; Crick 1970).

In addition to transcription, export, and translation, the life cycle of an mRNA involves further steps, including mRNA processing and quality control (Ben-Ari *et al.* 2010). All these processes rely on the coordinated binding of the mRNA by various RNA-binding proteins (RBPs), which package it into an mRNA ribonucleoprotein particle (mRNP) (Meinel & Sträßer 2015; Singh *et al.* 2015; Wende *et al.* 2019).

1.1.1. Transcription

RNA polymerase II (Pol II) is one of three nuclear polymerases and is responsible for transcribing protein-coding genes into mRNA. Furthermore, Pol II transcribes long non-coding RNAs (lncRNAs), the majority of cellular small nuclear RNAs (snRNAs), and microRNAs (miRNAs). Transcription by Pol II is essential for almost all cellular processes, including gene expression, proliferation, and differentiation (Archuleta *et al.* 2024). The Pol II core enzyme is a multi-subunit complex formed by the 12 subunits Rpb1-12 (Cramer *et al.* 2000, 2001; Li *et al.* 2022). Structurally, Pol II is organized in four domains – core, shelf, jaw-lobe, and clamp – that interact with each other and undergo conformational changes during transcription (Cramer *et al.* 2000, 2001; Li *et al.* 2022). Rpb1, the largest Pol II subunit, plays a key role in transcription regulation (Bernecky *et al.* 2016). Its C-terminal domain (CTD) contains numerous heptapeptide repeats with the consensus sequence Y_1-S_2-P_3-T_4-S_5-P_6-S_7. These residues are phosphorylated and dephosphorylated throughout transcription to regulate the activity of Pol II (Harlen & Churchman 2017; Jeronimo *et al.* 2016). The CTD is not required for transcription *in vitro* but is crucial in cells, where it serves as a binding platform for a variety of proteins involved in co-transcriptional processes (Gerber *et al.* 1995; Jeronimo *et al.* 2013; Yahia *et al.* 2023).

Although the Pol II core enzyme alone can synthesize RNA from a DNA template, cellular promoter-specific transcription initiation requires its interaction with general transcription factors (GTFs). Together with Pol II, they form the preinitiation complex at the core promoter (Sharma *et al.* 2024). Following promoter binding, Pol II enters elongation in a process known as promoter escape. This transition relies on ATP hydrolysis and Pol II CTD phosphorylation, with the latter allowing the release of initiation factors and the recruitment of elongation factors (Rodríguez-Molina *et al.* 2023; Zhan *et al.* 2024). These factors increase productive elongation, for example by suppressing transient Pol II pausing or by enhancing transcription on chromatin templates (Sims *et al.* 2004). Termination, the final step of transcription, involves CTD dephosphorylation and Pol II release from the DNA (Jeronimo *et al.* 2016; Rodríguez-Molina *et al.* 2023).

1.1.2. mRNA processing

Before the mRNA is exported to the cytoplasm and translated into a protein, three tightly coordinated processing steps – capping, splicing, and polyadenylation – convert the newly synthesized precursor-mRNA (pre-mRNA) into a mature mRNA molecule (Figure 1).

Shortly after transcription initiation, an N7-methylated guanosine (m7G) is attached to the 5′ end of the pre-mRNA, which is at this stage only 20-25 nt long. This cap structure protects the mRNA from degradation by 5′ exoribonucleases and is recognized by various proteins during transcription and translation (Decroly *et al.* 2012; Ramanathan *et al.* 2016). One protein complex that binds the 5′ cap already co-transcriptionally is the highly conserved cap-binding complex (CBC). In yeast, the CBC consists of the large subunit Cbp80 (NCBP1 in humans) and the small subunit Cbp20 (NCBP2 in humans) (Seidler & Sträßer 2024). It protects the mRNA from degradation and has also been shown to function in transcription elongation, splicing and mRNA export, where it acts as an assembly platform for different factors regulating gene expression (Müller-McNicoll & Neugebauer 2014; Rambout & Maquat 2020; Sen *et al.* 2019).

Genes contain protein-coding sequences, termed exons, and non-coding sequences, termed introns. During splicing, introns are identified and removed from the pre-mRNA to generate a continuous coding sequence (Gehring & Roignant 2021). In eukaryotes, splicing is facilitated by the spliceosome, which comprises five small nuclear ribonucleoprotein particles (snRNPs): U1, U2, U4, U5, and U6. These snRNPs

assemble stepwise on splice sites within the transcript and excise the intronic regions (Wilkinson *et al.* 2020). Additionally, alternative splicing events can combine different exons or retain certain introns. As a result, multiple mRNA variants are generated from the same gene, increasing diversity in gene expression and enabling the organism to respond to environmental changes (Kelemen *et al.* 2013).

In the final step, the 3′ end of the pre-mRNA is processed. This involves the multi-subunit cleavage and polyadenylation complex (CPAC). First, the CPAC binds to a poly(A) signal sequence (PAS) within the nascent mRNA and thereby defines its 3′ end. Subsequently, the mRNA is cleaved approximately 20 nt downstream of the PAS, and a poly(A) polymerase synthesizes a sequence of adenines onto the free 3′ end (Rodríguez-Molina & Turtola 2023). Similar to the 5′ m7G cap, this 3′ poly(A) tail stabilizes the mRNA by protecting it from degradation and is recognized by several poly(A) binding proteins (PAP) in the nucleus and cytoplasm. Both modifications have been shown to synergistically enhance translation (Passmore & Coller 2022).

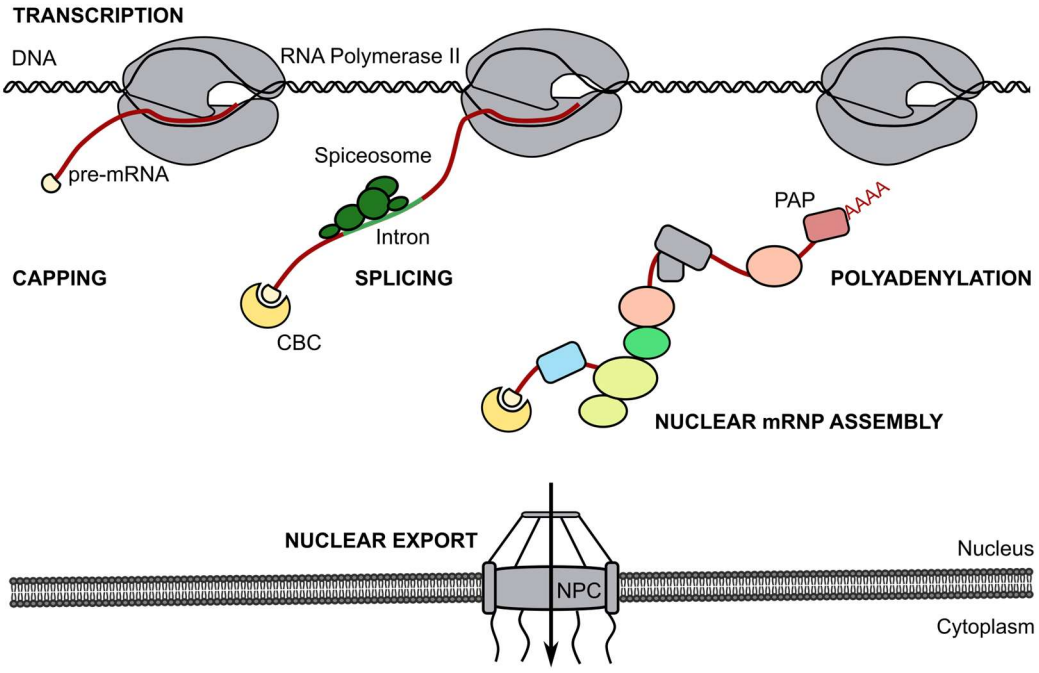

Figure 1: Steps of mRNA processing. During transcription, RNA polymerase II synthesizes pre-mRNA from protein-coding genes. This pre-mRNA undergoes three major processing steps: addition of a 5′ cap, removal of introns by the spliceosome, and cleavage followed by polyadenylation at the 3′ end. Simultaneously, RNA-binding proteins (RBPs) associate with the mRNA to form an mRNP. The mature mRNP is subsequently exported from the nucleus into the cytoplasm through the nuclear pore complex (NPC). This figure was adapted from Zarnack et al. (2020) licensed under the Creative Commons Attribution (CC BY) licence.

1.1.3. mRNA export

The nucleus is separated from the cytoplasm by a double lipid bilayer membrane, the nuclear envelope. Cytoplasmic transfer of nuclear molecules, including different types of RNA, proteins, and protein complexes, occurs through the nuclear pore complex (NPC) (De Magistris 2021; Lin & Hoelz 2019). Already in 1950, electron microscopy (EM) revealed pores covering the nuclear envelope (Callan & Tomlin 1950). Later, EM studies enabled three-dimensional (3D)-reconstructions of the NPC in various organisms. The ~52 MDa yeast NPC consists of 552 proteins, termed nucleoporins (Kim *et al.* 2018). In humans, approximately 1000 proteins assemble into a ~120 MDa complex (Lin *et al.* 2016). Whereas the number of NPC copies on the nuclear envelope varies with organism, cell type, or cell cycle stage, their structural composition is highly conserved (De Magistris 2021; Winey *et al.* 1997). A symmetric core surrounds a central transport channel through the nuclear envelope, where phenylalanine-glycine repeat-containing nucleoporins (FG Nups) create a diffusion barrier. This core is extended by asymmetric nucleoporins, forming the nuclear basket and cytoplasmic filaments (Lin & Hoelz 2019).

While some molecules diffuse passively, others pass through the NPC using active transport mechanisms mediated by export adapter proteins (Paine *et al.* 1975; Timney *et al.* 2016). Mature mRNPs, for instance, are bound by the heterodimeric export factor Mex67/Mtr2 (NXF1/NXT1 in humans) in the nucleoplasm (De Magistris 2021). Subsequently, Mex67/Mtr2 docks at the NPC and facilitates export through the NPC-channel by interacting with the FG nups (Derrer *et al.* 2019; Santos-Rosa *et al.* 1998; Segref 1997).

1.2. The TREX complex

A key mediator coupling mRNA transcription with nuclear export is the TREX complex (Sträßer *et al.* 2002; Xie & Ren 2019). In *Saccharomyces cerevisiae*, the TREX complex consists of the heteropentameric THO complex, comprising Tho2, Hpr1, Mft1, Thp2 and Tex1, which associates with the DEAD-box helicase Sub2, the nuclear export adaptor Yra1, and the serine-arginine-rich (SR-like) proteins Gbp2 and Hrb1 (Hurt *et al.* 2004; Sträßer *et al.* 2002). Although originally identified in yeast, TREX is highly conserved from yeast to humans, with species-specific variations in its exact subunit composition (Table 1). In humans, the hexameric THO complex lacks an ortholog of yeast Thp2 and instead includes the core subunits THOC1-THOC7 (Katahira 2012). In

the fission yeast *Schizosaccharomyces pombe,* TREX composition is broadly similar to that of *S. cerevisiae* but is missing a Thp2 ortholog while containing a THOC5 ortholog (Seidler & Sträßer 2024). The *Arabidopsis thaliana* TREX complex features multiple paralogs of Sub2, Yra1 and Mft1 as well as THOC5 (Germain *et al.* 2010; Kammel *et al.* 2013; Pfaff *et al.* 2018; Seidler & Sträßer 2024). No clear orthologs of Gbp2 and Hrb1 were identified in humans or *A. thaliana*.

Table 1: TREX components in *S. cerevisiae* and their orthologs in *S. pombe, H. sapiens* and *A. thaliana*. Adapted from Seidler & Sträßer (2024), with permission granted by the authors.

S. cerevisiae	***S. pombe***	***H. sapiens***	***A. thaliana***
Hpr1	tho1	THOC1	HPR1/THO1/EMU
Tho2	tho2	THOC2	THO2
Tex1	tho3	THOC3	TEX1
-	tho5	THOC5	THO5A
-	-	-	THO5B
-	-	THOC6	THO6/DWA1
Mft1	tho7	THOC7	THO7A
-	-	-	THO7B
Thp2	-	-	-
Gbp2	hrb1	-	-
Hrb1	hrb1	-	-
Sub2	uap56	DDX39B/UAP56	UAP56A
-	-	DDX39A/URH49	UAP56B
Yra1	mlo3, tho4	ALYREF/THOC4	ALY1
-	-	-	ALY2, ALY3, ALY4

Structural studies have shown that the overall architecture of the THO complex and its association with Sub2/DDX39B is conserved between yeast and human (Chen *et al.* 2021a; Pacheco-Fiallos *et al.* 2023; Pühringer *et al.* 2020; Schuller *et al.* 2020; Xie & Ren 2019). Tho2 (THOC2) and Hpr1 (THOC1) form a central platform onto which Thp2, Mft1 (THOC7), Tex1 (THOC3) and Sub2 (DDX39B) assemble. Although these individual complexes appear highly similar, their oligomeric states differ. In yeast, the THO-Sub2 complex predominantly forms dimers, whereas the endogenous human THO-DDX39B complex has been observed as a ring-shaped tetramer (Pacheco-Fiallos *et al.* 2023; Schuller *et al.* 2020). Notably, recombinantly expressed THO-

Sub2/DDX39B complexes can adopt a wide range of oligomeric states, from dimers up to octamers, depending on the expression system and experimental conditions (Chen *et al.* 2021a; Pühringer *et al.* 2020; Schuller *et al.* 2020; Xie & Ren 2019).

1.2.1. The TREX complex during mRNP biogenesis

The TREX complex is involved in multiple steps of mRNA metabolism, including co-transcriptional regulation, mRNA maturation, quality control, and nuclear export (Bhattacharjee *et al.* 2025; Katahira 2012). Assembly of the TREX complex on nascent mRNA occurs co-transcriptionally through interaction of the THO complex with the phosphorylated CTD of Pol II, particularly at positions S_2 and S_5 (Figure 2; Heath *et al.* 2016; Hurt *et al.* 2004; Meinel *et al.* 2013; Sträßer *et al.* 2002). Recruitment of the TREX complex also depends on the presence of RNA (Meinel *et al.* 2013). Tho2 is the primary THO complex subunit for RNA binding and has been shown to be essential for THO's presence at transcribed genes (Peña *et al.* 2012). After binding, the THO complex enables cooperative loading of Sub2/DDX39B and Yra1/ALYREF, both simultaneously interacting with THO subunits and the mRNA, thereby promoting the formation of a mature TREX-mRNP particle (Abruzzi *et al.* 2004; Chi *et al.* 2013; Taniguchi & Ohno 2008).

During transcription, the TREX complex also interacts with the Prp19 complex (Prp19C), which was discovered through its function in splicing but also plays a role in multiple other cellular processes, such as genome maintenance and protein degradation (Chanarat & Sträßer 2013; Tarn *et al.* 1994). Prp19C is recruited to active genes where it interacts with Pol II and the TREX complex. The Prp19C-TREX interaction is mediated by the Prp19C component Syf1. Notably, deletion of the Syf1 C-terminus not only impairs the interaction of Prp19C with Pol II but also leads to reduced TREX occupancy on transcribed genes. These findings indicate that Prp19C is a transcription elongation factor, stabilizing the recruitment of TREX during transcription (Chanarat *et al.* 2011). Prp19C and subsequent TREX recruitment rely on the splicing factor Mud2, which directly interacts with the S_2-phosphorylated Pol II CTD (Figure 2; Minocha *et al.* 2018).

TREX occupancy increases from the 5′ to 3′ end of genes but is not detected on chromatin downstream of the polyadenylation site (Abruzzi *et al.* 2004; Gómez-González *et al.* 2011; Kim *et al.* 2004; Sträßer *et al.* 2002). This distribution suggests that the TREX complex functions during transcription elongation and 3′ end processing,

before being released from the template along with the mature mRNA. Consistently, the TREX complex has been shown to interact with multiple factors involved in mRNA cleavage and polyadenylation (Johnson *et al.* 2009; Luna *et al.* 2005; Oeffinger *et al.* 2007).

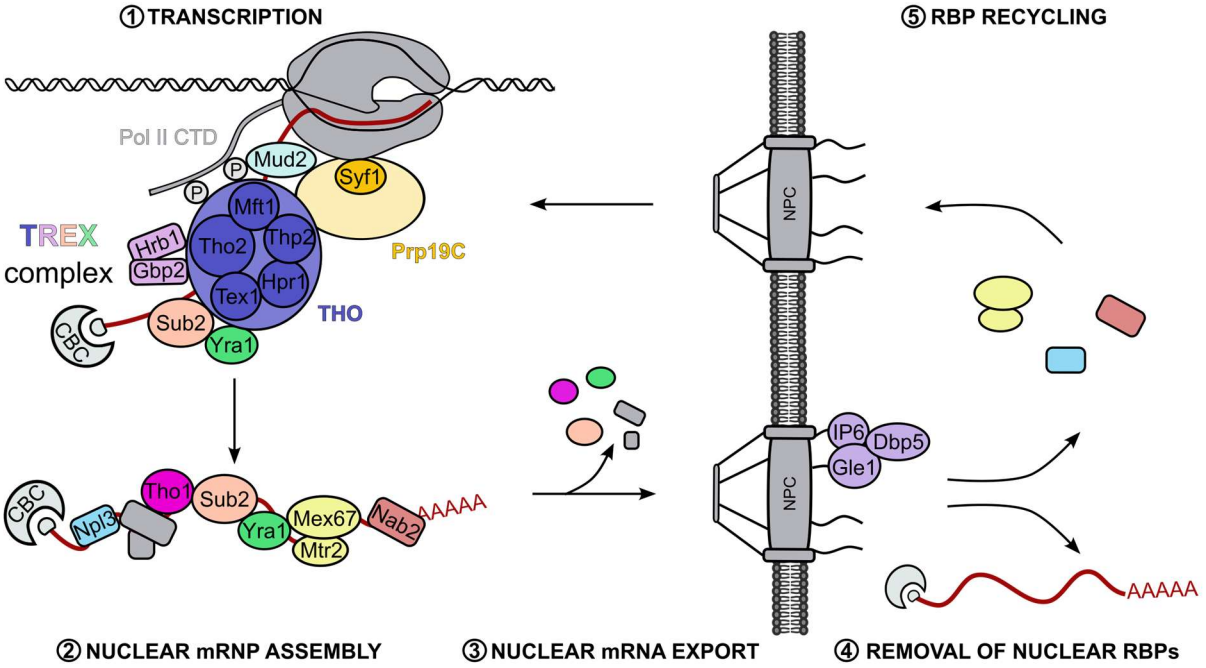

Figure 2: TREX in mRNP biogenesis and nuclear mRNA export. During transcription, nuclear RNA-binding proteins (RBPs), including the cap-binding complex (CBC) and TREX complex (THO complex, Sub2, Yra1, Hrb1, and Gbp2), assemble on the newly synthesized mRNA. Mud2 and the Prp19 complex contribute to stable TREX recruitment (1). This assembly leads to the formation of a nuclear mRNP that is transported towards the nuclear pore complex (NPC) (2). The exporter Mex67-Mtr2 is recruited by Yra1 and mediates transport of the mRNP through the NPC into the cytoplasm. Before export, remaining TREX components as well as additional RBPs are removed from the mRNP (3). On the cytoplasmic side of the NPC, the DEAD-box helicase Dbp5 removes the remaining nuclear RBPs to prevent re-import, allowing the mRNA to be released into the cytoplasm for translation (4). The nuclear RBPs are then re-imported into the nucleus to participate in another round of mRNA export (5). Adapted from Seidler & Sträßer (2024), licensed under CC BY-NC-ND 4.0 licence, with permission for adaptations granted by the authors.

TREX plays an important role in mRNA export by recruiting the export factor Mex67/Mtr2 (NXF1/NXT1 in humans) to mature mRNA (Figure 2; De Magistris 2021). Because Mex67/Mtr2 does not directly recognize mRNA, its association with the transcript relies on recruitment by the TREX-adaptor protein Yra1. Overexpression of Mex67 has been shown to suppress the export defect associated with *yra1* mutants, supporting the role of Yra1 in Mex67 recruitment (Iglesias *et al.* 2010; Sträßer & Hurt 2000). Hpr1 also contributes to this process by interacting with the ubiquitin-associated (UBA) domain of Mex67 (Gwizdek *et al.* 2006).

1.2.2. Physiological relevance of the TREX complex

In yeast, the role of the different TREX components has been extensively characterised. Loss of either SR-like protein, Gbp2 or Hrb1, has no detectable effect on cell viability or mRNA export (Hurt *et al.* 2004; Sträßer *et al.* 2002). In contrast, both depletion and overexpression of Sub2 cause severe defects in mRNA export (Sträßer & Hurt 2001). Similarly, thermosensitive (ts) mutants of Yra1, a direct interaction partner of Sub2, show nuclear accumulation of poly(A) RNA (Sträßer & Hurt 2001). Notably, overexpression of Yra2 suppresses the lethality associated with deletion of *YRA1*. Yra2 is a non-essential homolog of Yra1 and was not identified as a component of the TREX complex, yet these findings suggest that the two proteins share overlapping functions (Zenklusen *et al.* 2002).

Defects in the THO components Tho2, Hpr1, Mft1, and Thp2 lead to a variety of phenotypes, including impaired 3′ end processing, defective release of mRNA from the transcription site, hyperrecombination, as well as growth defects (Chávez & Aguilera 1997; Jimeno *et al.* 2002; Libri *et al.* 2002; Rougemaille *et al.* 2007; Saguez *et al.* 2008). These mutants frequently accumulate so-called “heavy” chromatin, in which defective mRNPs are confined in the nucleus with DNA, 3′ end processing factors and nucleoporins (Rougemaille *et al.* 2008).

The THO complex also plays a central role in regulating cellular R-loop levels. R-loops form co-transcriptionally when the nascent RNA anneals to the DNA template strand. Although R-loops are physiological structures that contribute to processes such as transcription initiation and termination, their excessive accumulation has been shown to compromise genome stability (Crossley *et al.* 2019; Gómez-González *et al.* 2011). Impairment of Hpr1, either through deletion or depletion, leads to an increase in R-loops, which in turn provides an obstacle for both transcription elongation and DNA replication (Huertas & Aguilera 2003; Pérez-Calero *et al.* 2020). In agreement with this, Δ*hpr1* cells display replication fork slowing or pausing, and Hpr1 depletion increases DNA damage throughout the cell cycle (San Martin-Alonso *et al.* 2021; Wellinger *et al.* 2006).

In humans, the functional significance of the TREX complex becomes even clearer. TREX participates in a wide range of cellular processes, such as stress responses, mitosis, embryonic development and maintenance of genome stability (Bhattacharjee *et al.* 2025). Loss of function mutants of THOC2 and THOC6 have been shown to associate with diverse neurodevelopmental disorders, for example, intellectual

disability, autism, attention deficit hyperactivity disorder, epilepsy, or cerebral palsy (Bhattacharjee *et al.* 2025). Furthermore, TREX has been directly implicated in cancer, with multiple components reported to be upregulated in different tumour types (Bai *et al.* 2021; Heath *et al.* 2016; Lee *et al.* 2023; Li *et al.* 2007; Saito *et al.* 2013). For instance, THOC1 expression in breast tumours correlates with tumour size and metastatic potential (Guo *et al.* 2005), and its depletion suppresses proliferation in both breast and liver cancer cells (Cai *et al.* 2020; Chou *et al.* 2022). Accordingly, individual TREX components are promising therapeutic targets (Heath *et al.* 2016).

1.3. DEAD-box RNA helicases

DEAD-box helicases are part of the helicase superfamily 2 (SF2) and form the largest family of RNA helicases. They are found in bacteria, eukaryotes, and archaea, where they contribute to diverse cellular functions (Gorbalenya & Koonin 1993; Linder & Jankowsky 2011). Characteristically, DEAD-box proteins contain a highly conserved core formed by two globular recombinase A (RecA)-like domains (Figure 3A). This core comprises 12 sequence motifs at defined positions, enabling the nucleotide- and RNA-binding activities of the helicases. Motif II includes the name-giving Asp-Glu-Ala-Asp (DEAD) region, which can be slightly altered in some helicases (DexD) (Fairman-Williams *et al.* 2010; Linder *et al.* 1989). Often, the core is extended by N- and C-terminal regions, reaching lengths up to several hundred amino acids (Fairman-Williams *et al.* 2010). Although the structure and function of many DEAD-box helicases are generally well characterised, the roles of these terminal domains frequently remain elusive. In some cases, they confer substrate specificity to the otherwise non-specific helicases (Diges 2001; Kossen *et al.* 2002; Linden *et al.* 2008). For example, the C-terminal extension of *Thermus thermophilus* DEAD-box helicase Hera contains both an RNA-binding domain (RBD) and a Dimerisation domain (DD), illustrating how terminal regions can confer additional functional properties (Klostermeier & Rudolph 2009; Rudolph & Klostermeier 2009).

1.3.1. Mechanism and functions of DEAD-box helicases

Progressive helicases separate duplexes by translocating along their substrate. In contrast, DEAD-box helicases use a local strand separation mechanism that does not involve translocation (Harms *et al.* 2014; Pyle 2008). They bind to double-stranded regions, causing a destabilization of the duplex and consequently strand separation

(Hilbert *et al.* 2009; Linder & Jankowsky 2011). This reaction depends on ATP and is facilitated by conformational changes in the DEAD-box helicase (Figure 3B). The two opposing RecA-like domains of the core bind RNA opposite the ATP-binding site. In doing so, they bend the RNA and interact exclusively with the RNA's sugar-phosphate backbone, explaining the lack of substrate specificity in most DEAD-box helicases (Andersen *et al.* 2006; Sengoku *et al.* 2006; Von Moeller *et al.* 2009).

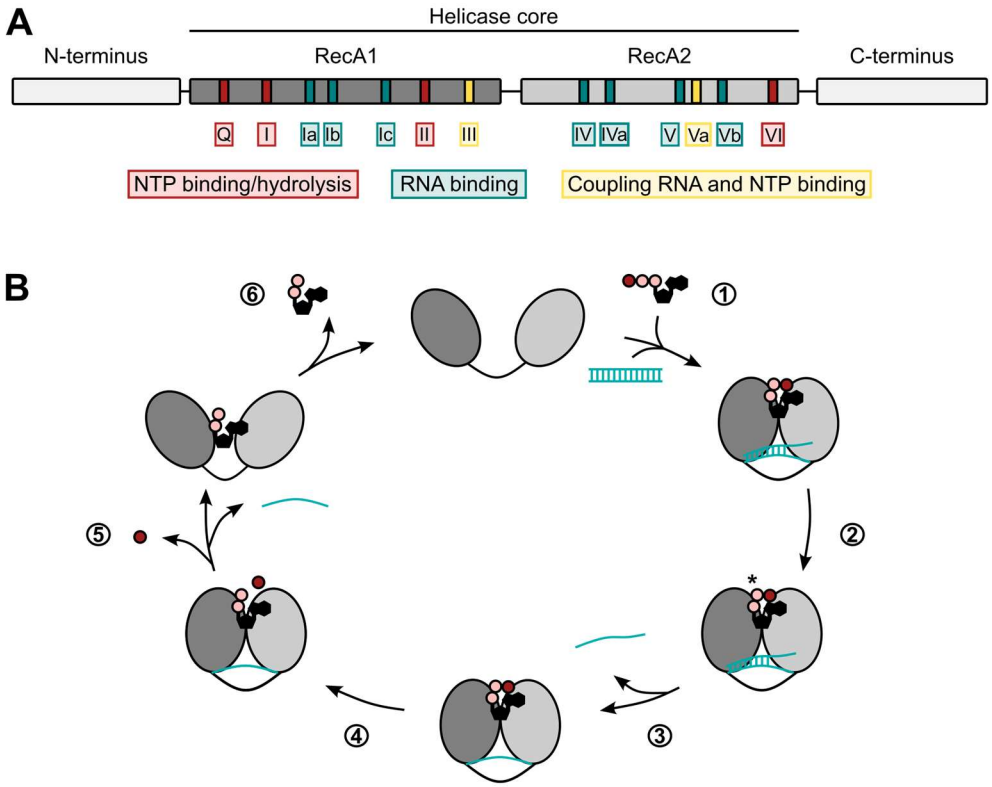

Figure 3: DEAD-box helicases. (A) Domain organisation of DEAD-box helicases. The highly conserved helicase core consists of two RecA-like domains (RecA1 and RecA2), often flanked by N-terminal and C-terminal regions. Conserved motifs within the core domains are important for NTP binding and hydrolysis (red), RNA binding (cyan) and coupling of NTP and RNA binding (yellow). Adapted from Bohnsack et al. (2023) with permission from Springer Nature (licence number: 6203020601397). **(B)** Schematic representation of the conformational cycle of DEAD-box helicases. (1) Cooperative binding of ATP (α- and β-phosphates shown in light pink, γ-phosphate in red) and double-stranded RNA (dsRNA; cyan) induces a transition of the DEAD-box protein from an open to a closed conformation, leading to closure of the gap between the RecA-like domains (dark and light grey ovals). The RNA is bent and bound opposite to the ATP-binding site. (2) Activation into the hydrolysis- and unwinding-competent state (marked by *). (3) The first RNA strand of the dsRNA dissociates. (4) ATP is hydrolysed and (5) the γ-phosphate is released, leading to dissociation of the remaining RNA strand and reopening of the helicase core. (6) ADP is released and the helicase can enter a new cycle. Adapted from Harms et al. (2014), licensed under the Creative Commons CC BY-NC 3.0 licence.

For many DEAD-box helicases, duplex unwinding relies on ATP binding but not necessarily on ATP hydrolysis (Aregger & Klostermeier 2009; Chen *et al.* 2008). The

length and stability of the double strand, as well as the presence of single-stranded extensions to the duplex, have also been shown to affect the strand separation (Jarmoskaite & Russell 2011; Rogers *et al.* 2001; Yang & Jankowsky 2006). In some cases, helicase activity is additionally regulated by helicase oligomerisation (Kinoshita *et al.* 2021; Marcaida *et al.* 2020; Putnam *et al.* 2015). Moreover, DEAD-box helicases are often part of large multi-protein complexes, in which other factors modulate their enzymatic activities (Sloan & Bohnsack 2018). For example, both ATP and RNA-binding of eukaryotic initiation factor 4A (eIF4A) are enhanced by its interaction with eIF4G. In contrast, the exon junction complex component CWC22 locks the RecA-like domains of eIF4A in a conformation that impairs ATP and RNA binding (Buchwald *et al.* 2013; Hilbert *et al.* 2011).

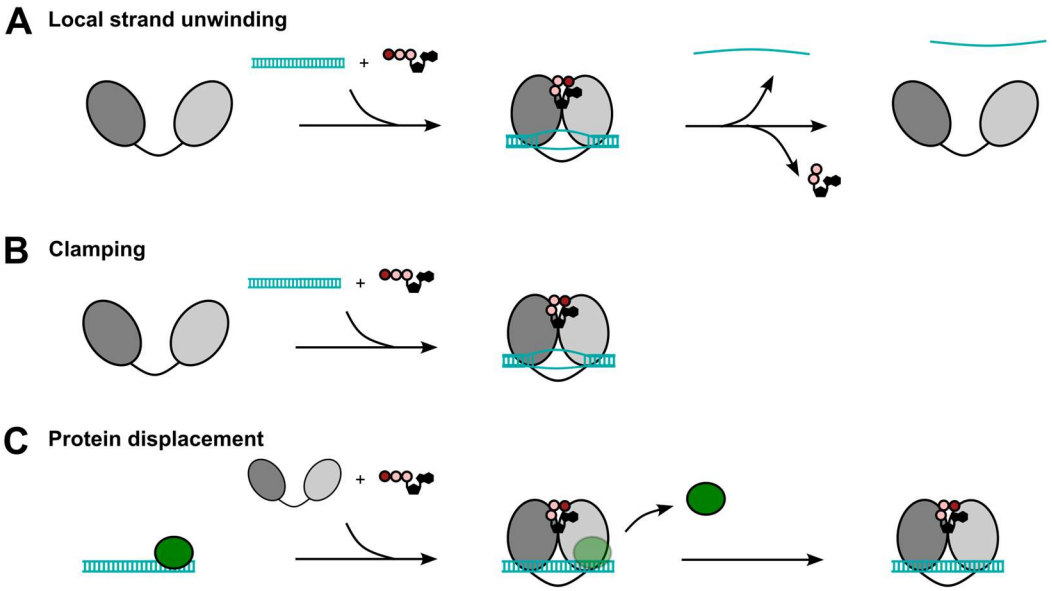

Figure 4: Mechanisms of DEAD-box helicases. DEAD-box helicases can **(A)** unwind double-stranded RNA by local strand separation; **(B)** act as RNA clamps, forming a stable complex with RNA and ATP when their ATPase activity is blocked; or **(C)** displace other RNA-binding proteins (RBPs) from the substrate. Adapted from Bohnsack et al. (2023) with permission from Springer Nature (licence number: 6203020601397).

In a typical ATPase cycle, ATP hydrolysis into ADP drives dissociation of the helicase from the RNA, since ADP reduces its RNA affinity (Iost *et al.* 1999). As a result, the complex disassembles, and the helicase can rebind to a new substrate (Figure 4A; Theissen *et al.* 2008). For some helicases, however, the cycle arrests prior to ATP hydrolysis. These proteins are commonly referred to as RNA clamps, as the complexes they form with ATP and RNA can persist for many hours (Figure 4B; Liu *et al.* 2014). Furthermore, DEAD-box helicases have been shown to displace RNA-bound proteins independently of their unwinding activity (Figure 4C; Bowers *et al.* 2006; Fairman *et al.*

2004). For instance, the export protein Mex67 is removed from the mRNA by DEAD-box protein 5 (Dbp5) during the final steps of mRNP export into the cytoplasm (Lund & Guthrie 2005).

1.3.2. Biological roles of DEAD-box helicases

DEAD-box helicases are highly abundant proteins that play crucial roles in all steps of cellular RNA metabolism (Figure 5; Linder & Jankowsky 2011; Taschuk & Cherry 2020). They can participate in one or multiple stages of RNA processing. For example, the yeast DEAD-box helicase Dbp2 (human DDX5) is implicated in multiple processes, including transcription, pre-mRNA splicing, R-loop resolution, as well as mRNA export and decay (Aydin *et al.* 2024; Hondele *et al.* 2019; Xing *et al.* 2019). This wide range of essential functions within highly interconnected pathways makes it challenging to distinguish between the direct and indirect effects of the helicase activity.

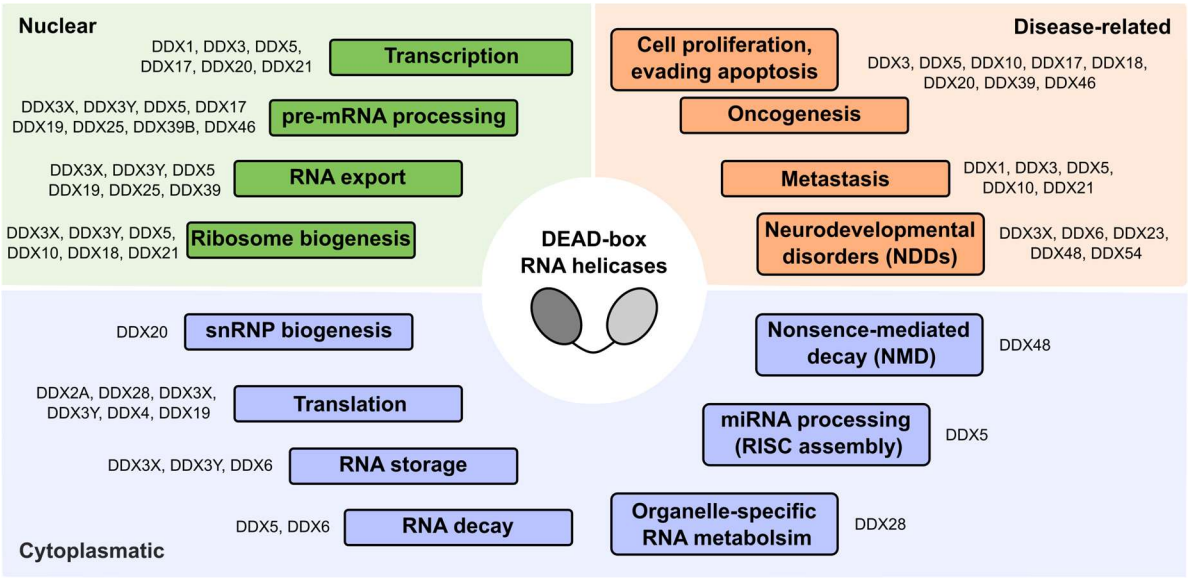

Figure 5: Cellular functions of DEAD-box helicases. Nuclear (green), cytoplasmic (blue), and disease-related (orange) processes in which DEAD-box helicases have been implicated are shown, together with example helicases for each process. This figure was created based on Bohnsack et al. (2023), Linder & Jankowsky (2011), and Tabassum & Ghosh (2023).

Dysfunction of helicases often leads to severe consequences and is frequently linked to cancer or other diseases, making them promising targets for small-molecule therapeutics (Figure 5). However, effective target sites, such as the ATP-binding pockets, are highly conserved among DEAD-box helicases. This conservation makes it difficult to design molecules that selectively inhibit specific proteins (Bohnsack *et al.* 2023). One successful example is targeting the DEAD-box helicase eIF4A, which functions in translation and is dysregulated in many cancer (Bohnsack *et al.* 2023).

Notably, eIF4A contains a pocket that is conserved only in a subset of DEAD-box proteins and can therefore serve as a potential drug target. Two classes of inhibitors, rocaglates and pateamine A, prevent RNA release from eIF4A and thereby inhibit translation initiation (Bordeleau *et al.* 2005; Chen *et al.* 2021b; Chu *et al.* 2019; Iwasaki *et al.* 2016). Another eIF4A inhibitor, hippuristanol, impairs its RNA binding (Shen & Pelletier 2020).

1.4. DEAD-box helicase and TREX component Sub2

The highly conserved *S. cerevisiae* DEAD-box helicase Sub2 and its human ortholog DDX39B (also known as UAP56) play essential roles in multiple steps of gene expression through interactions with diverse protein partners. DDX39B promotes cell proliferation and is significantly upregulated in various cancer types (Awasthi *et al.* 2018; Bohnsack *et al.* 2023; Zhang *et al.* 2022).

1.4.1. Cellular functions of DEAD-box helicase Sub2/DDX39B

During splicing, both Sub2 and DDX39B function in spliceosome assembly (Libri *et al.* 2001; Shen *et al.* 2008). The ATP-binding, ATPase, and dsRNA unwinding activities of DDX39B are required for its recruitment and the interaction with different spliceosome subunits (Shen *et al.* 2008).

DDX39B also contributes to R-loop resolution. Depletion of DDX39B leads to accumulation of cellular R-loops, resulting in genome instability and replication fork stalling. Conversely, DDX39B overexpression reduces R-loop levels and R-loop-mediated genome instability in cells with elevated R-loop accumulation (Pérez-Calero *et al.* 2020).

Furthermore, Sub2 and DDX39B are components of the TREX complex and are essential for correct mRNA export. Sub2 is recruited to active chromatin by the THO complex (Katahira 2012; Schuller *et al.* 2020; Sträßer *et al.* 2002; Sträßer & Hurt 2001). A crystal structure revealed that the THO complex interacts with both RecA-like domains of Sub2, thereby clamping Sub2 into a half-open conformation that primes it for RNA binding. In contrast, the structure of Sub2 bound to an ATP analogue, RNA, and a C-terminal fragment of Yra1 depicts Sub2 in a closed conformation (Ren *et al.* 2017). Both THO and Yra1 stimulate Sub2's ATPase activity and are proposed to cooperate in loading Sub2 onto the RNA (Chang *et al.* 2013; Ren *et al.* 2017).

Another interaction partner of Sub2 is Tho1, a conserved protein involved in mRNP biogenesis (Jimeno *et al.* 2006). The *Arabidopsis thaliana* Tho1 ortholog, MOS11, was described as a nuclear export factor, as its deletion leads to nuclear poly(A) RNA accumulation (Germain *et al.* 2010). The human ortholog SARNP (also known as CIP29), is crucial for nuclear export and cell viability, and is upregulated in liver and pancreatic tumours (Choong *et al.* 2001; Fukuda *et al.* 2002). *THO1* deletion in yeast causes no apparent phenotype. However, its overexpression suppresses the hyperrecombination phenotype as well as mRNA export and growth defects associated with defects in the THO complex (Jimeno *et al.* 2006; Piruat & Aguilera 1998). A similar suppression is observed upon Sub2 overexpression, suggesting that the two proteins either have similar functions or modulate each other's activities (Fan *et al.* 2001). Indeed, MOS11 and SARNP stimulate the helicase activities of their corresponding Sub2 orthologs (Chang *et al.* 2013; Rödel *et al.* 2024; Sugiura *et al.* 2007). Tho1, on the other hand, inhibits unwinding by Sub2, likely due to its intrinsic nucleic acid annealing activity (Miosga 2022). Notably, SARNP's interaction with DDX39B is mutually exclusive with THO binding, and SARNP promotes the release of DDX39B-bound mRNPs from the THO-complex while stabilizing DDX39B-RNA interaction (Hohmann *et al.* 2025; Xie *et al.* 2023).

Both Sub2 and DDX39B also interact with the TREX-2 complex, a five-subunit complex that binds to the NPC. TREX-2 stimulates the ATPase activity of Sub2/DDX39B and triggers their RNA release by initiating conformational changes in Sub2/DDX39B via a conserved trigger loop region (Hohmann *et al.* 2025; Xie *et al.* 2025).

Recent studies propose a model for human mRNA export centred on DDX39B and its dynamic interactions with mRNP components (Figure 6; Hohmann *et al.* 2025; Xie *et al.* 2025). In this model, the mRNA is bound by ALYREF and other export adapters. The THO complex is then recruited through its interaction with DDX39B protomers, assembling the TREX complex on the mRNA. ATP-dependent RNA clamping by DDX39B promotes dissociation of THO. SARNP then binds DDX39B, stabilizing the DDX39B-ALYREF-mRNP complex and preventing reassociation of the THO complex. When the mRNP reaches the NPC, the TREX-2 complex removes DDX39B from the mRNP, enabling export mediated by NXF1-NXT1.

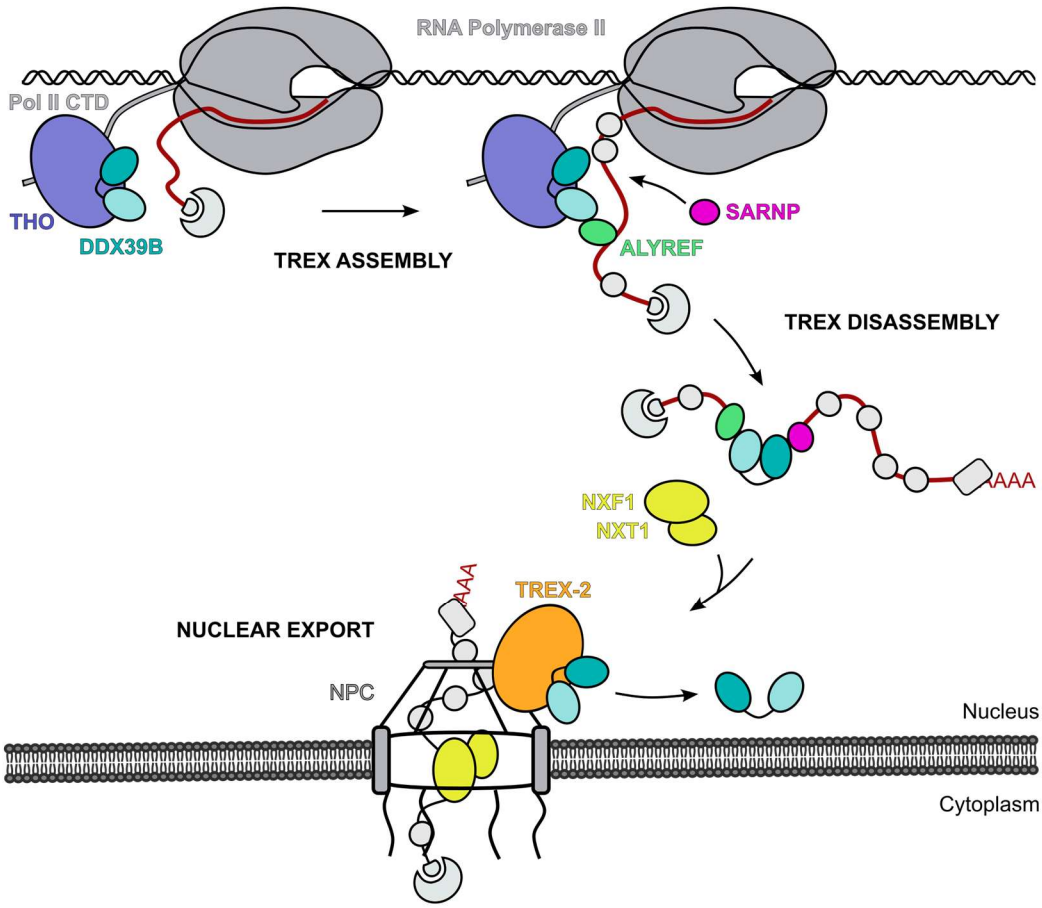

Figure 6: A DDX39B-centred model for mRNA export. The THO complex is recruited to active genes through its interaction with the C-terminal domain of RNA polymerase II and clamps DDX39B in a half-open conformation. DDX39B interacts with ALYREF, which is bound to the nascent RNA, leading to TREX complex assembly. In this intermediate state, DDX39B remains half-open before it clamps onto the RNA, thereby promoting THO dissociation. The binding of SARNP to DDX39B stabilises the DDX39B-bound mRNP. TREX-2 is associated with the nuclear pore complex (NPC) and triggers RNA release from DDX39B, thereby removing it from the mRNP. Subsequently, NXF1-NXT1 mediates mRNA export. This figure was created based on (Hohmann *et al.* 2025; Xie *et al.* 2025).

In addition to its interaction with TREX-2 during mRNA export, DDX39B also interacts with two TREX-2-like complexes, LENG8-PS and SAC3D1-PS. All three complexes stimulate DDX39B's ATPase activity and RNA release but differ in cellular localization: TREX-2 is found in the nuclear envelope, LENG8-PS in the nucleoplasm, and SAC3D1-PS in the cytoplasm. LENG8-PS is a module of the nuclear Poly(A) tail exosome targeting (PAXT) connection and therefore involved in the nuclear decay of specific, often non-functional RNAs. Through its interaction with LENG8-PS, DDX39B is proposed to act not only in mRNA export but also in the fate determination of polyadenylated RNA and mRNA decay (Bugai *et al.* 2025; Clarke *et al.* 2025).

1.4.2. Structural basis of the Sub2-Tho1 interaction

A large-scale deep-learning-based modelling of *S. cerevisiae* protein complexes first predicted the interaction between Sub2 and Tho1, mediated by a conserved CTD of Tho1 (Humphreys *et al.* 2021). This prediction was later supported by a co-crystal structure of the yeast Tho1-CTD with human DDX39B. Interestingly, the Tho1-CTD binds two DDX39B protomers, forming a DDX39B-Tho1-CTD 2:1 complex (Figure 7A; Xie *et al.* 2023).

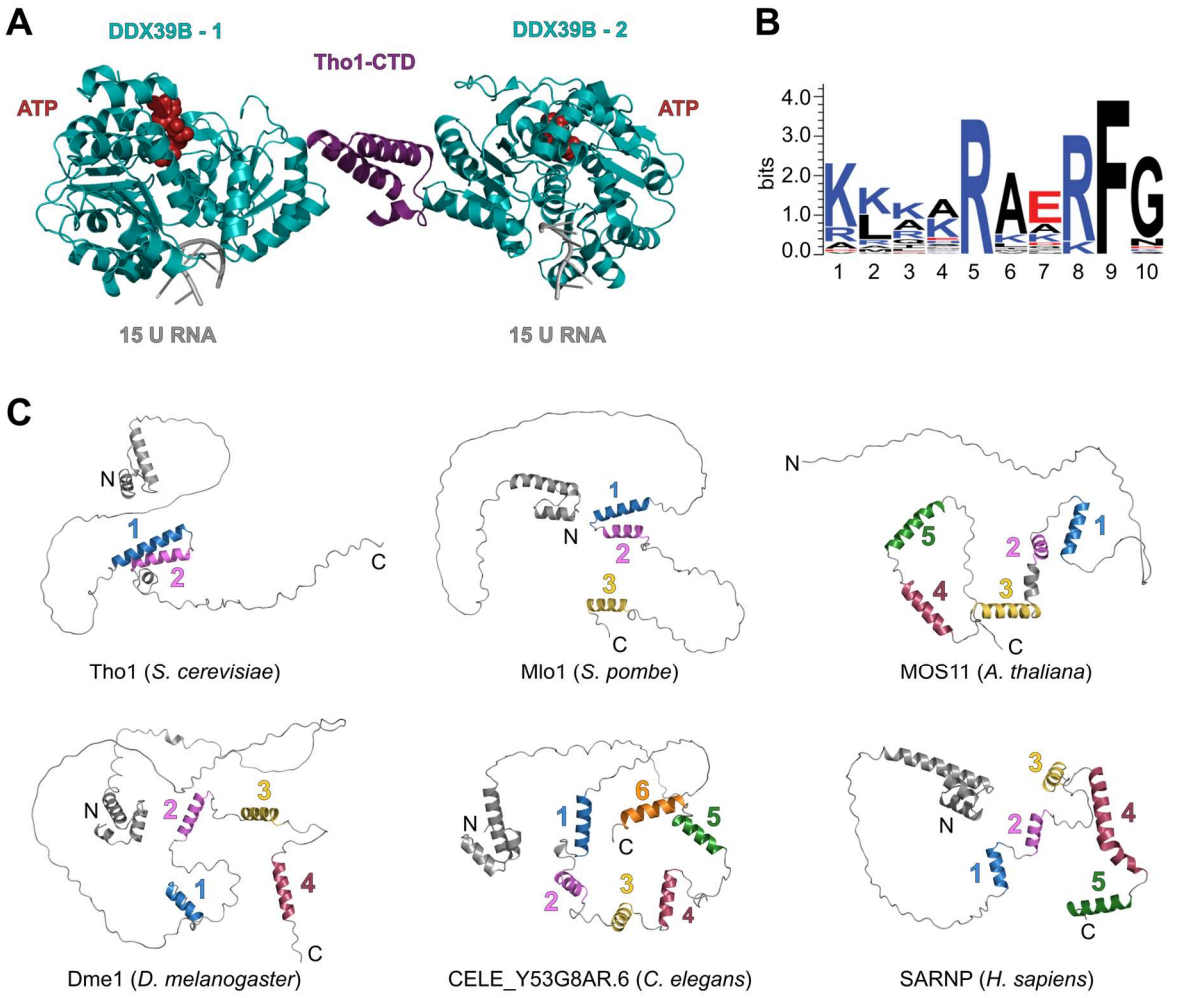

Figure 7: Conserved α-helical motifs in Tho1 and its orthologs. (A) Crystal structure of a 2:1 complex formed by two protomers of human DDX39B (cyan) and the CTD of Tho1 (purple) (8ENK). The interaction is mediated by two conserved α-helical interaction motifs within the Tho1-CTD. DDX39B is bound to ATP (red spheres) and 15 nt poly(U) RNA (grey). **(B)** Sequence logo showing the conservation of the 10-amino-acid interaction motif. Panel taken from Xie et al. (2023) licensed under CC BY-NC-ND 4.0. **(C)** Comparison of AlphaFold predictions for *S. cerevisiae* Tho1 (AF-P40040), *S. pombe* Mlo1 (AF-O74871), *A. thaliana* MOS11 (AF-Q9LZ08), *Drosophila melanogaster* Dmel (AF-Q9VHC8), *Caenorhabditis elegans* CELE_Y53G8AR.6 (AF-Q9N3G0) and *Homo sapiens* SARNP (AF-P82979). The number of α-helical motifs ranges from two in *S. cerevisiae* to six in *C. elegans*. Helices containing α-helical motifs are highlighted. This figure was created based on Xie et al. (2023).

The interaction is mediated by a tandem repeat of conserved α-helical motifs with the consensus sequence $K_1x_2x_3x_4R_5x_6x_7R/K_8F_9G_{10}$ (Figure 7B; Jacobsen *et al.* 2016; Xie *et al.* 2023). These motifs have also been termed DDX39B Interacting Motif (DIM) or UAP56 Clamping Motif (UCM) (Hohmann *et al.* 2025; Xie *et al.* 2023).

Whereas Tho1 contains two such motifs, connected by a short linker, other orthologs typically comprise more (Supplementary Figure S1; Jacobsen *et al.* 2016; Xie *et al.* 2023). For example, *Schizosaccharomyces pombe* and *Drosophila melanogaster* possess three and four of these motifs, respectively, while *A. thaliana* MOS11 and human SARNP contain five. *Caenorhabditis elegans* CELE_Y53G8AR.6 even has six helical motifs (Figure 7C; Jacobsen *et al.* 2016; Xie *et al.* 2023).

1.5. Aims and objectives of this study

Overexpression of the nucleic acid-binding protein Tho1 has been shown to suppress multiple phenotypes observed in yeast cells lacking the THO complex component Hpr1 (Jimeno *et al.* 2006; Piruat & Aguilera 1998). However, the molecular basis for this suppression remains unclear.

A model proposed by Jimeno et al. suggests that increased Tho1 expression promotes the loading of Tho1 protomers onto the mRNA, thereby alleviating R-loop-associated defects. This mechanism relies on Tho1's established ability to bind RNA (Jimeno *et al.* 2006). Consistent with this notion, Tho1 has previously been reported to exhibit nucleic acid annealing activity and resolve R-loop-like structures *in vitro* (Miosga 2022). Nevertheless, it remains unresolved whether these activities actually account for the observed *in vivo* effects, or whether suppression of the Δ*hpr1* phenotypes requires Tho1's interaction with Sub2. Evidence for a direct physical interaction between the two proteins has since emerged (Humphreys *et al.* 2021; Miosga 2022). Furthermore, during the course of this work, a co-crystal structure revealed a 2:1 complex formed between the human Sub2 ortholog DDX39B and the CTD of Tho1 (Humphreys *et al.* 2021; Miosga 2022; Xie *et al.* 2023). The functional relevance of this complex remains unknown, raising the question of whether Tho1's function involves direct modulation of Sub2's activity. Together, these open questions highlight a significant gap in our understanding of how THO complex-associated factors contribute to maintaining genome stability and facilitate mRNA biogenesis.

To address these questions, this study pursued three main objectives. The first was to determine whether the intrinsic biochemical activities of Tho1 are sufficient to explain

its cellular function. To this end, a quantitative fluorescence anisotropy-based RNA-binding assay was established to systematically characterise the nucleic acid binding properties of full-length Tho1 and a series of truncation mutants. A real-time Förster resonance energy transfer (FRET)-based assay was additionally employed to monitor RNA/DNA annealing and strand displacement. Finally, the ability of these mutants to suppress a temperature-induced growth defect in Δ*hpr1* cells was assessed to directly link biochemical activity with cellular function.

The second objective was to investigate whether and how the Tho1-Sub2 interaction, and the stoichiometry of their association, have functional consequences. While orthologs of Tho1 have been reported to stimulate the helicase activity of their cognate DEAD-box proteins, full-length Tho1 has been shown to counteract Sub2-mediated unwinding (Chang *et al.* 2013; Miosga 2022; Rödel *et al.* 2024; Sugiura *et al.* 2007). In contrast, the Tho1-CTD, which is sufficient for 2:1 complex formation with DDX39B, was found to stimulate Sub2 unwinding (Miosga 2022; Xie *et al.* 2023). Fluorescence-based real-time unwinding assays were employed to dissect the mechanism underlying this stimulation, using interface mutants of both Sub2 and Tho1. The *in vivo* relevance of this interaction was also tested in Δ*hpr1* cells. Parallel experiments with the *A. thaliana* Sub2 ortholog UAP56 were conducted to examine the evolutionary conservation of helicase stimulation.

The third objective extended this analysis to the *A. thaliana* Tho1 ortholog MOS11, with the aim of elucidating the role of multiple helical motifs in helicase interaction. Unlike Tho1, which contains two such motifs, MOS11 comprises five (Jacobsen *et al.* 2016; Xie *et al.* 2023). Its nucleic acid-binding and annealing activities were characterised, and its effect on UAP56-mediated unwinding was assessed using MOS11 mutants in which different numbers or combinations of helical motifs were mutated.

2. Material

2.1. Equipment and devices

Table 2: Used equipment and devices with their corresponding suppliers.

Name	Supplier
ÄKTA™ purifier System	GE Healthcare, Chicago, USA
Bio Dancer	New Brunswick Scientific, Edison, USA
Biological Safety Cabinet Herasafe™	Thermo Fisher Scientific, Waltham, USA
Centrifuge 5424	Eppendorf, Hamburg, Germany
Centrifuge 5430 R	Eppendorf, Hamburg, Germany
Centrifuge 8KS	Sigma-Aldrich Chemie, Taufkirchen, Germany
Centrifuge Avanti JXN-26	Beckman Coulter, Krefeld, Germany
Centrifuge Heraeus Megafuge 40R	Thermo Fisher Scientific, Waltham, USA
ChemoCam Imager	Intas Science Imaging Instruments, Göttingen, Germany
Concentrator RVC 2-18 CD plus	Christ, Osterode, Germany
Electrophoresis Power Supply – EPS 301	GE Healthcare, Chicago, USA
Epson Perfection 3200 Photo	Seiko Epson Corporation, Suwa, Japan
Falcon, 15 ml	Sarstedt AG & Co. KG, Nümbrecht, Germany
Falcon, 50 ml	Sarstedt AG & Co. KG, Nümbrecht, Germany
Gel iX Imager	Intas Science Imaging Instruments, Göttingen, Germany
Incubator BM 400	Memmert, Schwabach, Germany
Incubator IKA KS 4000 ic control	IKA-Werke, Staufen, Germany
Incubator Innova 4000	New Brunswick Scientific, Edison, USA
Mettler PM2000 Laboratory Balance Scale	Mettler-Toledo GmbH, Vienna, Austria
Milli-Q ® integral water purification system	Merck, Darmstadt, Germany
Mini-PROTEAN® Tetra Vertical Electrophoresis Cell	Bio-Rad Laboratories, Vienna, Austria
Mobicol “classic” column	MoBiTec, Göttingen, Germany
neoLab Rotator	neoLab Migge, Heidelberg, Germany
Nylon membrane Amersham Hybond™-N+	GE Healthcare, Chicago, USA
Optima XPN-80 Ultracentrifuge	Beckman Coulter, Krefeld, Germany
Owl EasyCast B1A electrophoresis system	Thermo Fisher Scientific, Waltham, USA
Parafilm® “M” Laboratory Film	Amcor, Zürich, Switzerland

pH meter pH 1000L	pH meter pH 1000L
Pipettetips	Sarstedt AG & Co. KG, Nümbrecht, Germany
Protino Ni-IDA 2000 column	Macherey-Nagel, Düren, Germany
Reaction tubes	Eppendorf, Hamburg, Germany
Sonifier 250	Branson Ultrasonics Corporation, Danbury, USA
Stopped flow SF-61SX2	TgK Scientific Limited, Bradford-on-Avon, UK
Superdex 75 Increase 10/300 GL	Cytiva, Marlborough, USA
Superdex 200 Increase 10/300 GL	Cytiva, Marlborough, USA
Tecan Infinite F Plex	Tecan Trading AG, Männedorf, Switzerland
Tecan Infinite F200 Pro	Tecan Trading AG, Männedorf, Switzerland
Tecan Sunrise	Tecan Trading AG, Männedorf, Switzerland
Thermocycler peqSTAR XS	VWR International, Darmstadt, Germany
Thermocycler Tpersonal 48	Biometra, Jena, Germany
Thermomixer 5436	Eppendorf, Hamburg, Germany
Trans-Blot Turbo Transfer System	Bio-Rad Laboratories, Vienna, Austria
Typhoon FLA 9500	GE Healthcare, Chicago, USA
Vivaspin protein concentrator spin column, 10K MWCO	Cytiva, Marlborough, USA
WPA CO8000 Cell Density Meter	Biochrom, Cambridge, UK
Zeba™ Spin Desalting Columns, 7K MWCO	Thermo Fisher Scientific, Waltham, USA
Zeba™ Spin Desalting Columns, 40K MWCO	Thermo Fisher Scientific, Waltham, USA

2.2. Chemicals

Table 3: Used chemicals with their corresponding suppliers.

Name	**Supplier**
Acetic acid	Carl Roth, Karlsruhe, Germany
Acrylamide – Solution (40%) – Mix 29:1	AppliChem, Darmstadt, Germany
Adenosine triphosphate (ATP)	Jena Bioscience, Jena, Germany
Adenylyl-imidodiphosphate (AMPPNP)	Jena Bioscience, Jena, Germany
Agar bacteriology grade	AppliChem, Darmstadt, Germany
Agarose Basic	AppliChem, Darmstadt, Germany
Ammonium sulfate	Merck, Darmstadt, Germany
Ammonium persulfate (APS)	Sigma-Aldrich Chemie, Taufkirchen, Germany
Ampicillin	AppliChem, Darmstadt, Germany

Bacto Peptone	Becton, Dickinson and Company (BD), Erembodegem, Belgium
Bacto Yeast Extract	Becton, Dickinson and Company (BD), Erembodegem, Belgium
Benzamidine hydrochloride	MP Biomedicals, Irvine, USA
β-Mercaptoethanol	Merck, Darmstadt, Germany
β-Nicotinamide adenine dinucleotide (NAD+)	Fluka Chemie, Buchs, Switzerland
Boric acid	Merck, Darmstadt, Germany
Bromophenol blue	AppliChem, Darmstadt, Germany
Coomassie Brilliant Blue G-250	AppliChem, Darmstadt, Germany
CheLuminate-HRP ECL solution	Intas Science Imaging Instruments, Göttingen, Germany
Chloroform	Merck, Darmstadt, Germany
D-(+)-Galactose	AppliChem, Darmstadt, Germany
D-(+)-Glucose monohydrate	Sigma-Aldrich Chemie, Taufkirchen, Germany
DEPC H_2O	Carl Roth, Karlsruhe, Germany
Deoxyadenosine triphosphate (dATP)	Thermo Fisher Scientific, Waltham, USA
Deoxycytidine triphosphate (dCTP)	Thermo Fisher Scientific, Waltham, USA
Deoxyguanosine triphosphate (dGTP)	Thermo Fisher Scientific, Waltham, USA
Deoxythymidine triphosphate (dTTP)	Thermo Fisher Scientific, Waltham, USA
Dimethylsulfoxid (DMSO)	Invitrogen, Waltham, USA
Dithiothreitol (DTT)	AppliChem, Darmstadt, Germany
Ethanol ≥99,5%	Thermo Fisher Scientific, Waltham, USA
Ethylenediaminetetraacetic acid disodium salt dehydrate (EDTA)	Sigma-Aldrich Chemie, Taufkirchen, Germany
Glycerin ROTIPURAN® ≥99,5%, p.a.	Carl Roth, Karlsruhe, Germany
HDGreen™ Plus DNA stain	Intas Science Imaging Instruments, Göttingen, Germany
HEPES	Carl Roth, Karlsruhe, Germany
Hydrochloric acid (HCl)	Carl Roth, Karlsruhe, Germany
Herring Sperm DNA	Thermo Fisher Scientific, Waltham, USA
IGEPAL	Sigma-Aldrich Chemie, Taufkirchen, Germany
Imidazole	Merck, Darmstadt, Germany
Isopropanol (2-Propanol)	Carl Roth, Karlsruhe, Germany
Isopropyl β-D-1-thiogalactopyranoside (IPTG)	Carl Roth, Karlsruhe, Germany
Kanamycin	AppliChem, Darmstadt, Germany
Leupeptin	Merck, Darmstadt, Germany
L-Histidine	Sigma-Aldrich Chemie, Taufkirchen, Germany

Liquid nitrogen	Linde GmbH, Pullach, Germany
L-Leucine	Sigma-Aldrich Chemie, Taufkirchen, Germany
L-Tryptophan	Sigma-Aldrich Chemie, Taufkirchen, Germany
Magnesium chloride ($MgCl_2$)	New England Biolabs
Magnesium sulfate ($MgSO_4$)	Merck, Darmstadt, Germany
MES	Carl Roth, Karlsruhe, Germany
Methanol	Merck, Darmstadt, Germany
MTS-4-NHS	Biozol, Hamburg, Germany
Pepstatin A	Merck, Darmstadt, Germany
Phenylmethylsulfonyl fluoride (PMSF)	AppliChem, Darmstadt, Germany
Polythylene glycol 4000 (PEG-4000)	Fluka Chemie, Buchs, Switzerland
Potassium chloride (KCl)	ORG Laborchemie, Bunde, Germany
Potassium dihydrogen phosphate (KH_2PO_4)	Merck, Darmstadt, Germany
Potassium hydroxide (KOH)	Merck, Darmstadt, Germany
Powdered milk, fat free, blotting grade	Carl Roth, Karlsruhe, Germany
Protino Ni-NTA Agarose	Macherey-Nagel, Düren, Germany
Sodium acetate (NaOAc)	Merck, Darmstadt, Germany
Sodium chloride (NaCl)	Merck, Darmstadt, Germany
Sodium dihydrogen phosphate monohydrate (NaH2PO4 * H2O)	Carl Roth, Karlsruhe, Germany
Sodium dodecyl sulfate (SDS)	AppliChem, Darmstadt, Germany
Sodium hydroxide (NaOH)	Merck, Darmstadt, Germany
Tetramethylethylenediamine (TEMED)	Carl Roth, Karlsruhe, Germany
Trichloroacetic acid ≥99%, p.a. (TCA)	Carl Roth, Karlsruhe, Germany
Tris(2-carboxyethyl)22hosphine (TCEP)	Sigma-Aldrich Chemie, Taufkirchen, Germany
Tris	AppliChem, Darmstadt, Germany
Triton X-100	AppliChem, Darmstadt, Germany
Tween 20	Sigma-Aldrich Chemie, Taufkirchen, Germany
Uracil	Sigma-Aldrich Chemie, Taufkirchen, Germany
Yeast extract	AppliChem, Darmstadt, Germany

2.3. Kits

Table 4: Used kits and their purpose.

Kit	Supplier	Purpose
Mix & Go *E. coli* Transformation Kit & Buffer Set	Zymo research (Freiburg, Germany)	Preparation of Z-competent™ *E. coli cells*
NucleoSpin Plasmid (NoLid)	Macherey-Nagel, Düren, Germany	Plasmid isolation from *E. coli* cells
NucleoSpin Gel and PCR Clean-up Kit	Macherey-Nagel, Düren, Germany	Purification of PCR products
Pierce™ BCA Protein Assay Kit	Thermo Fisher Scientific, Waltham, USA	Determination of protein concentration

2.4. Standards

Table 5: DNA and protein standards.

Standard	Supplier
1 kb Plus DNA Ladder	NEB, Frankfurt/Main, Germany
Unstained Protein Standard, Broad Range (10-200 kDa)	NEB, Frankfurt/Main, Germany
Color Prestained Protein Standard, Broad Range (11-245 kDa)	NEB, Frankfurt/Main, Germany

2.5. Enzymes

Table 6: Enzymes used in this study.

Enzyme	Supplier
Phusion High Fidelity DNA polymerase	NEB, Frankfurt/Main, Germany
Q5 High-Fidelity DNA polymerase	NEB, Frankfurt/Main, Germany
Taq DNA polymerase	NEB, Frankfurt/Main, Germany
DpnI (recognition site: Gm6A^TC)	NEB, Frankfurt/Main, Germany
His-TEV protease	Own preparation
Proteinase K	Thermo Fisher Scientific, Waltham, USA
Zymolyase 100T	Carl Roth, Karlsruhe, Germany

2.6. Antibodies

Table 7: Antibodies used for Western blot.

Antibody	Source	Type	Dilution	Supplier
Anti-Tho1	Rabbit	Polyclonal	1:5000	Pineda Lab
Anti-Pgk1	Mouse	Polyclonal	1:10000	22C5D8, 59250 Invitrogen, Waltham, USA
Anti-rabbit-HRPO	Goat	Monoclonal	1:3000	Bio-Rad, Hercules, USA
Anti-mouse-HRPO	Goat	Monoclonal	1:3000	Bio-Rad, Hercules, USA

2.7. Buffers

Table 8 summarizes the compositions of all buffers used in this study. In general, buffers were prepared using Milli-Q water (Merck, Darmstadt, Germany). Stock solutions were either autoclaved at 120°C for 20 min or, if heat-sensitive, filtered through a 0.22 µm sterile filter.

Table 8: Buffers and solutions organised by purpose.

Purpose	Name	Composition/Supplier
Gibson assembly	5x Isothermal reaction buffer (ISO)	500 mM Tris-HCl, pH 7.5 50 mM $MgCl2{\cdot}7H_2O$ 1 mM dATP, 1 mM dTTP, 1 mM dCTP, 1 mM dGTP 50 mM DTT, 25% (w/v) PEG-8000 5 mM NAD^+
Agarose gel electrophoresis	6x Gel Loading Dye, Purple	NEB, Frankfurt/Main, Germany
	50x Tris-acetate-EDTA buffer (TAE)	2 M Tris, pH 8.0 1 M Na-Oac 50 mM EDTA
PCR	5x Q5® reaction buffer	NEB, Frankfurt/Main, Germany
	10x Q5® reaction buffer	100 mM Tris-HCl, pH 9.0 0.5 M KCl 1% (w/v) Triton X-100 15 mM $MgCl_2$
Harvesting of *E. coli* cells	1x Sodium Chloride-Tris EDTA buffer (STE)	10 mM Tris-HCl, pH 8.0 100 mM NaCl 0.1 mM EDTA
Protein purification	100x Protease inhibitor	8 ng/ml Leupeptin 137 ng/ml Pepstatin A 17 ng/ml PMSF 0.33 mg/ml Benzamidine solved in 100% EtOH

Protein purification	Lysis buffer	150 mM KCl 50 mM HEPES-KOH, pH 7.5 10% Glycerin 15 mM Imidazol 0.15% IPEGAL
	Wash buffer 1	300 mM KCl 50 mM HEPES-KOH, pH 7.5 10% Glycerin 15 mM Imidazol 0.15% IPEGAL
	Wash buffer 2	500 mM KCl 50 mM HEPES-KOH, pH 7.5 10% Glycerin 15 mM Imidazol 0.15% IPEGAL
	Wash buffer 3	700 mM KCl 50 mM HEPES-KOH, pH 7.5 10% Glycerin 15 mM Imidazol 0.15% IPEGAL
	Wash buffer 4	1000 mM KCl 50 mM HEPES-KOH, pH 7.5 10% Glycerin 15 mM Imidazol 0.15% IPEGAL
	Elution buffer	150 mM KCl 50 mM HEPES-KOH, pH 7.5 10% Glycerin 250 mM Imidazol
	Gelfitration buffer	50 mM KCl 50 mM HEPES-KOH, pH 7.5 10% Glycerin
SDS-PAGE	4x Stacking gel buffer	0.5 M Tris-HCl, pH 6.8 8 mM EDTA 0.4% (w/v) SDS
	4x Seperating gel buffer	1.5 M Tris-HCl, pH 8.8 8 mM EDTA 0.4% (w/v) SDS
	4x Laemmli SDS sample buffer	250 mM Tris-HCl, pH 6.8 9% (w/v) SDS 40% (v/v) glycerol 0.2% (w/v) bromphenol blue 100 mM DTT
	5x SDS running buffer	125 mM Tris-HCl 0.95 M glycine 0.5% (w/v) SDS
	Coomassie G-250 staining solution	15% (v/v) EtOH 85% (v/v) Milli-Q water 4% (w/v) ammonium sulfate 1.5% (w/v) β-cyclod
Preparation of nucleic acid substrates	5x Annealing buffer	250 mM KCl 50 mM HEPES-KOH, pH 7.5
EMSA	2x Binding buffer	20 mM MES, pH 6.5 10% Glycerin# 4 mM TCEP

EMSA	10x TBE buffer	1 M Tris-HCl pH 8.3 1 M boric acid 25 mM EDTA
Protein activity assay	Helicase buffer	50 mM HEPES-KOH, pH 7.5 4 mM TCEP
Crosslinking Buffer	MTS-4-NHS Crosslinking	50 mM HEPES-KOH, pH 7.5 50 mM KCl 10% glycerol 0.5 mM $MgCl_2$
Yeast transformation	Solution 1	10 mM Tris-HCl, pH 7.5 1 mM EDTA 100 mM LiOAc
	Solution 2	10 mM Tris-HCl, pH 7.5 1 mM EDTA 100 mM LiOAc 40% PEG 4000
Alkaline lysis	Pre-treatment solution	7.5% β-mercaptoethanol 1.85 M NaOH
Western Blot	1x TBST	50 mM Tris-HCl, pH 7.5 150 mM NaCl 0.1% (v/v) Tween 20
	Semi-dry blotting buffer	25 mM Tris 192 mM glycine 20% (v/v) methanol

2.8. Plasmids

All Plasmids used or generated in this study are listed in Table 9. Plasmids for recombinant expression of Tho1, Sub2 and their orthologs or mutants were derived from vector pT7-His6-TEV. This vector carries a T7 promoter and terminator located upstream and downstream of the inserted gene, respectively, as well as a *lacI* gene to allow IPTG-inducible protein expression. Additionally, the plasmid contains an N-terminal hexahistidine (His6) tag and a TEV protease cleavage site located upstream of the inserted gene. Kanamycin was used as a selection marker. *A. thaliana* genes encoding *MOS11* and *UAP56* were amplified from cDNA kindly provided by Prof. Dr. Karl-Heinz Kogel (Justus Liebig University Giessen). Genomic DNA of *Schizosaccharomyces pombe,* for the amplification of *MLO1* was kindly provided by Dr. Cornelia Kilcher (Justus Liebig University Giessen).

Overexpression of Tho1 and Tho1 mutants in yeast cells was performed using plasmids derived from pRS424 vector. In this vector, the inserted *THO1* constructs are flanked by the 5' and 3' untranslated regions (UTRs) of endogenous *THO1*. Ampicillin was used for selection in *E. coli*, while *TRP1*, encoding phosphoribosylanthranilate isomerase, served as a selection marker in *S. cerevisiae* by enabling tryptophan biosynthesis.

Constructs intended for genomic integration of *THO1* and *THO1* mutants were amplified from YepGal-derived plasmids. These vectors contain the *GAL1* promotor upstream of the inserted gene for inducible protein expression, and the *ADH1* terminator downstream. A leucine cassette was used as the selection marker.
Some plasmids were generated by Karin Pietsch (K.P.), Giuseppina Di Nolfo (G.D.N.), Jan Kohlert (J.K.), and Amelie Müller (A.M.) during their bachelor's theses, and by Minhaz Mannan (M.M.) during his master's thesis, conducted concurrently with this work.

Table 9: Plasmids used in this study.

Plasmid	Description	Reference
pT7-His6-TEV-*THO1*	For recombinant expression of Tho1 in *E. coli*	(Miosga 2022)
pT7-His6-TEV-*MLO1*	For recombinant expression of *Schizosaccharomyces pombe* Mlo1 in *E. coli*	This work
pT7-His6-TEV-*MOS11*	For recombinant expression of *Arabidopsis thaliana* MOS11 in *E. coli*	M.M.
pT7-His6-TEV- *tho1*-ΔSAP	For recombinant expression of Tho1-ΔSAP (deletion of aa 1-50) in *E. coli*	(Miosga 2022)
pT7-His6-TEV- *tho1*-ΔCTD	For recombinant expression of Tho1-ΔCTD (deletion of aa 117-183) in *E. coli*	(Miosga 2022)
pT7-His6-TEV- *tho1*-ΔCTE	For recombinant expression of Tho1-ΔCTE (deletion of aa 184-218) in *E. coli*	(Miosga 2022)
pT7-His6-TEV-*tho1*-CTD	For recombinant expression of Tho1-CTD (aa 117-183) of Tho1 in *E. coli*	(Miosga 2022)
pT7-His6-TEV-ΔSAP ΔLinker	For recombinant expression of Tho1-ΔSAP ΔLinker (deletion of aa 1-116) in *E. coli*	(Miosga 2022)
pT7-His6-TEV-*SUB2*	For recombinant expression of *S. saccharomyces* Sub2	(Miosga 2022)
pT7-His6-TEV-s*ub2*-D302R	For recombinant expression of Sub2 interface mutant D302R in *E. coli*	This work
pT7-His6-TEV-*tho1*-CTD-R139D	For recombinant expression of Tho1-CTD with Sub2 interface mutation R139D in *E. coli*	This work
pT7-His6-TEV-*tho1*-CTD-R159D	For recombinant expression of Tho1-CTD with Sub2 interface mutation R159D in *E. coli*	This work
pT7-His6-TEV-*tho1*-CTD-R139D-R159D	For recombinant expression of Tho1-CTD with mutations R139D and R159D in *E. coli*	This work
pT7-His6-TEV-*tho1*-CTD-R139K	For recombinant expression of Tho1-CTD with Sub2 interface mutation R139K in *E. coli*	This work
pT7-His6-TEV-*tho1*-CTD-K142R	For recombinant expression of Tho1-CTD with Sub2 interface mutation K142R in *E. coli*	This work
pT7-His6-TEV-*tho1*-CTD-F143Y	For recombinant expression of Tho1-CTD with Sub2 interface mutation F143Y in *E. coli*	This work
pT7-His6-TEV-*tho1*-CTD-G144A	For recombinant expression of Tho1-CTD with Sub2 interface mutation G144A in *E. coli*	This work
pT7-His6-TEV-*tho1*-CTD-R159K	For recombinant expression of Tho1-CTD with Sub2 interface mutation R159K in *E. coli*	This work
pT7-His6-TEV-*tho1*-CTD-K162R	For recombinant expression of Tho1-CTD with Sub2 interface mutation K162R in *E. coli*	This work

pT7-His6-TEV-*tho1*-CTD-F163Y	For recombinant expression of Tho1-CTD with Sub2 interface mutation F163Y in *E. coli*	This work
pT7-His6-TEV-*tho1*-CTD-G164A	For recombinant expression of Tho1-CTD with Sub2 interface mutation G164A in *E. coli*	This work
pRS424	high copy number plasmid, 2µ, with TRP maker	(Sikorski & Hieter 1989)
pRS424-*THO1*	ORF + 500 bp of 5' and 300 bp of 3' UTR of *THO1* was cloned into pRS424	This work
pRS424-tho1-ΔSAP	Overexpression of Tho1-ΔSAP (deletion of aa 1-50) in *S. cerevisiae*	K.P. and G.D.N
pRS424-tho1-ΔCTD	Overexpression of Tho1-ΔCTD (deletion of aa 117-183) in *S. cerevisiae*	K.P. and G.D.N
pRS424-tho1-ΔCTE	Overexpression of Tho1-ΔCTE (deletion of aa 184-218) in *S. cerevisiae*	K.P. and G.D.N
pRS424-*tho1*-ΔSAP ΔLinker	Overexpression of Tho1-ΔSAP ΔLinker (deletion of aa 1-116) in *S. cerevisiae*	K.P. and G.D.N
YepGal Tho1 wt	Overexpression of Tho1 after integration of P_{GAL1}*:THO1* in genomic *THO1* locus	This work
YepGal Tho1-CTD	Overexpression of Tho1-CTD after integration of P_{GAL1}*:THO1-CTD* in genomic *THO1* locus	This work
YepGal Tho1-CTD-R139K	Overexpression of Tho1-CTD-R139K after integration of P_{GAL1}*:THO1-CTD R139K* in genomic *THO1* locus	This work
YepGal Tho1-CTD-R159K	Overexpression of Tho1-CTD-R159K after integration of P_{GAL1}*:THO1-CTD R159K* in genomic *THO1* locus	This work
pT7-His6-TEV-*AtUAP56*	For recombinant expression of *A. thaliana* UAP56	M.M.
pT7-His6-TEV-*AtUAP56*-D284R	For recombinant expression of *A. thaliana* UAP56 interface mutant D284R in *E. coli*	J.K.
pT7-His6-TEV-*Sub2*-S329C	For recombinant expression of Sub2 cysteine mutant S329C in *E. coli*	This work
pUC57 MOS11_mut_RK	Purchased vector encoding *A. thaliana* MOS11 with mutations R106K, R135K, R160K, R181K	ProteoGenix (Schiltigheim, France)
pUC57 MOS11_mut_RD	Purchased vector encoding *A. thaliana* MOS11 with mutations R106D, R135D, R160D, R181D	ProteoGenix (Schiltigheim, France)
pT7-His6-TEV-*MOS11*-Mot.0	For recombinant expression of *A. thaliana* MOS11 with mutations R87K, R106K, R135K, R160K, R181K	A.M.
pT7-His6-TEV-*MOS11*-Mot.1	For recombinant expression of *A. thaliana* MOS11 with mutations R106K, R135K, R160K, R181K	A.M.
pT7-His6-TEV-*MOS11*-Mot.1 RD	For recombinant expression of *A. thaliana* MOS11 with mutations R106D, R135D, R160D, R181D	A.M.
pT7-His6-TEV-*MOS11*-Mot.1+2	For recombinant expression of *A. thaliana* MOS11 with mutations R135K, R160K, R181K	A.M.
pT7-His6-TEV-*MOS11*-Mot.1-3	For recombinant expression of *A. thaliana* MOS11 with mutations R160K, R181K	A.M.
pT7-His6-TEV-*MOS11*-Mot.1-4	For recombinant expression of *A. thaliana* MOS11 with mutations R181K	A.M.
pT7-His6-TEV-*MOS11*-Mot.1+3	For recombinant expression of *A. thaliana* MOS11 with mutations R106K, R160K, R181K	This work

pT7-His6-TEV-*MOS11*-Mot.1+4	For recombinant expression of *A. thaliana* MOS11 with mutations R106K, R135K, R181K	This work
pT7-His6-TEV-*MOS11*-Mot.1+5	For recombinant expression of *A. thaliana* MOS11 with mutations R106K, R135K, R160K	This work

2.9. Oligonucleotides

All Oligonucleotides listed in Table 10, were purchased from Biolegio B.V. (Nijmegen, Netherlands).

Table 10: Oligonucleotides used for cloning.

Name	**Sequence 5′-3′**
BbseqA302	ATCTTCCCCATCGGTGATGTC
BbseqB236	TAGAGGCCCCAAGGGGTTAT
PF843_Sp-Mlo1-5‘_fwd	GAAAACCTGTATTTTCAGGGCATGTCAGATTACAAGAGTCTTAAAGTTGC
PF844_Sp-Mlo1-5’_rev	GCAACTTTAAGACTCTTGTAATCTGACATGCCCTGAAAATACAGGTTTTC
PF845_Sp-Mlo1-3‘_fwd	CGCTTTGGTGTTGCTGCCAAGAATTAAGGATCCGGCTGCTAACAAAGCCC
PF846_Sp-Mlo1-3’_rev	GGGCTTTGTTAGCAGCCGGATCCTTAATTCTTGGCAGCAACACCAAAGCG
PF847_Mos11-5’_fwd	GAAAACCTGTATTTTCAGGGCATGGCGACCAACGGAGAGAAGG
PF848_Mos11-5’_rev	CCTTCTCTCCGTTGGTCGCCATGCCCTGAAAATACAGGTTTTC
PF849_Mos11-3’_fwd	GCTGTATCAGGAAGCGCTGCCTAAGGATCCGGCTGCTAACAAAGCCCG
PF850_Mos11-3’_rev	CGGGCTTTGTTAGCAGCCGGATCCTTAGGCAGCGCTTCCTGATACAGC
PF851_RBD_5’_fwd	GGAGCCAGCACAAGCACTTACAATGGCTCCCGCTTTGTCACC
PF852_RBD_5’_rev	GGTGACAAAGCGGGAGCCATTGTAAGTGCTTGTGCTGGCTCC
PF853_RBD_3’_fwd	GGGCCTTGTCAGTAGGAAAAATGAATAAAGGCTCAAGCCGTTTTGGTGG
PF854_RBD_3’_rev	CCACCAAAACGGCTTGAGCCTTTATTCATTTTTCCTACTGACAAGGCCC
PF855_RBD+CTE_3’_for	GCAACCGCTCTGGTTACAGAAGAtaaAGGCTCAAGCCGTTTTGGTGG
PF856_RBD+CTE_3’_rev	CCACCAAAACGGCTTGAGCCTttaTCTTCTGTAACCAGAGCGGTTGC
PF857_deltaSAP_5’_for	GGAGCCAGCACAAGCACTTACAATGGAACAAAACCAGGAACAAGGG
PF858_deltaSAP_5’_rev	CCCTTGTTCCTGGTTTTGTTCCATTGTAAGTGCTTGTGCTGGCTCC
PF859_deltaRBD_5’_for	GGAGCCAGCACAAGCACTTACAATGGCAGATTATTCTTCCCTTACTG
PF860_deltaRBD_5’_rev	CAGTAAGGGAAGAATAATCTGCCATTGTAAGTGCTTGTGCTGGCTCC

PF861_pRS424_Seq_for	GTGTCCTTTCAGGATGCGCTAC
PF862_pRS424_Seq_ rev	GCGGCCGCTCTAGAACTAGTG
PF863_AtUAP56_5'_for	AAACCTGTATTTTCAGGGCATGGGAGACGCTAG
PF864_AtUAP56_5'_rev	CTAGCGTCTCCCATGCCCTGAAAATACAGGTTT
PF865_AtUAP56_3'_for	CAACCTACATGCCTTCTTAAGGATCCGGCTGCTAACAAAGC
PF866_AtUAP56_3'_rev	GCTTTGTTAGCAGCCGGATCCTTAAGAAGGCATGTAGGTTG
PF871_UAP56_D284R_ fwd	CGGAAGTTGAATGACCTTCTTAGAGCGTTGGACTTCAATCAAG
PF872_UAP56_D284R_ rev	CTTGATTGAAGTCCAACGCTCTAAGAAGGTCATTCAACTTCCG
MM30_KanR Fragment FOR	TTTCCCGGGGATCGCAGTGGTGAG
MM31_KanR Vektor REV	CTCACCACTGCGATCCCCGGGAAA
DB141_Sub2_D302R_rev	GAACTCCAAATCTCTTAATAATTGAGCCAATTTACG
DB142_Sub2_D302R_fwd	CTCAATTATTAAGAGATTTGGAGTTCAATCAAG
MM69_CTD_R139K_fwd	TAAGAAACTGCACAAAGCTAACAAATTCG
MM70_CTD_R139K_rev	CGAATTTGTTAGCTTTGTGCAGTTTCTTA
MM75_CTD_R159K_fwd	AAGACAGATAAATAAAGTGGAGAAGTTTG
MM75_CTD_R159K_rev	CAAACTTCTCCACTTTATTTATCTGTCTT
PF873_CTD_R139D_fwd	CTTTTAAATAAGAAACTGCACGATGCTAACAAATTCGGTC
PF874_CTD_R139D_rev	GACCGAATTTGTTAGCATCGTGCAGTTTCTTATTTAAAAG
PF875_CTD_R159D_fwd	CAAAGACAGATAAATGATGTGGAGAAGTTTGGTGTTGAC
PF876_CTD_R159D_rev	GTCAACACCAAACTTCTCCACATCATTTATCTGTCTTTG
PF877_MOS11_R87K_ fwd	GATATCCAGAAGAAGATTCGAAAAGCTGAGAGGTTTGGTG
PF878_MOS11_R87K_rev	CACCAAACCTCTCAGCTTTTCGAATCTTCTTCTGGATATC
PF879_MOS11_R87D_ fwd	GATATCCAGAAGAAGATTCGAGATGCTGAGAGGTTTGGTG
PF880_MOS11_R87D_ rev	CACCAAACCTCTCAGCATCTCGAATCTTCTTCTGGATATC
PF881_MOS11_Mot2-3_fwd	CTGCAGCAGTGGTGAATGGCTCAGAGGGAACG
PF882_MOS11_Mot2-3_rev	CGTTCCCTCTGAGCCATTCACCACTGCTGCAG
PF883_MOS11_Mot3-4_fwd	CTTCTGCGACCTCTACTACTGATAAGACTGAGG
PF884_MOS11_Mot3-4_rev	CCTCAGTCTTATCAGTAGTAGAGGTCGCAGAAG
PF885_MOS11_Mot4-5_fwd	GAGACTAAAGTTGATTCTGCTGAAGAAAATAAG
PF886_MOS11_Mot4-5_rev	CTTATTTTCTTCAGCAGAATCAACTTTAGTCTC

PF887_Sub2_S329C_fwd	CCAAACTATTAAACGCCTGTAACTTTCCGGCTATCACCG
PF888_Sub2_S329C_rev	CGGTGATAGCCGGAAAGTTACAGGCGTTTAATAGTTTGG
PF889_5'-YepGal-Tho1_fwd	CGTCAAGGAGAAAAAACGGATCCATGGCAGATTATTCTTCCCTTAC
PF890_5'-Tho1-YepGal_rev	GTAAGGGAAGAATAATCTGCCATGGATCCGTTTTTTCTCCTTGACG
PF891_3'-Tho1-YepGal_fwd	CAACCGCTCTGGTTACAGAAGATAAGGCGCGCCACTTCTAAATAAGCGAA
PF892_3'-YepGal-Tho1_rev	TTCGCTTATTTAGAAGTGGCGCGCCTTATCTTCTGTAACCAGAGCGGTTG
PF893_5'-YepGal-CTD_fwd	CGTCAAGGAGAAAAAACGGATCCATGGCTCCCGCTTTGTCACCAGAAG
PF894_5'-CTD-YepGal-rev	CTTCTGGTGACAAAGCGGGAGCCATGGATCCGTTTTTTCTCCTTGACG
PF895_3'-CTD-YepGal_fwd	CCTTGTCAGTAGGAAAAATGAATAAGGCGCGCCACTTCTAAATAAGCGAA
PF896_3'-YepGa-CTD-rev	TTCGCTTATTTAGAAGTGGCGCGCCTTATTCATTTTTCCTACTGACAAGG
PF903_pGAL_fwd_2	GAATTTTTTTCACCACTAGAATTGTTCTTGGAGCCAGCACAAGCACTTACATTTCAAAAATTCTTACTTTTTTTTTGGATGGACGC
PF898_pLEU_rev	GGAAAGAACCGAAACTAGAATGAAAAACTCCACCAAAACGGCTTGAGCCTAACTGTGGGAATACTCAGGTATCGTAAG
PF899_pGal_rev	CATCGCTTCGCTGATTAATTACCCC
PF900_5'UTR_fwd	CAAATGTGTCCTTTCAGGATGCGC
PF901_YepGal_seq	GGGGTAATTAATCAGCGAAGCGATG

All Oligonucleotides used for binding, annealing, or helicase *in vitro* assays (listed in Table 11) were synthesized and purchased from Biolegio B.V. (Nijmegen, Netherlands) or Eurogentec (Seraing, Belgium). Oligonucleotides delivered as dried pellets were dissolved in DEPC-treated water (Carl Roth, Germany). Sequences were taken either from Ma et al. (2013) or Putnam and Jankowsky (2013). RNA oligonucleotides were stored at -80°C, and DNA oligonucleotides were stored at -20°C.

Table 11: Oligonucleotides used for *in vitro* assays.

Name	**Sequence 5'-3'**	**Label**	**Ref**
6FAM-RNA_10	AGCACCGUAA	6-FAM (5')	Put
RNA_13	AGCACCGUAAAGA		Put
RNA_13-BHQ-2	AGCACCGUAAAGA	BHQ®-2 (3')	Put
Cy3-RNA_13	AGCACCGUAAAGA	Cy3 (5')	Put
6FAM-RNA_13	AGCACCGUAAAGA	6-FAM (5')	Put
6FAM-DNA_13	AGCACCGTAAAGA	6-FAM (5')	Put

6FAM-RNA_16	AGCACCGUAAAGACGC	6-FAM (5')	Ma
RNA_13_ Cy5	UCUUUACGGUGCU	Cy5 (5')	Put
DNA_13_Cy5	TCTTTACGGTGCT	Cy5 (5')	Put
RNA_16_21_Cy5	GCGUCUUUACGGUGCUUAAAACAAAAC AAAACAAAAC	Cy5 (5')	Ma
DNA_Ma_16_21_Cy5	GCGTCTTTACGGTGCTTAAAACAAAACA AAACAAAAC	Cy5 (5')	Ma
DNA_Ma_Long_Top	GTTTTGTTTTGTTTTGTTTTAAGCACCGTAAA GACGC		Ma
RNA_13_25	UCUUUACGGUGCUUAAAACAAAACAAA ACAAAACAAAA		Put
RNA_13_25 Cy5	UCUUUACGGUGCUUAAAACAAAACAAA ACAAAACAAAA	Cy5 (5')	Put
DNA_13_25 Cy5	TCTTTACGGTGCTTAAAACAAAACAAAAC AAAACAAAA	Cy5 (5')	Put
5OH_RNA_38_BHQ2	AAAACAAAACAAAACAAAACAAAAUAGC ACCGUAAAGA	BHQ®-2 (3')	Put

2.10. Media

Table 12 provides a list of all media used for the cultivation of *E. coli* and *S. cerevisiae* cells. All media were prepared with Milli-Q water (Merck, Germany) and autoclaved for 20 minutes at 121°C. LB medium was supplemented with the appropriate antibiotic at a final concentration of 25 µg/ml. For selective yeast media, amino acids were omitted as needed. For agar plates, 2% (w/v) agar was added to the media before autoclaving.

Table 12: Used media organised by purpose.

Purpose	Name	Composition	Reference
Z-competent™ *E. coli* cells	SOB	2% (w/v) tryptone 0.5% (w/v) yeast extract 10 mM NaCl 2.5 mM KCl 10 mM $MgCl_2$ 10 mM $MgSO_4$ pH 6-7	(Hanahan 1983)
***E. coli* transformation - recovery**	SOC	2% (w/v) tryptone 0.5% (w/v) yeast extract 10 mM NaCl 2.5 mM KCl 10 mM $MgCl_2$ 10 mM $MgSO_4$ 20 mM glucose pH 6- 7	(Hanahan 1983)
***E. coli* cultivation**	LB	1% (w/v) peptone 0.5% (w/v) yeast extract 85.6 mM NaCl pH 7.2	(Bertani 1951)

Yeast cultivation in Glucose	YPD	2% (w/v) peptone 2% (w/v) glucose 1% (w/v) yeast extract	(Sherman 1991)
	SDC	0.67% (w/v) yeast nitrogen base 0.06% (w/v) complete synthetic mix of aa 2% (w/v) glucose	(Werner-Washburne *et al.* 1996)
Yeast cultivation in Galactose	YPG	2% (w/v) peptone 2% (w/v) galactose 1% (w/v) yeast extract	(Sherman 1991)
	SGC	0.67% (w/v) yeast nitrogen base 0.06% (w/v) complete synthetic aa mix 2% (w/v) galactose	(Sherman 1991)

2.11. *E. coli* strains

All plasmids constructed in this work were transformed in *E. coli* strain DH5α, while protein expression was performed in *E. coli* Rosetta 2 cells.

Table 13: *E. coli* strains used for cloning and protein expression.

Strain	Genotype	Reference
DH5α	F– φ80lacZΔM15 Δ(lacZYA-argF)U169 recA1 endA1 hsdR17(rK–, mK+) phoA supE44 λ–thi-1 gyrA96 relA1	(Taylor *et al.* 1993)
Rosetta (DE3)	F- ompT hsdSB(rB- mB-) gal dcm (DE3) pRARE2 (CamR)	(Wood 1966)

2.12. Yeast strains

Table 14 summarizes all yeast strains used or generated in this study. All strains were derived from strain W303, referred to as wild type in the text.

Table 14: Yeast strains used for cloning and protein expression.

Yeast Strain	Genotype	Reference
W303	MATa, ura3-1, trp1-1, his3-11,15, leu2-3,112, ade2-1, can1-100 GAL+	(Thomas & Rothstein 1989)
W303 pRS424	MATa, ura3-1, trp1-1, his3-11,15, leu2-3,112, ade2-1, can1-100 GAL+, pRS424	This work
W303 Δ*hpr1*	MATa, ura3-1, trp1-1, his3-11,15, leu2-3,112, ade2-1, can1-100, GAL+, HPR1::HIS3	This work
W303 Δ*hpr1* pRS424	MATa, ura3-1, trp1-1, his3-11,15, leu2-3,112, ade2-1, can1-100, GAL+, HPR1::HIS3, pRS424	This work
W303 Δ*hpr1* pRS424 *THO1*-wt	MATa, ura3-1, trp1-1, his3-11,15, leu2-3,112, ade2-1, can1-100, GAL+, *HPR1::HIS3, pRS424-THO1*	This work
W303 Δ*hpr1* pRS424 tho*1*-ΔSAP	MATa, ura3-1, trp1-1, his3-11,15, leu2-3,112, ade2-1, can1-100, GAL+, *HPR1::HIS3, pRS424-tho1-ΔSAP*	This work

W303 Δ*hpr1* pRS424 tho*1*-ΔCTD	MATa, ura3-1, trp1-1, his3-11,15, leu2-3,112, ade2-1, can1-100, GAL+, *HPR1::HIS3, pRS424-tho1-ΔCTD*	This work
W303 Δ*hpr1* pRS424 tho*1*-ΔCTE	MATa, ura3-1, trp1-1, his3-11,15, leu2-3,112, ade2-1, can1-100, GAL+, *HPR1::HIS3, pRS424-tho1-ΔCTE*	This work
W303 Δ*hpr1* pRS424 tho*1*-ΔSAPΔLinker	MATa, ura3-1, trp1-1, his3-11,15, leu2-3,112, ade2-1, can1-100, GAL+, *HPR1::HIS3, pRS424-tho1-ΔSAPΔLinker*	This work
W303 Δ*hpr1* pRS424 tho*1*-CTD	MATa, ura3-1, trp1-1, his3-11,15, leu2-3,112, ade2-1, can1-100, GAL+, *HPR1::HIS3, pRS424-tho1-CTD*	This work
W303 Δ*hpr1* P_{GAL1}*:THO1*	MATa, ura3-1, trp1-1, his3-11,15, leu2-3,112, ade2-1, can1-100, GAL+, *HPR1::HIS3, THO1::P_{GAL1}:THO1:LEU*	This work
W303 Δ*hpr1* P_{GAL1}*:tho1-CTD*	MATa, ura3-1, trp1-1, his3-11,15, leu2-3,112, ade2-1, can1-100, GAL+, *HPR1::HIS3, THO1::P_{GAL1}: tho1-CTD:LEU*	This work
W303 Δ*hpr1* P_{GAL1}*:tho1-CTD R139K*	MATa, ura3-1, trp1-1, his3-11,15, leu2-3,112, ade2-1, can1-100, GAL+, *HPR1::HIS3, THO1::P_{GAL1}: tho1-CTD R139K:LEU*	This work
W303 Δ*hpr1* P_{GAL1}*:tho1-CTD R159K*	MATa, ura3-1, trp1-1, his3-11,15, leu2-3,112, ade2-1, can1-100, GAL+, *HPR1::HIS3, THO1::P_{GAL1}: tho1-CTD R159K:LEU*	This work

3. Methods

A majority of the following methods are derived from *Current Protocols in Molecular Biology* from Ausubel *et al.* (1987).

3.1. Microbiological techniques

3.1.1. Determination of optical density (OD)

Cell growth was monitored by measuring the optical density at 600 nm (OD_{600}) of 1 ml *E. coli* or yeast cultures in a cuvette using WPA CO8000 Cell Density Meter (Biochrom, UK). Cultures with an OD_{600} above 0.7 were diluted to maintain measurements within the linear range. The respective growth medium was used as a blank.

3.1.2. Preparation of Z-competent™ *E. coli* cells

Z-competent™ DH5α and Rosetta (DE3) were prepared using the Mix & Go *E. coli* Transformation Kit & Buffer Set (Zymo research, Germany) following the manufacturer's instructions. Cells were divided into 50 µl aliquots for each transformation and stored at -80°C.

3.1.3 Transformation of *E. coli* cells

Z-competent *E. coli* cells were thawed on ice for 5 min. Subsequently, 100 ng of plasmid DNA was added, and the mixture was incubated on ice for 20 min. Rosetta (DE3) cells were additionally heat-shocked at 42°C for 90 s to enhance transformation efficiency. For recovery, 400 µl of SOC medium was added, followed by an incubation at 37°C and 200 rpm for 1 h. Cells were pelleted by centrifugation at 700 x *g* for 1 min, and the supernatant was carefully removed until approximately 100 µl of medium remained. The cell pellet was resuspended, plated on LB agar plates containing 25 µg/ml of the appropriate antibiotic, and incubated overnight at 37°C.

3.1.4. Transformation of competent *S. cerevisiae* cells

A pre-culture of *S. cerevisiae* cells was grown overnight in YPD medium. From this, a 50 ml main culture with an initial OD_{600} of 0.2 was prepared, sufficient for approximately five to six transformations. The main culture was incubated at 30°C with shaking at 170 rpm until it reached mid-log phase (OD_{600} of 0.6-0.8). Cells were harvested by centrifugation at 2800 x *g* for 3 min. The cell pellet was washed once with 10 ml sterile water and centrifuged again at 2800 x *g* for 3 min. The supernatant was discarded, the

pellet washed with 500 µl of Solution I, transferred into a 2 ml reaction tube, and centrifuged again under the same conditions. After removing the supernatant, cells were resuspended in 250 µl of Solution I and kept on ice until further use.
For each transformation, 300 µl of Solution II was mixed with 5 µl of single-stranded (ss) carrier DNA (2 mg/ml) and either 500 ng of plasmid DNA or 10 µg of a PCR fragment for genomic integration. Then, 50 µl of *S. cerevisiae* cells were added to each transformation reaction. For genomic integration, 35 µl DMSO was additionally added. Reactions without DNA served as negative controls. Transformation mixtures were incubated at room temperature for 30 min on a rotating wheel, followed by a heat shock at 42°C for 10 min and a subsequent 5 min incubation on ice. The samples were then diluted with 1 ml of sterile water, centrifuged at 2800 x *g* for 3 min and the supernatant was discarded. For genomic integrations, cells were resuspended in 3 ml of YPD or YPG medium and incubated at 30°C and 170 rpm, overnight for recovery. On the following day cells were centrifuged again (2800 x *g* for 3 min), resuspended in 100 µl of water, and plated onto selective SDC plates. After 3-4 days, single colonies were picked, restreaked out onto fresh plates and screened by colony PCR.

3.1.5. Dot Spot assay

Dot Spot assays were performed to test the thermosensitive growth phenotypes of Δ*hpr1* yeast cells. Either freshly transformed cells carrying an expression plasmid or strains with genomic integration of the respective gene construct were used. A small amount of cells was scraped from agar plates and resuspended in 1 ml of sterile water. The cell density was adjusted to an OD_{600} of 0.2, followed by the preparation of three tenfold serial dilutions. For each dilution, as well as the undiluted suspension, 10 µl was spotted onto selective SDC agar plates. Plates were incubated at 30°C and 37°C for 2-3 days. For plasmid expression, at least three biological replicates were performed for each strain. In the case of genomic integrations, the assay was repeated in three independent experiments.

3.2. Basic molecular biological methods

3.2.1. Plasmid preparation

Following transformation, positive *E. coli* colonies were picked from the plate, transferred into 3 ml of LB medium and incubated overnight at 37°C and 180 rpm. Plasmid isolation was carried out using the *NucleoSpin* Plasmid (NoLid) Kit (Macherey

& Nagel, Germany) following the manufacturer's instructions. Plasmid concentration was determined with the NanoDrop 1000 Spectrophotometer (Thermo Scientific, USA). DNA was stored at -20°C.

3.2.2. Polymerase chain reaction (PCR)

All PCR reactions were performed using either a peqSTAR XS (VWR) or a Tpersonal 48 (Biometra, Germany) thermocycler. For cloning-related PCR reactions, Q5 High-Fidelity DNA Polymerase was used. Experimental conditions, summarised in Tables 15 and 16, were based on the protocol "*PCR Using Q5® High-Fidelity DNA Polymerase (NEB #M0491)*" (NEB, 2023) with minor modifications. The annealing temperature was selected according to the melting temperatures of the respective primers, and the elongation time was adjusted based on the expected length of the PCR product.

Table 15: Setup for a PCR using Q5® High-Fidelity DNA Polymerase.

Step	50 µl	Final concentration
5X Q5 Reaction Buffer	10 µl	1X
2.5 mM dNTPs	5 µl	250 µM
5 µM Forward primer	5 µl	0.5 µM
5 µM Reverse primer	5 µl	0.5 µM
Template DNA	Variable	< 1000 ng
Q5 High-Fidelity DNA Polymerase	0.5 µl	0.2 U/µl
Nuclease-free water	To 50 µl	

Table 16: Q5® High-Fidelity DNA Polymerase thermocycling conditions.

Step	Temperature	Time
Initial denaturation	98°C	30 sec
25-35 cycles	98°C 50-72°C 72°C	5-10 sec 10-30 sec 20-30 sec/kb
Final extension	72°C	2 min
Hold	4-10°C	

3.2.3. Colony PCR of *E. coli* clones

Colony PCR was performed to confirm successful uptake of plasmid DNA in transformed cells. For each transformation, five to ten colonies were picked and

transferred into 20 µl of sterile water. These cell suspensions served as templates for the PCR reaction. Forward and reverse primers were designed to bind to plasmid regions flanking the inserted gene. The experimental conditions were determined according to the instructions in "*PCR Protocol for Taq DNA Polymerase with Standard Taq Buffer (M0273)*" (NEB 2023) and are summarised in Tables 17 and 18.

Table 17: Setup for a PCR using TAC DNA polymerase.

Step	**50 µl**	**Final concentration**
10X TAC Reaction Buffer	5 µl	1X
2.5 mM dNTPs	5 µl	250 µM
5 µM Forward primer	5 µl	0.5 µM
5 µM Reverse primer	5 µl	0.5 µM
Template	5 µl	< 1000 ng
TAC DNA Polymerase	1 µl	0.2 U/µl
Nuclease-free water	To 50 µl	

Table 18: TAC DNA Polymerase thermocycling conditions.

Step	**Temperature**	**Time**
Initial denaturation	98°C	5 min
25-35 cycles	98°C 50-72°C 72°C	5-10 sec 10-30 sec 20-30 sec/kb
Final extension	72°C	2 min
Hold	4-10°C	

3.2.4. Colony PCR of *S. cerevisiae* clones

After transformation, single colonies were restreaked on selective medium and grown for 1-2 days at 30°C. Successful genomic integration was subsequently confirmed by colony PCR. Prior to PCR, cells were lysed enzymatically by scraping a small number of cells from the plate and resuspending them in 15 µl of a 2.5 mg/ml zymolyase solution. Cells were incubated for 20 min at room temperature, 5 min at 37°C, and 5 min at 95°C in a Tpersonal 48 thermocycler (Biometra, Germany). The lysate was then diluted with 60 µl of water, and 5 µl of diluted lysate was used as template. The PCR setup and cycling conditions followed the protocol described in *Colony PCR of E. coli clones* (Chapter 3.2.3). To verify correct integration into the gene locus, primers

that bind to the genomic regions upstream and downstream of the targeted locus were selected.

3.2.5. Gel electrophoresis for nucleic acids

All PCR products were analysed by gel electrophoresis. Gels were prepared by dissolving 1% (w/v) agarose in 1x TAE buffer, followed by heating in a microwave until fully dissolved and cooling down to lukewarm. Intas HDGreen™ Plus DNA dye was added, and the solution was poured into a gel tray. Once solidified, the gel was transferred into an electrophoresis chamber and covered with 1x TAE buffer. Samples were mixed with 6x Purple Gel Loading dye (NEB, Germany) and loaded onto the gel. A 1 kb Plus DNA Ladder (NEB, Germany) was used as a size marker. Electrophoresis was performed at 130 V for 20-30 min and gels were subsequently analysed by exposure to UV light using an Intas Gel iX Imager. If PCR products showed unspecific amplification, the entire reaction was subjected to gel electrophoreses. The band of the expected size was excised and purified using the *NucleoSpin* Gel and PCR Clean-up Kit (Macherey-Nagel, Germany) according to the manufacturer's instructions.

3.2.6. Plasmid cloning by Gibson Assembly

All plasmids generated in this work were constructed using Gibson Assembly (Gibson et al., 2009). Both insert and backbone fragments were amplified by PCR with Q5 DNA-polymerase, as described in Chapter 3.2.2. To remove template DNA, PCR products were treated with DpnI for 1 h at 37°C, followed by heat inactivation at 80°C for 20 min. The resulting fragments were purified using the *NucleoSpin* Gel and PCR Clean-up kit (Macherey-Nagel, Germany) according to the manufacturer's instructions. Gibson Assembly was carried out following the *Gibson Assembly Protocol* (E5510) (NEB 2023). Recombinant plasmids were subsequently transformed into *E. coli* DH5α cells (Chapter 3.1.3).

3.2.7. Sequencing

All generated plasmids were verified by Sanger sequencing (Sanger *et al.* 1977). For each reaction, 600-1000 ng of plasmid DNA was mixed with 0.6 µl of a 100 µM primer and Milli-Q water (Merck, Germany) to a total volume of 15 µl. Sequencing was performed by Microsynth Seqlab (Göttingen, Germany).

3.3. Basic biochemical methods

3.3.1. Precipitation of DNA

PCR fragments generated for genomic integration were precipitated by adding 1/10 volume of sodium acetate (NaOAc), followed by 2.5 volumes of 100% ice-cold EtOH. Samples were incubated at -20°C overnight and centrifuged at maximum speed for 20 min at 4°C. The supernatant was discarded, and the pellet was washed with 800 µl of 80% EtOH, followed by centrifugation at maximum speed for 10 min at 4°C. After discarding the supernatant, the pellet was dried in a vacuum concentrator RVC 2-18 Cdplus (Christ, Osterode) for 10-20 min and subsequently dissolved in 30 µl of water. DNA concentration was determined using a NanoDrop 1000 Spectrophotometer (Thermo Scientific, Germany).

3.3.2. Alkaline lysis of yeast cells and protein precipitation

To analyse protein expression by western blotting, proteins were extracted from yeast cells using an alkaline lysis protocol followed by protein precipitation with trichloroacetic acid (TCA) (Karakasili *et al.* 2014). Yeast cultures were grown to an OD_{600} of 0.6, and 10 ml of culture was harvested by centrifugation at 2800 x *g* for 3 min. Cell pellets were washed once with 3 ml of cold water and subsequently resuspended in 500 µl cold water. For alkaline lysis, 150 µl of freshly prepared pre-treatment solution (1.85 M NaOH and 7.5% β-mercaptoethanol) were added to the cell suspension. Samples were incubated on ice for 20 min. To precipitate proteins, 1/10 of the sample volume of TCA was added, and the mixture was thoroughly vortexed. After an additional 20 min incubation on ice with intermittent vortexing, samples were centrifuged at 10000 x *g* for 20 min at 4°C. The supernatant was removed. Pellets were resuspended in 85 µl of 1x Laemmli buffer, and the pH was adjusted by adding 20 µl of 2 M Tris base. The samples were incubated at 95°C for 3 min, followed by a final centrifugation at maximum speed for 3 min. The resulting supernatant containing the solubilized protein was subjected to SDS-PAGE and subsequent analysis by western blot.

3.3.3. SDS-PAGE

Proteins were separated based on their molecular weight using sodium dodecyl sulfate-polyacrylamide gel electrophoresis (SDS-PAGE). Protein samples were mixed with Laemmli Buffer and incubated at 95°C for 3 min, followed by centrifugation at

maximum speed for 3 min. Up to 20 µl of the resulting supernatant was loaded onto the gel. Depending on the experiment, different molecular weight markers were used. For Coomassie-stained gels, the *Unstained Protein Standard, Broad Range (10-200 kDa)* (NEB, Germany) was used. For western blot analysis, the *Color Prestained Protein Standard, Broad Range (10-250 kDa)* (NEB, Germany) was applied. The acrylamide concentration was 4% (v/v) for the stacking gel and varied in the separating gel based on target protein size: 12% (v/v) polyacrylamide for full-length proteins and up to 17% (v/v) for the Tho1-CTD. Electrophoresis was carried out in 1x SDS-PAGE running buffer at 300 V and 75 mA per gel for 20-30 min. For gel staining, gels were covered in Coomassie G-250 solution for at least 20 min or overnight for optimal staining, followed by destaining in water. Gels prepared for western blotting were used directly without prior staining.

3.3.4. Western Blot

Protein expression was verified by western blotting. After separation by SDS-PAGE, proteins were transferred onto a nitrocellulose membrane (Porablot NCL, Macherey-Nagel, Germany) using a semi-dry blotting device *Trans-Blot Turbo Transfer System* (Bio-Rad, Austria). Transfer was performed at 25 V for 30 min. Subsequently, the membrane was blocked in 5% milk (w/v, prepared in 1x TBST buffer) for 1 h and incubated overnight at 4°C with the respective primary antibody. On the following day, the membrane was washed three times with 1x TBST for 10 min each and then incubated with a horseradish peroxidase-coupled secondary antibody for 1 h at room temperature. The membrane was washed three times with 1x TBST buffer for 10 min. Detection was performed using *CheLuminate-HRP ECL* solution (Applichem, Germany), and signals were visualized with *ChemoCam* Imager (Intas, Germany).

3.4. Protein Purification

3.4.1. Expression of recombinant proteins in *E. coli*

Pre-cultures of *E. coli* Rosetta (DE3), freshly transformed with an expression vector for His-tagged proteins, were grown overnight at 37°C and 150 rpm in 50 ml LB medium with the appropriate antibiotic (25 µg/ml). The next day, a 500 ml main culture with an OD_{600} of approximately 0.2 was prepared from the pre-culture and grown at 37°C and 160 rpm to an OD_{600} of 0.7. Protein expression was induced by the addition of 1 mM isopropyl beta-D-thiogalactoside (IPTG), and cells were cultured overnight at 20°C and

130 rpm. The cells were harvested by centrifugation at 5000 x *g* and 20°C for 15 min. The supernatant was discarded, and the cell pellet was washed in 20 ml of 1x STE buffer and centrifuged again at 5000 x *g* and 4°C for 15 min. Afterwards, the supernatant was discarded and the cell pellet was either frozen in liquid nitrogen and stored at -80°C or immediately used for protein purification.

3.4.2. Purification of recombinant proteins from *E. coli*

For protein purification, cells were lysed in 20 ml of lysis buffer by sonication using a Branson Sonifier 250 ultrasound disruptor. The lysate was ultracentrifuged at 40000 rpm and 4°C for 45 min. The resulting supernatant was subjected to nickel-affinity purification with Protino® Ni-IDA columns (Macherey-Nagel, Germany), which were previously equilibrated with lysis buffer. The column was washed stepwise with 5 ml of wash buffers 1-4, containing increasing concentrations of KCl, before final washing with 5 ml lysis buffer. His-tagged proteins were eluted using 250 mM imidazole.

All DEAD-box helicases used in this work were eluted in ten steps with 250 µl elution buffer per step. Absorbance at 280 nm was measured for the eluted fractions using the NanoDrop 1000 Spectrophotometer (Thermo Fisher Scientific, USA). The four fractions containing the highest protein concentrations were pooled and incubated with TEV protease overnight at 4°C in a rotating wheel. To remove nonspecific proteins and the TEV protease, samples underwent size exclusion chromatography (SEC) using a Superdex 200 10/300 GL (Cytiva, USA) column and the ÄKTA purifier (GE Healthcare, USA). The column was equilibrated with gel filtration buffer before the sample was applied to the sample loop. SEC was performed with 1.5 column volumes at a flow rate of 0.3 ml/min, and the eluted samples were fractionated in 1 ml aliquots by the fraction collector Frac-950. Fractionation was monitored by the UV absorbance at 280 nm, and peak fractions were analysed by SDS-PAGE. All buffers for helicase purification were freshly supplemented with 2 mM TCEP immediately before use. The concentration of purified proteins was measured by the NanoDrop.

For all Tho1 mutants and orthologs, elution was done in five steps with 500 µl elution buffer, and fractions were analysed by SDS-PAGE. The two fractions containing the highest amount of protein were pooled and buffer exchanged via 10K MWCO Zeba Spin desalting columns (Thermo Fisher Scientific, USA). The His-tag was TEV-cleaved overnight on a rotating wheel at 4°C. The following day, uncleaved protein and the His-

tagged TEV protease were removed by nickel-affinity purification. For this purpose, samples were passed through Protino® Ni-NTA agarose (Macherey-Nagel, Germany) equilibrated with gel filtration buffer. Eluates were subjected to gel filtration on a Superdex 75 10/300 GL (Cytiva, USA) column, as described for helicase purification. Due to the lack of aromatic amino acids that absorb at 280 nm, protein elution during gel filtration was monitored at 230 nm and final protein concentration was determined using BCA assay. All proteins were flash frozen in liquid nitrogen and stored at -80°C.

3.4.3. Determination of protein concentration by Bicinchoninic acid assay (BCA)

To measure the protein concentration of Tho1 and its orthologs, a BCA was performed using the Pierce™ BCA Protein Assay Kit (Thermo Fisher Scientific, USA) according to the manufacturer's instructions with the following modifications. BCA Reagent A and Reagent B were mixed in a 50:1 ratio, and 200 µl of the working solution was distributed into each well of a 96-well plate. Subsequently, 5 µl of undiluted protein sample was added to each well and incubated for 30 min at 37°C, followed by cooling at room temperature for 5 min. The absorbance at 560 nm (bandwidth 10 nm) was measured using a Tecan Infinite F Plex plate reader. A standard curve was generated with a dilution series of bovine serum albumin (BSA), and fit with the function:

$$y = mx + b \tag{1}$$

This curve was used to calculate the protein concentration c_1 in µg/ml:

$$c_1 = \frac{(Abs_{sample} - Abs_{background}) - b}{m} \tag{2}$$

Finally, the protein concentration c_2 in µM was calculated:

$$c_2 = \frac{x}{MW}\ 10^6 \tag{3}$$

3.5. Functional assays for purified proteins

3.5.1. Electrophoretic mobility shift assay (EMSA)

The electrophoretic mobility shift assay (EMSA) was used to analyse the RNA binding of proteins or ternary complex formation between RNA and two interacting proteins. The assay is based on the reduced electrophoretic mobility of a fluorescently labelled RNA upon protein binding. RNA substrates were labelled with either Cyanine3 (Cy3)

or 6-Carboxyfluorescein (6-FAM). Unless stated otherwise, Sub2/UAP56 (5 µM) and the respective Tho1 protein (10 µM) were pre-incubated in 11.8 µl binding buffer containing 1 mM AMPPNP and 0.5 mM $MgCl_2$ for 10 min. Subsequently, labelled RNA was added to a final concentration of 100 nM, and the reaction was incubated for 15 min. 10 µl of each sample was loaded onto a native polyacrylamide gel (10% polyacrylamide in 1x TBE buffer). Electrophoresis was carried out at 100 V and 100 mA for 75 min in 1x TBE buffer. Gels were subsequently analysed using a Typhoon FLA 9500 (GE Healthcare, USA) scanner.

3.5.2. Nucleic acid binding assay based on Anisotropy

Nucleic acid binding was measured by monitoring changes in fluorescence anisotropy of 6-FAM-labelled substrates upon protein binding, as described by Andreou et al. (2019). For this purpose, either RNA of various lengths (10, 13, or 16 nt) or 13 nt DNA was used. Measurements were performed in 384-well plates (Greiner, 384 Flat Bottom Polystyrene) using a Tecan Infinite F Plex plate reader (Tecan Trading AG, Switzerland). Proteins were pre-incubated in 10 µl of helicase buffer for 10 min at room temperature. In parallel, a 12 µl solution containing helicase buffer and 20 nM fluorescently labelled nucleic acid substrate was prepared in a separate well. The reaction was initiated by adding 10 µl of the nucleic acid-containing solution to the protein-containing solution (final nucleic acid concentration: 10 nM), and fluorescence anisotropy was monitored for 10 min at room temperature. Depending on the protein and experimental requirements, reactions were performed either in the absence or presence of 2 mM ATP and 1 mM $MgCl_2$. Fluorescence anisotropy was measured at 535 nm (25 nm bandwidth) following excitation at 485 nm (20 nm bandwidth) using polarization filters.

Anisotropy *r* was calculated using

$$r = \frac{I_{VV} - GI_{VH}}{I_{VV} + 2GI_{VH}} \quad (4)$$

with I_{VV} denoting vertical excitation and vertical emission and I_{VH} denoting vertical excitation and horizontal emission. The grating factor G is an instrument specific factor, that was experimentally determined.

Protein titration data were fitted to hyperbolic binding curves using the following equation:

$$r = r_{min} + \frac{c}{K_d + c}(r_{max} - r_{min}) \quad (5)$$

Here, *r* is the total anisotropy, r_{min} is the minimal anisotropy of the free substrate, r_{max} is the maximal anisotropy of the bound substrate, *c* is the protein concentration and K_d is the dissociation constant.

3.5.3. Nucleic acid substrate preparation for unwinding assays

Before measuring nucleic acid unwinding activity, double-stranded substrates were prepared by annealing complementary oligonucleotides. All DNA and RNA oligonucleotides used for substrate generation were derived from published sequences and are listed in Table 11 (Ma *et al.* 2013; Putnam & Jankowsky 2013). Oligonucleotide stock solutions were mixed in a 1:1 molar ratio to achieve a final concentration of 1 µM in 100 µl of 1x annealing buffer. The mixture was heated to 95°C in a thermocycler and subsequently cooled by decreasing the temperature in 5°C increments until reaching 4°C. The annealed substrates were used immediately or stored at -20°C.

3.5.4. Real-time fluorescence unwinding assay

Unwinding was measured using a fluorescence-based real-time unwinding assay, modified from Ordabayev et al. (2018). Reactions were performed at room temperature in a 96-well plate (Greiner 96 Flat Bottom Black Polystyrene) using a Tecan infinite F Plex plate reader (Tecan Trading AG, Switzerland). Substrates were prepared as described in Chapter 3.5.3. and consisted of a 13 nt top strand labelled with either 6-FAM or Black Hole Quencher 2 (BHQ-2), and a 13 nt or 38 nt bottom strand labelled with Cyanine5 (Cy5). Unless otherwise stated, reactions were carried out in 200 µl helicase buffer, containing 2 mM ATP, 1 mM $MgCl_2$, 1 µM Sub2/UAP56 and 2 µM Tho1-CTD/MOS11. For substrates labelled with BHQ-2 and Cy5, unwinding was detected as increasing Cy5 fluorescence at 670 nm (20 nm bandwidth) after excitation at 620 nm (10 nm Bandwidth). Fraction unwound was calculated by normalizing measured Cy5 intensities to signal obtained from a Cy5 labelled 38 nt RNA.

Substrates, containing a 6-FAM-labelled top strand were measured in three different channels:

***F*D|D:** Buffer-corrected signal of 6-FAM donor emission at 535 nm (25 nm bandwidth) after donor excitation at 485 nm (20 nm bandwidth)

***F*A|A:** Buffer-corrected signal of Cy5 acceptor emission at 670 nm (20 nm bandwidth) after acceptor excitation at 620 nm (10 nm bandwidth)

***F*A|D:** Buffer-corrected signal of Cy5 acceptor emission at 670 nm (20 nm bandwidth) after donor excitation at 485 nm (20 nm bandwidth)

Optionally, fluorescence anisotropy was simultaneously measured as described in Chapter 3.5.2.
Unwinding was monitored by an increase in $F_{D|D}$ and a decrease $F_{A|D}$ intensities, with the latter representing FRET between donor and acceptor. pdRNA substrates consisting of a 13 nt top and 38 nt bottom strand, labelled with either donor or acceptor only (Supplementary Figure S2) were used to calculate donor bleed-through β and acceptor crosstalk α as follows:

Donor bleed-through β into $F_{A|D}$ channel using the donor-only sample:

$$\beta = \frac{F_{A|D}}{F_{D|D}} \tag{6}$$

Acceptor crosstalk α upon donor excitation using the acceptor-only sample:

$$\alpha = \frac{F_{A|D}}{F_{A|A}} \tag{7}$$

Table 19: Correction factors for the $F_{A|D}$ channel.

Reaction	**β**	**α**
No protein	0.022 ± 0.0003	0.023 ± 0.0003
Sub2	0.024 ± 0.0025	0.023 ± 0.0005
Sub2 + Tho1-CTD	0.020 ± 0.004	0.023 ± 0.0007

As the donor did not show crosstalk in the $F_{A|A}$ channel and the acceptor did not show crosstalk in the $F_{D|D}$ channel, correction of the $F_{A|D}$ channel (nF) was performed using:

$$nF = F_{A|D} - \alpha - \beta \quad (8)$$

Analysis of the pdRNA substrate showed that the more than 90% of the signal in the $F_{A|D}$ channel originated from FRET, with <10% contribution from crosstalk and bleed-through. Unwinding was therefore represented as the fraction duplex remaining calculated by normalizing $F_{A|D}$ intensities to reactions without protein. Data analysis was done in Origin Pro (version 2024b, OriginLab Corporation, Northampton, MA, USA).

Unwinding curves obtained for MOS11, and mutants were fitted with an exponential function:

$$y = A_1 e^{-x/t_1} + y_0 \quad (9)$$

with A_1 representing the amplitude, t_1 the time constant, and y_0 the endpoint of the reaction.

The initial velocity (v_o) was calculated as:

$$v_0 = \frac{1 - y_0}{t_1} \quad (10)$$

Due to an initial delay in measuring, the first seconds of the reaction were not recorded, affecting the measured A_1 value. However, since fitting was performed using normalized values, this effect was compensated by substituting ($1 - y_0$) for A_1, to accurately determine the initial velocity.

3.5.5. Stopped-flow measurements for fast unwinding kinetics

For very fast unwinding kinetics, stopped-flow measurements were performed to capture the initial seconds of the reaction. A stopped-flow device (SF-61SX2, TgK Scientific, Bradford-on-Avon, UK) equipped with an LED light source (LED L470A with prefilter SP OD4 500 nm, 12.5 mm) for excitation was used. As in the real-time fluorescence unwinding assay described in Chapter 3.5.4., substrates were labelled with 6-FAM and Cy5, and identical buffer conditions were maintained. $F_{D|D}$ intensities

were measured using a ET525/50 band-pass filter), and $F_{A|D}$ intensities with a ET670/50 band-pass filter (Chroma Technology, Olching, Germany).
Sub2 (2 µM) and the Tho1-CTD (1 µM) were pre-incubated in helicase buffer for 10 min before being transferred into syringe 1. Syringe 2 contained a 20 nM solution of the respective nucleic acid substrate in helicase buffer. The reaction was started by mixing the contents of both syringes in a 1:1 ratio, resulting in final concentrations of 1 µM Sub2, 0.5 µM Tho1-CTD, and 10 nM of substrate. Reactions were monitored for 5 min at 25°C. Data were analysed with Origin Pro (version 2024b; OriginLab Corporation, Northampton, MA, USA), and the fraction duplex was calculated by normalizing buffer-corrected fluorescence signals to the initial signal at the start of the reaction.

3.5.6. Nucleic acid annealing assay

Nucleic acid annealing assays were performed as described by Miosga (2022). Reactions were carried out at room temperature in a 96-well plate (Greiner, 96 Flat Bottom Black Polystyrene) in a total volume of 200 µl helicase buffer. Tho1 or its orthologs (10 µM) were pre-incubated with 20 nM of 16 nt BHQ-2-labelled RNA or DNA top strands for 10 min in 100 µl helicase buffer. Reactions were initiated by adding 100 µl of a solution containing 20 nM Cy5-labelled RNA or DNA bottom strands. Annealing was monitored by a decrease in Cy5 fluorescence at 670 nm (20 nm bandwidth) following excitation at 620 nm (25 nm bandwidth) for 60 min. Cy5 fluorescence intensities were normalized to the initial signal at the start of the reaction.

3.5.7. Nucleic acid binding-annealing-displacement assay

To separately assess the RNA binding, RNA/DNA annealing, and strand displacement activities of Tho1 and its domain mutants, a stepwise experimental approach was employed. Measurements were performed at room temperature using a 96-well plate (Greiner, 96 Flat Bottom Black Polystyrene). In the first step, 16 nt 6-FAM-labelled RNA (final concentration 10 nM) was incubated with Tho1 (0.03-2 µM) for 5 min, and RNA binding was quantified by fluorescence anisotropy as described in Chapter 3.5.2. Subsequently, a 37 nt Cy5-labelled DNA bottom strand (final concentration 10 nM) was added, and annealing was monitored by an increase in the $F_{A|D}$ intensities for 25 min. Finally, a 37 nt unlabelled DNA top strand (final concentration 10 nM) was added, and strand displacement was measured by decreasing $F_{A|D}$ intensities for an additional 25 min. Data were analysed using Origin Pro (version 2024b; OriginLab Corporation,

Northampton, MA, USA). For the annealing reactions, $F_{A|D}$ intensities of protein titration data were fitted using the Hill equation:

$$y = \frac{(max-min)\,x^n}{(K^n + x^n)+min} \quad (11)$$

Here, *K* is the half-saturation constant and *n* the Hill coefficient.

For strand displacement reactions, $F_{A|D}$ fluorescence intensities were normalized to the initial value at the start of the reaction and plotted as a function of time.

3.5.8. Statistical analysis

Data are presented as mean of a minimum of three independent experiments, with error bars representing the standard deviation. Statistical analysis was performed using a two-tailed Student's *t*-test, with significance thresholds defined as $p < 0.05$ (*), $p < 0.01$ (**) and $p < 0.001$ (***). For data shown in Figure 39, 41, and 43, statistical analysis was performed by Apl. Prof. Dr. Peter Friedhoff using Python (v.3.11). Data processing and management were handled using the pandas and numpy libraries. To determine if significant differences in velocities existed between wild-type MOS11 and various Mot mutants, a one-way Analysis of Variance (ANOVA) was employed. For datasets yielding a significant ANOVA result ($p < 0.05$), post-hoc comparisons were conducted to identify specific group differences. These included pairwise t-tests with a Bonferroni correction to strictly control the family-wise error rate and Benjamini-Hochberg (FDR) procedure to adjust p-values for multiple hypothesis testing.

3.6. Structural studies of proteins and protein complexes

3.6.1. AlphaFold 3 modelling

Structural models were generated using the AlphaFold 3 server to predict the assembly of the Tho1-CTD/MOS11 with Sub2/UAP56 (Abramson *et al.* 2024). Five models were generated, from which single models were chosen for representation. PAE plots were generated using the PAE viewer web server (Elfmann & Stülke 2023).

3.6.2. Heterobifunctional crosslinking

The protocol for heterobifunctional crosslinking using S-{4-[(2,5-Dioxo-1-pyrrolidinyl)oxy]-4-oxobutyl}methanesulfonothioate (MTS-4-NHS, Biozol) was adapted from Storozhuk et al. (2024). Reactions were performed in a total volume of 20 µl in crosslinking buffer, with or without 1 mM of nucleotide (AMPPNP or ATP) or 2.5 mM

RNA. UAP56/Sub2 at a final concentration of 5 µM was incubated with 2.5 µM of the Tho1-CTD for 3 min. Unless stated otherwise, the reaction was initiated by the addition of 500 µM MTS-4-NHS and stopped after 5 min by adding Tris-containing Laemmli buffer. Samples were boiled at 95°C for 2 min, and 17 µl of each sample was analysed by SDS-PAGE and visualized using Coomassie staining (Chapter 3.3.3). Samples for LC-MS analysis were cut from the Coomassie-stained gel.

3.6.3. Hydrogen/deuterium exchange mass spectrometry (HDX-MS)

HDX experiments were carried out by Dr. Wieland Steinchen at Marburg University, using a two-arm robotic autosampler (LEAP Technologies) and an ACQUITY ultra-performance liquid chromatography (UPLC) M-Class System with HDX Technology coupled to a G2-Si high-definition mass spectrometry (HDMS) mass spectrometer (Waters). Sub2 and Sub2-D302R (25 µM) were diluted in deuterated buffer and incubated for 10, 100, 1000 or 10000 s at 25°C before being quenched. Samples were digested on protease columns containing immobilized pepsin or a mixture of proteases XIII and XVIII, and peptides were separated on a C18 column, before HDMS analysis. Peptide identification was performed with ProteinLynx Global SERVER (PLGS, Waters) using non-deuterated samples, and deuterium incorporation was quantified with DynamX 3.0 (Waters) as described in Joiner et al. (2023). Datasets from both digestion regimes were combined, and spectra were manually reviewed. For analyses only high-confidence peptides consistently detected across replicates were included. Residue-specific exchange values were derived from overlapping peptides by selecting the shortest peptide covering the residue of interest.

3.6.4. Liquid Chromatography-Mass Spectrometry (LC-MS)

LC-MS analysis was performed by Dr. Uwe Linne and Tina Krieg at the core facility for mass spectrometry and elemental analysis at Marburg University. Coomassie-stained gel slices containing proteins were destained and dried, followed by in-gel tryptic digestion and peptide extraction. Mass spectrometric measurements were carried out using a timsTOF Pro instrument (Bruker Daltonics) coupled to a nanoElute HPLC system with a C18 reverse-phase column. Data were acquired in DDA PASEF mode and processed using Bruker Data Analysis software and Proteome Discoverer 2.4 (Thermo Fisher Scientific, Bremen). Peptide spectra were searched against a database containing the sequences of UAP56, Tho1-CTD, common contaminants such as trypsin and keratin, and the *E. coli* proteome.

4. Results

4.1. Domain characterisation of the nucleic acid annealing protein Tho1

The conserved mRNP component Tho1 is a 218 amino acid (aa) protein. It is composed of an N-terminal SAF-A/B, Acinus, and PIAS (SAP) domain (aa 4-38), an acidic, unstructured linker (aa 39-116), a C-terminal domain (CTD or Tho1/MOS11-CTD, aa 117-183) and a positively charged C-terminal extension (CTE, aa 184-218) (Figure 8A and B). The SAP domain and CTD represent Tho1's only structured regions, while more than half of the protein is unstructured. In his dissertation, Dr. Matthias Miosga conducted a detailed *in vitro* characterisation of Tho1 and described a novel nucleic acid annealing activity mediated by Tho1's CTE (Miosga 2022). In the subsequent chapters, those previous findings on the *in vitro* activity of Tho1 and different Tho1 mutants will be reproduced and extended, and their *in vivo* relevance in *S. saccharomyces* cerevisiae will be evaluated.

4.1.1. Purification of recombinant Tho1 protein

For conducting *in vitro* experiments with Tho1, it was crucial to obtain highly pure protein. Tho1 was recombinantly expressed in *E. coli* Rosetta (DE3) cells, with a hexahistidine (6xHis) tag followed by a TEV cleavage site attached to the N-terminus of the protein. In the initial purification step, the protein was loaded onto a Ni-IDA affinity column, allowing selective retention via the His-tag. SDS-PAGE analysis of the eluate revealed that His-tagged Tho1 migrated at approximately 40 kDa, higher than the calculated molecular mass of 27 kDa (Figure 8C). To remove the His-tag, the eluate was buffer-exchanged into imidazole-free buffer using a Zeba desalting column, followed by overnight TEV cleavage. SDS-PAGE showed a slightly faster-migrating band for Tho1, indicating that most of the protein had been successfully cleaved, with a minor fraction of His-tagged Tho1 remaining (Figure 8C). The TEV eluate was loaded onto Ni-NTA beads to retain uncleaved Tho1 and the His-tagged TEV protease. SDS-PAGE confirmed the successful removal of His-tagged Tho1. However, additional bands at approximately 75, 35, 21, and 15 kDa were visible (Figure 8C). Finally, Tho1 was subjected to size exclusion chromatography to remove contaminants or degradation products. Because Tho1 lacks aromatic amino acids absorbing at 280 nm, elution was monitored at 230 nm.

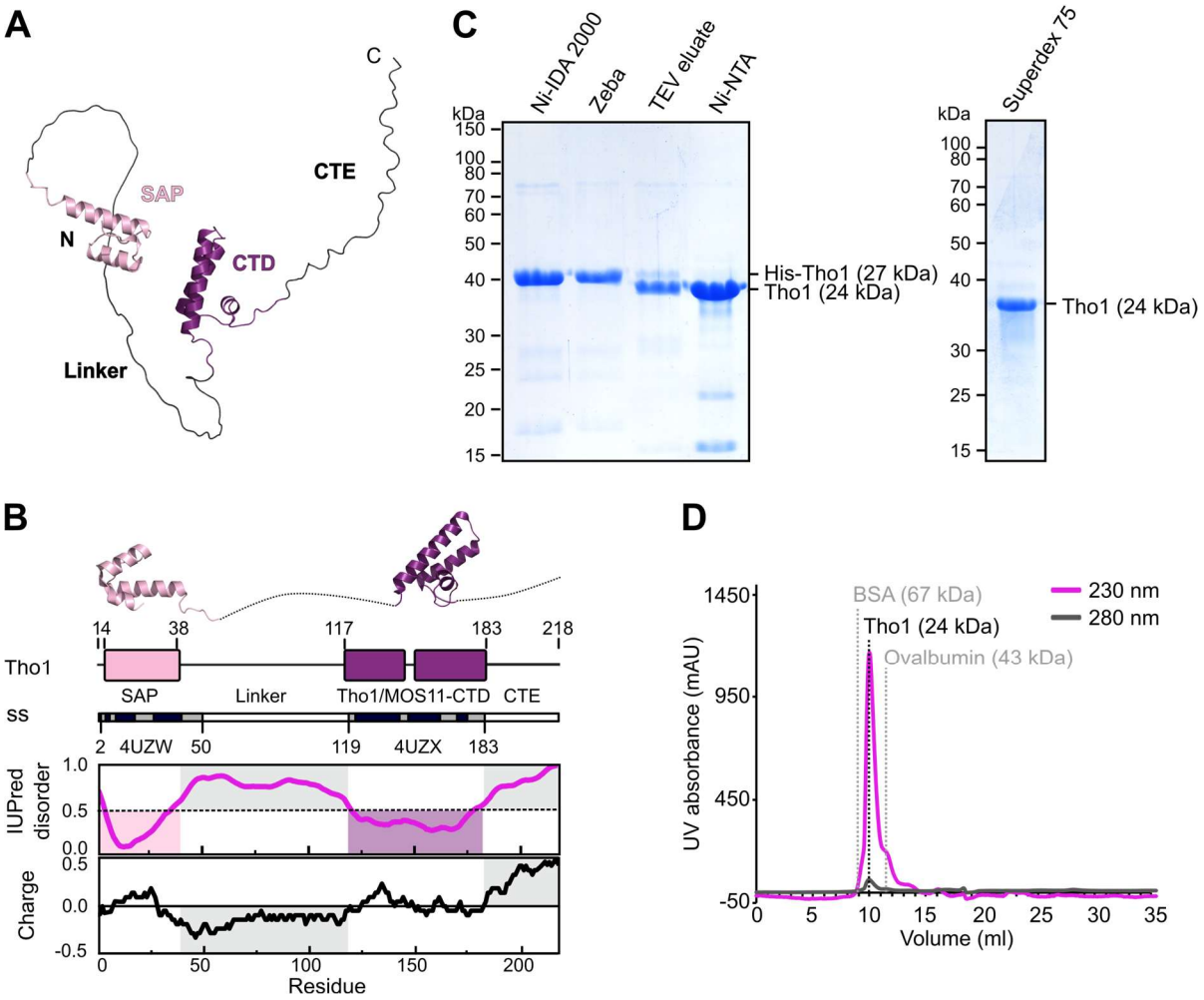

Figure 8: Purification of Tho1 yielded highly purified protein. (A) AlphaFold model of Tho1 (AF-P40040-F1). **(B)** Tho1 domain organization. The N-terminal SAF-A/B, Acinus, and PIAS domain (SAP, aa 4-38, 4UZW) is shown in light pink, while the C-terminal domain (CTD, aa 117-183, 4UZX) is depicted in purple. The IUPred disorder plot reveals ordered regions corresponding to the SAP and CTD domains. The VOLPES charge distribution indicates a negative linker region and a positively charged C-terminal extension (CTE). **(C)** SDS-PAGE (12%) analysis of Tho1 samples obtained during different steps of the purification protocol. His-tagged Tho1 was initially enriched using affinity chromatography (Ni-IDA 2000), followed by buffer-exchange (Zeba), TEV cleavage (TEV eluate) and a second affinity chromatography (Ni-NTA). The final purification step was performed by size-exclusion chromatography (Superdex 75). The gel was stained with Coomassie Blue. Bands corresponding to His-tagged Tho1 and cleaved Tho1 are indicated on the right. **(D)** The size-exclusion chromatogram shows a single Tho1 peak eluting at approximately 10 ml in the UV absorbance trace at 230 nm. Only a small peak is visible at 280 nm. According to the manufacturer's specifications, the marker proteins BSA (67 kDa) and Ovalbumin (43 kDa) elute at approximately 9 ml and 11 ml, respectively.

The size exclusion chromatogram revealed that Tho1 predominantly eluted in a single peak. Notably, this peak appeared earlier than expected when compared to the marker proteins BSA (67 kDa) and Ovalbumin (43 kDa) (Figure 8D). However, no other significant peaks were observed, and SDS-PAGE analysis of the peak fraction

confirmed the presence of pure Tho1 (Figure 8C). The resulting protein was used for *in vitro* activity assays.

4.1.2. Quantitative analysis of Tho1 binding to short ssRNA

Tho1 binds both single-stranded (ss) and double-stranded (ds) RNA and DNA substrates (Jacobsen *et al.* 2016; Jimeno *et al.* 2006; Miosga 2022). However, efficient binding by Tho1 is predominantly observed with ssDNA and ssRNA substrates of at least 60 nt and 15 nt, respectively (Jimeno *et al.* 2006; Xie *et al.* 2023). EMSA experiments revealed that a stable interaction of Tho1 with shorter substrates (13 nt RNA or 18 nt DNA) is highly impaired, indicating a length specificity for Tho1's nucleic acid interactions (Miosga 2022).

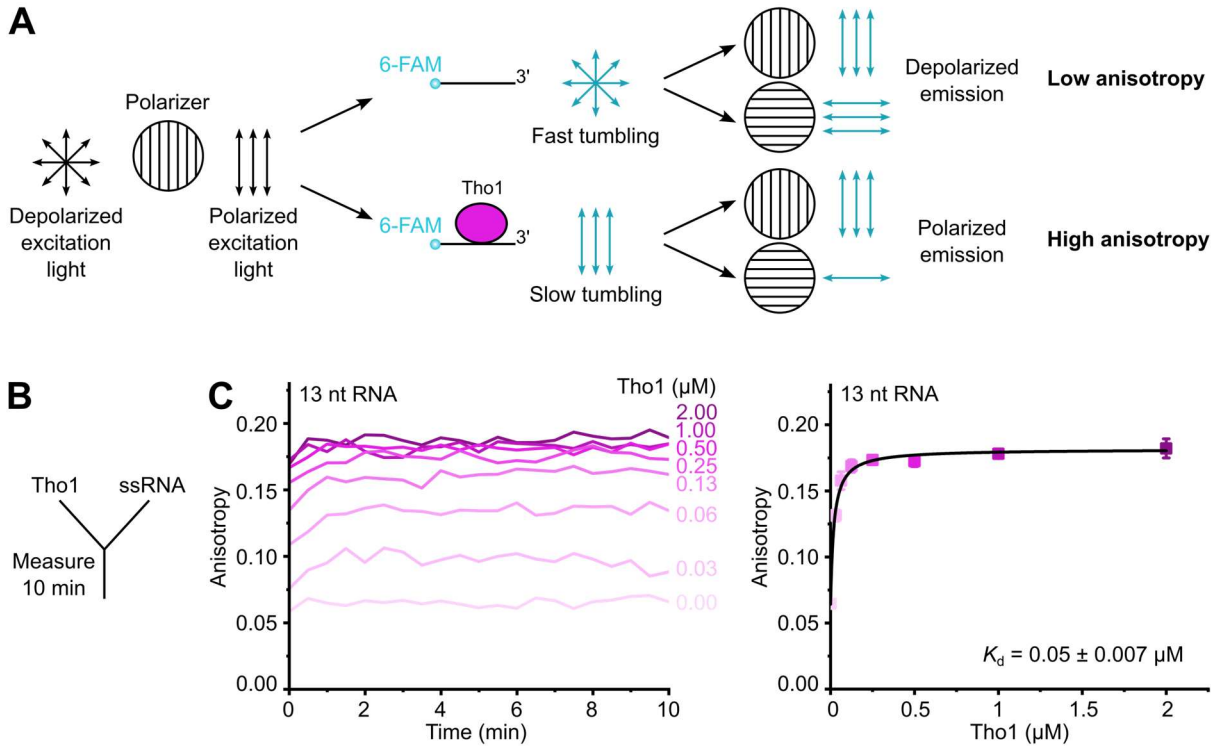

Figure 9: Tho1 binds short 13 nt ssRNA. (A) Principle of the fluorescence anisotropy-based binding assay with a 6-FAM-labelled 13 nt ssRNA. Irradiation of free RNA with plane-polarized light leads to emission of depolarized light due to rapid rotation of the RNA molecules, resulting in low fluorescence anisotropy values. In contrast, bound RNA rotates slowly and emits polarized light, leading to increased fluorescence anisotropy. Adapted from Cheow et al. (2014) with permission by ACS Publications (https://pubs.acs.org/doi/10.1021/ac502605f). **(B)** Scheme of the assay. **(C)** Tho1 titrations (0.03-2 µM) with 10 nM 13 nt RNA. Example binding kinetics (left) show a concentration-dependent maximum fluorescence anisotropy. All curves reach saturation within 2 min. Binding isotherms (right, at t = 10 min) showing mean ± SD from *n* = 3 independent reactions were fitted with a hyperbolic function (black) to calculate the K_d value for Tho1 binding to RNA. Reactions without Tho1 served as controls.

To further analyse this effect and obtain quantitative results for Tho1 binding, a fluorescence-based real-time binding assay using fluorescence anisotropy was implemented, as described by Andreou et al. (2019). Binding of a protein to fluorescently labelled RNA reduces tumbling of the RNA molecule and consequently increases anisotropy (Figure 9A). A 13 nt 6-FAM-labelled RNA was mixed with Tho1, and fluorescence anisotropy was measured over a 10-min time course (Figure 9B). Titration of Tho1 at various concentrations (0.03-2 µM) with the RNA resulted in concentration-dependent increases in anisotropy (Figure 9C). Lower Tho1 concentrations showed lower anisotropy maxima that were reached after longer incubation times compared to higher Tho1 concentrations. However, all curves reached saturation within 2 min. Plotting the anisotropy values at 10 min and fitting the resulting curve with a hyperbolic function yielded a dissociation constant (K_d) of 0.05 ± 0.007 µM for Tho1. This assay demonstrated that Tho1 can bind to 13 nt ssRNA, despite the absence of a stable complex in gel-based assays (Miosga 2022).

4.1.3. Tho1 requires its C-terminal extension for nucleic acid-related activities

Previous studies have linked individual domains of Tho1 to specific protein functions. The SAP domain binds DNA, but not RNA, consistent with the finding that a Tho1 mutant lacking this domain (Tho1-ΔSAP, aa 51-218) retains RNA-binding activity (Jacobsen *et al.* 2016; Jimeno *et al.* 2006). However, Tho1-ΔSAP can still interact with both dsDNA and ssDNA, leaving the function of this non-conserved domain unclear (Miosga 2022). The Tho1-CTE, specifically its 17 aa C-terminal region, mediates nucleic acid binding as well as annealing (Miosga 2022). In contrast, the Tho1-CTD is not needed for nucleic acid interactions but instead mediates interaction with Sub2 (Humphreys *et al.* 2021; Miosga 2022; Xie *et al.* 2023).

To validate and extend these findings on the functions of Tho1 domains, five Tho1 mutants described by Miosga (2022) were selected for further analyses. Three mutants lacked a single domain (Tho1-ΔSAP, -ΔCTD, -ΔCTE), a fourth lacked both the SAP domain and linker (Tho1-ΔSAPΔLinker), and a fifth consisted solely of the CTD (Tho1-CTD) (Figure 10A). While four of the His-tagged mutants were successfully purified (Figure 10B), the Tho1-ΔSAPΔLinker mutant could not be purified by affinity chromatography despite multiple purification attempts (data not shown). Therefore, this mutant was excluded from the *in vitro* characterisation.

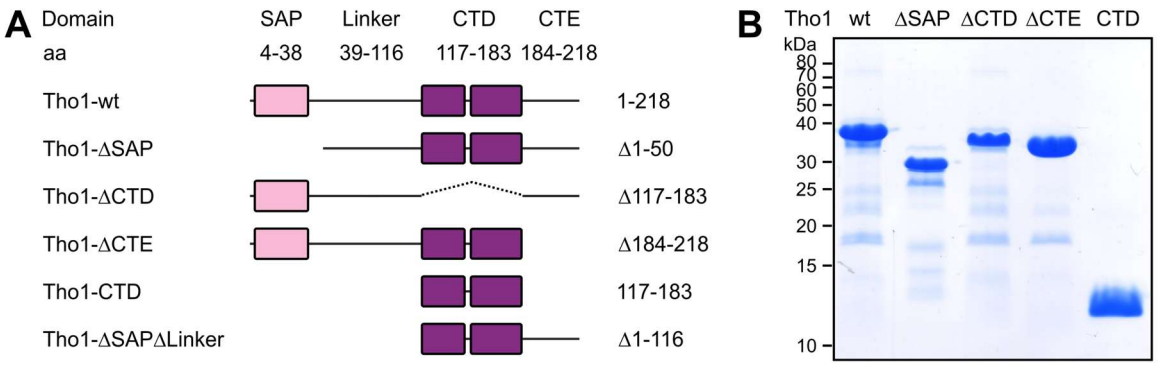

Figure 10: Tho1-domain mutants were purified in high quantities. (A) Schematic representation of the selected Tho1 mutants. **(B)** SDS-PAGE (12%) analysis of the purified proteins. Tho1-ΔSAPΔLinker could not be purified. Purification was performed in one step by affinity chromatography using Ni-IDA 2000 columns by Karin Pietsch and Giuseppina Di Nolfo as part of their bachelor's theses conducted in 2022. All purified proteins remained His-tagged.

The Tho1 orthologs CIP29 and MOS11 are primarily involved in the export of mRNA transcripts with high GC content – regions prone to forming co-transcriptional R-loops (Rödel *et al.* 2024; Xie *et al.* 2023). Consistent with a potential role in R-loop resolution, Tho1 reduces elevated R-loop levels in yeast cells lacking the THO complex component Hpr1 and exhibits nucleic acid annealing activity *in vitro* (Miosga 2022). This activity was proposed to contribute to R-loop resolution by promoting RNA removal through reannealing of the DNA strands (Miosga 2022). Using a fluorescence-based in-solution assay, Miosga (2022) demonstrated that Tho1 dramatically accelerates strand displacement of the RNA in a partial duplex RNA/DNA hybrid substrate with an invading complementary ssDNA strand. While annealing activities of Tho1 domain mutants were previously characterized, these experiments used fixed protein concentrations and may have missed subtle quantitative differences. Moreover, strand displacement activity had only been tested with wild-type Tho1 (Miosga 2022). To address these limitations, a fluorescence-based three-step assay was established to simultaneously monitor RNA binding, RNA/DNA annealing, and strand displacement (Figure 11A). The assay was carried out in 96-well plates using a Tecan Infinite F Plex plate reader. First, proteins were incubated with a 16 nt 6-FAM-labelled ssRNA top strand, and RNA-binding was measured by fluorescence anisotropy. Next, a 37 nt Cy5-labelled ssDNA bottom strand complementary to the RNA top strand was added. Annealing of the two strands brought the fluorophores into proximity, allowing FRET from the donor dye 6-FAM to the acceptor dye Cy5. Consequently, annealing was monitored as an increase in Cy5 acceptor fluorescence upon 6-FAM donor emission ($F_{A|D}$, representing FRET with a Förster distance of ~6.1 nm).

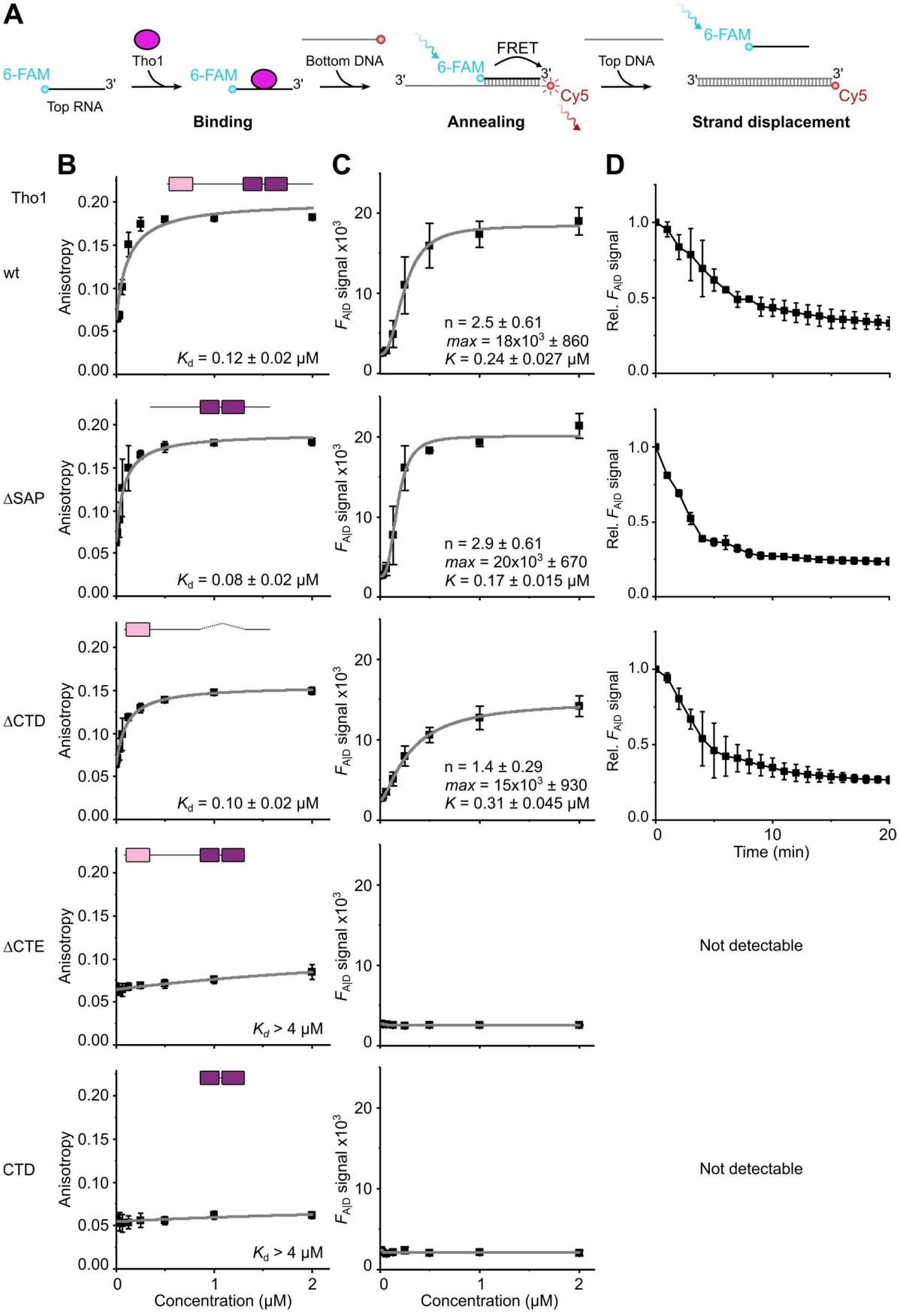

Figure 11: The Tho1-CTE is essential for nucleic acid binding and annealing. (A) Scheme of the fluorescence-based three-step assay used to measure (B) RNA binding, (C) RNA/DNA annealing and (D) strand displacement. **(B)** Binding isotherms (t = 5 min) for Tho1 wild-type

and domain mutants (0.03-2 µM) with 16 nt 6-FAM-labelled RNA (10 nM). Data were fitted with a hyperbolic function (grey) to calculate K_d values. **(C)** Acceptor (Cy5) fluorescence following donor (6-FAM) excitation ($F_{A|D}$) measured 25 min after the addition of the 37 nt DNA bottom strand (10 nM) to reactions containing increasing concentrations of Tho1 (0.03-2 µM). Data were fitted using a Hill equation (grey) to calculate the Hill coefficient (n), max $F_{A|D}$ intensities and *K* values. **(D)** Kinetic traces of strand displacement reactions performed with 2 µM Tho1 after addition of the 37 nt DNA invader top strand (10 nM). Due to the absence of annealing activity, strand displacement was not detectable for Tho1-ΔCTE and Tho1-CTD mutants. Black lines connect data points. All panels show mean ± SD from *n* = 3 experiments. The experiment was performed with Karin Pietsch and Giuseppina Parlato-Di Nolfo as part of their bachelor's theses.

Finally, a 37 nt unlabelled DNA invader strand fully complementary to the DNA bottom strand was added. Successful strand displacement removed the RNA top strand, thereby increasing the distance between the fluorophores and consequently decreasing the $F_{A|D}$ signal (Figure 11A).

Wild-type Tho1 and Tho1-ΔSAP exhibited comparable activities in RNA binding, RNA/DNA annealing, and strand displacement (Figure 11B-D). The Tho1-ΔCTD mutant also displayed wild-type-like RNA binding (P = 0.1559, Figure 11B), but showed reduced annealing activity, as indicated by significantly lower maximum $F_{A|D}$ signals (P = 0.0148, Figure 11C). Notably, whereas the curves for wild-type Tho1 and Tho1-ΔSAP annealing reactions followed a sigmoidal pattern (Hill coefficient n > 2), this was not observed for the Tho1-ΔCTD mutant. Nonetheless, it could still displace the RNA top strand with the invading DNA strand (Figure 11D). In contrast, neither Tho1-ΔCTE nor the Tho1-CTD showed detectable RNA-binding or annealing activities. Consequently, strand displacement could not be assessed for these mutants.

In summary, whereas the SAP and CTD domains were dispensable for the measured nucleic acid-related activities, the presence of the Tho1-CTE was essential.

4.1.4. The C-terminal domain of Tho1 suppresses the ts phenotype in Δ*hpr1* cells

The distinct *in vitro* activities of the Tho1 domain mutants make them a promising toolset to investigate Tho1's cellular function. Although deletion of *THO1* does not cause an apparent phenotype in *S. cerevisiae*, its overexpression suppresses the temperature-sensitive (ts) growth defect in Δ*hpr1* cells with a defective THO complex, independent of its SAP domain (Jimeno *et al.* 2006).

To assess which of the other Tho1 domains contribute to this phenotype, genes encoding wild-type *THO1* as well as all *tho1* mutants were cloned into the high-copy vector pRS424 and transformed into wild-type and Δ*hpr1* yeast cells (Figure 12,

Supplementary Figure S3). Western blot analysis of whole-cell extracts confirmed overexpression of all proteins in the presence of endogenous Tho1 (Figure 12B). Overexpression of none of the Tho1 mutants impaired growth in wild-type yeast cells, excluding protein-induced lethality (Supplementary Figure S3).

In Δ*hpr1* cells, growth defects were already observed at 30°C and became more severe at 37°C (Figure 12C). Overexpression of wild-type Tho1 suppressed the growth defect at 37°C without affecting growth at 30°C. Consistent with Jimeno et al. (2006), deletion of the SAP domain did not impair phenotype suppression and even slightly enhanced cell growth at both temperatures. Additional deletion of the linker region in Tho1-ΔSAPΔLinker resulted in a phenotype similar to that observed for the ΔSAP mutant. In contrast, the absence of either the Tho1-CTD or Tho1-CTE prevented growth at 37°C. Interestingly, the Tho1-CTD alone, despite lacking the CTE, was sufficient to suppress the growth defect at 37°C.

Together, these results indicate that the SAP domain and linker region are not crucial for suppressing the ts phenotype, whereas the CTD plays a key role, and the CTE contributes under certain conditions.

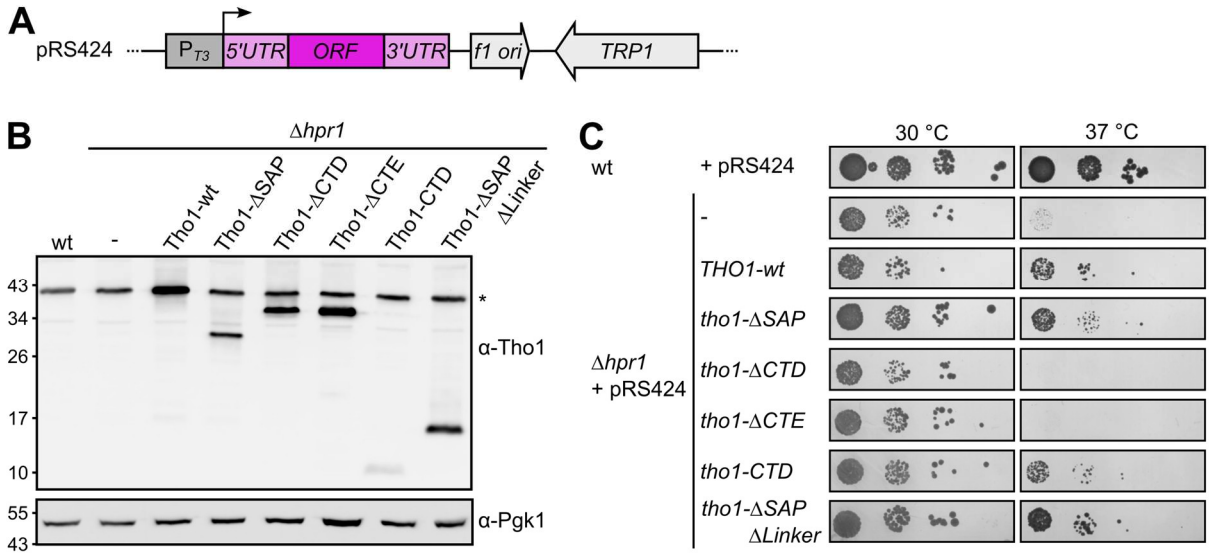

Figure 12: Tho1 domains contribute differently to ts phenotype suppression in Δ*hpr1* cells. (A) Schematic representation of the overexpression vector pRS424. The open reading frame (*ORF*) of the respective *THO1* construct was inserted between the endogenous *THO1* 5′ and 3′ UTRs. *TRP1* served as a selection marker. **(B)** Total protein levels of whole-cell extracts from wild-type or Δ*hpr1* cells overexpressing Tho1 or the indicated domain mutant. The polyclonal Tho1 antibody was used to detect the wild-type protein and mutants. Constructs were expressed in the presence of endogenous Tho1, and full-length Tho1 is indicated by an asterisk (*). Pgk1 served as a loading control. Representative blot of three biological replicates. **(C)** Dot spots of Δ*hpr1* cells overexpressing *THO1* or the indicated *tho1* mutant. Tenfold serial dilutions of the cells were spotted onto SDC (-Trp) plates and grown at the indicated temperatures for three days. Representative result of three biological replicates. Wild-type and Δ*hpr1* cells transformed with pRS424 served as positive and negative controls, respectively.

4.2. Functional interaction of the Tho1-CTD with Sub2

The TREX component Sub2 is a conserved DEAD-box RNA helicase consisting of an unstructured N-terminal motif (NTM) and two RecA-like domains (RecA1 and RecA2) (Figure 13A and B). The characteristic DECD motif is located within the RecA1 domain (Figure 13B). Upon ATP and RNA binding, Sub2 undergoes a conformational change into a closed state, which reverts to an open conformation following ATP hydrolysis and RNA release (Figure 13A). While most characterized interaction sites of Sub2 or its human ortholog DDX39 with other proteins – including Tho1/SARNP – are located within the RecA-like domains, the NTM mediates interactions with TREX-2 and TREX-2-like complexes (Bugai *et al.* 2025; Xie *et al.* 2025). Interactions of DDX39B or *A. thaliana* UAP56 with their respective Tho1 orthologs, SARNP and MOS11, were shown to stimulate helicase activity (Chang *et al.* 2013; Dufu *et al.* 2010; Rödel *et al.* 2024; Sugiura *et al.* 2007). In contrast, Tho1 counteracts unwinding by Sub2, likely due to its annealing activity (Miosga 2022). The mechanism underlying helicase stimulation remains unclear. The following chapters focus on the interaction between Sub2 and Tho1, particularly the Tho1-CTD, and its influence on Sub2's RNA-binding and helicase activity.

4.2.1. Purification of recombinant Sub2

To investigate the interaction between Tho1 and Sub2, Sub2 was first purified. As described for Tho1, His-tagged Sub2 was expressed in Rosetta (DE3) cells and purified by affinity chromatography (Figure 13C). The His-tag was removed by TEV cleavage, and SDS-PAGE analysis of the TEV eluate confirmed successful cleavage (Figure 13C). Size-exclusion chromatography was then used to separate Sub2 (51 kDa) from the smaller TEV protease (28 kDa). The chromatogram at 280 nm displayed multiple peaks, with the most prominent at approximately 13 ml (Figure 13D). SDS-PAGE showed that this peak fraction contained Sub2 of high purity (Figure 13C). Sub2, like Tho1, eluted earlier than expected relative to the marker proteins BSA (67 kDa) and β-lactoglobulin (35 kDa). However, none of the other peak fractions contained Sub2 (data not shown). The Sub2-containing fraction was used in subsequent *in vitro* assays.

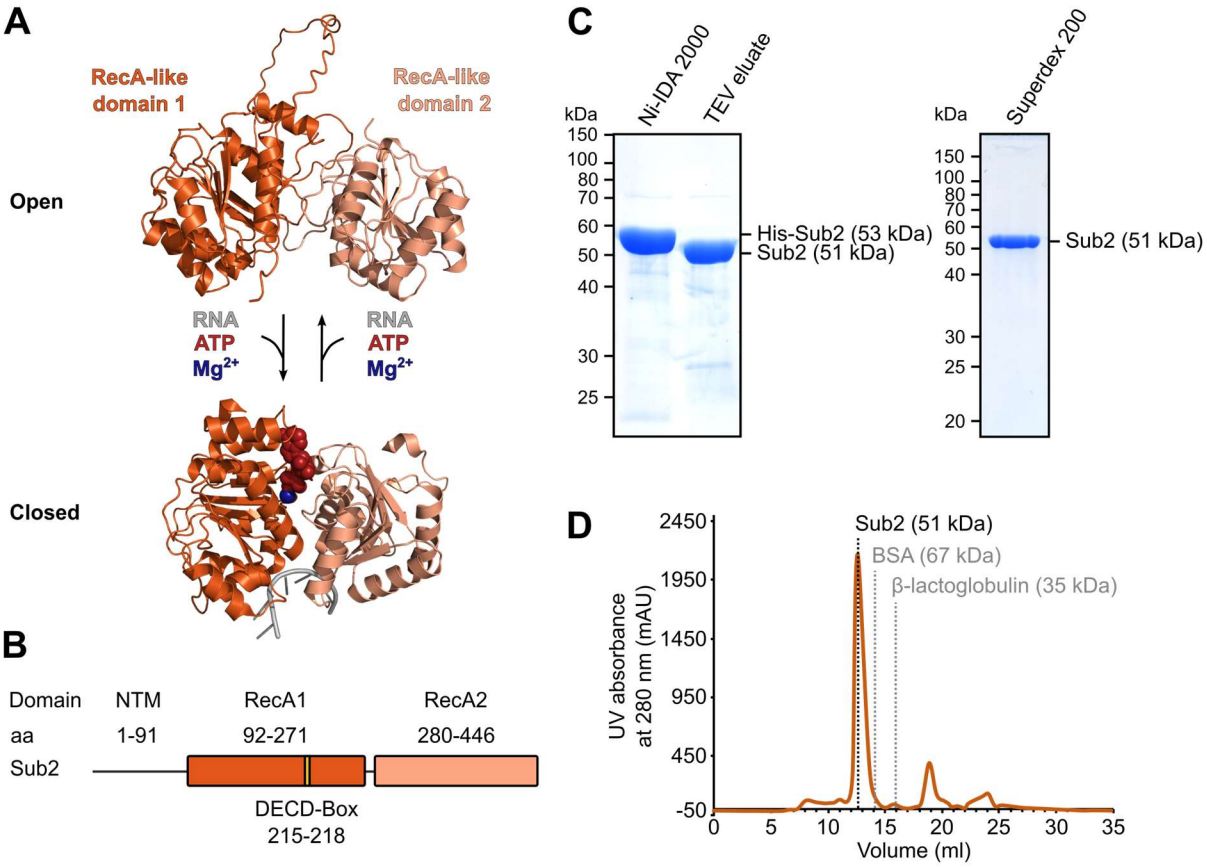

Figure 13: Purification of Sub2 yielded highly purified protein. (A) Model of the open conformation of Sub2 (top; DOI: 10.5452/ma-bak-cepc-0534) and crystal structure of the ATP- and RNA-bound closed state (bottom; PDB: 5SUP). **(B)** Domain organization of Sub2. RecA-like domain 1 (RecA1) is shown in dark orange, and RecA-like domain 2 (RecA2) in light orange. The DECD-Box (yellow) is located within RecA-like domain 1. **(C)** SDS-PAGE analysis of Sub2 during purification. Sub2 was first enriched by affinity chromatography (Ni-IDA 2000), followed by TEV protease cleavage (TEV eluate) and size-exclusion chromatography (Superdex 200). The positions of the His-tagged and cleaved proteins are indicated. **(D)** UV absorbance at 280 nm showing the elution of Sub2 at approximately 13 ml. According to the manufacturer's instructions, the marker proteins BSA (67 kDa) and β-lactoglobulin (35 kDa) elute at approximately 14 ml and 16 ml, respectively.

4.2.2. The Tho1-CTD mediates interaction with Sub2

The dot spot assays with the Tho1 domain mutants revealed that the Tho1-CTD alone is sufficient to suppress the ts phenotype of Δ*hpr1* cells (Figure 12). However, this domain lacked detectable RNA-binding or annealing activities (Figure 11; Miosga, 2022), raising the question of how it facilitates suppression *in vivo*. As mentioned above, the Tho1-CTD mediates interaction with Sub2, which was initially suggested by a structural model of the Tho1-Sub2 complex (Figure 14A; Humphreys *et al.*, 2021). This prediction was later supported by a co-crystal structure of the Tho1-CTD interacting with two protomers of human DDX39B (Xie *et al.* 2023). Furthermore, Miosga (2022) experimentally confirmed the interaction between the Tho1-CTD and

yeast Sub2 by examining ternary complex formation of Tho1 domain mutants with Sub2 and RNA in an EMSA. This assay allows discrimination between free RNA and RNA-protein complexes based on their different migration rates in a native gel.

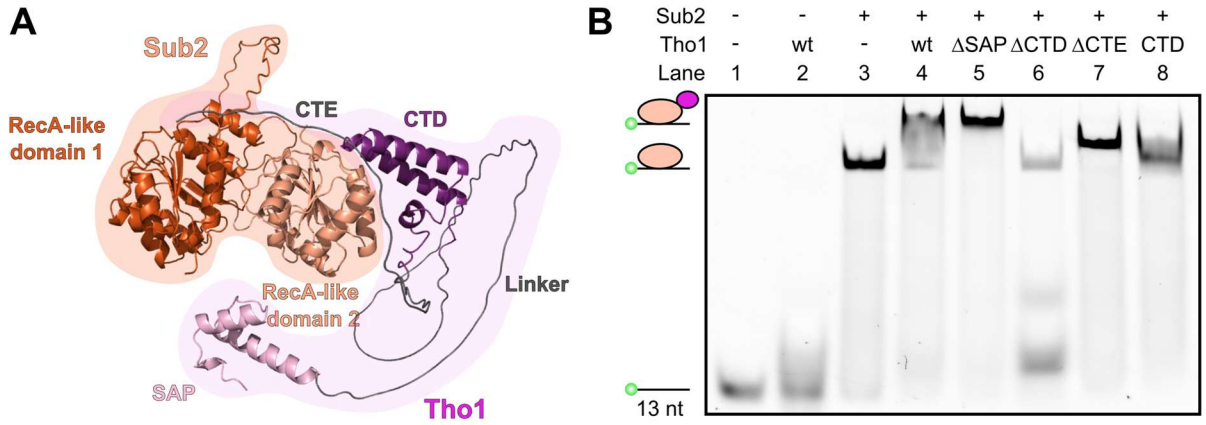

Figure 14: The Tho1-CTD mediates ternary complex formation with Sub2 and RNA. (A) Predicted interaction between Sub2 (left, orange) and Tho1 (right, pink), mediated by the Tho1-CTD (DOI: 10.5452/ma-bak-cepc-0534; Humphreys *et al.* 2021). **(B)** Ternary complex formation of Tho1 domain mutants with Sub2 and RNA was analysed by EMSA. Sub2 (5 µM) was incubated with 13 nt Cy3-labelled RNA (100 nM) and the indicated Tho1 mutants (10 µM) in the presence of 1 mM AMPPNP and subsequently separated on a 10% native polyacrylamide gel. The Cy3-labelled RNA was detected using a Typhoon FLA 9500 laser scanner. The positions of free RNA and RNA-protein complexes are indicated. A representative result from two independent experiments is shown.

These results were independently reproduced in this work (Figure 14B). The 13 nt Cy3-labelled ssRNA alone migrated faster through the gel, while addition of Sub2 slowed down migration and thus caused an upward shift of the ssRNA band, indicating binding (Figure 14B, lanes 1 and 3). In the presence of Tho1, no clear shift was discernible, although the RNA signal is slightly dispersed upwards (Figure 14B, lane 2). Incubation with both Sub2 and Tho1 resulted in a higher supershift, indicating ternary complex formation with the RNA (Figure 14B, lane 4). This shift was even more pronounced for the Tho1-ΔSAP mutant (Figure 14B, lane 5). The Tho1-ΔCTE also induced a significant shift, although it displayed slightly higher mobility than wild-type Tho1 or Tho1-ΔSAP (Figure 14B, lane 7). In contrast, the Tho1-ΔCTD mutant produced no detectable supershift (Figure 14B, lane 6). Instead, two additional bands appeared in the lower section of the gel, both showing reduced mobility relative to free RNA. Notably, the Tho1-CTD caused a slight but reproducible upshift of the Sub2-ssRNA band (Figure 14B, lane 8).

In summary, the data confirm the previous findings by Miosga (2022), demonstrating that the CTD of Tho1 is both necessary and sufficient for the interaction with Sub2.

4.2.3. The Tho1-CTD slightly increases Sub2's RNA-binding affinity

The observation that the Tho1-CTD does not bind RNA yet still forms a complex with Sub2 and RNA indicates that RNA interaction in this context is mediated exclusively by Sub2. To determine whether the Tho1-CTD modulates the RNA-binding affinity of Sub2, a series of binding assays was conducted (Figure 15).

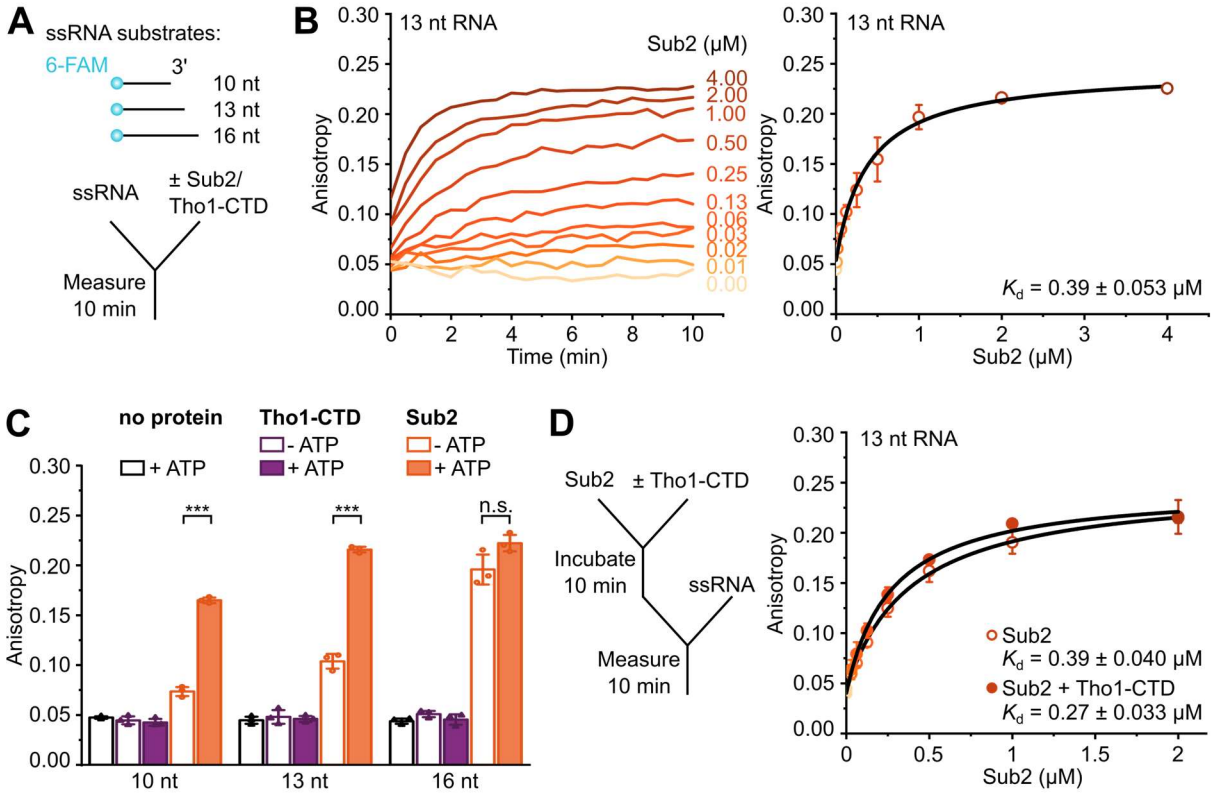

Figure 15: Sub2 binding to short RNA substrates. (A) Schematic overview of the binding assay and the 6-FAM-labelled RNA substrates tested. **(B)** Representative binding kinetics (left) and equilibrium titration (right, t = 10 min) of Sub2 (0.01-4 μM) binding to a 13 nt RNA. **(C)** Fluorescence anisotropy measured after 10 min of incubation of indicated RNA substrates (10 nt, 13 nt, and 16 nt) with either Sub2 (2 μM) or the Tho1-CTD (2 μM) in the presence or absence of ATP (2 mM). **(D)** Comparison of Sub2 binding to 13 nt ssRNA with or without the Tho1-CTD (2 μM), showing the assay scheme (left) and the corresponding equilibrium titrations at 10 min (right). RNA concentrations were 10 nM in all reactions. Data represent means ± SD of *n* = 3 experiments, respectively.

Sub2 bound to 13 nt 6-FAM-labelled RNA within 3 min of incubation, with a K_d of 0.39 ± 0.05 μM (Figure 15B). Comparison of Sub2 binding to ssRNA substrates of different lengths (10 nt, 13 nt, and 16 nt) in the presence or absence of ATP revealed that the maximal fluorescence anisotropy upon Sub2 binding increased slightly with RNA length, although the single-stranded RNAs exhibited similar baseline anisotropies (Figure 15C). ATP was required for efficient binding of Sub2 to 10 nt or 13 nt RNAs, whereas the longer 16 nt RNA was bound even in the absence of ATP. The Tho1-CTD

alone did not bind any of the tested RNA substrates under either condition. However, pre-incubation of Sub2 with the Tho1-CTD before adding 13 nt RNA resulted in a modest but significant decrease in K_d ($P = 0.0142$), indicating that the Tho1-CTD slightly enhances Sub2's RNA-binding affinity (Figure 15D).

4.3. The Tho1-CTD stimulates Sub2-mediated unwinding

4.3.1. The Tho1-CTD enhances partial duplex RNA unwinding by Sub2

Miosga (2022) studied the effects of different Tho1 domain mutants on Sub2-mediated unwinding and reported that while full-length Tho1 counteracts unwinding, the Tho1-CTD alone enhances it. After observing that the Tho1-CTD had only a minor effect on Sub2 binding to short RNA, its influence on Sub2's helicase activity was examined in detail.

To monitor unwinding by Sub2, a fluorescence-based real-time unwinding assay was implemented (Figure 16A), based on a principle similar to the annealing assay described in Chapter 4.1.3. A partial duplex RNA (pdRNA) substrate was used, in which the 13 nt top strand was labelled with 6-FAM and the 38 nt bottom strand with Cy5. Unwinding in the absence or presence of Sub2 was monitored for 15 min (phase 1), followed by the addition of either buffer or Tho1-CTD, before the measurement continued for an additional 45 min (phase 2). Fluorescence signals were detected in three channels (Figure 16B): donor (6-FAM) fluorescence upon donor excitation ($F_{D|D}$), acceptor (Cy5) fluorescence upon acceptor excitation ($F_{A|A}$), and acceptor fluorescence upon donor excitation ($F_{A|D}$).

In the presence of ATP and Sub2, a slight increase in $F_{D|D}$ accompanied by an anti-correlated decrease in $F_{A|D}$ was observed, indicating a loss of FRET due to unwinding of the pdRNA (Figure 16C, right panel). $F_{A|A}$ is not affected by FRET, thus the signal in this channel remained constant. Addition of the Tho1-CTD in phase 2 triggered a rapid increase in $F_{D|D}$ and decrease in $F_{A|D}$ (Figure 16D, right panel), indicating a stimulation of unwinding. The reactions are ATP-dependent, as control reactions lacking ATP showed no unwinding (Figure 16B and C, left panels).

These results show that, while Sub2 alone exhibits moderate helicase activity, this activity is further enhanced by the Tho1-CTD.

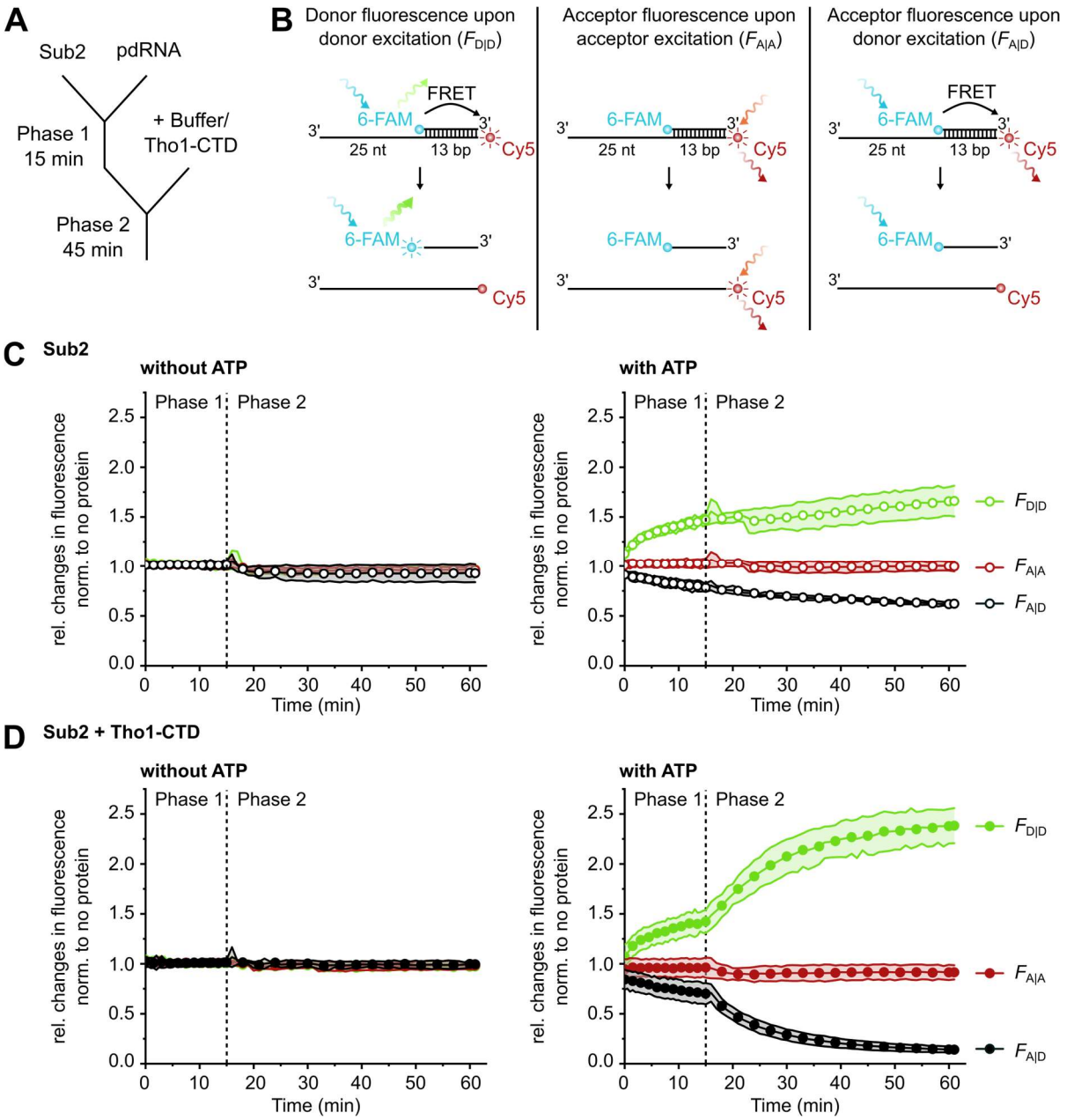

Figure 16: Sub2-mediated unwinding is accelerated by the Tho1-CTD. (A) Scheme of the assay. **(B)** Unwinding of a partial duplex (pd) RNA substrate consisting of a 6-FAM-labelled 13 nt top strand and Cy5-labelled 38 nt bottom strand was monitored in three channels: donor (6-FAM) fluorescence after donor excitation ($F_{D|D}$, green), acceptor (Cy5) fluorescence after donor excitation ($F_{A|D}$, black), and acceptor fluorescence after acceptor excitation ($F_{A|A}$, red). Arrows indicate which fluorophore is excited and measured in each channel. **(C)** Strand separation of the pdRNA (10 nM) by Sub2 (1 µM) led to increasing distances between the donor and acceptor dyes, resulting in loss of FRET. This was observed as a decrease in $F_{A|D}$ and a corresponding increase in $F_{D|D}$, while $F_{A|A}$ remained unchanged. Control reactions without ATP showed no unwinding. **(D)** Addition of the Tho1-CTD (2 µM) in phase 2 enhanced Sub2-mediated unwinding in both FRET-dependent channels in the presence of ATP (1 mM). Relative changes in fluorescence intensity were calculated by normalizing raw fluorescence signals to corresponding reactions without protein. Data are shown as mean ± SD of n = 3 experiments.

4.3.2. Substrate binding of Sub2 is insufficient for efficient pdRNA unwinding

The newly established real-time unwinding assay, using a 6-FAM-labelled top strand in the pdRNA substrate, not only monitored strand separation but also allowed simultaneous measurement of the 6-FAM anisotropy. This setup enabled direct analysis of pdRNA unwinding in the context of substrate binding (Figure 17).

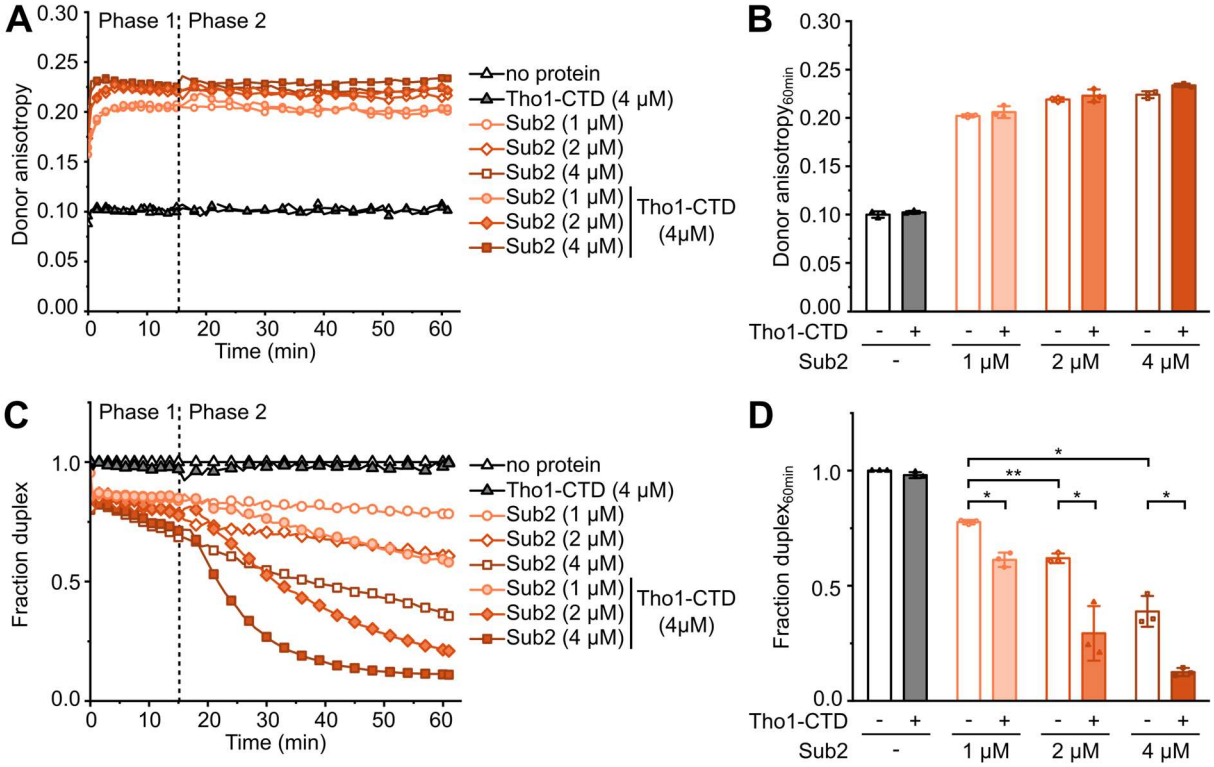

Figure 17: Sub2 binds pdRNA rapidly but unwinds inefficiently without the Tho1-CTD. The real-time unwinding assay allows simultaneous monitoring of Sub2 binding (A+B) and unwinding (C+D). **(A)** Representative Sub2 binding kinetics during the real-time unwinding assay are shown for the indicated Sub2 concentrations in the absence (empty symbols) or presence (filled symbols) of the Tho1-CTD (4 µM). **(B)** Comparison of fluorescence anisotropy after 60 min, shown as mean ± SD from n = 3 experiments. **(C)** Corresponding unwinding kinetics for the reactions shown in (A). **(D)** Comparison of the fraction duplex remaining after 60 min, shown as mean ± SD from n = 3 experiments. Reactions lacking protein or containing the Tho1-CTD alone served as controls.

Assays performed with different Sub2 concentrations (1 µM, 2 µM, and 4 µM) showed that substrate binding was complete within the first three minutes in all reactions, with lower Sub2 concentrations yielding slightly reduced maximum anisotropy values (Figure 17A and B). In contrast, unwinding – hereafter represented as fraction duplex, calculated by normalizing $F_{A|D}$ intensities to reactions lacking protein – occurred only slowly, particularly at lower Sub2 levels (Figure 17C). Addition of the Tho1-CTD (4 µM) significantly stimulated unwinding in all reactions without affecting anisotropy

(Figure 17 A and C). The extent of stimulation depended on the Sub2 concentration, with the strongest enhancement at 4 µM Sub2 (~3.2-fold), followed by 2 µM (~2.1-fold), and 1 µM Sub2 (~1.3-fold) (Figure 17D). The Tho1-CTD alone neither bound nor unwound the pdRNA.

In summary, binding of the substrate by Sub2 is fast but does not lead to efficient unwinding in the absence of the Tho1-CTD.

4.3.3. The Tho1-CTD stimulates Sub2-mediated unwinding at low concentrations

As the Sub2 concentration influenced the degree of stimulation in the unwinding assay, the effect of varying Tho1-CTD concentrations in the presence of a constant amount of Sub2 (1 µM) was tested (Figure 18).

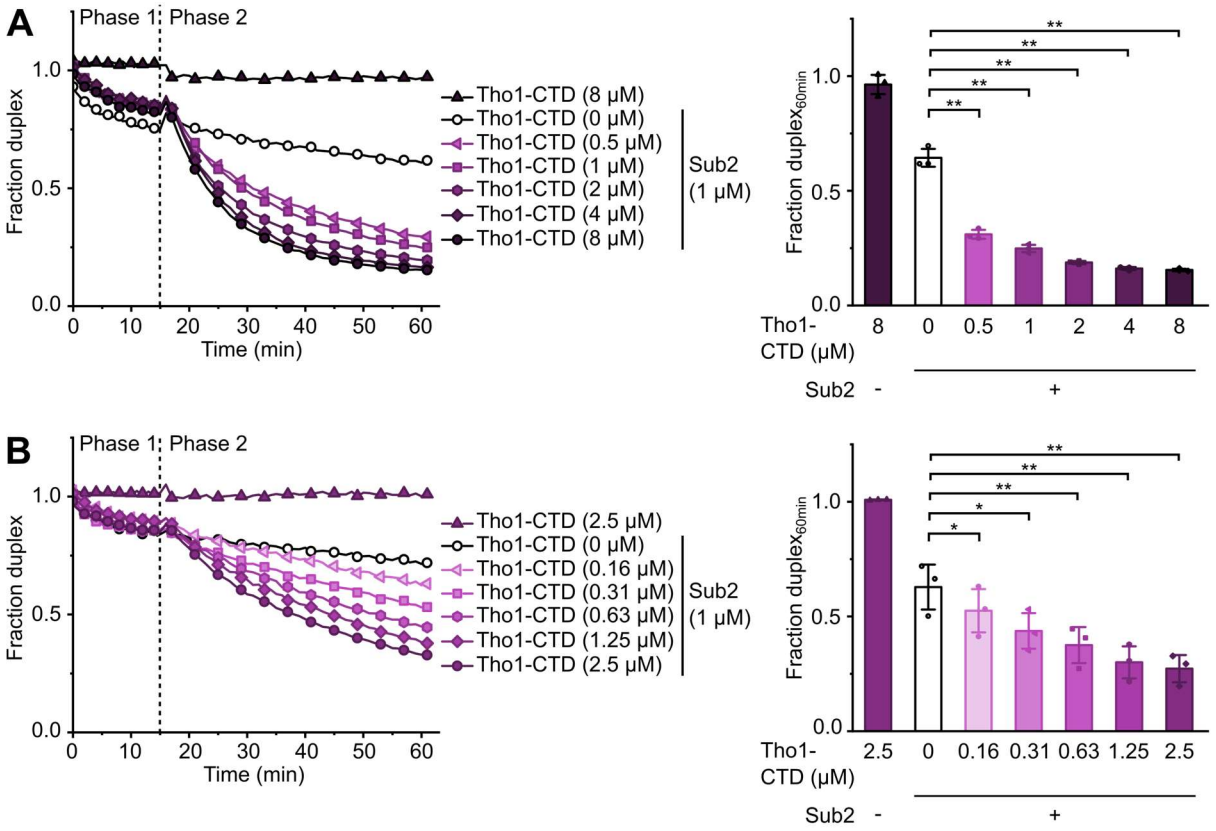

Figure 18: Sub2-mediated unwinding increases with Tho1-CTD concentration. pdRNA (10 nM) unwinding by Sub2 (1 µM) was measured either alone or in the presence of **(A+B)** 0.5-8 µM or **(C+D)** 0.16-2.5 µM Tho1-CTD during phase 2 of the reaction. The highest Tho1-CTD concentrations in each set were used for control reactions without Sub2. Shown are representative (A+C) unwinding kinetics and (B+D) quantifications of fraction duplex remaining after 60 min, presented as mean ± SD of $n = 3$ experiments. Notably, both the unwinding activity of Sub2 alone and the stimulation by the Tho1-CTD were higher in this assay compared to the measurements shown in Figure 17. This difference can be attributed to the fact that the Sub2 proteins used in these experiments were obtained from different purifications: the less active Sub2 in Figure 17 was purified without a gel filtration step, potentially resulting in lower purity and hence lower activity.

Using micromolar Tho1-CTD concentrations (0.5-8 µM) resulted in robust unwinding, with maximal stimulation observed at 2 µM Tho1-CTD or higher (Figure 18A and B). However, Tho1-CTD concentrations below that of Sub2 (i.e., <1 µM) were already sufficient for significant helicase stimulation, and additional experiments with even lower concentrations revealed weak but significant helicase stimulation even at 0.16 µM Tho1-CTD (Figure 18C and D).

In summary, stimulation of Sub2-mediated unwinding by the Tho1-CTD is concentration-dependent. Tho1-CTD concentrations as low as half of the Sub2 concentration are sufficient to achieve near-maximal stimulation, whereas increasing the Tho1-CTD beyond a twofold molar excess over Sub2 did not further enhance the effect.

4.4. Helicase stimulation depends on protein-protein interaction

4.4.1. A Tho1-interface mutant of Sub2 is not stimulated by the Tho1-CTD

The first step toward understanding the mechanism underlying Tho1-CTD-mediated stimulation of Sub2 unwinding was to examine whether this effect results from a direct protein-protein interaction. It was previously shown that a single amino acid substitution in human DDX39B, from aspartic acid (D) to arginine (R) at position 283 within its Tho1-CTD interaction interface, abolishes interaction with human SARNP (Xie *et al.* 2023).

Sequence comparison of DDX39B, Sub2, and *A. thaliana* UAP56 revealed strong conservation of this residue (Figure 19A). The corresponding amino acid in Sub2, D302, is likewise positioned within the predicted interaction interface with the Tho1-CTD (Figure 19B). Therefore, a Sub2-D302R mutant was generated and purified to a level comparable to wild-type Sub2 (Figure 19C). Subsequently, it was tested for its ability to form a ternary complex with RNA and the Tho1-CTD (Figure 19D). While the RNA signal was slightly supershifted in the presence of wild-type Sub2 and the Tho1-CTD, this shift was absent with Sub2-D302R, indicating a loss of interaction between the two proteins.

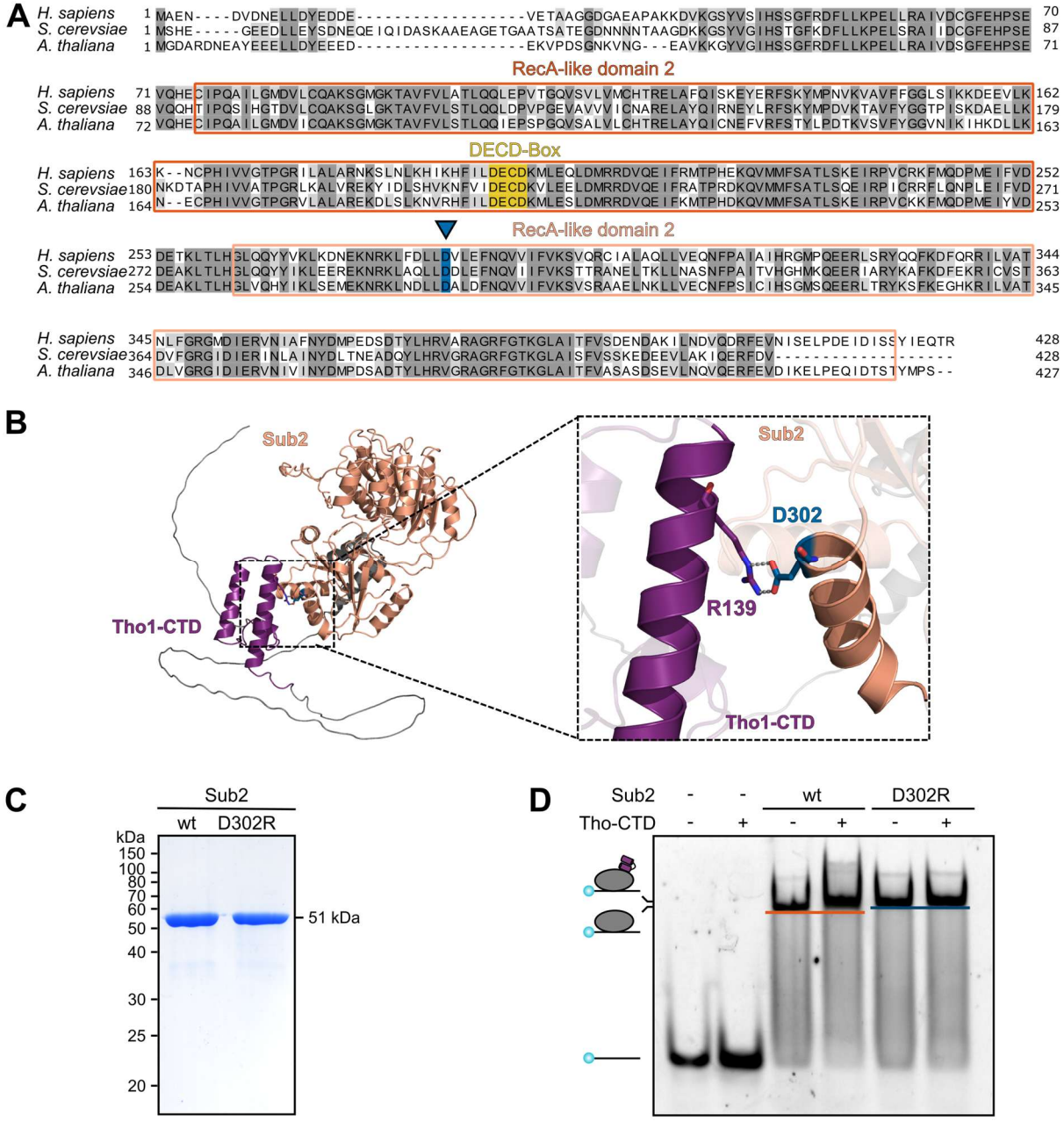

Figure 19: Interface mutant Sub2-D302R does not interact with the Tho1-CTD. **(A)** Sequence alignment of human DDX39B (UniProt: Q13838), yeast Sub2 (UniProt: Q07478) and *A. thaliana* UAP56 (UniProt: Q56XG6). The conserved aspartic acid residue, mutated to disrupt interaction with the Tho1-CTD, is indicated by a blue triangle. Alignment was performed using Clustal and JalView (Waterhouse *et al.* 2009). **(B)** Predicted Sub2-Tho1 interaction (left) with a close-up of the interaction interface (right) (DOI: 10.5452/ma-bak-cepc-0534; Humphreys *et al.* 2021). The amino acid mutated in Sub2-D302R and the corresponding residue in the Tho1-CTD (R139) are shown as sticks. **(C)** SDS-PAGE (12%) analysis of 2 µg purified Sub2 and Sub2-D302R. **(D)** EMSA assessing ternary complex formation of Sub2 and Sub2-D302R with the Tho1-CTD and 6-FAM-labelled 13 nt RNA. The labelled RNA was detected using a Typhoon FLA 9500 laser scanner. Formed complexes are indicated. The slight shift in the RNA signal observed for Sub2 in the presence of the Tho1-CTD, and the absence of this shift for Sub2-D302R, are highlighted with red and blue lines, respectively. Representative result of two experiments.

To ensure that the mutation in Sub2-D302R affected only the interaction interface with the Tho1-CTD and did not induce unintended changes in the protein structure, hydrogen/deuterium exchange mass spectrometry (HDX-MS) was performed by Dr. Wieland Steinchen (Marburg University). In HDX-MS, a protein is exposed to deuterium-containing solvent, allowing exchange of backbone hydrogens with the heavier isotope deuterium, which is subsequently detected by mass-spectrometry.

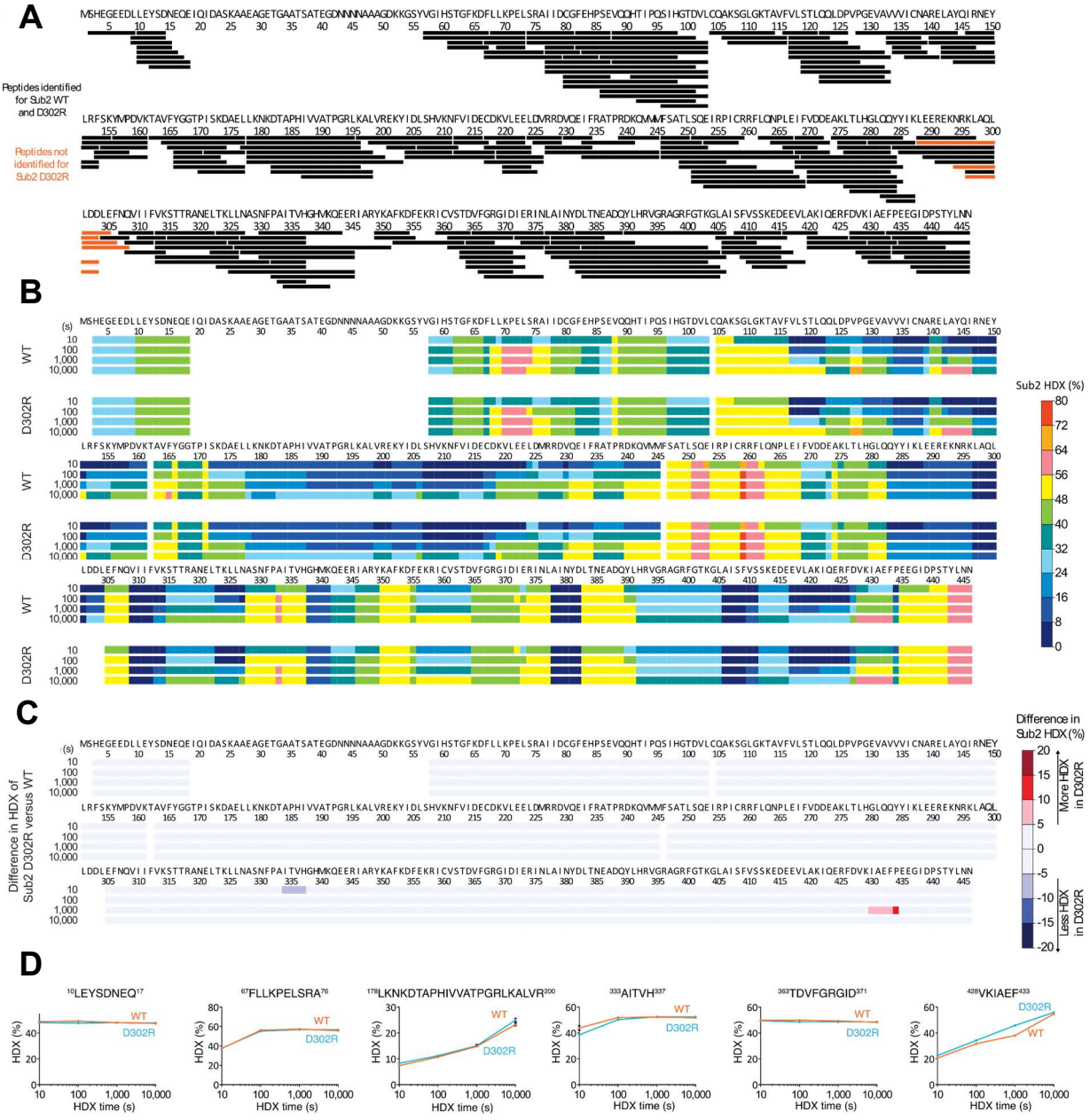

Figure 20: Sub2 and Sub2-D302R show only minor differences in HDX-MS. (A) Peptides identified by HDX-MS are indicated as black bars. **(B)** Percentage of deuterium incorporation (HDX) in Sub2 and Sub2-D302R at specific residues. **(C)** Differences in HDX for Sub2-D302R relative to Sub2. Blue regions mark lower deuterium incorporation in Sub2-D302R compared to Sub2, whereas red regions mark higher incorporation. **(D)** HDX of selected representative Sub2 peptides. Data are shown as mean ± SD of *n* = 3 technical replicates. HDX measurements and analyses were performed by Dr. Wieland Steinchen (Marburg University).

The rate and extent of this exchange depend on the protein's folded state. Therefore, HDX-MS can be used to study the conformation of individual proteins and map structural changes (Vinciauskaite & Masson 2023).

Sub2-D302 exhibited only two minor regions of change (Figure 20). In region 334-337, a slight decrease in deuterium incorporation was detected after 10 s of HDX, whereas a small increase was observed in residues 430-434 after 1000 s (Figure 20D). The changes were relatively subtle (up to -5% and 15%, respectively) and were measured only at a single time point during the HDX experiment (Figure 20). Therefore, Sub2-D302R was considered structurally similar to wild-type Sub2.

After demonstrating that the interaction mutant was properly folded, retained wild-type-like RNA-binding capability, and specifically lacked interaction with the Tho1-CTD, pdRNA unwinding by Sub2-D302R was analysed (Figure 21).

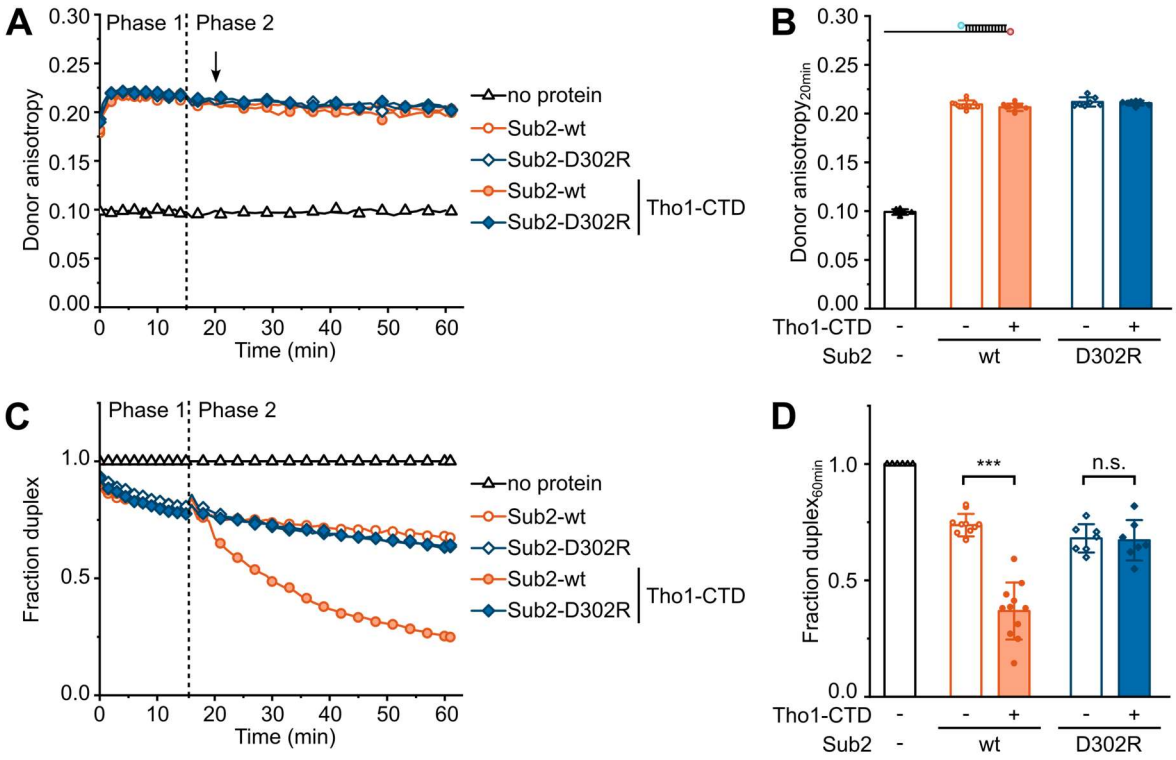

Figure 21: Interface mutant Sub2-D302R is not stimulated by the Tho1-CTD. **(A)** Representative binding kinetics of Sub2 and Sub2-D302R (1 µM) in the absence or presence of the Tho1-CTD (2 µM). The time points used for quantification in (B) are indicated by a black arrow. **(B)** Quantification of donor anisotropy measured 20 min after the start of the reaction, or 5 min after the addition of the Tho1-CTD, respectively. Data are shown as mean ± SD from $n \geq 6$ experiments. **(C)** Corresponding unwinding kinetics for the reactions shown in (A). Addition of the Tho1-CTD in phase 2 enhanced unwinding by Sub2 but not by Sub2-D302R. **(D)** Quantification of fraction duplex remaining after 60 min, shown as mean ± SD from $n \geq 6$ experiments.

Sub2 and Sub2-D302R alone exhibited comparable binding and unwinding activities (Figure 21). However, whereas the Tho1-CTD strongly stimulated unwinding by wild-type Sub2 in phase 2, no stimulation was observed for Sub2-D302R (Figure 21C and D).

Taken together, the mutation in the Tho1-interaction interface of Sub2 abolished its physical interaction with the Tho1-CTD, which is essential for Tho1-CTD-mediated helicase stimulation.

4.4.2. Tho1 counteracts unwinding independently of Sub2 interaction

In contrast to the helicase stimulation observed for the Tho1-CTD, addition of full-length Tho1 has been shown to reverse an ongoing Sub2-mediated unwinding reaction (Miosga 2022). This effect is lost in Tho1 mutants lacking annealing activity, suggesting that Tho1 counteracts unwinding by annealing the RNA strands (Miosga 2022).

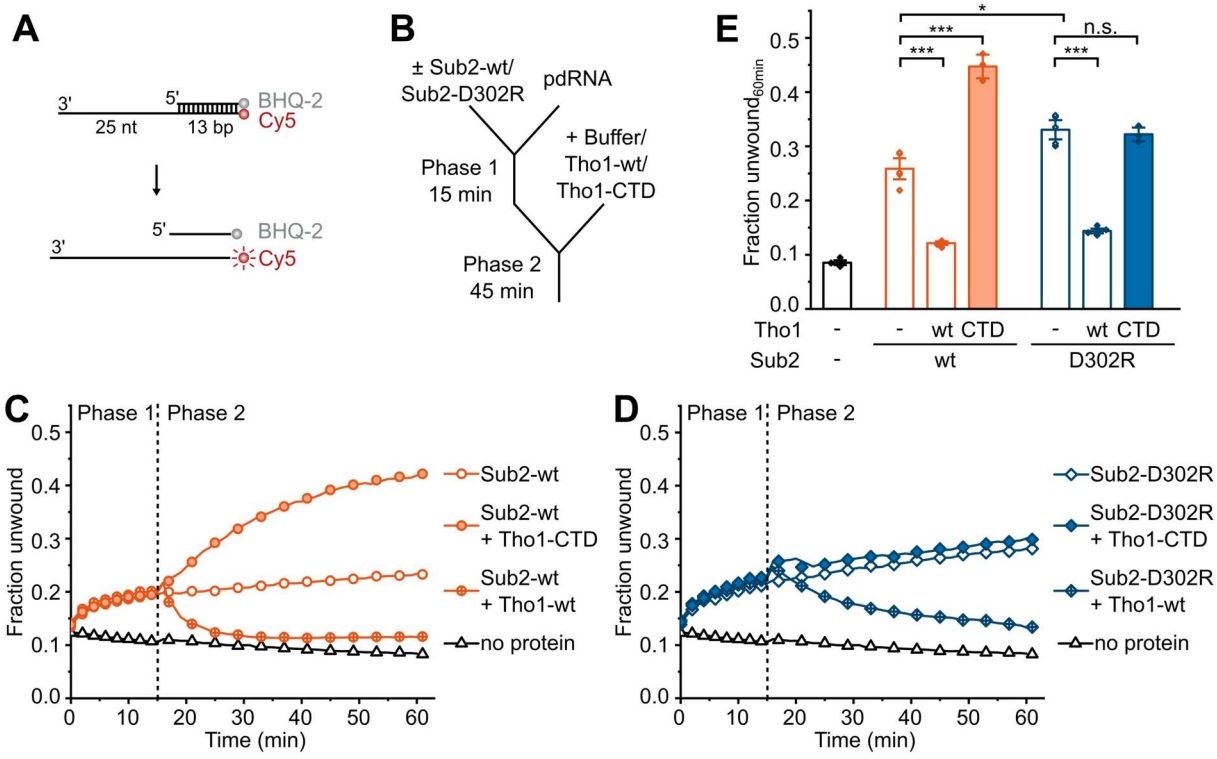

Figure 22: Full-length Tho1 still counteracts unwinding of Sub2-D302R. (A) The pdRNA substrate used for this assay consisted of a BHQ-2-labelled 13 nt top strand and a 38 nt Cy5-labelled bottom strand. Unwinding was monitored as an increase in Cy5 fluorescence. **(B)** Scheme of the assay, analogous to the previously described real-time unwinding assay in Figure 16. **(C+D)** Representative time courses of pdRNA (10 nM) unwinding by 1 µM of (C) Sub2 or (D) Sub2-D302R. In phase 2 of the reaction either buffer, full-length Tho1 (2 µM) or the Tho1-CTD (2 µM) was added. Fraction unwound was calculated by normalizing the measured Cy5 intensities to signals obtained from a 38 nt Cy5-labelled ssRNA. **(C)** Quantified fraction unwound after 60 min shown as mean ± SD of $n \geq 3$ experiments.

To confirm that the observed counteraction by Tho1 results from its intrinsic annealing activity and to test whether protein-protein interactions also contribute, the effect of Tho1 on unwinding by wild-type Sub2 or the interface mutant Sub2-D302R was examined (Figure 22). For this purpose, the real-time fluorescence assay was slightly modified by using a substrate with a BHQ-2-labelled 13 nt top strand (Miosga 2022). In the pdRNA substrate, BHQ-2 quenches Cy5 fluorescence, whereas the quench is lost upon strand separation. Thus, unwinding can be monitored by measuring the increase in Cy5 fluorescence emission (Figure 22A and B).

Control reactions without protein showed a fraction unwound of approximately 0.1, indicating that ~10% of the substrate remained single-stranded (Figure 22C-E). In reactions containing wild-type Sub2, the signal increased rapidly after addition of the Tho1-CTD, confirming helicase stimulation (Figure 22C). As expected, this stimulation was absent for Sub2-D302R (Figure 22D). Addition of full-length Tho1, in contrast, reduced the signals for both Sub2 and Sub2-D302R (Figure 22C-E).

These findings indicate that unwinding counteraction by full-length Tho1 occurs independently of the Tho1-Sub2 interaction.

4.5. Helicase stimulation requires a single-stranded RNA overhang

Sub2 and DDX39B not only unwind RNA/RNA duplexes, but also different DNA/RNA hybrids – substrates frequently associated with R-loops (Pérez-Calero *et al.* 2020; Saguez *et al.* 2013). To test whether the Tho1-CTD also stimulates Sub2-mediated unwinding of DNA/RNA hybrids, partial duplex or blunt-end DNA, RNA, or hybrid substrates were analysed.

Sub2 did not unwind pdDNA or blunt-end DNA substrates (Supplementary Figure S4). Unwinding of the hybrid partial duplexes or blunt-end substrates proceeded considerably faster than pdRNA and the reactions were too rapid to be captured in the plate reader assay (data not shown). Therefore, unwinding kinetics were monitored by stopped-flow experiments. In a stopped-flow device, two solutions are rapidly combined and injected into an observation cell, where the flow is halted. This setup enables monitoring within milliseconds after mixing, thus capturing even very fast reactions (Fischer & Lohman 2004). Sub2, pre-incubated with buffer or the Tho1-CTD, was mixed with 6-FAM/Cy5-labelled substrates, and the reaction was measured for five minutes (Figure 23A).

Sub2 unwound a DNA/RNA hybrid with a 3′ ssRNA overhang substantially faster than pdRNA, and this activity was further enhanced by the Tho1-CTD (Figure 23B, left and middle panels). The corresponding RNA/DNA hybrid with a DNA overhang was unwound even more rapidly, although in this case the Tho1-CTD had no additional stimulatory effect (Figure 23B, right panel).

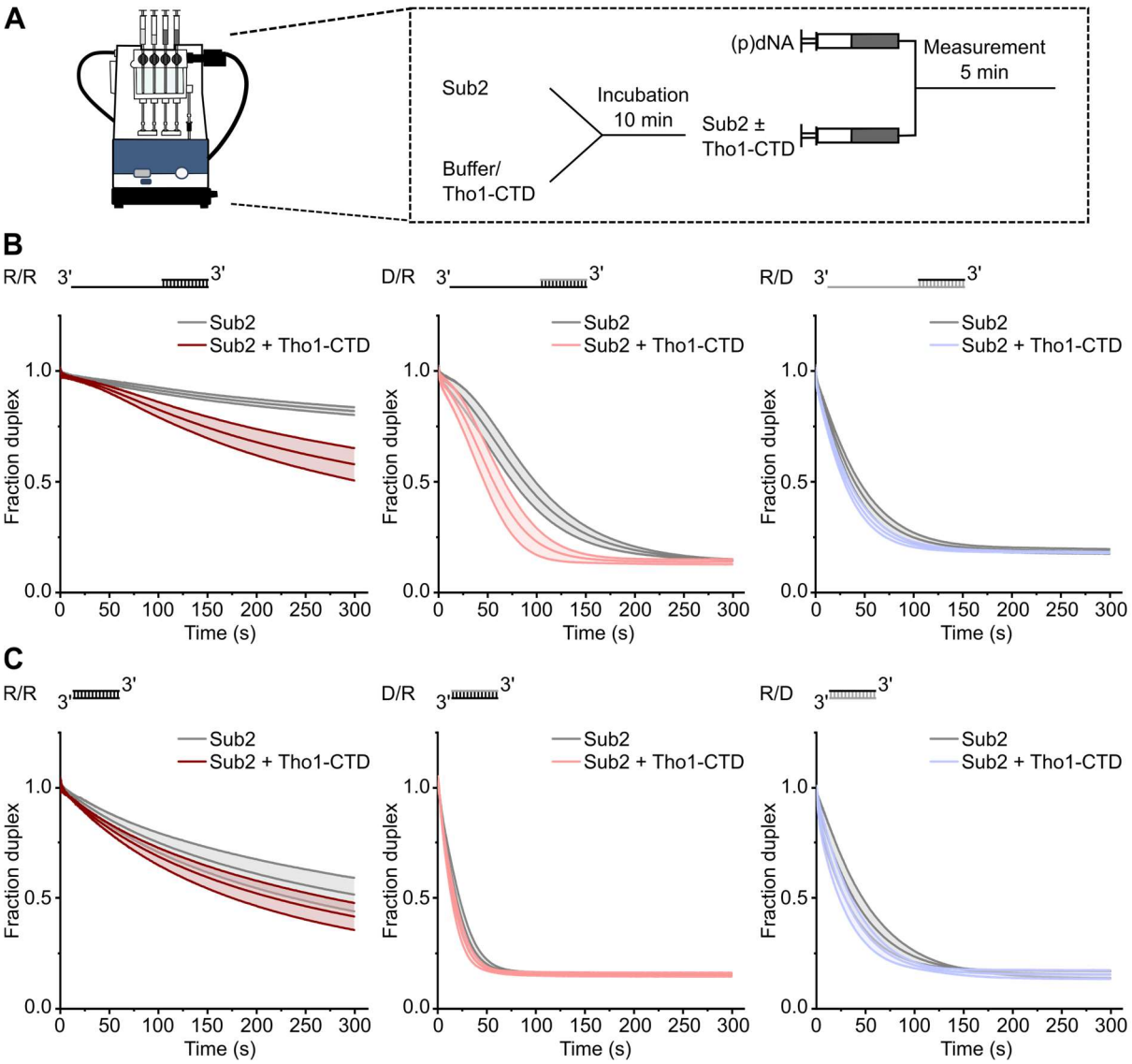

Figure 23: The Tho1-CTD-mediated helicase stimulation is substrate-dependent. **(A)** Scheme of the stopped-flow unwinding assay. The tested substrates consisted either of two RNA strands (R/R) or DNA/RNA hybrids (D/R and R/D). 13 nt top strands were labelled with 6-FAM, and 13 nt or 38 nt bottom strands were labelled with Cy5. Unwinding of **(B)** partial duplex substrates with a 25 nt 3′ single-stranded overhang or **(C)** blunt-end duplexes by Sub2 (1 µM) was measured in the absence or presence of the Tho1-CTD (0.5 µM). Data represent mean ± SD of *n* = 3 experiments.

To test whether a single-stranded RNA overhang is required to observe helicase stimulation, blunt-end substrates were tested (Figure 23C). RNA/RNA and DNA/RNA substrates lacking an ssRNA overhang were already unwound faster by Sub2 alone

than the corresponding partial duplex substrates (Figure 23C, left and middle panels). In contrast, unwinding of the RNA/DNA duplex by Sub2 was unaffected by the absence of an ssDNA region (Figure 23C, right panel). The Tho1-CTD did not accelerate Sub2-mediated unwinding of any of the tested blunt-end substrates (Figure 23C).
Together, these findings indicate that the presence of an ssRNA, but not an ssDNA, overhang reduces unwinding by Sub2, and that this inhibitory effect can be overcome through Tho1-CTD stimulation.

The partial duplex substrate tested so far contained a 3′ ssRNA overhang, which was required to observe helicase stimulation. To assess whether the orientation of the overhang influences this effect, pdRNA and DNA-RNA substrates carrying either 3′ or 5′ overhangs were examined for unwinding by Sub2 and the effect of the Tho1-CTD (Figure 24A and B). To ensure minimal substrate alteration other than the overhang orientation, the duplex region was kept identical, while the overhang was shifted from the bottom to the top strand, thereby converting a 3′ overhang into a 5′ overhang (Figure 24A). The top strand was labelled with BHQ-2 at its 3′ end and the bottom strand with Cy5 at its 5′ end.
As observed in Figure 22, the 3′ overhang pdRNA substrate was not fully annealed, with approximately 20% single-stranded species observed in the control reaction without protein. In contrast, the 5′ overhang substrate was almost entirely double-stranded under the same conditions, indicating more efficient annealing of the RNA strands in this substrate. Sub2 alone exhibited moderate unwinding on both pdRNA substrates (Figure 24C and D). Addition of the Tho1-CTD led to a small enhancement, which was slightly less pronounced for the 5′ overhang substrate. In contrast, for both DNA/RNA hybrids with a 3′ overhang or RNA/DNA hybrids with a 5′ overhang, Sub2 alone already showed higher unwinding, and addition of the Tho1-CTD further stimulated the reaction (Figure 24E and F).
Overall, these results indicate that stimulation by the Tho1-CTD operates independently of overhang orientation.

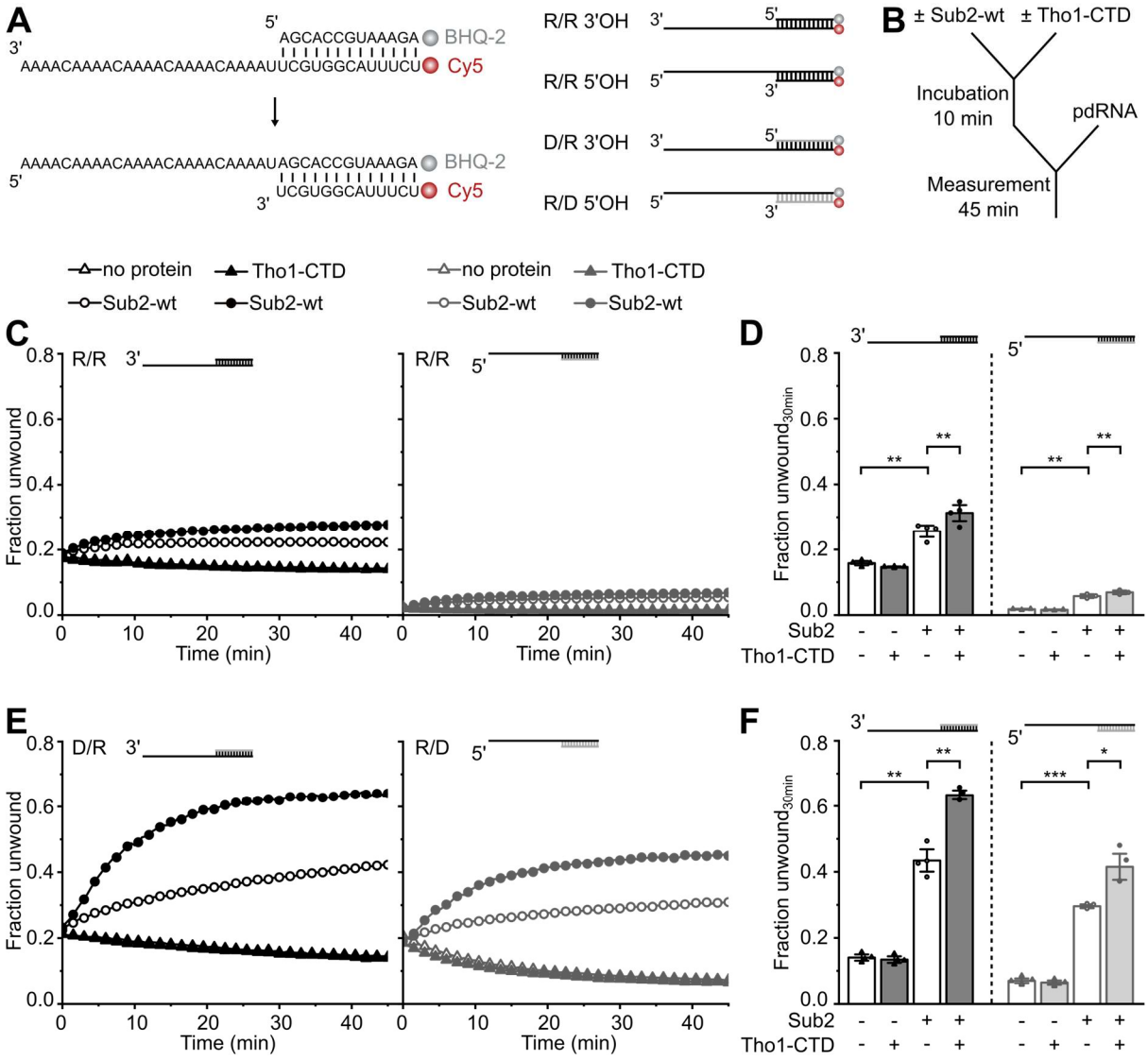

Figure 24: The Tho1-CTD stimulates unwinding on 3′ and 5′ overhang substrate. **(A)** Scheme of the unwinding reaction (left) and the different substrates used (right). The 13 nt top strands were labelled with BHQ-2 at the 3′ end and the 38 nt bottom strands were labelled with Cy5 at the 5′ end. pdRNA substrates (R/R) and DNA/RNA hybrids (D/R and R/D) were tested. **(B)** Scheme of reaction. **(C+E)** Exemplary unwinding kinetics of (C) pdRNA and (E) DNA/RNA hybrid substrates carrying either a 3′ overhang (left) or 5′ RNA overhang (right). **(D+F)** Quantification of (D) pdRNA and (F) DNA/RNA hybrid unwinding reactions corresponding to the reactions shown in (C) and (E), respectively. Data represent the fraction unwound after 30 min as mean ± SD from *n* = 3 experiments. All reactions were carried out using 0.5 µM Sub2, 1 µM Tho1-CTD, 2 mM ATP and 10 nM substrate.

4.6. Both helical motifs are required for Tho1-CTD function

In the co-crystal structure of the Tho1-CTD in complex with two DDX39B protomers, interactions with the helicases are mediated by two conserved α-helical motifs within the Tho1-CTD (Jacobsen *et al.* 2016; Xie *et al.* 2023). To model the corresponding interaction in yeast, AlphaFold 3 was used to predict a complex comprising two Sub2

molecules and the Tho1-CTD bound to the 13/38 pdRNA substrate used in the unwinding assays (Abramson *et al.* 2024). In these models, one Sub2 protomer was positioned near the 3′ end of the single-stranded region, while the second was located on the duplex region of the same RNA molecule (Figure 25A and B). As observed in the crystal structure, the Tho1-CTD was positioned between the two Sub2 protomers. Predicted Aligned Error (PAE) plots indicated high confidence in these models (Figure 25C and D).

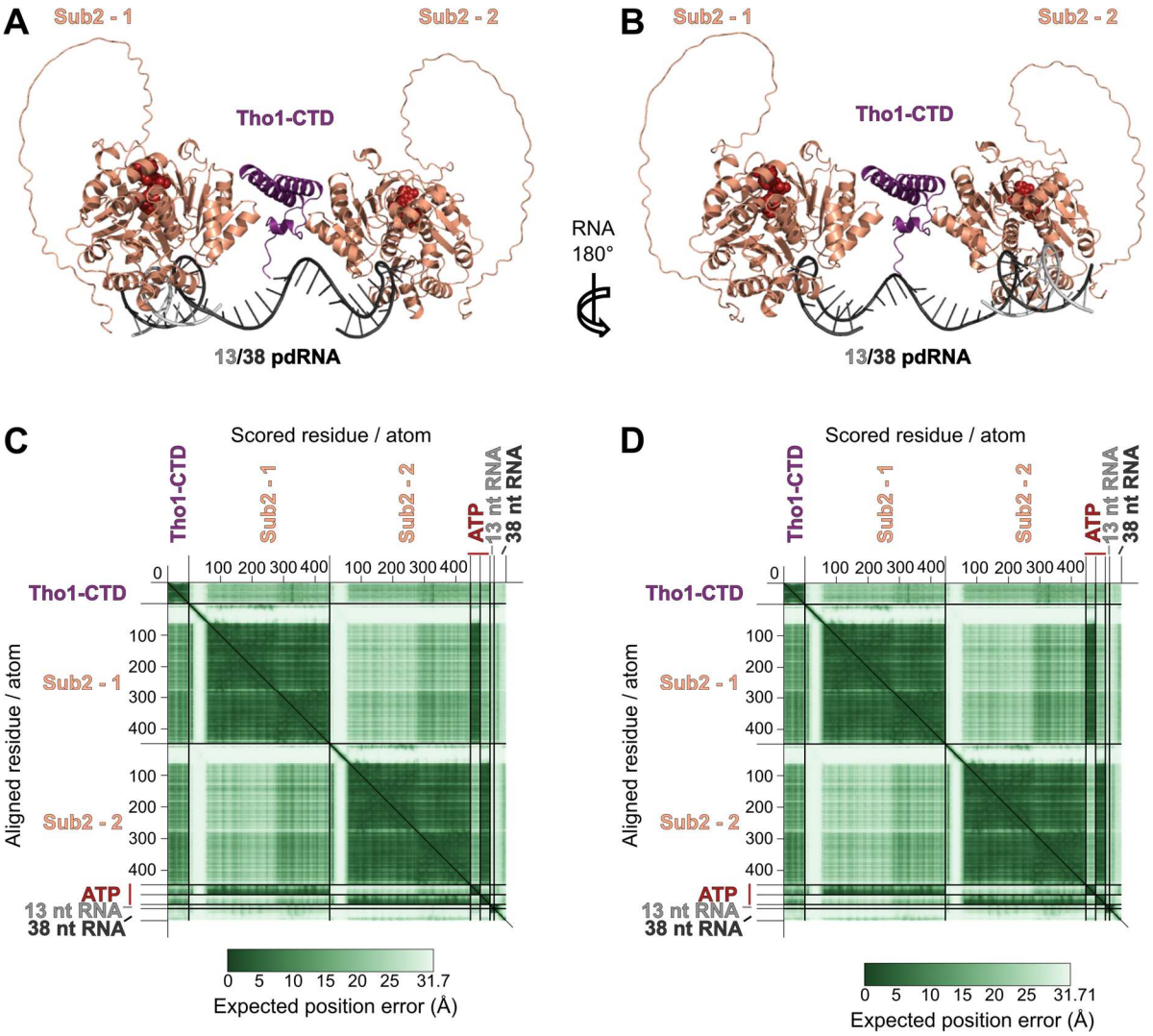

Figure 25: A model for the Sub2-Tho1 complex formation. (A) Complex of two Sub2 protomers and the Tho1-CTD bound to a 13/38 pdRNA predicted by AlphaFold 3 (Abramson *et al.* 2024). One Sub2 protomer is bound to the single-stranded region of the substrate, while the second Sub2 interacts with the duplex. ATP molecules are displayed as red spheres. **(B)** Alternative model of the complex in (A) likewise generated with AlphaFold 3, with the orientation of the pdRNA rotated by 180°. **(C+D)** PAE plots for the models shown in (A) and (B) (Elfmann & Stülke 2023). Low predicted errors (green) reflect high confidence in the relative placement of model components. Individual components are indicated. Shown are two representative models out of five generated.

4.6.1. Mutating a key residue in one helical motif abolishes helicase stimulation

As shown in Chapter 4.4.1, the Tho1-CTD failed to stimulate the helicase activity of the Sub2-D302R mutant incapable of interacting with the Tho1-CTD. However, both the findings of Xie et al. (2023) and the AlphaFold 3-generated yeast model (Figure 25) suggest a complex consisting of two Sub2 protomers and one Tho1-CTD protomer. This raises the question of whether helicase stimulation requires a 2:1 stoichiometry or can occur through interaction with a single Sub2 protomer. As this cannot be resolved using the Sub2 mutant, the interaction interface on the Tho1-CTD was systematically disrupted. To this end, mutants were generated in which either one or both helical motifs were impaired, and their effects on unwinding by Sub2 were assessed (Figure 26).

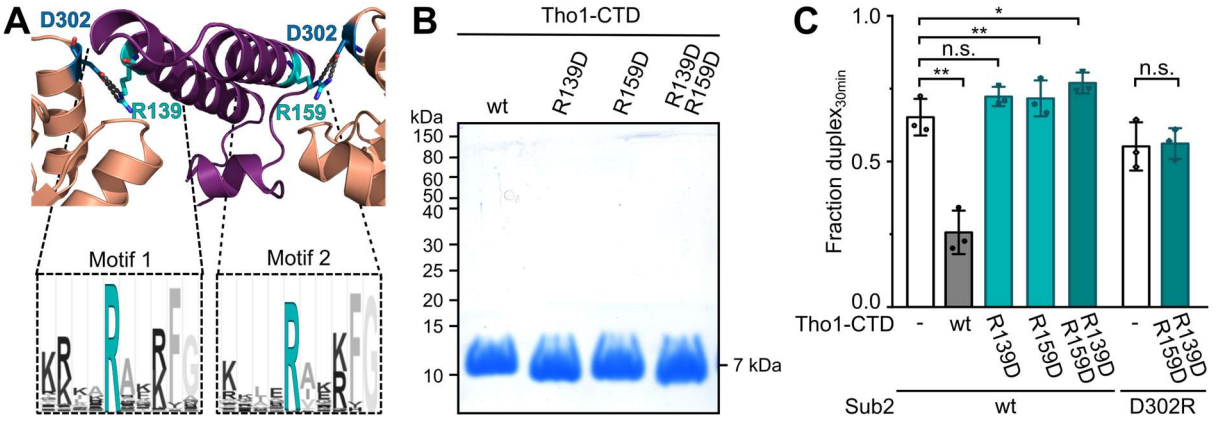

Figure 26: Conserved Tho1-CTD arginines are required for Sub2 stimulation. (A) Close-up of the predicted interaction interface of the 2:1 Sub2-Tho1-CTD complex shown in Figure 25A, with sequence logos of both helical motifs (Pfam: PF18592). The conserved arginine residues R139 and R159 (cyan) interact with Sub2-D302 (blue). **(B)** SDS-PAGE (17%) analysis of 2 µg purified Tho1-CTD and mutants thereof. Mutations were introduced in either one of the two motifs (R139D and R159D, respectively) or in both (R139D/R159D). **(C)** Unwinding of a 13/38 pdRNA by Sub2 or Sub2-D302R (1 µM) was analysed in the absence or presence of 2 µM of wild-type Tho1-CTD or the indicated mutant. Fraction duplex remaining after 30 min is presented as mean ± SD of *n* = 3 experiments.

The conserved Tho1-CTD arginine residues (R139 and R159) that mediate interaction with Sub2 residue D302 were substituted with aspartic acids, generating Tho1-CTD single (R139D and R159D, respectively) and double (R139D/R159D) mutants (Figure 26A). SDS-PAGE confirmed successful purification of all mutants (Figure 26B). Consistent with the complete loss of stimulation observed for Sub2-D302R, the Tho1-CTD-R139D/R159D double mutant did not stimulate Sub2-mediated pdRNA unwinding (Figure 26C). Notably, mutation of either motif alone in the single mutants was sufficient to abolish helicase stimulation (Figure 26C). An attempt to restore the interaction

interface by combining Sub2-D302R with the Tho1-CTD-R139D/R159D was unsuccessful, as no stimulation was observed.

After demonstrating that mutation of a single conserved arginine in the Tho1-CTD prevented helicase stimulation, the importance of other conserved residues within the helical motifs was examined (Figure 27). In addition to the two previously analysed arginine residues, now substituted with lysines (R139K, R159K), three additional highly conserved positions in each motif were selected for mutagenesis: lysines at positions 142 and 162 were replaced with arginines (K142R, K162R); phenylalanines at positions 143 and 163 were substituted with tyrosines (F143Y, F163Y); and glycines at positions 144 and 164 were replaced with alanines (G144A, G164A) (Figure 27A).

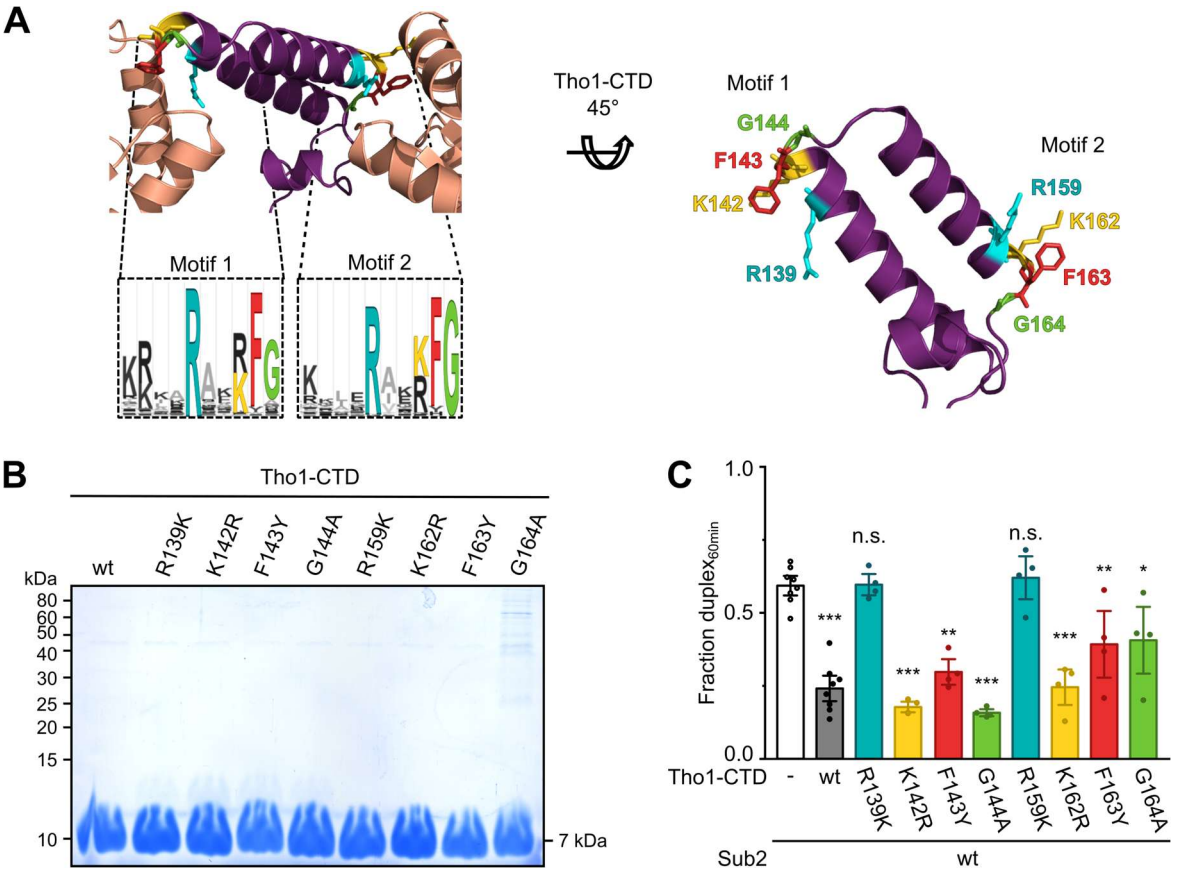

Figure 27: Analysis of different Tho1-CTD interface mutants. (A) Left: Close-up of the predicted interaction interface of the 2:1 Sub2-Tho1-CTD complex shown in Figure 25A, with sequence logos of both helical motifs (Pfam: PF18592). Right: Tho1-CTD alone, rotated by 45°. Conserved arginine (R, cyan), lysine (K, yellow), phenylalanine (F, red), and glycine (G, green) residues used for mutations are shown as sticks. **(B)** SDS-PAGE (17%) analysis of Tho1-CTD and mutants thereof. Arginines were replaced by lysines and vice versa (R139K, R159K, K142R, K162R), phenylalanines were substituted by tyrosines (F143Y, F163Y) and glycines were exchanged for alanines (G144A, G164A). **(C)** Unwinding of a 13/38 pdRNA by Sub2 (1 µM) with or without 2 µM of wild-type Tho1-CTD or the indicated mutant. Fraction duplex remaining after 60 min is shown as mean ± SD of $n \geq 3$ experiments.

All mutants were successfully purified (Figure 27B). While both Tho1-CTD-R139K and -R159K failed to stimulate Sub2-mediated unwinding, helicase stimulation remained detectable for all other mutants. Only minor decreases in the extent of unwinding stimulation were observed for Tho1-CTD-F143Y, -F163Y, and -G164A (Figure 27C).

4.6.2. Both Tho1-CTD helical motifs are required for ts phenotype suppression

Since the 2:1 Sub2-Tho1 interaction proved essential for helicase stimulation *in vitro*, the ability of Tho1-CTD-R139K and -R159K to suppress the ts phenotype of ∆*hpr1* cells was tested. Initial experiments using plasmid-based expression yielded highly variable protein levels of the Tho1-CTD and its mutants, making it difficult to obtain reproducible results. To overcome this limitation, wild-type *THO1* and the respective mutant genes were genomically integrated at the endogenous *THO1* locus of both wild-type and ∆*hpr1* backgrounds (Figure 28A, Supplementary Figure S5). All constructs were placed under control of the *GAL1* promoter, which is strongly induced by galactose and repressed by glucose. Western blot analysis confirmed robust overexpression of the respective proteins in galactose-containing medium, while expression was efficiently repressed under glucose conditions (Figure 28B-E). This approach thus ensured stable expression of the Tho1-CTD and its mutants and enabled examination of their *in vivo* function in the absence of endogenous Tho1.
To assess growth phenotypes, cells were spotted onto plates containing galactose or glucose and incubated at 30°C or 37°C. Overexpression of the constructs in wild-type cells had no detectable effect on growth, indicating that elevated Tho1 or Tho1-CTD levels were not toxic (Supplementary Figure S5). At 30°C, all strains exhibited normal growth, and *THO1* repression under glucose conditions caused no major defects. In contrast, all ∆*hpr1*-derived strains displayed a severe growth defect on glucose-containing plates at 37°C (Figure 28F). Notably, strains carrying genomic integrations, and thus lacking native Tho1 expression under these conditions, grew even weaker than the ∆*hpr1* control strain. On galactose-containing medium, overexpression of either full-length Tho1 or the Tho1-CTD suppressed the ts phenotype, despite the absence of endogenous Tho1. In contrast, none of the Tho1-CTD mutants restored growth under these conditions.

Together, these results demonstrated that both helical motifs within the Tho1-CTD are essential not only for stimulation of Sub2's helicase activity *in vitro* but also for its function *in vivo*.

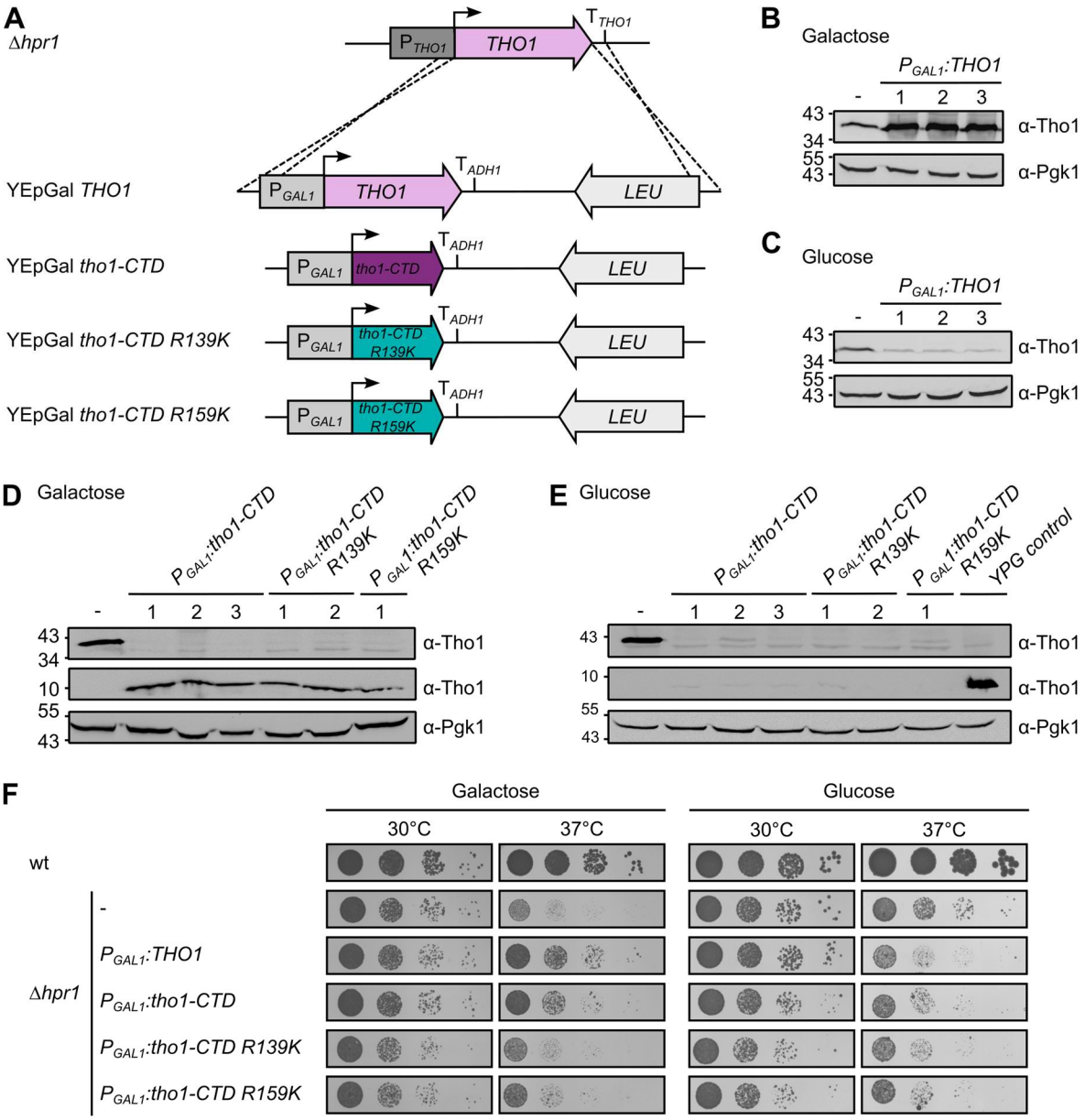

Figure 28: Mutations in the Tho1-CTD impede ts phenotype suppression. (A) Scheme of the genomic integration approach. The Δ*hpr1* strain expresses *THO1* from the endogenous promoter (P_{Tho1}). YepGal-derived constructs used for genomic integration contain wild-type *THO1* or the indicated mutants under control of the *GAL1* promoter (P_{GAL1}). *LEU* serves as a selection marker. **(B+C)** Total protein levels of Δ*hpr1* whole-cell extracts with genomic integration of P_{GAL1}:*THO1* grown in (B) galactose- or (C) glucose-containing medium. The polyclonal Tho1 antibody was used to detect wild-type Tho1. Pgk1 served as a loading control. **(D+E)** Western blot analysis of protein levels of the Tho1-CTD or the indicated mutants in Δ*hpr1* cells grown under either (D) galactose conditions (YPG) or (C) glucose conditions (YPD). **(F)** Dot spot assay of Δ*hpr1* cells expressing the indicated construct under P_{GAL1} control. Tenfold serial dilutions of cells were spotted onto galactose- or glucose-containing plates and incubated at the indicated temperatures for three days. Wild-type cells and native Δ*hpr1* cells were used as controls. Representative result of five technical replicates.

4.7. Helicase stimulation by the Tho1-CTD relies on a 2:1 complex

4.7.1. The Tho1-CTD stimulates *A. thaliana* UAP56

The crystal structure of the yeast Tho1-CTD with human DDX39B demonstrates conservation of this interaction (Xie *et al.* 2023). To also test functional conservation, the effect of the Tho1-CTD on the unwinding activity of *A. thaliana* UAP56 was examined. UAP56 was previously shown to be stimulated by the *A. thaliana* Tho1 ortholog MOS11 in a master's thesis by Minhaz Mannan conducted in our group (2022). This stimulatory effect was later independently reported by (Rödel *et al.* 2024).

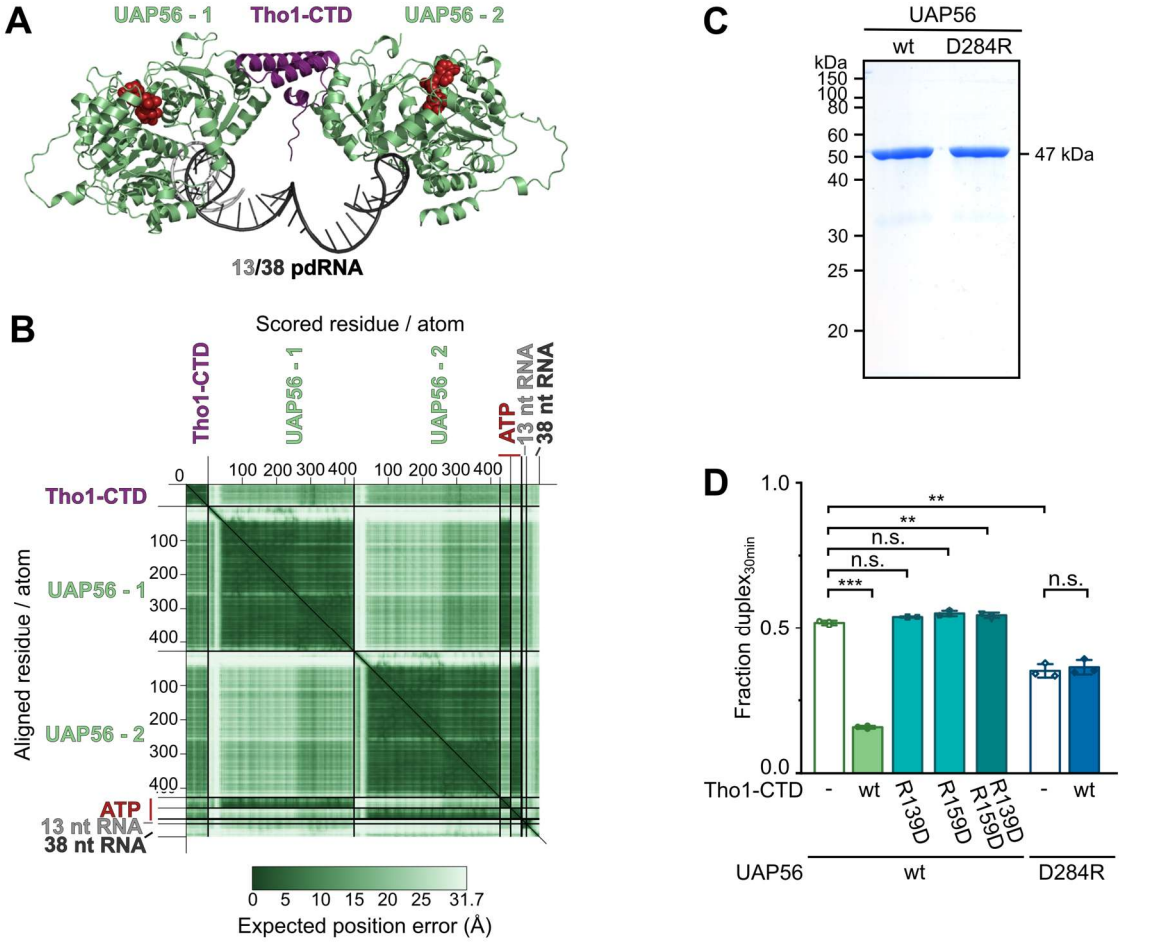

Figure 29: Helicase stimulation of *A. thaliana* UAP56 by the Tho1-CTD. (A) AlphaFold 3 prediction of a complex formed by two UAP56 molecules, the Tho1-CTD and a 38 nt RNA (Abramson *et al.* 2024). ATP molecules are shown as red spheres. **(B)** PAE plot for the model shown in (A). Low position errors (green) reflect high confidence in the relative placement of the indicated model components. Shown is one representative model out of five generated. **(C)** SDS-PAGE (12%) analysis of 2 µg wild-type UAP56 and interface mutant UAP56-D284R showing similar purities. UAP56 and UAP56-D284R were cloned by Minhaz Mannan during his master's thesis (2022) and Jan Kohlert during his bachelor's thesis (2024), respectively. **(D)** Unwinding of a 13/38 pdRNA was measured for 1 µM UAP56 or UAP56-D284R in the absence or presence of 2 µM of the Tho1-CTD or indicated mutants. Fraction duplex remaining after 30 min is shown as mean ± SD from *n* = 3 experiments.

AlphaFold 3 predictions for a 2:1 complex formed by two UAP56 protomers and the Tho1-CTD bound to a 38 nt-long RNA resembled both the crystal structure and the models generated for two Sub2 protomers and the Tho1-CTD (Figure 29A and B). UAP56 and the interface mutant UAP56-D284R, corresponding to Sub2-D302R/DDX39B-D283R, were recombinantly expressed and purified (Figure 29C). As observed for Sub2, unwinding of a 13/38 pdRNA substrate was stimulated in the presence of the Tho1-CTD, and this stimulation was abolished in the Tho1-CTD interface mutants (Figure 29D). The UAP56-D284R mutant alone exhibited stronger unwinding than the wild-type protein; however, its activity was not further enhanced by the Tho1-CTD.

These results indicate that the mechanism by which the Tho1-CTD stimulates Sub2/UAP56 is evolutionarily conserved.

4.7.2. UAP56-Tho1-CTD complexes can be crosslinked

The UAP56-Tho1-CTD AlphaFold 3 model revealed a non-conserved cysteine residue in UAP56 (C311), located at the predicted interaction interfaces and in proximity to several lysine residues within the Tho1-CTD (Figure 30A). This constellation enabled a crosslinking approach using the heterobifunctional crosslinker MTS-4-NHS (Storozhuk *et al.* 2024). MTS-4-NHS reacts with thiol groups of cysteines as well as primary amines in lysines, forming stable disulfide and amide bonds between interacting components (Figure 30B). For crosslinking, UAP56 was pre-incubated with AMPPNP and the Tho1-CTD for 3 min in the absence or presence of 38 nt RNA, after which the reaction was initiated by adding increasing MTS-4-NHS concentrations (5 µM, 50 µM, and 500 µM). Crosslinking was stopped after 5 min, and samples were analysed by SDS-PAGE (Figure 30C and D).

Without crosslinker, UAP56 migrated at approximately 50 kDa and the Tho1-CTD at approximately 10 kDa (Figure 30C and D, lane 1). While lower crosslinker concentrations produced only faint additional bands, distinct bands appeared at the highest concentrations: In the absence of RNA, a band migrating slower than free UAP56 formed (Figure 30C, lane 5, empty triangle). This band was also observed in reactions with RNA. Additionally, three high-molecular-weight bands, which were barely detectable without RNA, became prominent in the RNA-containing sample, suggesting formation of higher-order complexes (Figure 30D, lane 5).

To dissect which complexes corresponded to the UAP56-Tho1-CTD interaction and which originated from crosslinks within individual proteins, control reactions omitting one protein or AMPPNP/RNA were performed (Figure 30E). The Tho1-CTD alone did not form any additional bands under the tested conditions (Figure 30E, lanes 7 to 9). However, omission of the Tho1-CTD in UAP56-containing reactions resulted in loss of the smaller band as well as some of the higher bands (Figure 30E, lane 6). Notably, the lowest of those higher bands fully disappeared. A slight blur of the lower band likely reflected intramolecular crosslinks within UAP56, and the remaining higher bands might be due to intermolecular crosslinks between two or more UAP56 protomers (Figure 30E, lanes 4 to 6). Together, these controls allowed identification of two bands specifically representing UAP56-Tho1-CTD complexes. The migration behaviour of these complexes suggested a 1:1 complex formed by UAP56 and the Tho1-CTD for the lower band (Figure 30C-E, empty triangles) and a 2:1 complex for the higher band (Figure 30C-E, filled triangles).

However, the mobility of crosslinked complexes depends not only on their molecular mass but also on the crosslink position in each protein, which limits precise determination of stoichiometry. To scrutinize the identity of the crosslinked species, interface mutants of the Tho1-CTD and UAP56 were analysed using the same method (Figure 30F). Using mutants with substitutions in either interaction side (UAP56-D284R or the Tho1-CTD-R139D/R159D double mutant) abolished both specific bands (Figure 30F, lanes 5 and 8). Consistent with the Sub2 helicase assay, the interaction was not restored when both UAP56-D284R and Tho1-CTD-R139D/R159D were combined (Figure 30F, lane 9). When only one Tho1-CTD motif was intact, the higher band disappeared while the lower band remained, consistent with a 1:1 complex (Figure 30F, lanes 3 and 4). Notably, the amount of crosslinked 1:1 complexes was reproducibly higher for the mutant with only the second motif intact (R139D). Here, the UAP56-specific band, which was still prominent in the lanes with either wild-type Tho1-CTD or Tho1-CTD-R159D, was almost completely shifted.

Together, these results strongly suggest that the lower band represents a 1:1 complex of UAP56 and Tho1-CTD. The higher band, requiring both helical motifs of the Tho1-CTD, very likely corresponds to a 2:1 complex with two UAP56 protomers.

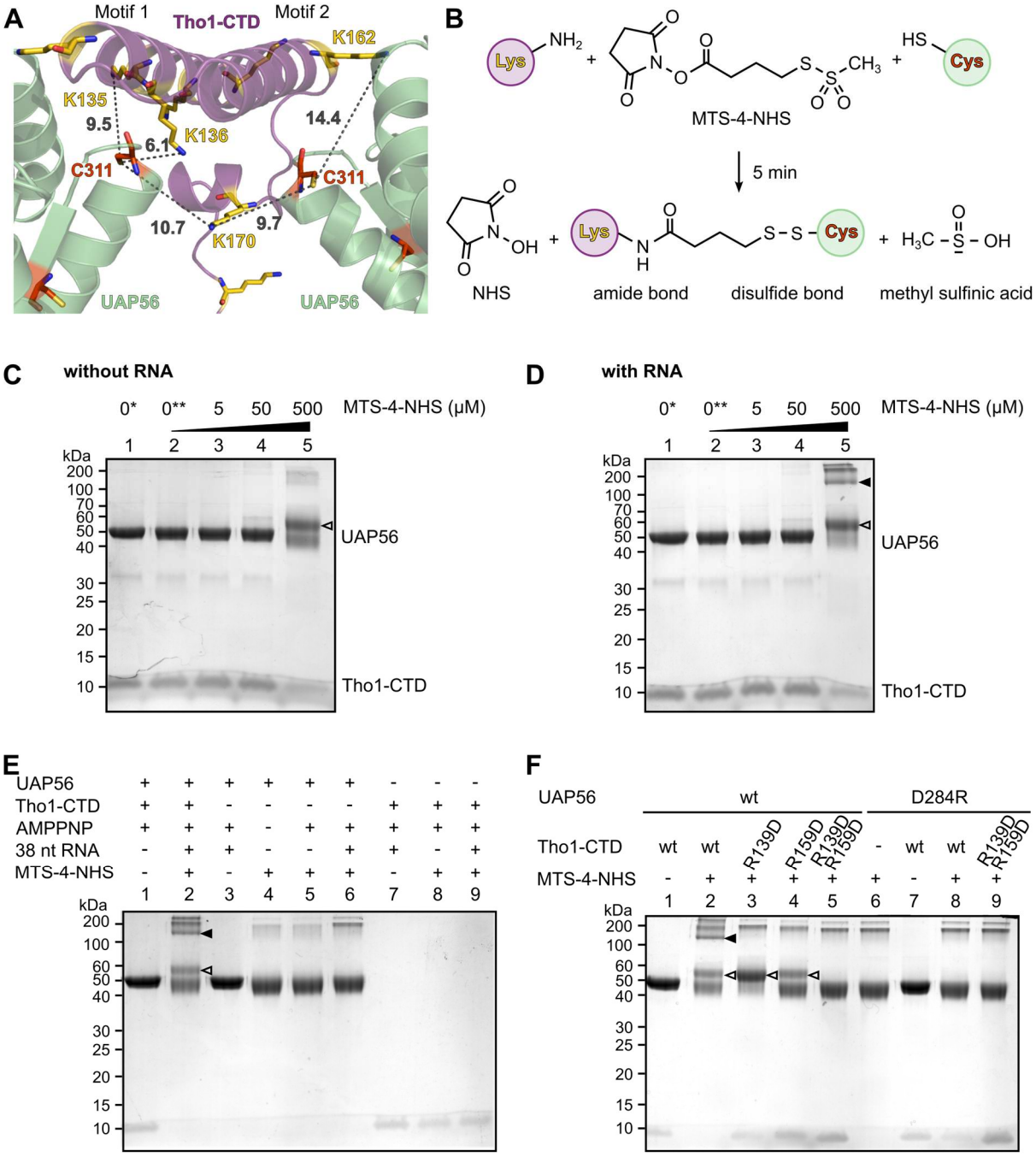

Figure 30: Crosslinking of the UAP56-Tho1-CTD complexes. (A) Close-up of the predicted 2:1 UAP56-Tho1-CTD interface shown in Figure 29A. UAP56 cysteine residues are highlighted in orange and Tho1-CTD lysine residues in yellow. Distances (Å) between the reactive groups of cysteine residue C311 and lysines potentially involved in crosslinking are indicated. **(B)** Scheme of MTS-4-NHS crosslinking. **(C+D)** SDS-PAGE (12%) analysis of crosslinking reactions with UAP56 and the Tho1-CTD in (C) the absence or (D) presence of 38 nt RNA. Control reactions with H_2O (*) and DMSO solvent (**) were included. **(E)** Crosslinking reactions with different combinations of UAP56, Tho1-CTD, AMPPNP and RNA as indicated. **(F)** Crosslinking reactions performed with Tho1-CTD and UAP56 interface mutants as indicated. All reactions were performed with 5 µM UAP56, 2.5 µM Tho1-CTD, 1 mM AMPPNP and 2.5 µM 38 nt RNA. Unless stated otherwise, 500 µM MTS-4-NHS was used. Empty triangles indicate the 1:1 UAP56-Tho1-CTD complex; filled triangles indicate the 2:1 complex. Shown are representative results from *n* = 3 experiments.

To further confirm the identity of the crosslinks between UAP56 and the Tho1-CTD, distinct bands were excised from an SDS-PAGE gel and analysed by LC-MS, performed by Dr. Uwe Linne and colleagues at Marburg University (Figure 31).

Control measurements of UAP56- and Tho1-CTD-specific bands in lane 1 correctly identified the respective proteins (Figure 31A and B, samples 6 and 7). Small amounts of the Tho1-CTD were also detected in the UAP56-specific sample (Figure 31B, sample 6), and vice versa, small amounts of UAP56 in the initial measurement of the Tho1-CTD sample (data not shown). Since this likely resulted from technical carryover between samples, the Tho1-CTD sample was remeasured. Upon remeasurement, no UAP56 peptides were detected, confirming that the original co-detection was due to carryover (Figure 31B, sample 7).

In contrast, the crosslinked bands contained peptides corresponding to both UAP56 and the Tho1-CTD, validating the formation of UAP56-Tho1-CTD complexes (Figure 31B, samples 3 and 4). Interestingly, the Tho1-CTD was consistently detected in all higher-order complexes, previously assumed to represent intermolecular UAP56 crosslinks (samples 1 and 2). As these samples were measured first, carryover can be excluded. Comparison of the migration behaviour with bands in control reactions lacking the Tho1-CTD revealed a slight upward shift in the presence of the Tho1-CTD (Figure 30E, lanes 2 and 6). These observations suggest that the higher-order bands correspond to intermolecular UAP56 complexes with one or more Tho1-CTD molecules attached.

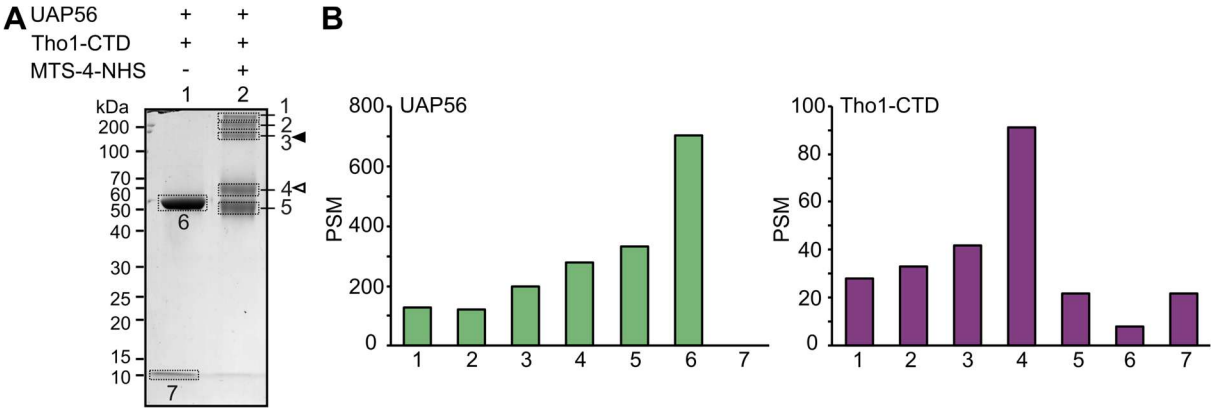

Figure 31: LC-MS confirms UAP56-Tho1-CTD crosslinks (A) SDS-PAGE (12%) of samples used for LC-MS. Bands from the protein control (lane 1) and the crosslink reaction (lane 2) were excised from the gel and analysed in the indicated order (1-7). **(B)** LC-MS results showing peptide spectrum match (PSM) values for UAP56 (left) and Tho1-CTD (right) in the samples indicated in (A). Experiments were performed by Dr. Uwe Linne and Tina Krieg (Marburg University).

A crosslinked 2:1 complex of UAP56 and the Tho1-CTD was detected only in the presence of a 38 nt RNA. Therefore, the influence of substrate length was examined in additional crosslinking experiments (Figure 32A).

While UAP56-Tho1-CTD 1:1 complexes formed independently of the RNA substrate or nucleotide, the 2:1 crosslink was only observed on 38 nt RNA in the presence of either AMPPNP or ATP (Figure 32A, lanes 2-5). In contrast, no 2:1 complex formed when a short 13 nt was used (Figure 32A, lane 7). Consistent with this, AlphaFold 3 generated 1:1, but not 2:1, UAP56-Tho1-CTD models on this short RNA substrate (Figure 32B). Notably, on a 13/38 pdRNA the band representing the 2:1 complex was very weak (Figure 32A, lanes 8 and 9).

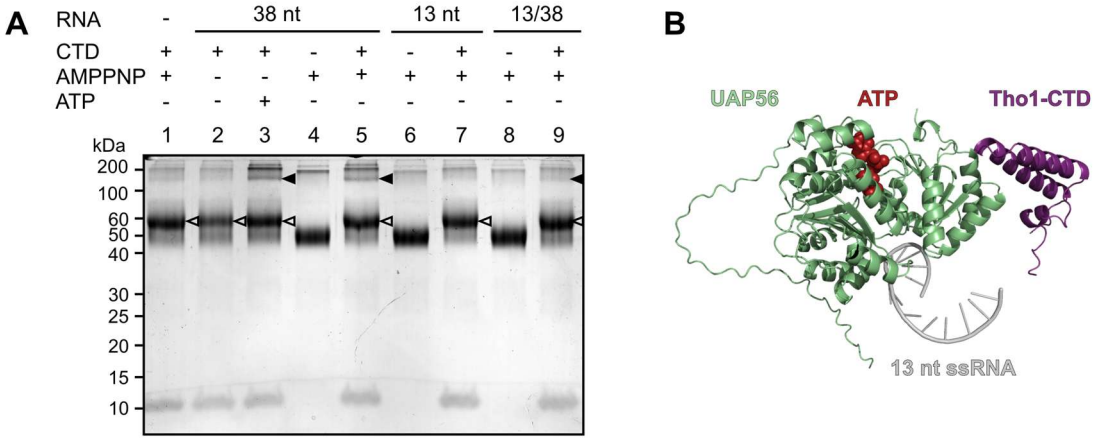

Figure 32: The UAP56-Tho1-CTD 2:1 complex only forms on a long ssRNA. (A) SDS-PAGE (12%) analysis of crosslinking reactions performed with 13 nt, 38 nt ssRNA or 13/38 nt pdRNA substrates. All reactions contained UAP56 (5 µM) with or without the Tho1-CTD (2.5 µM), AMPPNP (1 mM) or ATP (1 mM), as indicated. A representative result of *n* = 3 experiments is shown. **(B)** AlphaFold 3 prediction of a UAP56-Tho1-CTD complex formed on 13 nt RNA. Although two UAP56 protomers were included in the model input, all predictions yielded a 1:1 complex. Shown is one representative model out of five generated.

4.7.3. An introduced cysteine in Sub2 enables crosslinking to the Tho1-CTD

Although Sub2 contains six conserved cysteines, none are located near the Tho1-CTD interface. To confirm the specificity of the crosslinking reaction, an additional cysteine corresponding to UAP56 C311 was introduced at position S329 in Sub2 (Figure 33A). AlphaFold 3 models of a 2:1 complex between Sub2-S329C and the Tho1-CTD predicted that the additional cysteine is located near several Tho1-CTD lysine residues within the interaction interface (Figure 33B). Helicase assays confirmed that the mutation did not affect pdRNA unwinding by Sub2-S329C or stimulation by the Tho1-CTD (Figure 33C). Wild-type Sub2 did not form any detectable complexes with the Tho1-CTD, except faint background bands (Figure 33D, lanes 7 to 9). In contrast,

Sub2-S329C produced two distinct bands similar to the UAP56-Tho1-CTD complexes (Figure 33D, lanes 3 and 6).

These results demonstrate that the previously observed crosslinked complexes arose specifically from the Tho1-CTD interaction site and support the proposed 2:1 complex model.

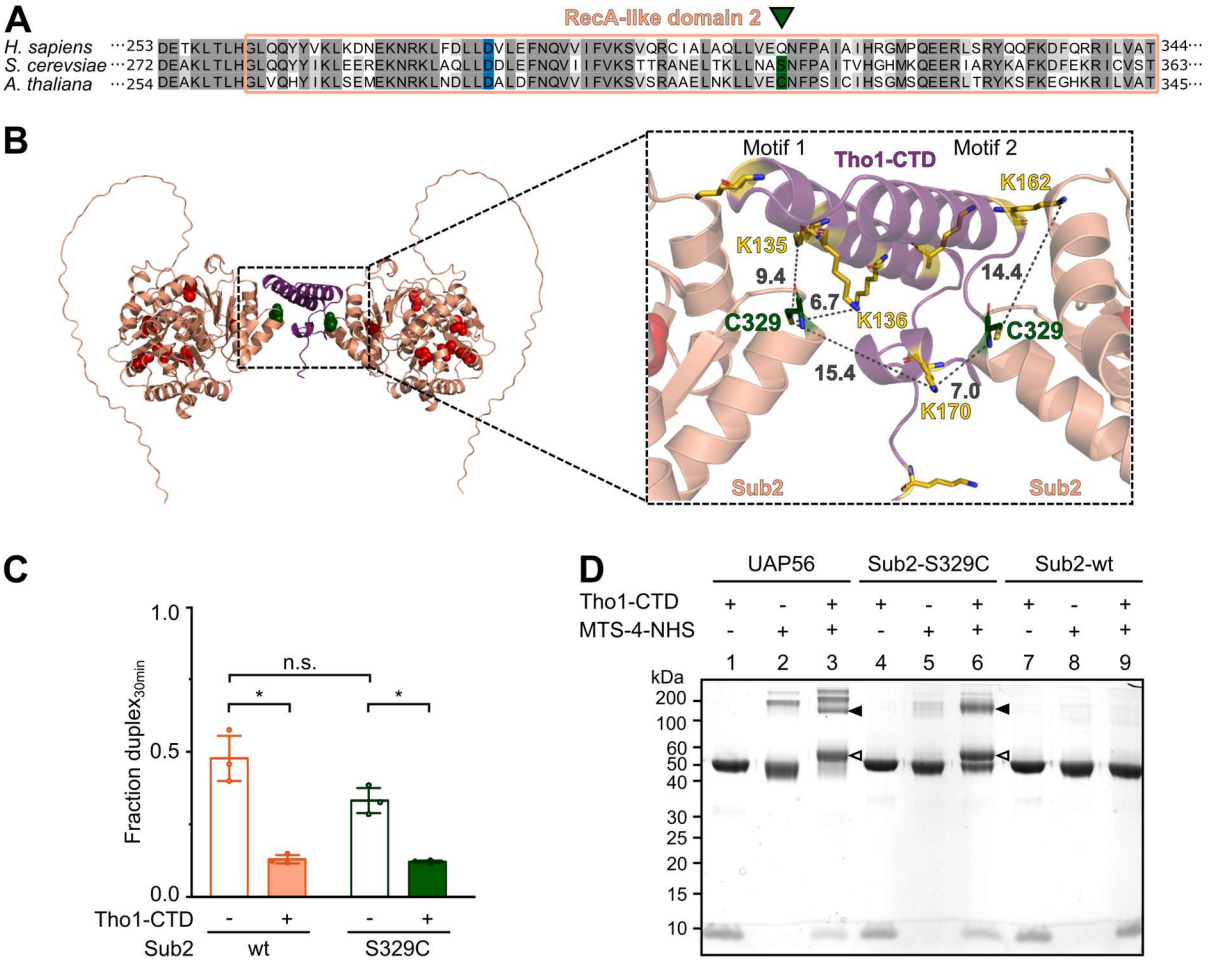

Figure 33: Crosslinking of a Sub2 cysteine mutant. (A) Sequence alignment excerpt of DDX39B, Sub2, and UAP56 from Figure 19A. UAP56 C311 and the corresponding residue in Sub2, S329, are marked with a green triangle. **(B)** AlphaFold 3 prediction of the 2:1 complex between Sub2-S329C and the Tho1-CTD, with the introduced cysteines shown as spheres (left). Close-up of the interface (right) shows C329 (green) near Tho1-CTD lysines (yellow). Distances (Å) between reactive groups are indicated. **(C)** Unwinding of a 13/38 pdRNA by 1 µM Sub2-wt or Sub2-S329C with or without 2 µM Tho1-CTD. Shown is fraction duplex remaining after 30 min as mean ± SD of *n* = 3 experiments. **(D)** SDS-PAGE (12%) analysis of crosslinking reactions performed with 2.5 µM UAP56, Sub2-wt or Sub2-S329C with or without the Tho1-CTD (5 µM) and MTS-4-NHS (500 µM). A representative result of *n* = 3 experiments is shown.

4.8. Characterisation of the *A. thaliana* Tho1 ortholog MOS11

The Tho1 ortholog MOS11 has been described as an export factor in *A. thaliana*, where it is predominantly involved in the export of GC-rich transcripts (Germain *et al.* 2010; Rödel *et al.* 2024). In addition, MOS11 stimulates RNA unwinding by UAP56 as shown by Minhaz Mannan during his master's thesis and by Rödel et al. (2024). MOS11 comprises 214 amino acids, making it similar in length to Tho1, but with notable structural differences: it lacks an N-terminal SAP domain and contains five instead of two of the conserved helical motifs (Figure 34A). The subsequent chapters focus on the *in vitro* characterisation of MOS11 and the mechanism underlying the stimulation of UAP56-mediated unwinding.

4.8.1 MOS11 displays weak annealing activity

To determine whether the structural differences between MOS11 and Tho1 translate into functional differences, the *in vitro* annealing activity of MOS11 was assessed using a fluorescence-based real-time annealing assay, as previously described (Miosga 2022). This assay monitors pairing of a BHQ-2-labelled 16 nt top strand with a partially complementary Cy5-labelled 37 nt bottom strand, resulting in quenching of the Cy5 fluorescence (Figure 34B). Miosga (2022) compared the annealing activities of Tho1, human SARNP, and *C. thermophilum* Tho1, showing that fungal orthologs exhibit strong annealing activity, whereas SARNP displays only moderate activity. To further explore differences among orthologs, MOS11 was compared not only to Tho1, but also to the *S. pombe* ortholog Mlo1. Like Tho1, Mlo1 contains an N-terminal SAP domain but possesses an additional third interaction motif (Figure 34A).

Incubation of MOS11 with two DNA strands led to a faster decrease in Cy5 fluorescence than in the no protein control ($P = 3.9 \times 10^{-7}$), indicating annealing activity (Figure 33C and D). In contrast, when RNA strands or RNA/DNA combinations were used, MOS11 showed only weak annealing activity (Figure 33D). Tho1 and Mlo1 displayed robust activity across all tested substrates. The strongest effects were observed on substrate combinations containing a long DNA strand, thus forming partial duplexes with an ssDNA overhang (DNA/DNA and RNA/DNA; Figure 33D). Both proteins promoted annealing of the RNA/DNA hybrid approximately fourfold more efficiently than MOS11. For DNA/DNA substrates, Tho1 showed an approximately fourfold higher activity, whereas Mlo1 exhibited an even stronger approximately sixfold increase compared to MOS11 (Figure 33D).

These results indicate that MOS11 likewise possesses intrinsic annealing activity, but that it is comparatively weak and largely restricted to DNA substrates.

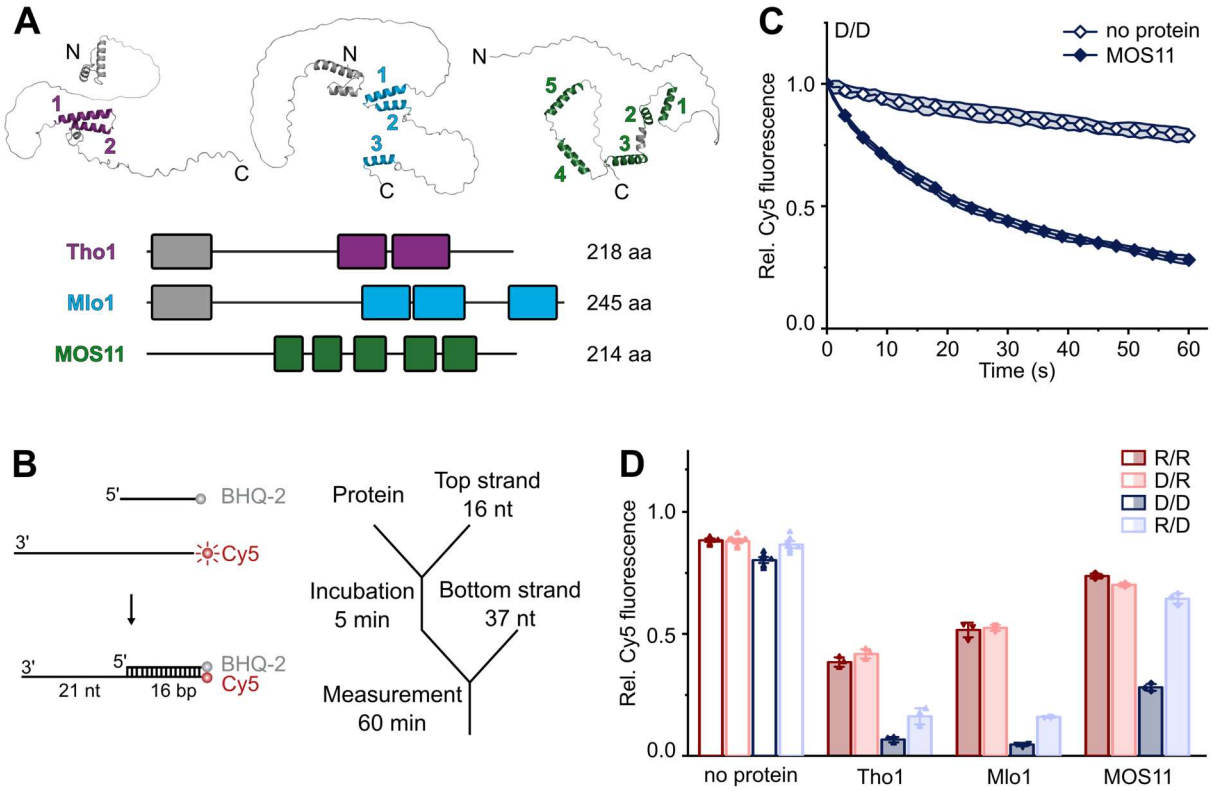

Figure 34: Comparison of annealing activity among Tho1-orthologs. (A) AlphaFold models of Tho1 (AF-P40040-F1), Mlo1 (AF-074871-F1) and MOS11 (AF-Q9LZ08-F1) are shown at the top, with the domain organization of each protein depicted at the bottom. The helical motifs in each protein are highlighted. **(B)** Scheme of the fluorescence-based real-time annealing assay. The 16 nt top strand is labelled with BHQ-2, and the 37 nt bottom strand with Cy5. **(C)** Time course of DNA annealing in the absence (empty diamonds) or presence (filled diamonds) of MOS11. **(D)** Comparison of 16/37 annealing activity of Tho1, Mlo1 and MOS11 on RNA (R/R), DNA (D/D), and hybrid (D/R, R/D) substrates. All reactions contained 10 nM of each substrate strand and 5 µM of the respective annealing protein. Relative Cy5 fluorescence was calculated by normalizing each reaction to its initial intensity. Measurements in the absence of protein and for Tho1 were taken from (Miosga 2022). Shown are mean ± SD of $n \geq 3$ replicates.

4.8.2. MOS11 nucleic acid binding is impaired in the presence of ATP

After observing only modest annealing activity for MOS11, its nucleic acid-binding properties were examined using fluorescence anisotropy. Measurements were performed with 6-FAM-labelled 13 nt RNA or DNA in the absence or presence of ATP (Figure 35A and B).

In the absence of ATP, MOS11 bound RNA with a K_d of 0.45 ± 0.05 µM and DNA with a K_d of 1.3 ± 0.23 µM (Figure 35A and B). The maximum anisotropy values reached were consistently higher for RNA (r_{max} = 0.16) than DNA (r_{max} = 0.14). Addition of ATP

markedly reduced binding to both DNA and RNA, an effect that was also observed with 10 nt and 16 nt RNA substrates (Figure 35A-C). MOS11 caused only a small increase in anisotropy with 10 nt RNA, whereas strong increases were detected for RNA substrates of 13 nt or longer, indicating length-dependent binding (Figure 35C).

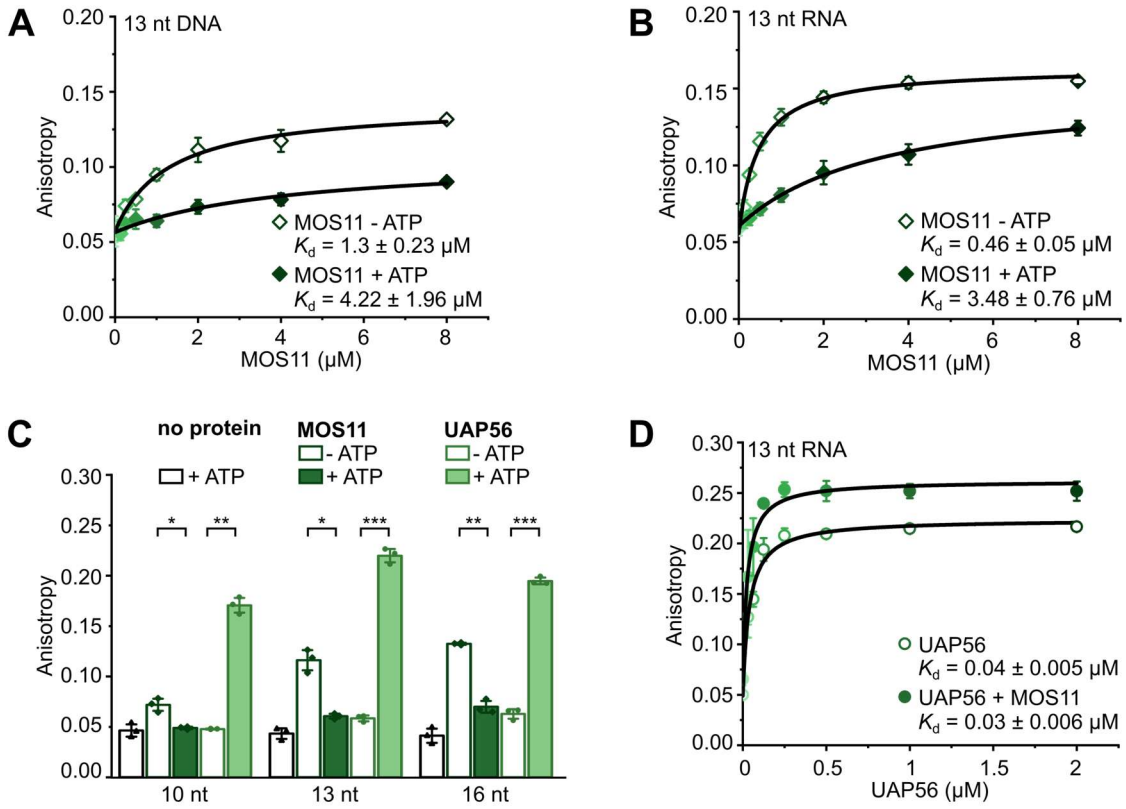

Figure 35: MOS11 and UAP56 nucleic acid binding. (A+B) Equilibrium titration (t = 10 min) of MOS11 (0.01-8 μM) binding to 6-FAM-labelled 13 nt (A) DNA or (B) RNA, in the absence (empty diamonds) or presence (filled diamonds) of ATP. **(C)** Fluorescence anisotropy measured after 10 min of incubation of different RNA substrates (10 nt, 13 nt and 16 nt) with either UAP56 (2 μM) or MOS11 (2 μM) in the absence or presence of ATP (2 mM). Control measurements without protein were used to determine the fluorescence anisotropy of unbound substrates. **(D)** Equilibrium titrations (t = 10 min) showing UAP56 binding to 13 nt ssRNA with or without MOS11 (2 μM). RNA concentrations were 10 nM in all reactions. Data are represented as mean ± SD of *n* = 3 experiments.

By contrast, UAP56 bound all tested substrates, but RNA binding was strongly ATP-dependent (Figure 35C). An ATP-independent interaction with 16 nt RNA, as seen for Sub2, was not detected for UAP56. Notably, the maximum anisotropy in reactions containing MOS11 was always lower than those for UAP56. Furthermore, MOS11 did not alter UAP56's RNA-binding affinity for the 13 nt substrate, as the K_d values remained similar (P = 0.2879; Figure 35D). Notably, reactions containing both UAP56 and MOS11 displayed increased maximal anisotropy. This could reflect simultaneous,

independent binding of both proteins or the formation of a UAP56-MOS11 complex on the RNA. However, this cannot be resolved using anisotropy measurements.
In summary, MOS11 binds nucleic acids in an ATP-inhibited manner but does not significantly influence the RNA-binding properties of UAP56.

4.9. MOS11 stimulates UAP56-mediated unwinding

Next, the effect of MOS11 on 13/38 pdRNA unwinding by UAP56 was assessed. As described above for Sub2 and the Tho1-CTD (Figure 17), a constant concentration of MOS11 (4 µM) was added to ongoing unwinding reactions containing varying concentrations of UAP56 (0.5 µM, 1 µM and 2 µM; Figure 36A).

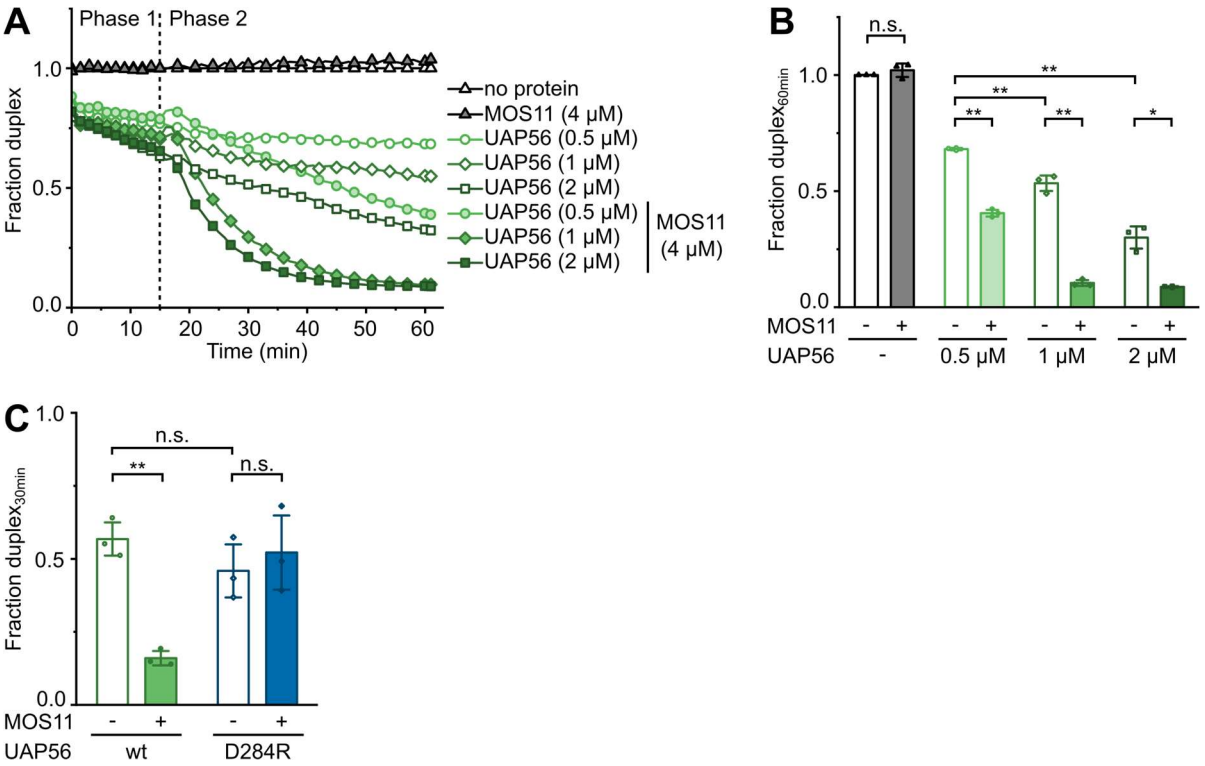

Figure 36: pdRNA unwinding by UAP56 is stimulated by MOS11. (A) Representative kinetics of 13/38 pdRNA unwinding by UAP56 at the indicated concentrations in the absence (empty symbols) or presence (filled symbols) of MOS11 (4 µM). **(B)** Comparison of the fraction duplex remaining after 60 min is shown as mean ± SD of *n* = 3 experiments. Reactions without protein or MOS11 alone served as controls. **(C)** Effect of MOS11 on 13/38 pdRNA unwinding by wild-type UAP56 and interface mutant UAP56-D284R. Shown is fraction duplex remaining after 30 min as mean ± SD of *n* = 3 experiments. The experiment was performed by Jan Kohlert as part of his bachelor's thesis.

MOS11 alone did not exhibit unwinding activity, but stimulated UAP56-mediated unwinding at all tested concentrations, with the weakest effect observed at the lowest UAP56 concentration (Figure 36A and B). Although unwinding proceeded faster with

2 µM UAP56 than with 1 µM, the presence of MOS11 resulted in nearly equivalent unwinding rates under both conditions (Figure 36A and B). Consistent with the observations for the Tho1-CTD (Figure 29D), the helicase activity of the UAP56-D284R mutant was not stimulated by MOS11 (Figure 36C).

These results show that unwinding stimulation of UAP56 by MOS11 relies on protein-protein interactions, similar to the effect observed with the Tho1-CTD.

4.9.1. MOS11 stimulates UAP56 unwinding independent of an ssRNA overhang

The stimulatory effect of MOS11 on UAP56's unwinding activity reported by Rödel et al. (2024) was measured using a 13 bp blunt-end duplex RNA in a gel-based assay. In that experimental setup, MOS11 induced only moderate stimulation, particularly compared with ALY1 (the *A. thaliana* ortholog of Yra1). However, MOS11 caused strong helicase stimulation on a 13/38 pdRNA (Figure 36). These observations are reminiscent of the substrate-dependent effect of the Tho1-CTD, where stimulation requires an ssRNA overhang (Figure 23). To test whether MOS11-mediated unwinding stimulation indeed depends on the RNA substrate architecture, unwinding of 13/38 pdRNA or 13 bp blunt-end duplex RNA substrates by Sub2 and UAP56 was measured in the absence or presence of either MOS11 or the Tho1-CTD (Figure 37).

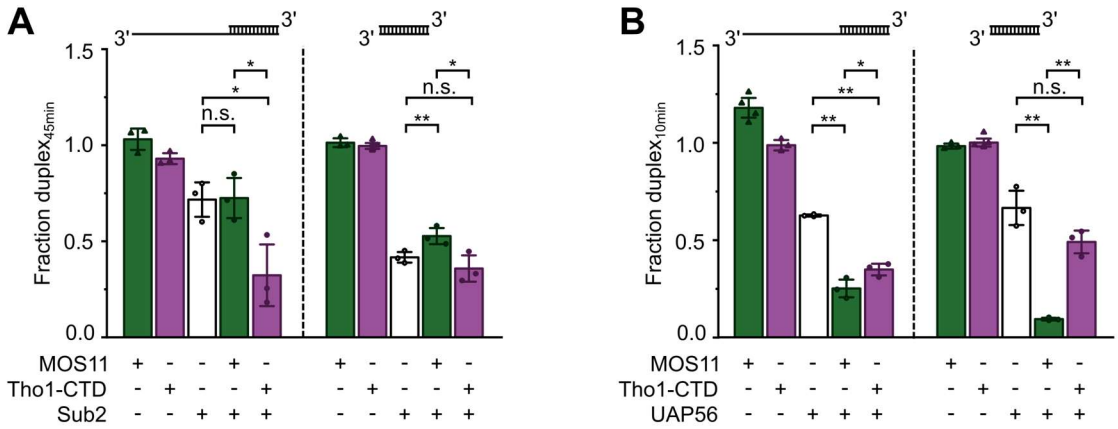

Figure 37: Comparison of unwinding stimulation by MOS11 and the Tho1-CTD. (A+B) Unwinding of a 13/38 pdRNA (left panels) or 13 bp duplex (right panels) by (A) Sub2 or (B) UAP56 was measured in the absence or presence of MOS11 or of the Tho1-CTD, as indicated. Control reactions with MOS11 or the Tho1-CTD alone showed no unwinding. Results were performed with 1 µM Sub2 or UAP56 and 2 µM Tho-CTD or MOS11. Fraction duplex remaining after (A) 45 min or (B) 10 min is shown as mean ± SD from *n* = 3 experiments.

Neither MOS11 nor the Tho1-CTD exhibited unwinding activity on any substrate. Sub2 alone unwound the blunt-end substrate more efficiently than the pdRNA, whereas UAP56 displayed comparable activities on both substrates. Consistent with previous

experiments, the Tho1-CTD stimulated unwinding of both Sub2 and UAP56 on the pdRNA substrate but had little to no effect on the blunt-end duplex substrate (Figure 37A and B). MOS11 did not stimulate Sub2 on either substrate (Figure 37A). In contrast, UAP56 unwinding was enhanced 2.5-fold for the pdRNA and even 7-fold for the blunt-end substrate in the presence of MOS11 (Figure 37B). Notably, the MOS11-mediated stimulation of blunt-end duplex unwinding by UAP56 was substantially stronger than previously observed in the gel-based assay (Rödel *et al.* 2024).
These results demonstrate that MOS11 provides robust stimulation of UAP56, enabling efficient unwinding of blunt-end substrates that are not activated by the Tho1-CTD.

4.9.2. Unwinding stimulation by MOS11 requires at least two helical motifs

While both MOS11 and the Tho1-CTD stimulate helicase activity, MOS11 displays a broader stimulatory effect, enhancing UAP56-mediated unwinding on a blunt-end substrate that the Tho1-CTD does not activate. This raises the question of whether the higher number of helical motifs in MOS11, and thus its additional UAP56-interaction sites, contribute to this effect.
To address this, MOS11 mutants were systematically analysed. First, two MOS11 mutants were generated in which conserved arginine residues in motifs two to five were substituted either with lysines (MOS11-Mot. 1 RK) or aspartic acids (MOS11-Mot. 1 RD), leaving only the first motif intact (Supplementary Figure S6). Both mutants failed to stimulate UAP56-mediated 13/38 pdRNA unwinding (Supplementary Figure S6A and B). However, while MOS11-Mot. 1 RK retained RNA-binding activity with a 13 nt RNA, binding was impaired in the R to D mutant (Supplementary Figure S6C). To avoid structural perturbations unrelated to helicase activation, all subsequent mutants contained only R to K exchanges (Figure 38A). Four additional MOS11 mutants with varying numbers of mutated motifs were generated (Figure 38B). All mutants bound 13 nt RNA, indicating that protein integrity was not affected (Figure 38C).

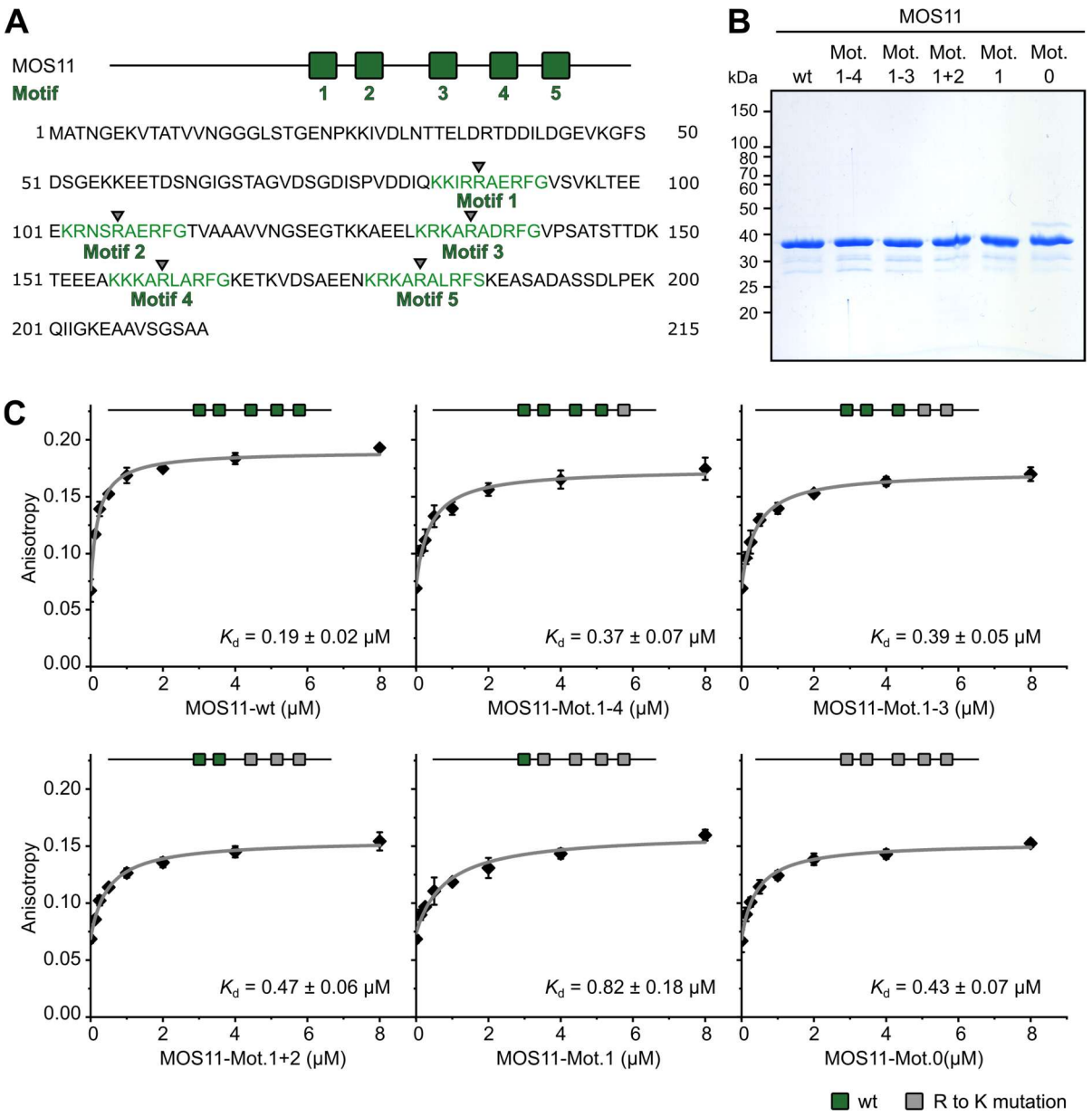

Figure 38: MOS11 mutants with different numbers of intact motifs bind to RNA. **(A)** MOS11 domain organization (top) and amino acid sequence (bottom; UniProt: Q9LZ08). Helical motifs 1-5 are highlighted in green. Arginine residues substituted in the MOS11 mutants are indicated by green triangles. **(B)** SDS-PAGE (12%) of 2 µg purified wild-type MOS11 and R to K mutants. Mutants contained a different number of intact motifs, indicated by the designations (e.g. MOS11 Mot. 1 has motifs 2-5 mutated while motif 1 remains intact). Cloning of the mutants was performed by Amelie Müller during her bachelor's thesis (2024). **(C)** Fluorescence anisotropy equilibrium titrations (t= 10 min) of wild-type MOS11 and mutants using 6-FAM-labelled 13 nt RNA. Scheme shows intact motifs in green and mutated motifs in grey. Data represent mean ± SD of *n* = 3 experiments.

The impact of these MOS11 mutants on UAP56-mediated unwinding of 13/38 pdRNA and 13 bp duplex RNA substrates was tested (Figure 39). For this analysis, unwinding velocities were compared rather than endpoint fraction duplex values. This approach was necessary because many reactions, particularly those on the duplex substrate,

reached similar minimal fraction duplex levels but differed significantly in their unwinding velocities. Thus, using velocities provided a more sensitive and informative measure for distinguishing the stimulatory effects of the different MOS11 mutants.

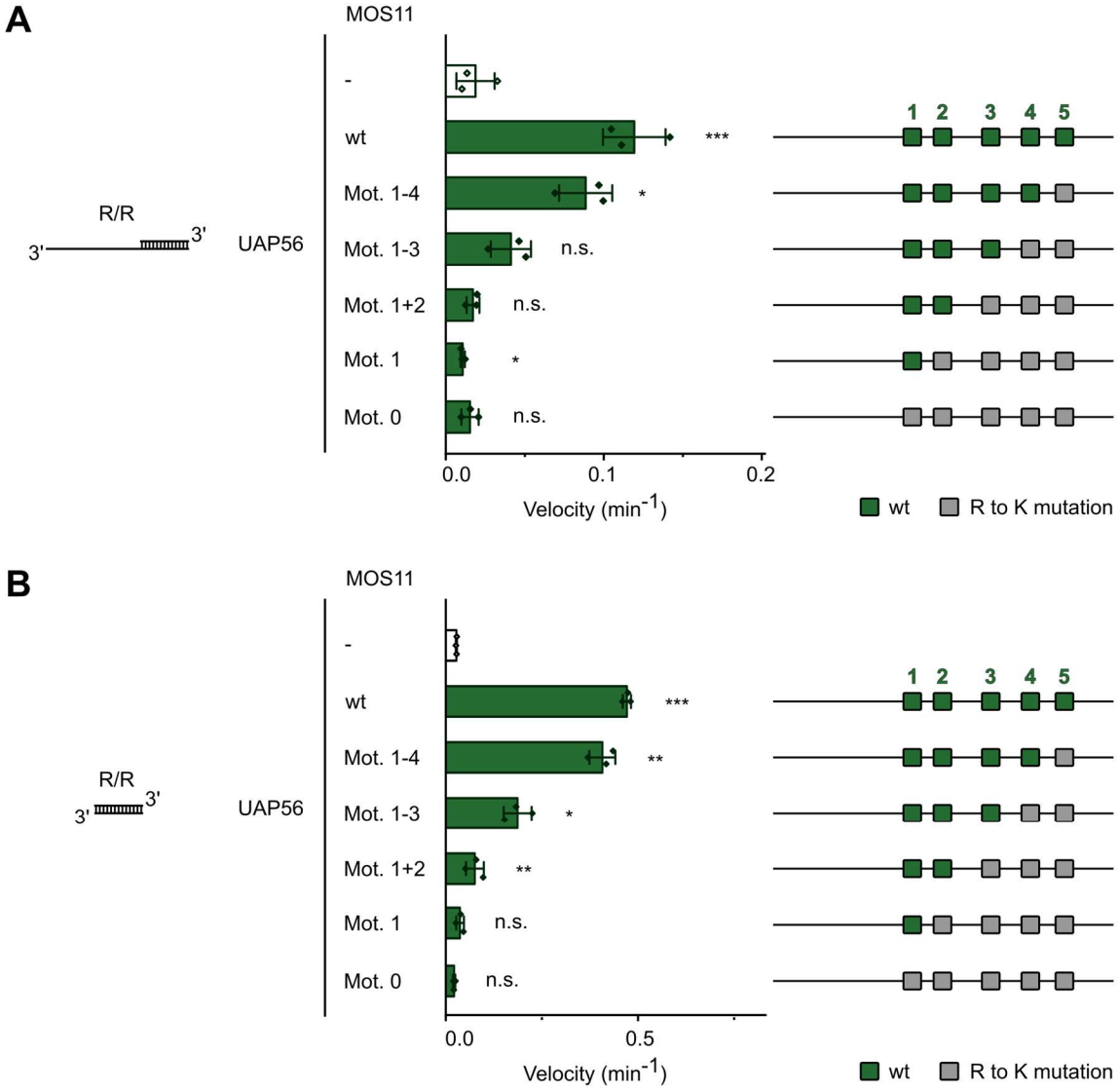

Figure 39: Effect of motif number on MOS11-mediated unwinding stimulation. (A+B) Velocities of UAP56-mediated (1 µM) unwinding of (A) 13/38 pdRNA or (B) 13 bp duplex RNA substrates in the absence or presence of 2 µM wild-type MOS11 or the indicated MOS11 mutants. The scheme on the right depicts MOS11 mutants, with intact motifs in green and mutated motifs in grey. Unwinding velocities (mean ± SD, *n* = 3) were derived from unwinding curves normalized to reactions without protein using an exponential fit.

This velocity analysis revealed that UAP56 unwound blunt-end duplexes slightly faster than pdRNA. MOS11 mutants with zero (Mot. 0) or only a single intact motif (Mot. 1) failed to stimulate unwinding of either substrate. The mutant containing two intact motifs (Mot. 1+2) significantly stimulated unwinding of the short duplex but not the pdRNA substrate. The presence of a third motif (Mot. 1-3) further enhanced stimulation

on the short duplex and resulted in weak, albeit not statistically significant, stimulation of pdRNA unwinding. Introducing a fourth intact motif (Mot. 1-4) restored stimulation on both substrates to levels comparable to wild-type MOS11.

In summary, at least two motifs are required for UAP56 helicase stimulation, and the extent of stimulation increases progressively with the number of intact motifs.

4.9.3. Motif flexibility influences unwinding stimulation by MOS11

MOS11 and the Tho1-CTD differ not only in the number of helical motifs but also in their spatial arrangement: the two helices of the Tho1-CTD are connected by only a short linker, resulting in a relatively rigid structure, whereas the linker regions connecting the single motifs in MOS11 are longer and more flexible (Figure 34A).

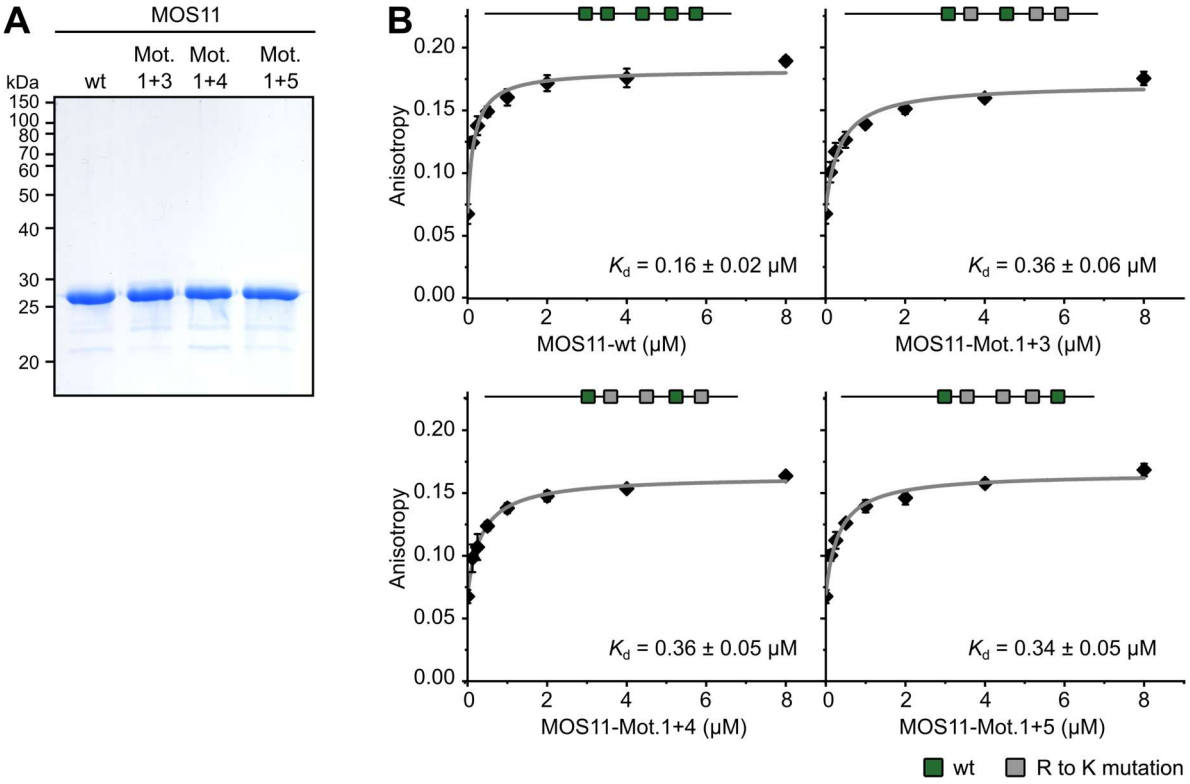

Figure 40: MOS11 mutants with two intact helical motifs still bind RNA. (A) SDS-PAGE (12%) analysis of 2 µg purified wild-type MOS11 and R to K mutants. Each mutant contained two intact motifs located at increasing distances of the protein. **(B)** Fluorescence anisotropy equilibrium titrations (t = 10 min) of wild-type MOS11 and mutants using 6-FAM-labelled 13 nt RNA. Schemes show intact motifs in green and mutated motifs in grey. Data represent mean ± SD of *n* = 3 experiments.

The MOS11-Mot. 1+2 mutant, which retained two adjacent intact motifs, showed only modest stimulation of UAP56-mediated unwinding of the short 13/13 RNA duplex (Figure 39B). These results are similar to those observed for the Tho1-CTD, which likewise failed to stimulate unwinding of this substrate (Figure 37B).

To determine whether this lack of stimulation was caused solely by the limited number of intact motifs or also influenced by motif arrangement, an additional set of MOS11 mutants was generated, each retaining two intact motifs positioned at increasing distances along the protein (Mot. 1+3, Mot. 1+4, Mot. 1+5; Figure 40A). All mutants bound to 13 nt RNA (Figure 40B) and were subsequently tested for their effects on UAP56-mediated unwinding (Figure 41).

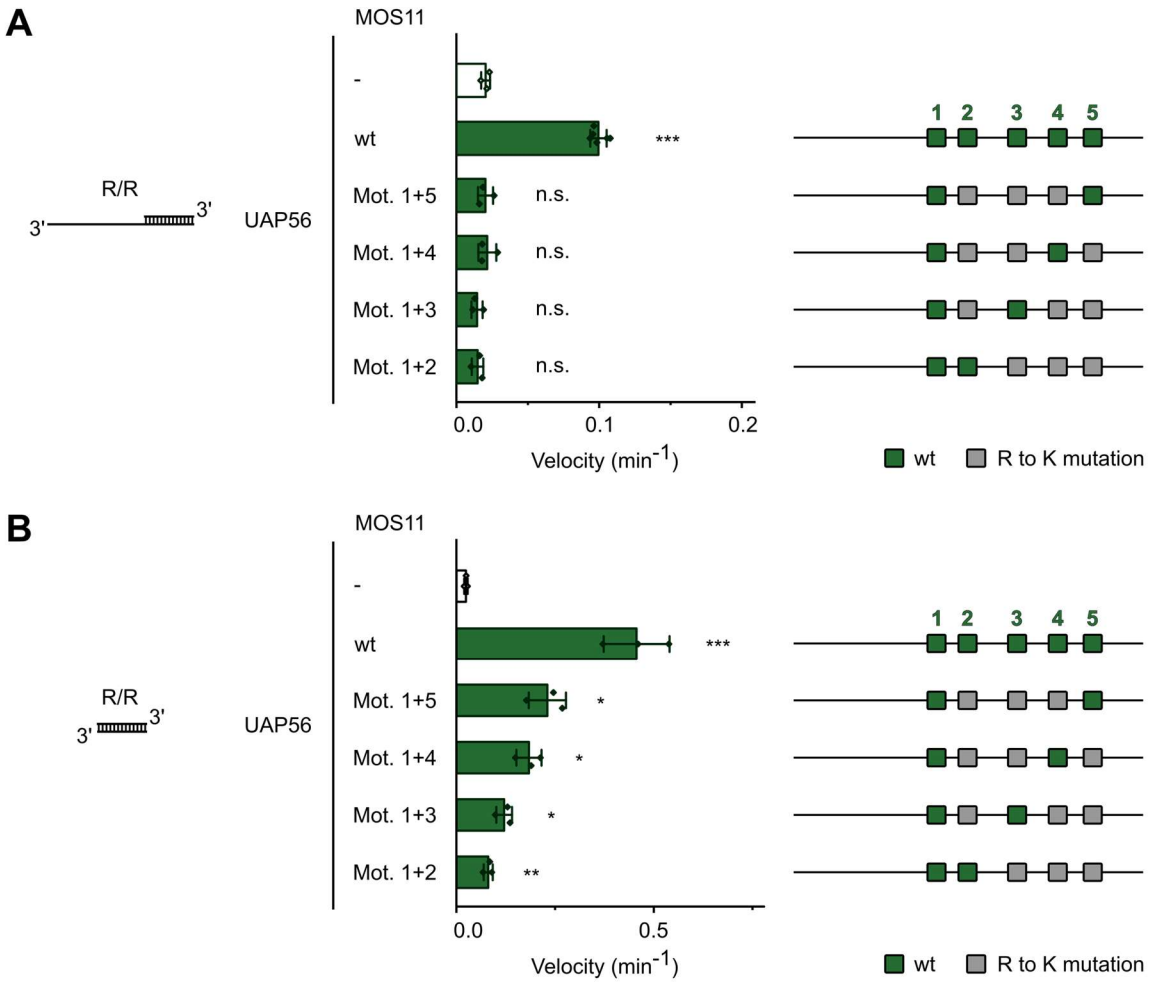

Figure 41: Effect of motif arrangement on unwinding stimulation by MOS11. (A+B) Unwinding of (A) 13/38 pdRNA or (B) 13 bp duplex RNA substrates by UAP56 (1 µM) was tested in the absence or presence of 2 µM wild-type MOS11 or the indicated MOS11 mutants with two intact helical motifs. Scheme of MOS11 mutants (right) indicates intact motifs in green and mutated motifs in grey. Unwinding velocities were derived from unwinding curves normalized to reactions without protein using an exponential fit. Data represent mean ± SD of *n* = 3 experiments

Testing these mutants revealed that increasing the distance between the two intact motifs did not enhance unwinding of the 13/38 pdRNA (Figure 41A). In contrast, unwinding stimulation of the 13 bp duplex substrate increased with greater spacing

between the intact motifs, with the strongest effect observed for the MOS11-Mot. 1+5 mutant (Figure 41B).

Taken together, while a higher number of intact motifs is advantageous for stimulation on both substrates, motif arrangement also plays an important role for the short duplex substrate.

4.9.4. MOS11 stimulates unwinding by UAP56 on blunt-end DNA/RNA hybrids

Finally, the substrate specificity of MOS11-mediated unwinding stimulation was examined using different 13 bp blunt-end duplex substrates composed of either RNA, DNA or DNA/RNA hybrids. UAP56-mediated unwinding was monitored in the absence or presence of MOS11, and fluorescence anisotropy was recorded to detect binding (Figure 42).

UAP56 alone neither bound nor unwound DNA duplexes. MOS11, either alone or together with UAP56, caused a slight increase in fluorescence anisotropy without promoting unwinding. Consistent with previous observations, UAP56-mediated unwinding of RNA duplexes was strongly enhanced by MOS11. Moreover, anisotropy traces were higher when both proteins were present, similar to the results obtained for the 13 nt ssRNA substrate (Figure 35D). Notably, the increase in anisotropy reflected approximately the contribution of MOS11 alone. As observed for Sub2, UAP56 unwound both hybrid substrates faster than the RNA duplexes. However, unlike the Tho1-CTD, MOS11 further enhanced unwinding in both cases. For the RNA/DNA hybrid substrate, fluorescence anisotropy kinetics closely resembled those obtained for RNA duplexes. In contrast, DNA/RNA hybrids showed a distinct pattern: MOS11 caused a slight increase in anisotropy, whereas reactions containing both MOS11 and UAP56 yielded traces similar to the control reaction without protein. Interestingly, anisotropy in the presence of UAP56 alone decreased in the first five minutes of the reaction to levels lower than the control.

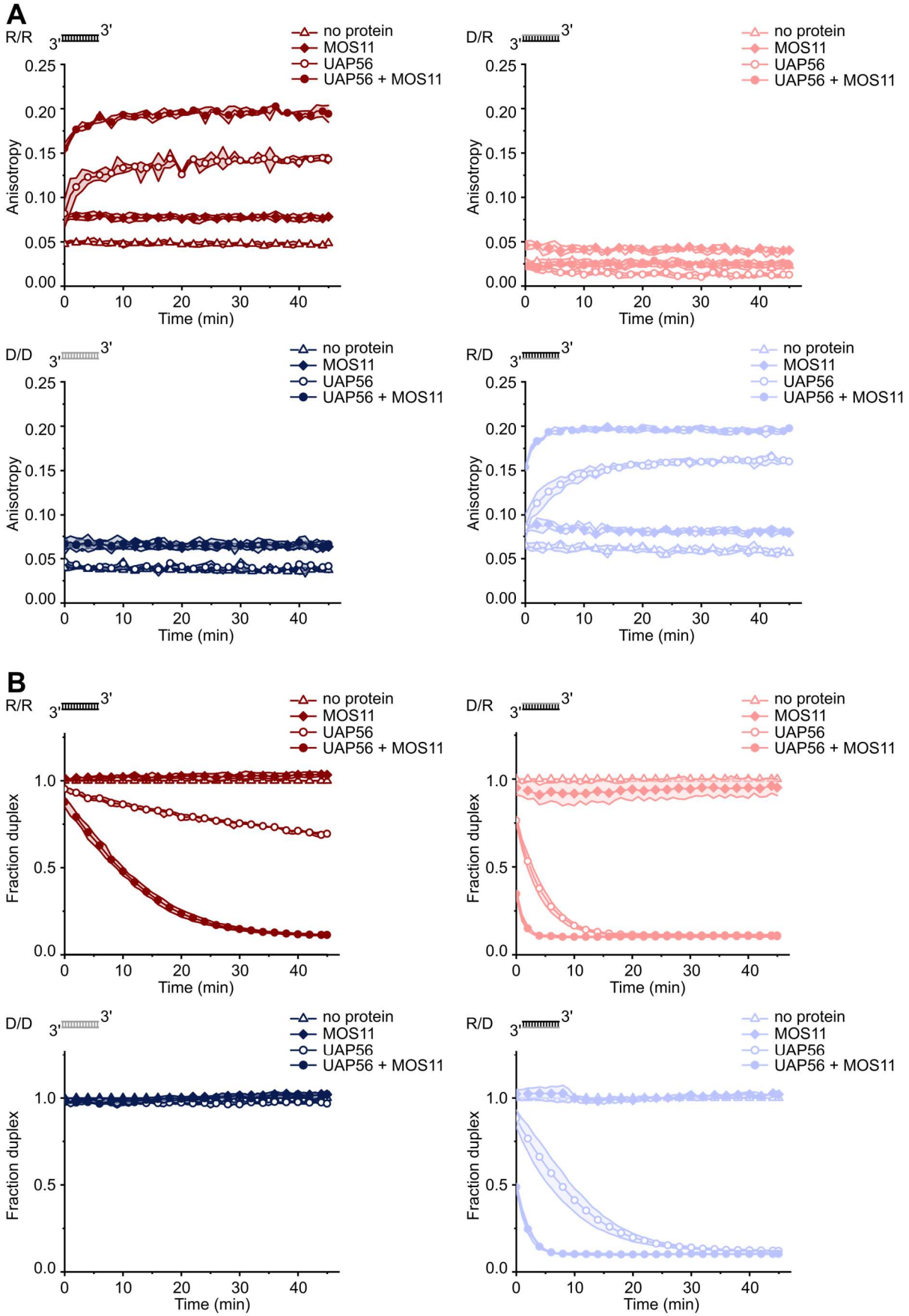

Figure 42: MOS11 stimulation on different substrates. (A) Anisotropy traces of either UAP56 (0.5 µM), MOS11 (1 µM) or both proteins in the presence of 13 bp blunt-end substrates consisting of either RNA (R/R), DNA (D/D), or DNA/RNA hybrids (D/R, R/D). No protein controls

represent fluorescence anisotropy of the respective free substrates. **(B)** Corresponding unwinding kinetics for reactions shown in (A). Control reactions lacking protein were used to calculate the fraction duplex remaining. Data show mean ± SD of *n* = 3 experiments.

To exclude the possibility that the observed stimulation of DNA/RNA hybrid unwinding were influenced by MOS11's intrinsic nucleic acid-binding activity, the effects of different MOS11 mutants on UAP56-mediated unwinding of a 13 bp RNA/DNA substrate were analysed (Figure 43).

The MOS11 mutant lacking intact motifs and thus unable to interact with the helicase, did not enhance unwinding, suggesting that stimulation indeed depended on the UAP56-MOS11 interaction. All mutants with two intact motifs yielded significant unwinding stimulation. While the positive influence of spatial separation between these motifs was less pronounced than for the RNA duplex substrate, a modest increase in stimulation with greater motif distance was still observed. The mutant retaining only a single intact motif exhibited a slight, but not statistically significant, enhancement of unwinding. This observation indicates that interaction of a single MOS11 motif with UAP56 alone might produce a small stimulatory effect.

In summary, MOS11 stimulates unwinding on both RNA and RNA/DNA hybrid substrates lacking an ssRNA overhang.

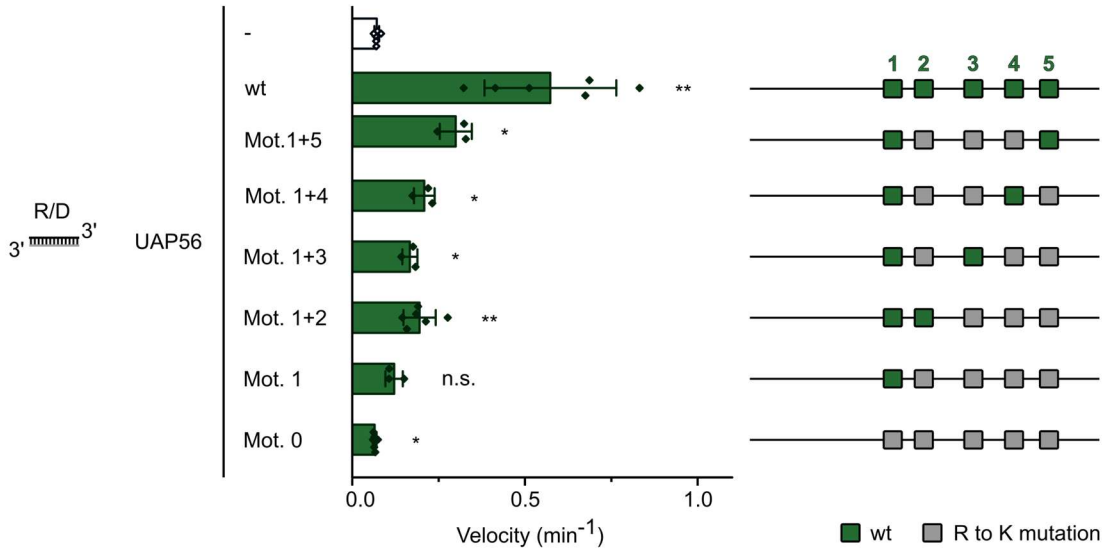

Figure 43: RNA/DNA unwinding stimulation by MOS11 mutants. Effect of wild-type MOS11 or the indicated mutants (1 µM) on unwinding of a 13 bp blunt-end RNA/DNA substrate by UAP56 (0.5 µM). Scheme on the right shows MOS11 mutants, with intact motifs indicated in green and mutated motifs in grey. Unwinding velocities were derived from unwinding curves normalized to reactions without protein using an exponential fit. Data represent mean ± SD of n ≥ 3 experiments.

5. Discussion

In recent years, components of the TREX complex and their associated cofactors have become an increasingly important focus of research, given their central roles in coordinating transcription, mRNP maturation, mRNA export, and genome stability (Heath *et al.* 2016). Defects in the largest TREX subunit, the THO complex, lead to diverse cellular phenotypes in yeast cells, including hyperrecombination, mRNA export defects, and growth defects (Chávez & Aguilera 1997; Jimeno *et al.* 2002; Libri *et al.* 2002; Saguez *et al.* 2008). Notably, these phenotypes are suppressed by overexpression of Tho1 (Fan *et al.* 2001; Jimeno *et al.* 2006; Piruat 1998). Despite this growing interest, the molecular mechanisms by which Tho1 suppresses these phenotypes, particularly the role of its nucleic acid-binding activity and its interaction with Sub2, have not been addressed. This study provides a biochemical characterisation of Tho1 and its *A. thaliana* ortholog MOS11 and elucidates their roles in stimulating the helicase activity of Sub2 and *A. thaliana* UAP56.

5.1. The nucleic acid annealing protein Tho1

This study builds on the work of Dr. Matthias Miosga, who performed a thorough *in vitro* characterisation of Tho1 and identified its nucleic acid annealing activity (Miosga 2022). The first part focused on extending key findings regarding Tho1 and determining the functional relevance of individual domains. Fluorescence-based RNA-binding assays were incorporated to obtain quantitative results that could later help evaluate the potential role of RNA binding *in vivo*. Furthermore, Tho1's annealing activity was compared with that of its *S. pombe* and *A. thaliana* orthologs.

5.1.1. RNA-binding activity of Tho1

Previous studies analysed the nucleic acid-binding activity of Tho1 by EMSAs and reported stable complex formation with DNA substrates of at least 60 nt and RNA substrates of at least 15 nt (Jacobsen *et al.* 2016; Jimeno *et al.* 2006; Miosga 2022; Xie *et al.* 2023). Such gel-based assays are widely used and offer several advantages, including high sensitivity, especially when employed with radioactively labelled samples, and the ability to discriminate between different protein-nucleic acid complexes. In addition, they can be coupled with downstream analyses such as electron microscopy or mass spectrometry. However, EMSAs have limited kinetic and

temporal resolution, and complexes that dissociate within the timescale of the experiment may be underestimated or undetected (Hellman & Fried 2007). Transferring the reaction from solution onto a native gel also alters the surrounding conditions of the complex, potentially affecting its stability.

Consistent with these limitations, EMSAs showed that Tho1 did not form a stable complex with a short, fluorescently labelled 13 nt RNA. Instead, it yielded a slight upward smear of the signal, indicating weak or transient interaction (Figure 14, Miosga 2022). In contrast, a fluorescence anisotropy-based approach clearly demonstrated Tho1 binding to 6-FAM-labelled 13 nt RNA (Figure 9). Measuring binding directly in solution not only ensured consistent experimental conditions but also enabled resolution of the binding kinetics. These results indicate that the RNA substrate length for Tho1 binding can be reduced to at least 13 nt. Nevertheless, it may preferentially bind longer RNAs, as the complex formed with 13 nt RNA was too unstable to be observed by EMSA. In agreement with this, two additional nucleotides in a 15 nt poly(U) RNA substrate were sufficient to produce stable Tho1-RNA complexes detectable by EMSA (Xie *et al.* 2023). Interestingly, Tho1 ortholog SARNP did not bind the 15 nt poly(U) RNA (Xie *et al.* 2023), whereas MOS11, like Tho1, interacted with 13 nt RNA (Figure 35). Together, these observations point to differences in RNA-binding affinities among Tho1 orthologs.

In summary, these findings highlight the sensitivity of solution-based fluorescence anisotropy assays for detecting weak or transient protein-RNA interactions. This makes them a valuable tool for exploring species-specific differences in nucleic acid binding among Tho1-family proteins. Systematic analyses of binding kinetics with substrates of varying length, combined with competition assays, could further define precise length requirements and binding preferences of Tho1 and its orthologs.

5.1.2. Tho1-domain characterisation

To analyse their biochemical activities *in vitro*, the Tho1 domain mutants were purified. All mutants yielded sufficient protein except Tho1-ΔSAPΔLinker. Although this protein was expressed in *E. coli* cells, affinity purification using Ni-IDA columns yielded no detectable protein, as no corresponding band appeared in SDS-PAGE (data not shown). Several factors could have contributed to the failure of this purification. The CTE of Tho1 is positively charged, whereas the acidic linker carries a negative charge (Figure 8). Using Prot pi (version 2.2.29.152), the net charge of His-tagged full-length

Tho1 was estimated at approximately -1 at pH 7.5. In contrast, deletion of the linker region in the His-tagged Tho1-ΔSAPΔLinker mutant substantially increased the net charge to approximately +10. This charge increase likely affected protein solubility or promoted aggregation, thereby interfering with efficient binding to the Ni-IDA resin. Moreover, truncation of the protein may have altered its folding and potentially buried the His-tag or sterically hindered its interaction with the resin. However, despite these purification challenges, Tho1-ΔSAPΔLinker expression in yeast cells was confirmed by Western blot, and the protein successfully suppressed the ts phenotype of Δ*hpr1* cells, indicating functionality under cellular conditions (Figure 12).

To analyse the *in vitro* activities of the remaining Tho1 mutants, a three-step fluorescence-based assay was employed that measured RNA binding, RNA/DNA annealing, and DNA/RNA strand displacement. Consistent with previous findings (Miosga 2022), mutants lacking RNA-binding activity were also unable to promote annealing, indicating a correlation between these two activities (Figure 11). However, the Tho1-ΔCTD mutant retained wild-type-like RNA-binding yet exhibited reduced annealing activity – an effect previously observed (Miosga 2022). Interestingly, whereas deletion of the entire domain did not impair ssRNA binding, a single amino acid substitution within its first helical motif (Tho1-F143D) completely abolished binding to pdRNA and RNA annealing activity (Miosga 2022). These observations suggest that while the ability to interact with nucleic acids is essential, binding to single strands alone is insufficient to promote efficient strand annealing. Furthermore, they indicate that the Tho1-CTD, particularly its helical motifs, contributes to nucleic acid interactions. Supporting this, a Tho1 mutant with substitutions in the conserved arginine and phenylalanine residues (R139A/F143A/R159A/F163A) failed to bind 15 nt poly(U) RNA (Xie *et al.* 2023). Consistently, R to D mutations in the helical motifs of MOS11 abolished its ssRNA-binding activity (Supplementary Figure S6). The sigmoidal annealing profiles observed for wild-type Tho1 and Tho1-ΔSAP indicate cooperative behaviour, suggesting that more than one Tho1 protomer participates in the annealing reaction. This cooperativity is absent in the Tho1-ΔCTD mutant, implying a potential role for the CTD in mediating Tho1-Tho1 interactions that may contribute to the annealing activity. However, further experiments are needed to elucidate the precise mechanism underlying nucleic acid annealing.

Strand displacement enhancement was detected in all mutants that retained annealing activity (Figure 11). However, whether the Tho1-ΔCTE and Tho1-CTD mutants are

capable of strand displacement despite lacking annealing activity could not be determined in this combined assay, as strand displacement in the experimental setup required prior annealing of the nucleic acid strands. To further investigate a direct link between these activities, additional experiments using pre-annealed substrates are necessary.

EMSA experiments confirmed previous findings by Miosga (2022) and provided additional insight into the roles of the CTE and CTD in complex formation with Sub2 (Figure 14). The Tho1-ΔCTE mutant still formed a ternary complex with Sub2 and RNA. This complex migrated faster through the gel than the one formed with full-length Tho1. In EMSAs, migration of molecules is influenced by multiple factors, including complex size or charge (Hellman & Fried 2007). More negatively charged species, for example, migrate faster. The positively charged CTE of Tho1 or Tho1-ΔSAP therefore slows migration of the complexes, while Tho1-ΔCTE, lacking this domain, migrates faster. The Tho1-CTD was shown to be both necessary and sufficient for the interaction with Sub2, although further quantitative titration is required to determine whether it alone achieves wild-type Sub2-binding affinity. In the EMSA performed with the Tho1-ΔCTD mutant, two additional bands appeared that were not present for other mutants, while the band corresponding to the Sub2-RNA complex was less intense. Tho1-ΔCTD no longer interacts with Sub2 but retains the ability to bind 16 nt RNA (Figure 11). If this mutant can also bind the shorter 13 nt RNA, it likely competes with Sub2 for RNA binding, resulting in multiple complexes in the gel corresponding to different Sub2-RNA or Tho1-ΔCTD-RNA combinations.

In summary, these results independently reproduced and extended key findings reported by Miosga (2022) through the application of fluorescence anisotropy-based binding assays. The CTE of Tho1 is required for RNA binding and annealing activity. The demonstrated role of the Tho1-CTD in mediating Sub2-interaction is consistent with previous predictions of the Tho1-Sub2 interaction interface and the crystal structure of the Tho1-CTD with human DDX39B (Humphreys *et al.* 2021; Xie *et al.* 2023). Moreover, in addition to mediating helicase interactions, the Tho1-CTD also contributes to nucleic acid binding and annealing. In contrast, the SAP domain has not influenced any of the activities tested to date (Jimeno *et al.* 2006; Miosga 2022). Although the SAP domain interacts with dsDNA, it is not conserved across all Tho1 orthologs, and its functional relevance remains to be investigated (Jacobsen *et al.* 2016).

5.1.3. Differential annealing activities of Tho1 orthologs

Real-time fluorescence-based nucleic acid annealing experiments were used to compare yeast Tho1 and its orthologs from *S. pombe* and *A. thaliana* (Figure 34). Notably, all proteins showed the highest annealing activity on DNA substrates, or RNA/DNA hybrids with long DNA strands for Tho1 and Mlo1, but reduced activity on RNA/RNA or DNA/RNA substrates with long RNA strands. This conserved preference for DNA suggests that the proteins' annealing mechanism is sensitive to RNA substrates with stable 2′-hydroxyl-stabilised secondary structures, which must be resolved prior to strand annealing.

Across all tested substrates, Tho1 and Mlo1 consistently exhibited stronger annealing activity than MOS11 (Figure 34), correlating with the presence of an intrinsically disordered, positively charged CTE (Figure 44). Mlo1 and Tho1 both contain such a region, whereas MOS11 possesses a negatively charged extension. The strong positive charge in the CTE likely promotes interactions with negatively charged nucleic acids, while its absence in MOS11 may account for the reduced annealing activity. In comparison, the C-terminal half of SARNP is also positively charged, yet it exhibits only weak annealing activity (Miosga 2022). In this case, the positive charge is predominantly contributed by rigid helical motifs, suggesting that charge density alone is insufficient and that the conformational flexibility of a disordered CTE is required to facilitate efficient annealing.

In summary, these observations suggest that annealing activity in the Tho1 family requires a specific synergy between positive charge and conformational disorder within the CTE. However, its precise role in the annealing mechanism and the factors underlying the distinct substrate preferences require investigation.

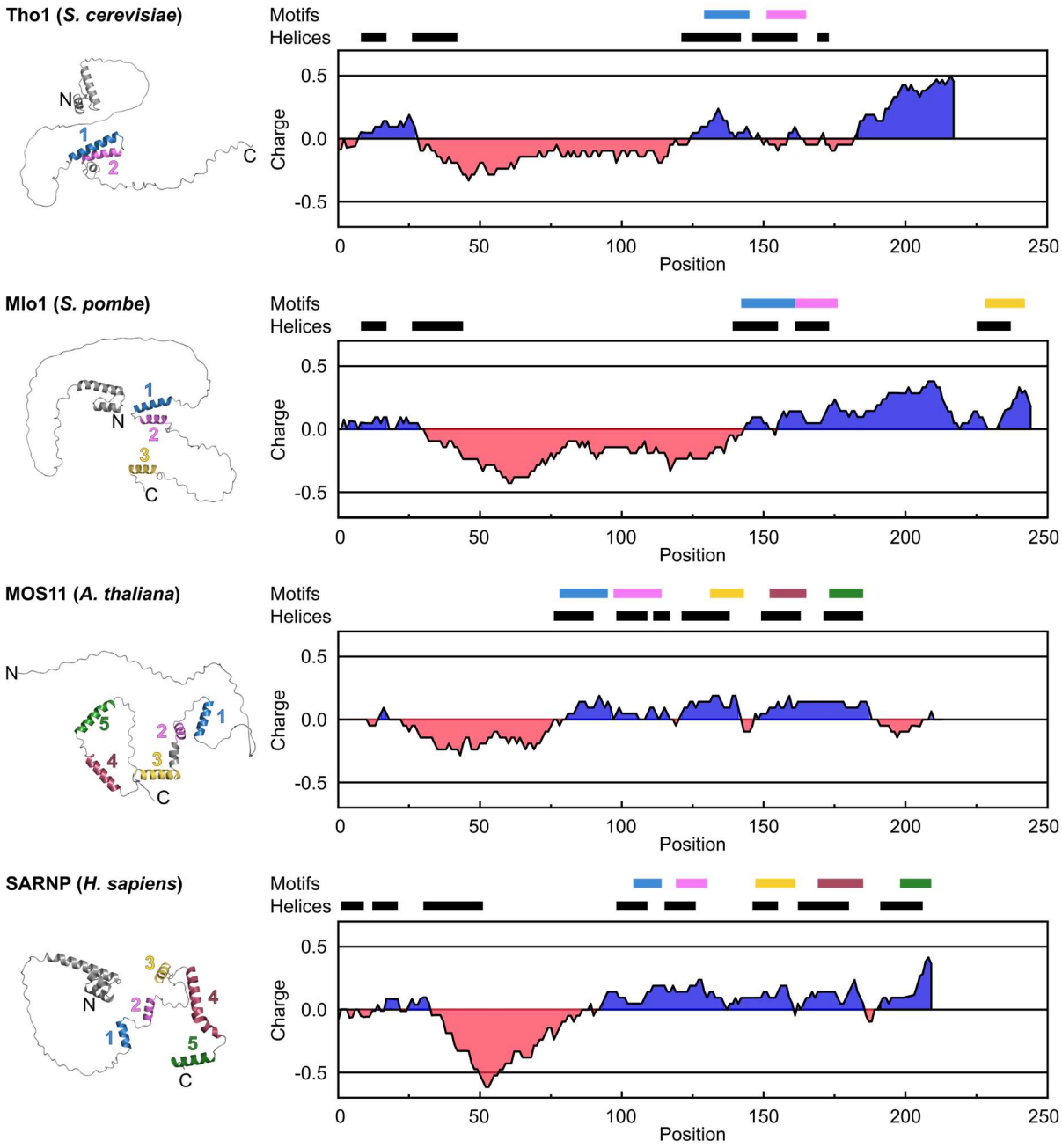

Figure 44: Comparison of charge distributions in Tho1 orthologs. AlphaFold-predicted structures of *S. cerevisiae* Tho1 (AF-P40040), *S. pombe* Mlo1 (AF-O74871), *A. thaliana* MOS11 (AF-Q9LZ08), and *H. sapiens* SARNP (AF-P82979) are displayed on the left. Charge distribution profiles for each protein are shown on the right, with helical motifs and α-helices indicated above. Positively charged regions are shown in blue and negatively charged regions in red. The charge profiles were generated by Apl. Prof. Dr. Peter Friedhoff. Details of the workflow are provided in the Supplementary Methods.

5.2. Tho1-CTD-mediated helicase stimulation

The second and main aim of this study was to define the biochemical basis of the functional interaction between Tho1 and Sub2. Specifically, the mechanism underlying the stimulatory effect of the Tho1-CTD on Sub2's helicase activity, as described by

Miosga (2022), was examined using real-time fluorescence-based unwinding assays. To evaluate the evolutionary conservation of this mechanism, the influence of the Tho1-CTD on *A. thaliana* UAP56 was also tested. Mutational analysis of the predicted binding interfaces on both Sub2/UAP56 and the Tho1-CTD was employed to determine how disruption of this interaction affects biochemical activities *in vitro* and suppression of the ts phenotype *in vivo*.

5.2.1. Mechanistic separation of Tho1 annealing and Sub2 stimulation

Although the molecular mechanism underlying nucleic acid annealing remains poorly defined, the annealing activity of Tho1 provides a plausible explanation for the counteraction of Sub2-mediated unwinding observed in the presence of full-length Tho1. Unwinding experiments using the Tho1-interaction-deficient Sub2-D302R mutant demonstrated that Tho1-mediated annealing, and the resulting counteraction of unwinding, occurs independently of direct protein-protein interaction (Figure 22). This indicates that the observed reduction in unwinding results from effects on the RNA substrate, rather than from direct inhibition of Sub2's catalytic activity. When Tho1 was truncated to its CTD, which retains Sub2 interaction but lacks the disordered CTE required for annealing, interaction-dependent helicase stimulation was observed (Figure 22). In line with this, Miosga (2022) showed that only Tho1 mutants retaining annealing activity substantially counteract Sub2-mediated unwinding. A similar effect is seen for MOS11 and SARNP, which exhibit minimal annealing activity on RNA substrates (Figure 34) and enhance the RNA unwinding activities of their respective helicases (Figure 36; Chang *et al.* 2013; Dufu *et al.* 2010; Miosga 2022; Rödel *et al.* 2024).

Taken together, these findings suggest that the stimulatory potential of the Tho1-CTD is present in full-length Tho1 but masked by its dominant re-annealing activity.

5.2.2. The Tho1-Sub2 interaction interface

Disrupting the interaction between the Tho1-CTD and Sub2-D302R or UAP56-D284R confirmed the requirement for direct protein-protein interaction for helicase stimulation (Figures 21 and 29). Furthermore, substitutions of either of the two highly conserved arginine residues (R139 and R159) within the α-helical interaction motifs of the Tho1-CTD also abolished the stimulatory effect on Sub2 and UAP56 (Figures 26, 27, and 29). These results demonstrated the importance of both interaction sites for helicase stimulation. The chemical specificity of this interface is underscored by the

failure of R to K substitutions. At the centre of both Motif 1 and Motif 2 interaction interfaces, R139 and R159 form salt bridges with Sub2-D302 and hydrogen bonds with Sub2-S329 (Figure 45). Although lysine preserves the positive charge and the potential to form a salt bridge with Sub2-D302, it cannot replace the bidentate hydrogen-bonding geometry of the arginine's guanidinium group. These arginines are therefore key residues essential for facilitating and stabilizing the Tho1-CTD-Sub2 interaction.

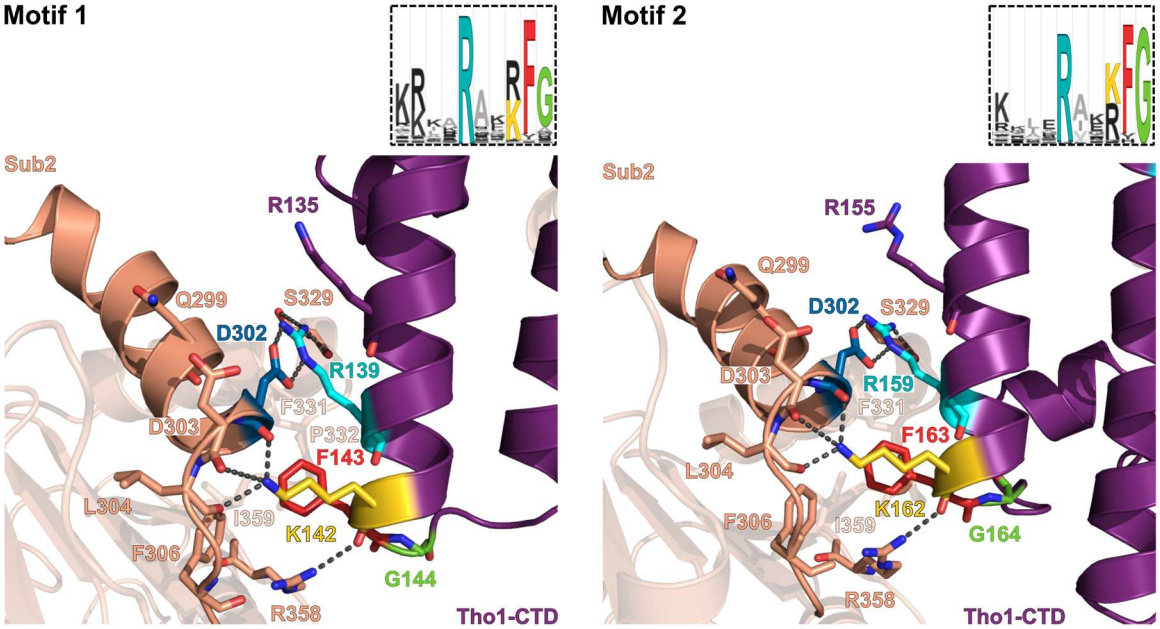

Figure 45: Positions of mutated residues in the Tho1-Sub2 interface. Close-up of the AlphaFold 3 prediction of the 2:1 complex shown in Figure 27, with the interaction interface of Sub2 and motif 1 (left) and motif 2 (right) of the Tho1-CTD. Amino acid residues involved in the interaction are depicted as sticks. Sub2 residue D302 (blue) was mutated to completely prevent interaction with the Tho1-CTD. Residues R139/R159 (cyan), K142/K162 (yellow), F143/F163 (red), and G144/G164 (green) substituted in the Tho1-CTD mutants are highlighted.

In contrast, mutation of other conserved residues within the motifs did not interfere with helicase stimulation (Figure 27). A closer examination of the predicted Tho1-CTD-Sub2 interaction surface indicates that these residues may play supporting or structural roles, explaining the lack of an effect (Figure 45). The phenylalanine residues F143 and F163 are buried in a hydrophobic pocket of Sub2 formed by F306, F331, P332 and I359. Tyrosine, which was used to substitute F143 and F163, has a nearly identical structure to phenylalanine but contains an additional para-hydroxyl (-OH) group. Hydrophobic packing with Sub2 is therefore likely maintained in the Tho1-CTD-F143Y and -F163Y mutants, provided that the pocket accommodates the hydroxyl group, and thus does not disrupt protein-protein interactions.

Both lysine residues K142 and K162 each interact with three carbonyl groups of Sub2 (D302, D303 and L304), thereby stabilizing the interaction interface. However, these lysines are the least conserved residues tested, and many orthologs contain arginines at these positions. Consequently, the K to R exchanges in these sites are unlikely to sufficiently disrupt the interface.

Although the glycine residues G144 and G164 are highly conserved, they are not located at the centre of the interaction interface. G144 is positioned at the boundary of the helix-linker region connecting both large α-helices of the Tho1-CTD, whereas G164 lies at the boundary of the linker region leading to the third, smaller α-helix. These residues presumably contribute to backbone flexibility rather than direct interaction with Sub2. Substitution of these glycines with alanine can be expected to preserve the overall backbone geometry of the Tho1-CTD and not interfere with Sub2 binding.

In conclusion, the absence of unwinding stimulation in the Tho1-CTD-R139K/D and Tho1-CTD-R159K/D mutants demonstrated that helicase activation requires two intact interaction sites. The continued stimulation observed for the other tested mutants can be explained by their positioning within the Tho1-CTD-Sub2 interaction interface together with the limited impact of conservative substitutions and therefore does not contradict this assumption. More drastic substitutions of these residues could disrupt Sub2 interactions but carry a greater risk of causing unwanted effects on overall protein structure or other activities. This was observed for the R to D mutations in MOS11, which abolished not only its UAP56 stimulation but also RNA-binding activity (Supplementary Figure S6).

5.2.3. Cross-species analysis of the Tho1-CTD helicase complexes

After demonstrating that mutation of either of the two helical motifs within the Tho1-CTD abolishes its functional interaction with Sub2, it was conceivable that helicase stimulation might be connected to the formation of a 2:1 complex, as observed for DDX39B and the Tho1-CTD (Xie *et al.* 2023). However, a major challenge was to directly assess the stoichiometry of the Sub2-Tho1-CTD complex and determining how mutations affected it, because the complex's stability was unknown and it was unclear whether it was transient or substrate-assisted.

In EMSAs, addition of the wild-type Tho1-CTD caused only a small shift, which was absent when Sub2-D302R was used (Figure 19D). However, a higher-order shift indicating a complex consisting of two Sub2 protomers and the Tho1-CTD was not

observed, preventing comparison between the Tho1-CTD wild-type and mutants. As discussed above, this restriction may be due to EMSA's inability to reliably detect transient interactions. A similar limitation was encountered in the helicase assays which showed a strong increase in unwinding but no further increase in fluorescence anisotropy upon introduction of the Tho1-CTD (Figure 17). Moreover, the anisotropy values did not exceed the maximum observed for binding of an ssRNA substrate (Figure 15). Here it is important to note that, in addition to the molecular mass of the protein-RNA complex, fluorescence anisotropy is affected by the local mobility of the fluorophore. Flexibility of the fluorophore linker and its surrounding environment may allow considerable local motion, thereby lowering the observed anisotropy and masking any effect arising from global size changes (Michel et al., 2020). Thus, the absence of an additional change in anisotropy does not exclude the formation of a complex between the Tho1-CTD, (two) Sub2 and RNA. However, it still renders this method unsuitable for distinguishing complex stoichiometries.

To overcome these limitations, the high conservation of the helical motifs in Tho1 and its orthologs was exploited: The Tho1-CTD has been shown to form cross-species complexes with human DDX39B (Xie *et al.* 2023). Supporting the conservation of this interaction, the Tho1-CTD also stimulated the helicase activity of UAP56 (Figure 29). Based on this observation, a cysteine residue in UAP56, conveniently positioned near the Tho1-CTD-interaction interface, was used. Heterobifunctional crosslinking, which can trap transient complexes, was employed to distinguish among distinct complex stoichiometries. Experiments using different UAP56 and Tho1-CTD mutants thereby allowed discrimination of 2:1 and 1:1 complexes, showing that formation of the 2:1 complex strictly required the presence of both intact interaction interfaces (Figure 30). A 1:1 complex between UAP56 and the Tho1-CTD formed in the absence of RNA or ATP/AMPPNP (Figure 32), in agreement with a previous report showing that DDX39B binds a SARNP peptide consisting of only one helical motif independent of RNA and nucleotides (Hohmann *et al.* 2025). In contrast, crosslinking of the 2:1 complex depended on the presence of nucleotide and a 38 nt RNA (Figure 32). A shorter 13 nt RNA did not support 2:1 complex formation, unlike the published crystal structure in which the DDX39B protomers independently bound to 15 nt RNAs. This discrepancy could be explained by differences in the experimental setups. Although the protein concentrations used for crystallization were not reported, such experiments typically require protein concentrations as high as possible without inducing aggregation or

precipitation (Dessau & Modis 2011). The crosslinking experiments were performed with 5 µM Sub2 and 2.5 µM Tho1-CTD. Higher concentrations may stabilize the 2:1 complex and thereby explain its presence in the crystal structure.

Notably, although the 2:1 complex formed on a 38 nt RNA, it was hardly detectable using the 13/38 pdRNA (Figure 32). Even on the 38 nt substrate, the majority of crosslinked UAP56 was found in the 1:1 stoichiometry, with only a minor fraction forming a 2:1 complex. One possible explanation is that the complex of all three proteins has a short lifetime, reducing the likelihood of successful crosslinking. Moreover, experiments using the Tho1-CTD mutants revealed increased 1:1 crosslinking in the absence of the first motif, suggesting differences in interface accessibility for crosslinking (Figure 30). As it is unclear how pdRNA binding differs from binding of the long ssRNA, it is difficult to estimate the possible impacts it might have on the complex orientation and therefore crosslink accessibility. Further experiments, e.g., varying protein/RNA concentrations or buffer conditions, may help to promote crosslinking of the 2:1 complex on a pdRNA.

5.2.4. The Tho1-CTD stimulates unwinding by facilitating Sub2 dimerisation

Testing different substrates in the unwinding assay revealed that Sub2 unwinds substrates containing an ssRNA overhang with reduced efficiency compared to short blunt-end duplexes (Figure 23). Although little is known about the substrate preferences of Sub2, other DEAD-box helicases preferentially bind single-stranded RNA or DNA (Donsbach *et al.* 2025; Putnam *et al.* 2015). In such cases, single-stranded regions often facilitate helicase loading onto the duplex and consequently promote efficient unwinding (Dharavath *et al.* 2025; Putnam *et al.* 2015; Song & Ji 2019; Toyama & Shimada 2024; Yang & Jankowsky 2006). In contrast, the unwinding data indicate that while Sub2 may preferentially bind ssRNA, the presence of an ssRNA overhang on partially duplex substrates interferes with productive unwinding. Consistent with this, attachment of an ssDNA overhang, which Sub2 does not bind, to the duplex did not impair unwinding. Furthermore, stimulation of Sub2's helicase activity by the Tho1-CTD was observed only in the presence of an ssRNA overhang.

Together with the strict requirement that both Sub2 interfaces in Tho1 remain intact, these findings support a model in which the Tho1-CTD functions as a molecular scaffold that increases Sub2 engagement with the substrate and thereby enhances helicase activity (Figure 46): In the absence of the Tho1-CTD, Sub2 tends to associate

with the ssRNA region rather than the double strand. Additionally, Sub2 binding to the single-stranded overhang near the double-stranded region may prevent positioning of a second Sub2 protomer on the duplex. These non-productive binding events reduce the probability of duplex engagement and strand separation, leading to infrequent unwinding events and low overall helicase activity (Figure 46, left panel).

Formation of a Tho1-CTD-bridged 2:1 complex overcomes this limitation by spatially coordinating two Sub2 molecules on the same RNA strand of the substrate. In this arrangement, one Sub2 protomer interacts with the ssRNA, while the second is positioned onto the double-stranded region. This configuration increases the likelihood of productive Sub2 interaction with the duplex, promoting more frequent strand-separation events and accelerating unwinding kinetics (Figure 46, middle panel).

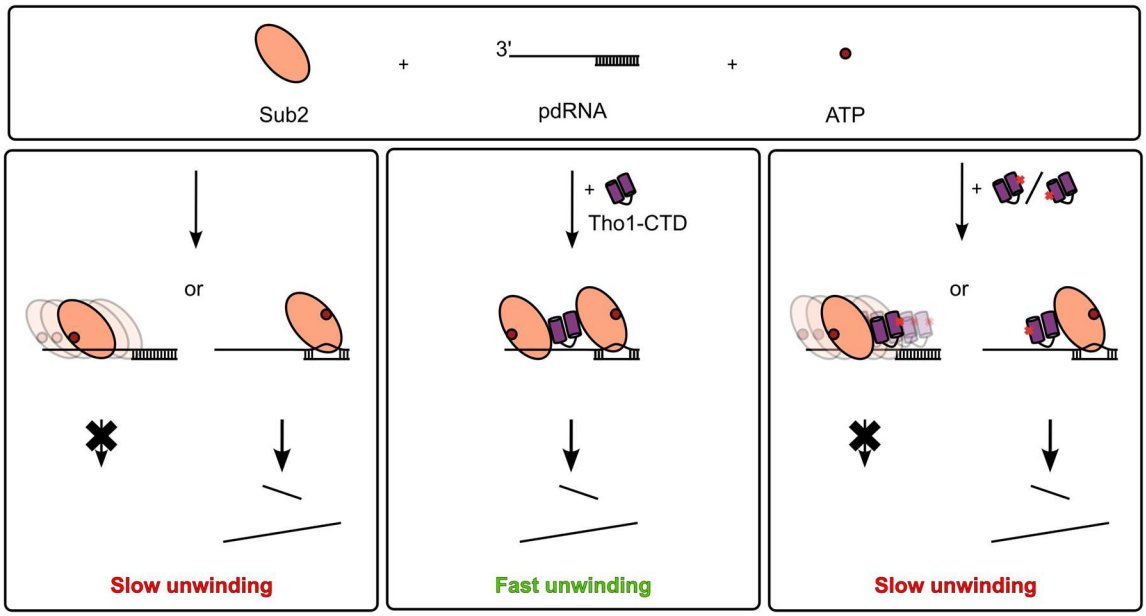

Figure 46: Model for Tho1-CTD-mediated unwinding stimulation by facilitating Sub2 dimerisation. Sub2 alone unwinds pdRNA substrates with low efficiency due to a high frequency of non-productive binding events (left panel). Interaction with the Tho1-CTD leads to Sub2 dimerisation on the substrate, allowing one protomer to associate with the single-stranded region, while the second protomer engages with the adjacent duplex, resulting in stimulated unwinding (middle panel). Mutations in the Tho1-CTD that prevent assembly beyond a 1:1 complex eliminate unwinding enhancement (right panel).

Disruption of this interaction by mutations in the Tho1-CTD that restrict complex formation to a 1:1 stoichiometry abolishes the bridging function. Under these conditions, Sub2 reverts to predominantly non-productive substrate binding, and helicase activity is reduced to levels comparable to those in the absence of the Tho1-CTD (Figure 46, right panel).

To validate this model, further experiments are required to quantitatively assess Sub2 binding to different RNA substrates. In particular, fluorescence anisotropy assays could compare Sub2 binding affinities for ssRNA and dsRNA.

5.2.5. Dimerisation of other DEAD-box helicases

Although most DEAD-box helicases function as monomeric enzymes, functional dimerisation has been observed in some cases. The C-terminal domains of *Thermus thermophilus* DEAD-box helicase Hera, as well as *Geobacillus stearothermophilus* CshA and *Escherichia coli* CsdA, contain dimerisation domains that mediate the formation of stable dimers (Huen *et al.* 2017; Klostermeier & Rudolph 2009; Rudolph & Klostermeier 2009; Xu *et al.* 2017). In the dimeric form of Hera, the active sites of the two helicase cores face each other, enabling cooperation between protomers. Inactivating or removing one core reduces the unwinding activity of the remaining protomer. However, the closure of the helicase core, which is coupled to ATP hydrolysis and RNA unwinding, occurs independently of the presence of the second protomer. The authors concluded that while an individual helicase protomer is a functional unwinding unit, the presence of a second Hera protomer in the dimeric state can be beneficial for unwinding (Donsbach *et al.* 2025). This mechanism is reminiscent of the proposed Tho1-CTD-mediated dimerisation of Sub2, in which the presence of the Tho1-CTD is not essential but advantageous for unwinding.

Another example of a DEAD-box helicase where cooperative interactions between multiple protomers enhance nucleic acid unwinding efficiency is *S. cerevisiae* Ded1 (DDX3X in humans). Mutational analysis revealed that Ded1 oligomerisation is mediated by its C-terminal region. Deletion of this region still allows Ded1 to dimerise, but restricts the formation of higher-order complexes and significantly compromises its unwinding ability (Putnam *et al.* 2015). Moreover, Ded1 was shown to preferentially associate with single-stranded RNA regions within pdRNA substrates, which serve as initial binding sites and facilitate local accumulation of Ded1 on the substrate (Putnam *et al.* 2015; Yang & Jankowsky 2006). Further insights into the mechanism of Ded1-mediated unwinding have recently been obtained from single-molecule optical tweezers experiments using a 16 bp RNA hairpin with an adjacent 25 nt ssRNA region. In this system, a first Ded1 protomer binds to the ssRNA, and subsequent oligomerisation promotes stepwise recruitment of additional Ded1 protomers onto the duplex, leading to its unwinding (Patrick *et al.* 2025). Efficient strand separation by

Ded1 depends on the length of the available ssRNA overhang. Substrates containing single-stranded regions of 25 nt can accommodate multiple Ded1 protomers and are unwound efficiently, whereas shorter overhangs limit protomer recruitment and result in reduced unwinding (Putnam *et al.* 2015). Similarly, the observed stimulation of Sub2/UAP56 by the Tho1-CTD strongly depended on the presence of an ssRNA overhang.

Oligomerisation is a key driver of efficient unwinding for all DEAD-box helicases discussed. Ded1 and Hera achieve this through self-oligomerisation, whereas Sub2 requires the Tho1-CTD to scaffold dimer formation. Moreover, Ded1 can form higher-order complexes, whereas Sub2's oligomerisation is restricted to dimers by the two helical motifs present in the Tho1-CTD.

5.2.6. Role of overhang orientation in Tho1-CTD-mediated unwinding stimulation

Whereas many processive helicases translocate along nucleic acids with a defined polarity, DEAD-box RNA helicases generally mediate local strand separation in a non-directional manner (Andreou & Klostermeier 2013; Rozen *et al.* 1990). Consistent with this mechanism, Sub2 unwound substrates with either 3′ or 5′ ssRNA overhangs (Figure 24). Notably, Sub2-mediated unwinding was more efficient on hybrid substrates compared to pdRNA substrates (Figures 23 and 24). Since DNA/RNA hybrids are usually less stable than RNA duplexes, they may be more prone to strand separation upon local destabilization by Sub2 binding.

The Tho1-CTD stimulated unwinding on all tested substrates except DNA/DNA duplexes. However, stimulation was reduced on the pdRNA substrate with a 5′ overhang (Figure 24D). To find possible explanations for this, AlphaFold 3 predictions of 2:1 Sub2-Tho1-CTD complexes were generated on pdRNA substrates with either 3′ or 5′ overhangs (Figure 47, Supplementary Figure S7). While the overall complex architecture and orientation of Sub2 molecules appeared similar for both substrates, strand-binding analysis revealed differences: on the 3′ overhang substrate, both Sub2 protomers bound the long strand of the substrate in all models, whereas on the 5′ overhang substrate, three out of five predictions showed the second protomer interacting with the short strand instead (Figure 47B).

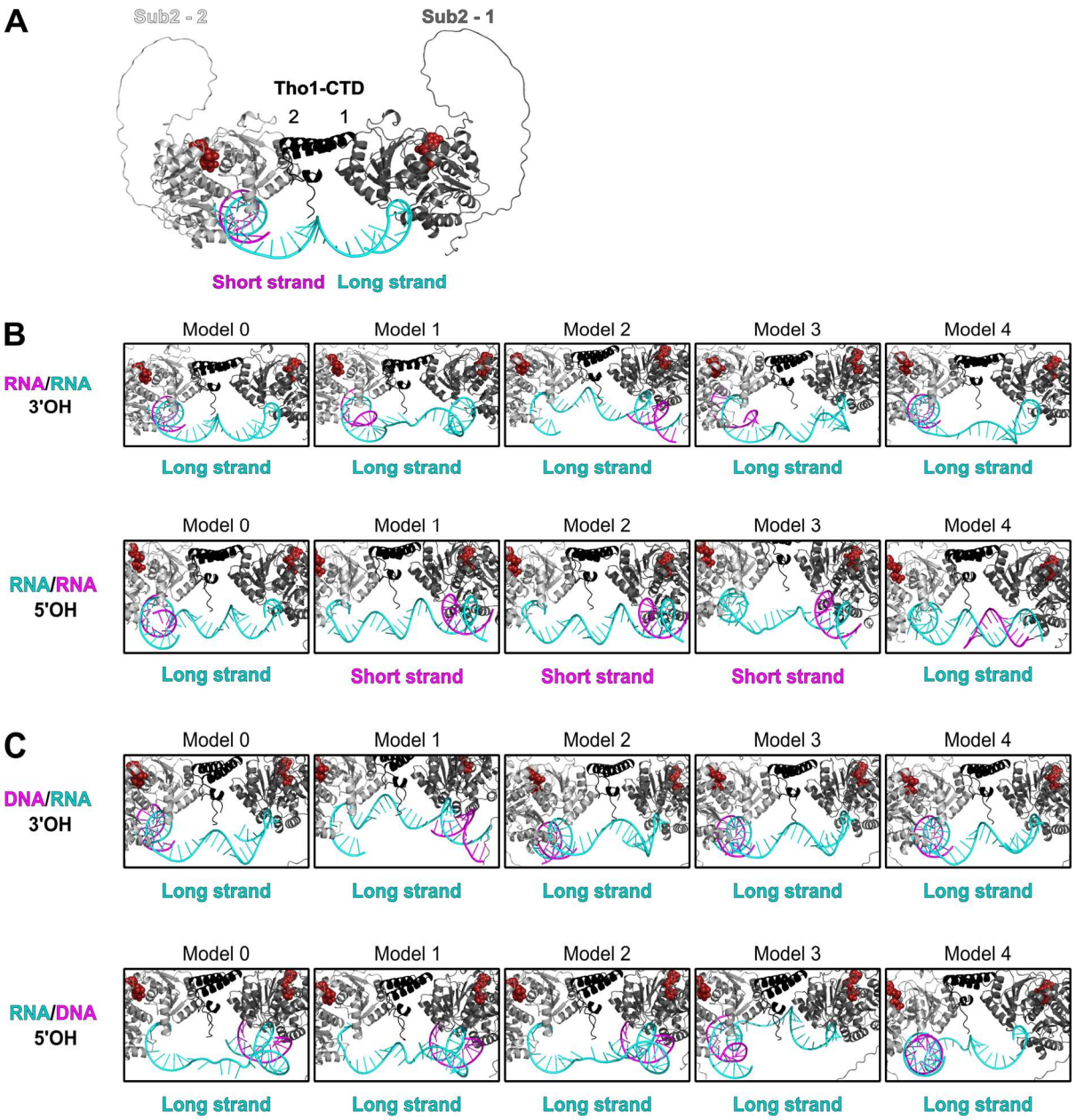

Figure 47: Predicted Sub2-Tho1-CTD 2:1 complexes on 3′ and 5′ overhangs. (A) Representative AlphaFold 3 prediction of a 2:1 complex formed by Sub2 (grey) and the Tho1-CTD (black) on a pdRNA substrate with a 3′ ssRNA overhang. The 13 nt top strand is shown in pink and the 38 nt bottom strand in cyan, allowing discrimination between strands and identification of which strand is bound by each Sub2 protomer. **(B+C)** AlphaFold 3 prediction of 2:1 complexes on (B) pdRNA substrates or (C) hybrid substrates with either 3′ or 5’ ssRNA overhangs. Close-up views of the five models generated for each condition are shown. Full views are available in Supplementary Figure S7.

The substrates were labelled with BHQ-2 and Cy5 on the same duplex site, resulting in quenching of Cy5 fluorescence when the strands were in proximity. When both Sub2 protomers bind the long strand, separation and release of the short strand result in loss of quenching and an increase in Cy5 fluorescence. Conversely, if protomers bind opposite strands, the separated short strand may remain in proximity to the long strand, leading to only partial loss of quenching and increasing the likelihood of strand re-

annealing. Notably, two of the five models still depicted both protomers bound to the long strand. Thus, on the 5′ overhang substrate, a mixture of both binding modes may cause the reduced stimulation by the Tho1-CTD (Figure 24).
In hybrid substrates, the AlphaFold 3 models exclude binding of the short DNA strand by Sub2, constraining both protomers to interact with the long RNA strand. As a result, all predictions for hybrid substrates positioned both helicases on the same strand regardless of overhang orientation (Figure 47C). Correspondingly, helicase stimulation by the Tho1-CTD was robust on both hybrid substrates (Figure 24).
Taken together, these results suggest that the reduced stimulation by the Tho1-CTD on pdRNA substrates with a 5′ overhang may not directly result from overhang orientation, but rather from substrate-dependent binding behaviour in this assay. Thus, Tho1-CTD-mediated helicase stimulation appears to be largely independent of overhang position. It is important to note, however, that AlphaFold 3 models are predictive and may not fully capture the complex conformations of real proteins. Nevertheless, they provide a valuable framework for hypothesizing potential mechanisms underlying the observed effects.

5.3. *In vivo* relevance of the Tho1-Sub2 interaction

Unlike its orthologs SARNP (human) and MOS11 (*A. thaliana*), both of which are directly implicated in mRNA export, deletion of Tho1 does not result in an apparent phenotype in yeast cells (Jimeno *et al.* 2006; Piruat & Aguilera 1998). Instead, Tho1 was originally identified as a *suppressor of the transcriptional defect of Hpr1 by overexpression*, as its overexpression alleviated several phenotypes in cells lacking the THO component Hpr1 (Jimeno *et al.* 2006; Piruat & Aguilera 1998; Stefanyshena & Sträßer 2026). One of these phenotypes, a ts growth defect at 37°C, was used in this study to assess the *in vivo* function of different Tho1 mutants and thereby evaluate the relevance of Tho1's nucleic acid-related activities and its interaction with Sub2 (Figures 12 and 28).
Consistent with previous reports, deletion of the SAP domain did not impair phenotype suppression (Jimeno *et al.* 2006). In contrast, removal of the CTD completely abolished the effect, whereas overexpression of the Tho1-CTD alone was sufficient to suppress the phenotype. In the initial dot spot assays (Figure 12), Tho1 domain mutants were expressed alongside endogenous Tho1, mirroring the experimental setup used by Jimeno et al. (2006). Importantly, insertion of Tho1 and the Tho1-CTD into the

endogenous *THO1* locus enabled overexpression in the absence of wild-type Tho1 and confirmed that the Tho1-CTD alone remained sufficient for phenotype suppression (Figure 28). These findings suggested a substantial cellular role for the Tho1-Sub2 interaction, whereas the loss of RNA-binding or nucleic acid annealing activity in the Tho1-CTD mutant did not appear to be relevant for this phenotype. Recent work has demonstrated a comparable requirement for the SARNP-DDX39B interaction in human cells, where the interaction-deficient DDX39B-D283R mutant caused a growth defect in K562 cells (Hohmann *et al.* 2025).
Strikingly, Tho1-CTD interface mutants unable to stimulate helicase activity failed to suppress the ts phenotype, indicating that the physiological relevance extends beyond mere Sub2 binding. Instead, 2:1 complex formation appears to play a role as well.
Following this train of thought, it seems contradictory that the Tho1-ΔCTE mutant was unable to suppress the ts phenotype, despite retaining the ability to interact with Sub2 (Figure 14). However, data from Miosga (2022) revealed that Tho1-ΔCTE does not stimulate Sub2's helicase activity, even though it lacks annealing activity that could otherwise mask helicase stimulation. In contrast, deletion of only the second half of the CTE (Tho1-Δ2nd half CTE) abolished nucleic acid binding and annealing activities but resulted in weak stimulation of unwinding (Miosga 2022). Given the strong positive charge of the CTE, deletion of the whole domain may have broader consequences for protein structure and functional interactions. It is therefore conceivable that complete removal of the CTE affects a productive interaction with Sub2, thereby explaining the lack of phenotype suppression observed *in vivo*. Although EMSAs indicated that Tho1-ΔCTE can still form a complex with Sub2 on a short RNA substrate, this may not reflect its behaviour on longer RNAs, particularly with respect to the formation of a 2:1 complex. In the wild-type protein, the negatively charged linker is neutralised by the positive CTE, yielding a net charge approximately -1 at pH 7.5 (Prot pi, version 2.2.29.152). Deletion of the CTE leaves the protein with a negative net charge of approximately -12. This could create electrostatic repulsion against the negatively charged RNA backbone, preventing the 2:1 Sub2-Tho1 complex from forming stably on associated nucleic acids. To analyse this, crosslinking experiments with Sub2-S329C and Tho1-ΔCTE could be performed to assess whether complexes still form with this mutant and, if so, in which stoichiometry. A possible further approach would be to include the half-CTE mutant in the dot spot assay, as it stimulates Sub2 unwinding

and allows testing a more direct correlation between helicase stimulation, nucleic acid-related activities, and phenotype suppression.

In summary, due to the lack of phenotype suppression observed with the Tho1-ΔCTE mutant, a potential *in vivo* role for Tho1's nucleic acid-binding activity, as proposed by Jimeno et al. (2006), cannot be ruled out. However, these results demonstrate the importance of the Tho1-Sub2 interaction.

5.4. The role of scaffold-architecture in helicase activation

According to the proposed model for helicase stimulation, the Tho1-CTD acts as a scaffold that bridges Sub2 and UAP56 dimerisation on a 13/38 pdRNA substrate (Figures 46 and 48). Interestingly, yeast Tho1 represents a structural minority: its two helical motifs are arranged in a relatively rigid helix-turn-helix structure connected by a short linker. In contrast, most Tho1 orthologs contain more than two helical motifs (Supplementary Figure S1; Xie *et al.* 2023). In these cases the helical motifs are connected by flexible linkers of varying lengths (Figure 7; Xie *et al.* 2023). The functional roles of both the number and the spatial arrangement of these motifs have remained unclear. To gain insights into this question, the mechanism by which the *A. thaliana* ortholog MOS11, containing five helical motifs, stimulates unwinding by UAP56 was analysed in this study.

For both Sub2 and UAP56, Tho1-CTD-mediated helicase stimulation was limited to substrates containing an ssRNA overhang and was not observed on short 13 bp blunt-end substrates (Figure 37). MOS11, on the other hand, stimulates UAP56's helicase activity independently of an ssRNA overhang (Figure 37). Analyses of MOS11 mutants with varying numbers of intact motifs revealed that on a short blunt-end substrate, two functional helical motifs in MOS11 are sufficient to stimulate UAP56 helicase activity (Figure 39), suggesting a mechanism related to that of the Tho1-CTD. However, increasing the number of available motifs enhanced stimulation and the degree of stimulation also positively correlated with greater spatial separation between the motifs (Figure 41).

AlphaFold 3 predictions of a 2:1 complex formed by UAP56 and MOS11 or its mutants on 13 bp duplex substrates were generated and analysed (Supplementary Table 1). In models with wild-type MOS11, UAP56 protomers interacted with two helical motifs in MOS11 showing no preferences for specific motifs. Notably, nearly all models positioned UAP56 on opposite strands of the duplex. Using MOS11 mutants with

greater spacing between the motifs increased the likelihood of UAP56 binding to opposite strands and at the same time improved the overall model quality (Supplementary Table 1). Combining these structural results with the experimental data on MOS11 mutants supports a model in which MOS11 acts as a flexible scaffold. Its higher number of motifs and their flexible arrangement allow one UAP56 to bind one strand of the duplex, while the second binds to the opposite strand, resulting in enhanced unwinding (Figure 48, left panel). By contrast, interaction with the Tho1-CTD permits binding of only one UAP56 protomer to the duplex. The rigid structure of the complex prevents the second protomer from engaging the opposite strand, thus yielding unwinding activity comparable to UAP56 alone.

MOS11 stimulates UAP56-mediated unwinding not only on RNA duplexes but also on RNA/DNA hybrid substrates (Figures 42 and 43). As with RNA duplexes, AlphaFold 3 models of the hybrid substrates show UAP56 protomers predominantly positioned on opposite strands (Supplementary Table 1). This arrangement suggests that one UAP56 protomer interacts with the DNA strand, which is rather unusual for an RNA helicase. However, although UAP56 lacks ssDNA-binding activity, it has been reported to interact with double-stranded DNA (Kammel *et al.* 2013). In contrast, unwinding experiments using a 13 bp DNA duplex did not show UAP56 binding (Figure 42). One explanation for this discrepancy is the use of substantially longer duplexes (25 nt and 29 nt) in the published study. In addition, the authors have already observed differences in UAP56 binding affinities between gel-based assays and microscale thermophoresis (MST) experiments, indicating that experimental conditions strongly impact complex detection. Hence, the absence of detectable binding to a short DNA duplex in the unwinding assays does not exclude UAP56-dsDNA interaction in general. Furthermore, binding prerequisites differ between DNA/RNA hybrids and DNA duplexes. In hybrids, one UAP56 protomer can bind the RNA strand, while interaction with MOS11 may position the second protomer near the DNA strand and thus potentially favour its binding. Although binding was monitored in the helicase assays, the rapid unwinding of hybrid substrates, together with the limitations of anisotropy measurement described above, prevented the resolution of individual binding events. In principle, UAP56 could bind the substrate by initially interacting with the RNA strand, followed by engaging the DNA strand. This would result in a transient increase in anisotropy that rapidly decreases after strand separation, as the labelled ssDNA product is not bound. Indeed, in reactions containing only UAP56, anisotropy values

decreased to levels slightly below those of the substrate alone within the first minutes of the reaction (Figure 42). This decrease may reflect ssDNA product formation, as the anisotropy of single strands was generally lower than that for double-stranded substrates. Because the interaction of UAP56 with the DNA is likely weak and short-lived, an initial increase in anisotropy was not detectable in this setup. Taken together, while the assay confirms unwinding by showing product formation, it lacks the temporal resolution to distinguish the individual binding steps of the 2:1 complex.

The results obtained for the pdRNA substrates differed markedly from those for blunt-end duplexes. In this case, unwinding stimulation required the presence of at least three intact motifs, and a mutant containing only two motifs failed to enhance unwinding, even when the spacing between motifs was increased (Figures 39 and 41). These findings support an alternative mechanistic model for this substrate (Figure 48, right panel). Whereas higher flexibility within MOS11 was beneficial for unwinding of short duplexes, it may become disadvantageous on substrates containing a single-stranded overhang. Like Sub2, UAP56 exhibited reduced unwinding activity in the presence of an ssRNA overhang (Figures 39 and 41), suggesting a preference for initial binding to the single-stranded region. While interaction with the Tho1-CTD promotes formation of a relatively rigid complex that positions a second UAP56 protomer on the duplex region, the increased linker flexibility of MOS11 may instead allow two UAP56 protomers to bind adjacent sites on the overhang. This could interfere with binding of an additional protomer to the duplex and therefore not promote unwinding. When three or more intact motifs are present, more than two helicases could associate with the complex. In this scenario, two UAP56 protomers bind the single-stranded region, while a third engages with the duplex, resulting in enhanced unwinding. This arrangement resembles the protomer assembly described for Ded1 on a similar substrate (Patrick *et al.* 2025). To experimentally determine the stoichiometry of the MOS11-UAP56 assembly, native mass spectrometry or mass photometry could be employed to assess the native mass distribution in solution. Site-specific cysteine-cysteine or cysteine-lysine crosslinking could subsequently stabilize the identified complexes to enable downstream functional and structural analyses.

In conclusion, both the Tho1-CTD and MOS11 stimulate unwinding by scaffolding helicase oligomerisation. The number of motifs and their flexibility directly influence the substrate specificity of the helicase stimulation.

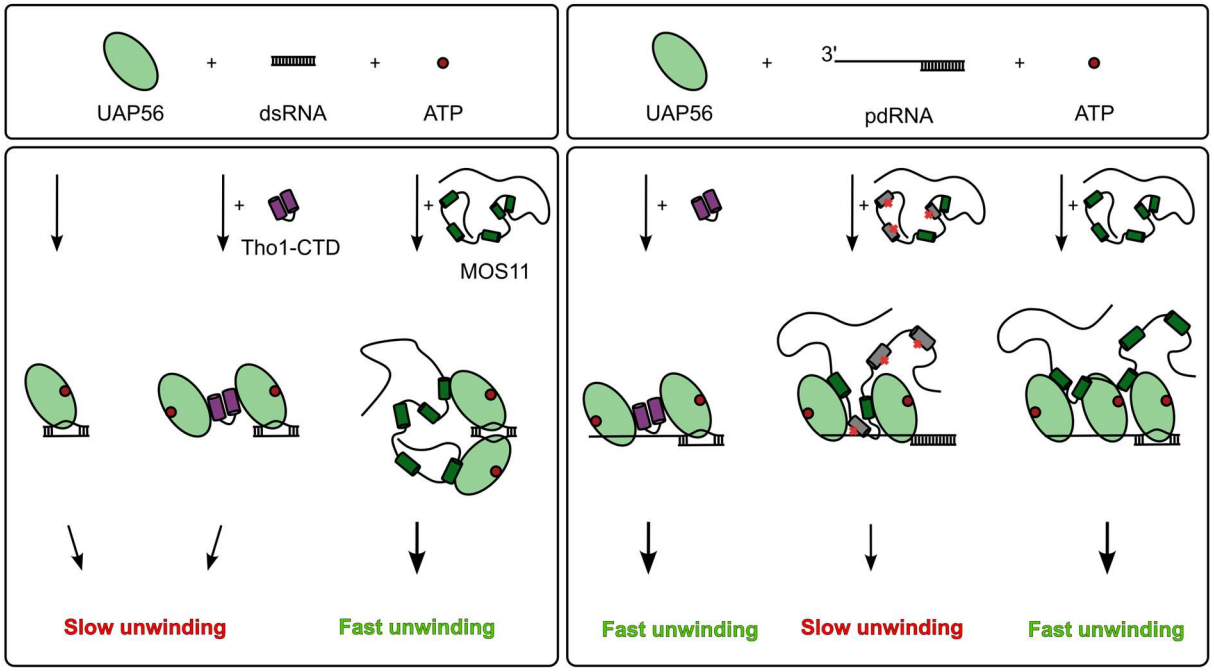

Figure 48: A model on the influence of scaffold flexibility on unwinding stimulation. Left panel: The Tho1-CTD does not stimulate UAP56-mediated unwinding of a short blunt-end substrate, as the rigid 2:1 complex formed with two UAP56 protomers does not permit both protomers to simultaneously engage with the duplex. In contrast, the greater flexibility of MOS11 enables two UAP56 protomers to interact with opposing strands of the duplex, thereby promoting unwinding. Right panel: On a pdRNA substrate containing an ssRNA overhang, the 2:1 complex between UAP56 and the Tho1-CTD positions one UAP56 protomer on the single-stranded region and the second on the duplex, resulting in stimulated unwinding. In a MOS11 mutant containing only two intact motifs, increased linker flexibility instead allows two protomers to bind the overhang, which does not support productive unwinding. When additional UAP56 protomers are able to associate with MOS11, interactions with both the overhang and the duplex become possible, resulting in enhanced unwinding.

5.5. Species-specificity of helicase stimulation

Both Tho1-CTD and MOS11 stimulate the helicase activity of UAP56 (Figure 37). These stimulatory effects were abolished in the UAP56 interface mutant (Figure 29D and 36C), indicating that both proteins share the same interaction site on the helicase. Interestingly, MOS11 did not stimulate Sub2-mediated unwinding, suggesting that its interaction with UAP56 is more specific than that of the Tho1-CTD. It is important to note that the Tho1-CTD represents only a truncated construct of full-length Tho1. In the wild-type protein, additional regions flanking the CTD may influence interaction specificity and could restrict interactions with helicases beyond Sub2. To test this hypothesis, minimal constructs of MOS11 containing only two helical motifs could be examined for their effect on Sub2 unwinding.

Furthermore, structural differences between Sub2 and UAP56 may also contribute to differential protein interactions. Although both helicases possess highly conserved interfaces for Tho1/MOS11 binding, sequence variations in other regions may modulate their interactions (Figure 19). Attempts to draw conclusions from AlphaFold 3 predictions were not successful, as modelled MOS11 complexes with UAP56 and Sub2 did not reveal significant differences between the two helicases (data not shown). Consequently, the lack of Sub2 helicase stimulation by MOS11 remains unclear without further validation. To better understand the conservation of these interactions, systematic testing of the effects of the Tho1-CTD or other Tho1 orthologs on the unwinding activity of Sub2 orthologs from diverse organisms could be performed.

5.6. Conclusions and outlook

This work reveals an evolutionarily conserved mechanism of helicase activation in which Tho1-family proteins stimulate the nucleic acid unwinding activity of yeast Sub2 and *A. thaliana* UAP56 DEAD-box helicases by acting as scaffolds that promote helicase oligomerisation. Detailed analysis of UAP56 stimulation by *A. thaliana* MOS11 showed that both the number of helical motifs and the flexibility of their spatial arrangement are critical determinants of the scaffold's function. Specifically, these structural features define its effective reach, which in turn determines the range of substrates that support stimulation as well as the extent of helicase oligomerisation. Importantly, the physiological relevance of this mechanism is supported by the *in vivo* requirement for two intact motifs within the Tho1-CTD to suppress the growth defect in Δ*hpr1* cells. Together, the *in vitro*, *in silico* and *in vivo* findings presented here establish a mechanistically versatile and biologically meaningful framework for understanding how Tho1-family members regulate DEAD-box helicase activity.

Xie et al. (2023) proposed a model where interactions between Tho1/SARNP and Sub2/DDX39B, together with binding of the resulting complexes to mRNA, contribute to mRNP compaction. Simultaneously, Yra1/ALYREF participate in these assemblies by binding Sub2/DDX39B via distinct interaction sites from those used by Tho1/SARNP. Whereas interaction with the helical motifs in Tho1/SARNP is mediated through the helicase's CTD, Yra1/ALYREF interact with the NTD (Ren *et al.* 2017; Xie *et al.* 2023). Recent studies on human ALYREF and *A. thaliana* ALY further show that these proteins also stimulate the helicase activities of their cognate helicases (Bhandari *et al.* 2024; Rödel *et al.* 2024). Similar to Tho1, both proteins contain two

helicase-interaction motifs, but their overall architectures provide structural flexibility comparable to that observed in MOS11 and SARNP.

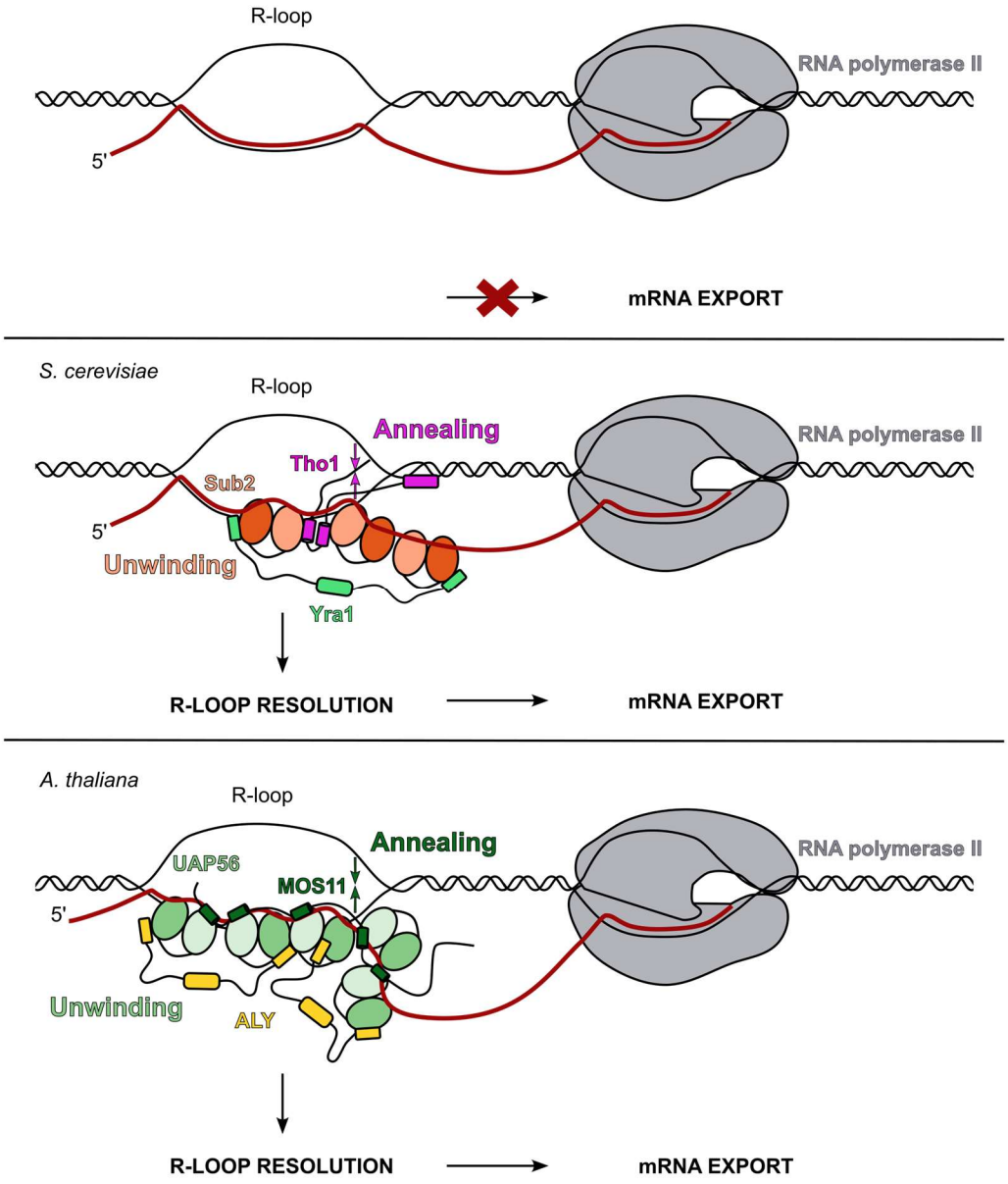

Figure 49: Model for cellular R-loop resolution in *S. cerevisiae* and *A. thaliana*. During transcription, R-loops can form and interfere with transcription, mRNP formation, and mRNA export. Assembly of higher-order complexes containing Sub2, Tho1 and Yra1 in yeast, or UAP56, MOS11 and ALY in *A. thaliana,* leads to accumulation of Sub2 or UAP56 protomers at the R-loop site. Through a local strand-separation mechanism, Sub2/UAP56 destabilise the RNA/DNA hybrid and promote R-loop resolution. Tho1/MOS11 may further contribute by re-annealing the two DNA strands.

Beyond helicase activation, ALYREF has been implicated in cooperating with DDX39B in R-loop resolution, dependent on ALYREF's ability to interact with nucleic acids (Bhandari *et al.* 2024). Notably, full-length Tho1, MOS11 and SARNP also interact with nucleic acids and have been linked to cellular R-loops. Deletion of MOS11 and the

depletion of SARNP lead to export defects of GC-rich mRNAs, which are particularly prone to R-loop formation, while overexpression of Tho1 reduces elevated R-loop levels in Δ*hpr1* cells (Miosga 2022; Rödel *et al.* 2024; Xie *et al.* 2023). Moreover, Tho1 has been shown to resolve RNA/DNA hybrids in *in vitro* strand displacement assays (Figure 11; Miosga 2022). Similarly, DDX39B has been reported to resolve R-loop-like structures *in vitro* and reduce cellular R-loop levels (Pérez-Calero *et al.* 2020).

Taken together, these observations suggest a model in which Tho1 family proteins contribute to R-loop resolution by directly interacting with their cognate helicases either alone or in cooperation with Yra1/ALY (Figure 49). Unwinding by a single helicase is often limited to destabilization of short duplex regions. The formation of higher-order assemblies, however, could locally concentrate Sub2/UAP56 at R-loop sites and thereby promote efficient resolution of these structures. Additionally, Tho1's intrinsic nucleic acid annealing activity may facilitate re-annealing of the two DNA strands. Although the annealing activity of MOS11 is comparatively weak, it is most pronounced on DNA substrates, suggesting that MOS11 could fulfil a similar function.

Experimental validation is essential to confirm and refine this proposed model. This study focused on the ts phenotype observed in Δ*hpr1* cells. However, loss of *HPR1* results in multiple cellular defects, including impaired mRNA export, hyperrecombination and increased R-loop formation (Jimeno *et al.* 2006; Piruat 1998; Stefanyshena & Sträßer 2026). Consequently, it remains difficult to dissect how these defects are mechanistically linked and how each contributes to the observed growth defect. To better define the cellular role of the Tho1-Sub2 interaction and its potential involvement in R-loop resolution, dedicated *in vivo* R-loop assays are required.

References

Abramson, J., Adler, J., Dunger, J., Evans, R., Green, T., Pritzel, A., *et al.* (2024). Accurate structure prediction of biomolecular interactions with AlphaFold 3. *Nature*, 630, 493–500.

Abruzzi, K.C., Lacadie, S. & Rosbash, M. (2004). Biochemical analysis of TREX complex recruitment to intronless and intron-containing yeast genes. *EMBO J.*, 23, 2620–2631.

Andersen, C.B.F., Ballut, L., Johansen, J.S., Chamieh, H., Nielsen, K.H., Oliveira, C.L.P., *et al.* (2006). Structure of the Exon Junction Core Complex with a Trapped DEAD-Box ATPase Bound to RNA. *Science*, 313, 1968–1972.

Andreou, A.Z., Harms, U. & Klostermeier, D. (2019). Single-stranded regions modulate conformational dynamics and ATPase activity of eIF4A to optimize 5′-UTR unwinding. *Nucleic Acids Res.*, 47, 5260–5275.

Andreou, A.Z. & Klostermeier, D. (2013). The DEAD-box helicase eIF4A: Paradigm or the odd one out? *RNA Biol.*, 10, 19–32.

Archuleta, S.R., Goodrich, J.A. & Kugel, J.F. (2024). Mechanisms and functions of the RNA polymerase II general transcription machinery during the transcription cycle. *Biomolecules*, 14, 176.

Aregger, R. & Klostermeier, D. (2009). The DEAD Box Helicase YxiN Maintains a Closed Conformation during ATP Hydrolysis. *Biochemistry*, 48, 10679–10681.

Ausubel, F.M., Brent, R., Kingston, R.E., Moore, D.D., Seidman, J.G., Smith, J.A., *et al.* (1987). Current protocols in molecular biology (New York: Greene and Wiley-interscience).

Awasthi, S., Chakrapani, B., Mahesh, A., Chavali, P.L., Chavali, S. & Dhayalan, A. (2018). DDX39B promotes translation through regulation of pre-ribosomal RNA levels. *RNA Biol.*, 15, 1157–1166.

Aydin, E., Schreiner, S., Böhme, J., Keil, B., Weber, J., Žunar, B., *et al.* (2024). DEAD-box ATPase Dbp2 is the key enzyme in an mRNP assembly checkpoint at the 3'-end of genes and involved in the recycling of cleavage factors. *Nat. Commun.*, 15, 6829.

Bai, X., Ni, J., Beretov, J., Wang, S., Dong, X., Graham, P., *et al.* (2021). THOC2 and THOC5 Regulate Stemness and Radioresistance in Triple-Negative Breast Cancer. *Adv. Sci.*, 8, 2102658.

Ben-Ari, Y., Brody, Y., Kinor, N., Mor, A., Tsukamoto, T., Spector, D.L., *et al.* (2010). The life of an mRNA in space and time. *J. Cell Sci.*, 123, 1761–1774.

Bernecky, C., Herzog, F., Baumeister, W., Plitzko, J.M. & Cramer, P. (2016). Structure of transcribing mammalian RNA polymerase II. *Nature*, 529, 551–554.

Bertani, G. (1951). STUDIES ON LYSOGENESIS I: The Mode of Phage Liberation by Lysogenic Escherichia coli. *J. Bacteriol.*, 62, 293–300.

Bhandari, J., Guillén-Mendoza, C., Banks, K., Eliaz, L., Southwell, S., Eyaa, D., *et al.* (2024). The molecular chaperone ALYREF promotes R-loop resolution and maintains genome stability. *J. Biol. Chem.*, 300, 107996.

Bhattacharjee, R., Agarwala, S., Mazurkiewicz, D., Gecz, J. & Kumar, R. (2025). Transcription-Export complex in neurodevelopmental disorders. *Curr. Opin. Genet. Dev.*, 94, 102380.

Bohnsack, K.E., Yi, S., Venus, S., Jankowsky, E. & Bohnsack, M.T. (2023). Cellular functions of eukaryotic RNA helicases and their links to human diseases. *Nat. Rev. Mol. Cell Biol.*, 24, 749–769.

Bordeleau, M.-E., Matthews, J., Wojnar, J.M., Lindqvist, L., Novac, O., Jankowsky, E., *et al.* (2005). Stimulation of mammalian translation initiation factor eIF4A activity by a small molecule inhibitor of eukaryotic translation. *Proc. Natl. Acad. Sci.*, 102, 10460–10465.

Bowers, H.A., Maroney, P.A., Fairman, M.E., Kastner, B., Lührmann, R., Nilsen, T.W., *et al.* (2006). Discriminatory RNP remodeling by the DEAD-box protein DED1. *Rna*, 12, 903–912.

Buchwald, G., Schüssler, S., Basquin, C., Le Hir, H. & Conti, E. (2013). Crystal structure of the human eIF4AIII–CWC22 complex shows how a DEAD-box protein is inhibited by a MIF4G domain. *Proc. Natl. Acad. Sci.*, 110.

Bugai, A., Hohmann, U., Lorenzo, A., Graf, M., Fin, L., Rouvière, J.O., *et al.* (2025). Molecular basis of polyadenylated RNA fate determination in the nucleus. *bioRxiv*, 2025–09.

Cai, S., Bai, Y., Wang, H., Zhao, Z., Ding, X., Zhang, H., *et al.* (2020). Knockdown of THOC1 reduces the proliferation of hepatocellular carcinoma and increases the sensitivity to cisplatin. *J. Exp. Clin. Cancer Res.*, 39, 135.

Callan, H.G. & Tomlin, S.G. (1950). Experimental studies on amphibian oocyte nuclei I. Investigation of the structure of the nuclear membrane by means of the electron microscope. *Proc. R. Soc. Lond. Ser. B - Biol. Sci.*, 137, 367–378.

Chanarat, S., Seizl, M. & Sträßer, K. (2011). The Prp19 complex is a novel transcription elongation factor required for TREX occupancy at transcribed genes. *Genes Dev.*, 25, 1147–1158.

Chanarat, S. & Sträßer, K. (2013). Splicing and beyond: the many faces of the Prp19 complex. *Biochim. Biophys. Acta BBA-Mol. Cell Res.*, 1833, 2126–2134.

Chang, C.-T., Walsh, M.J., Viphakone, N., Van Dijk, T.B., Philipsen, S. & Wilson, S.A. (2013). Chtop is a component of the dynamic TREX mRNA export complex. *EMBO J.*, 32, 473–486.

Chávez, S. & Aguilera, A. (1997). The yeast HPR1 gene has a functional role in transcriptional elongation that uncovers a novel source of genome instability. *Genes Dev.*, 11, 3459–3470.

Chen, C., Tan, M., Wu, Z., Zhang, Y., He, F., Lu, Y., *et al.* (2021a). Structural and functional insights into R-loop prevention and mRNA export by budding yeast THO-Sub2 complex. *Sci. Bull.*, 66, 2347–2352.

Chen, M., Asanuma, M., Takahashi, M., Shichino, Y., Mito, M., Fujiwara, K., *et al.* (2021b). Dual targeting of DDX3 and eIF4A by the translation inhibitor rocaglamide A. *Cell Chem. Biol.*, 28, 475–486.

Chen, Y., Potratz, J.P., Tijerina, P., Del Campo, M., Lambowitz, A.M. & Russell, R. (2008). DEAD-box proteins can completely separate an RNA duplex using a single ATP. *Proc. Natl. Acad. Sci.*, 105, 20203–20208.

Cheow, L.F., Viswanathan, R., Chin, C.-S., Jennifer, N., Jones, R.C., Guccione, E., *et al.* (2014). Multiplexed Analysis of Protein–Ligand Interactions by Fluorescence Anisotropy in a Microfluidic Platform. *Anal. Chem.*, 86, 9901–9908.

Chi, B., Wang, Q., Wu, G., Tan, M., Wang, L., Shi, M., *et al.* (2013). Aly and THO are required for assembly of the human TREX complex and association of TREX components with the spliced mRNA. *Nucleic Acids Res.*, 41, 1294–1306.

Choong, M.L., Tan, L.K., Lo, S.L., Ren, E.-C., Ou, K., Ong, S.-E., *et al.* (2001). An integrated approach in the discovery and characterization of a novel nuclear protein over-expressed in liver and pancreatic tumors. *FEBS Lett.*, 496, 109–116.

Chou, Y.-J., Lin, C.-C., Hsu, Y.-C., Syu, J.-L., Tseng, L.-M., Chiu, J.-H., *et al.* (2022). Andrographolide suppresses the malignancy of triple-negative breast cancer by reducing THOC1-promoted cancer stem cell characteristics. *Biochem. Pharmacol.*, 206, 115327.

Chu, J., Zhang, W., Cencic, R., Devine, W.G., Beglov, D., Henkel, T., *et al.* (2019). Amidino-rocaglates: a potent class of eIF4A inhibitors. *Cell Chem. Biol.*, 26, 1586–1593.

Clancy, S. & Brown, W. (2008). Translation: DNA to mRNA to protein. *Nat. Educ.*, 1, 101.

Clarke, B.P., Gao, S., Mei, M., Xie, D., Angelos, A.E., Vazhavilla, A., *et al.* (2025). Structural mechanism of DDX39B regulation by human TREX-2 and a related complex in mRNP remodeling. *Nat. Commun.*, 16, 5471.

Cramer, P., Bushnell, D.A., Fu, J., Gnatt, A.L., Maier-Davis, B., Thompson, N.E., *et al.* (2000). Architecture of RNA Polymerase II and Implications for the Transcription Mechanism. *Science*, 288, 640–649.

Cramer, P., Bushnell, D.A. & Kornberg, R.D. (2001). Structural Basis of Transcription: RNA Polymerase II at 2.8 Ångstrom Resolution. *Science*, 292, 1863–1876.

Crick, F. (1970). Central dogma of molecular biology. *Nature*, 227, 561–563.

Crossley, M.P., Bocek, M. & Cimprich, K.A. (2019). R-loops as cellular regulators and genomic threats. *Mol. Cell*, 73, 398–411.

De Magistris, P. (2021). The great escape: mRNA export through the nuclear pore complex. *Int. J. Mol. Sci.*, 22, 11767.

Decroly, E., Ferron, F., Lescar, J. & Canard, B. (2012). Conventional and unconventional mechanisms for capping viral mRNA. *Nat. Rev. Microbiol.*, 10, 51–65.

Derrer, C.P., Mancini, R., Vallotton, P., Huet, S., Weis, K. & Dultz, E. (2019). The RNA export factor Mex67 functions as a mobile nucleoporin. *J. Cell Biol.*, 218, 3967–3976.

Dessau, M.A. & Modis, Y. (2011). Protein crystallization for X-ray crystallography. *J. Vis. Exp. JoVE*, 2285.

Dharavath, S., Song, H. & Ji, X. (2025). Unraveling the mechanism of RNA duplex unwinding by DEAD-box helicase DDX3X: insights into cooperativity and roles of protomers. *Biochem. Biophys. Res. Commun.*, 777, 152206.

Diges, C.M. (2001). Escherichia coli DbpA is an RNA helicase that requires hairpin 92 of 23S rRNA. *EMBO J.*, 20, 5503–5512.

Donsbach, P., Kwas, C., Steimer, L., Samatanga, B., Andreou, A.Z. & Klostermeier, D. (2025). Inter-domain communication in the dimeric DEAD-box helicase Hera from T. thermophilus and implications for the mechanism of RNA unwinding. *Nucleic Acids Res.*, 53, gkaf080.

Dufu, K., Livingstone, M.J., Seebacher, J., Gygi, S.P., Wilson, S.A. & Reed, R. (2010). ATP is required for interactions between UAP56 and two conserved mRNA export proteins, Aly and CIP29, to assemble the TREX complex. *Genes Dev.*, 24, 2043–2053.

Elfmann, C. & Stülke, J. (2023). PAE viewer: a webserver for the interactive visualization of the predicted aligned error for multimer structure predictions and crosslinks. *Nucleic Acids Res.*, 51, W404–W410.

Fairman, M.E., Maroney, P.A., Wang, W., Bowers, H.A., Gollnick, P., Nilsen, T.W., *et al.* (2004). Protein Displacement by DExH/D “RNA Helicases” Without Duplex Unwinding. *Science*, 304, 730–734.

Fairman-Williams, M.E., Guenther, U.-P. & Jankowsky, E. (2010). SF1 and SF2 helicases: family matters. *Curr. Opin. Struct. Biol.*, 20, 313–324.

Fan, H.-Y., Merker, R.J. & Klein, H.L. (2001). High-Copy-Number Expression of Sub2p, a Member of the RNA Helicase Superfamily, Suppresses *hpr1* -Mediated Genomic Instability. *Mol. Cell. Biol.*, 21, 5459–5470.

Fischer, C.J. & Lohman, T.M. (2004). ATP-dependent translocation of proteins along single-stranded DNA: models and methods of analysis of pre-steady state kinetics. *J. Mol. Biol.*, 344, 1265–1286.

Fukuda, S., Wu, D.W., Stark, K. & Pelus, L.M. (2002). Cloning and characterization of a proliferation-associated cytokine-inducible protein, CIP29. *Biochem. Biophys. Res. Commun.*, 292, 593–600.

Gabaldón, T. & Pittis, A.A. (2015). Origin and evolution of metabolic sub-cellular compartmentalization in eukaryotes. *Biochimie*, 119, 262–268.

Gehring, N.H. & Roignant, J.-Y. (2021). Anything but ordinary–emerging splicing mechanisms in eukaryotic gene regulation. *Trends Genet.*, 37, 355–372.

Gerber, H.-P., Hagmann, M., Seipel, K., Georgiev, O., West, M.A., Litingtung, Y., *et al.* (1995). RNA polymerase II C-terminal domain required for enhancer-driven transcription. *Nature*, 374, 660–662.

Germain, H., Qu, N., Cheng, Y.T., Lee, E., Huang, Y., Dong, O.X., *et al.* (2010). MOS11: A New Component in the mRNA Export Pathway. *PLoS Genet.*, 6, e1001250.

Gómez-González, B., García-Rubio, M., Bermejo, R., Gaillard, H., Shirahige, K., Marín, A., *et al.* (2011). Genome-wide function of THO/TREX in active genes prevents R-loop-dependent replication obstacles. *EMBO J.*, 30, 3106–3119.

Gorbalenya, A.E. & Koonin, E.V. (1993). Helicases: amino acid sequence comparisons and structure-function relationships. *Curr. Opin. Struct. Biol.*, 3, 419–429.

Guo, S., Hakimi, M.-A., Baillat, D., Chen, X., Farber, M.J., Klein-Szanto, A.J., *et al.* (2005). Linking transcriptional elongation and messenger RNA export to metastatic breast cancers. *Cancer Res.*, 65, 3011–3016.

Gwizdek, C., Iglesias, N., Rodriguez, M.S., Ossareh-Nazari, B., Hobeika, M., Divita, G., *et al.* (2006). Ubiquitin-associated domain of Mex67 synchronizes recruitment of the mRNA export machinery with transcription. *Proc. Natl. Acad. Sci.*, 103, 16376–16381.

Hanahan, D. (1983). Studies on transformation of Escherichia coli with plasmids. *J. Mol. Biol.*, 166, 557–580.

Harlen, K.M. & Churchman, L.S. (2017). The code and beyond: transcription regulation by the RNA polymerase II carboxy-terminal domain. *Nat. Rev. Mol. Cell Biol.*, 18, 263–273.

Harms, U., Andreou, A.Z., Gubaev, A. & Klostermeier, D. (2014). eIF4B, eIF4G and RNA regulate eIF4A activity in translation initiation by modulating the eIF4A conformational cycle. *Nucleic Acids Res.*, 42, 7911–7922.

Heath, C.G., Viphakone, N. & Wilson, S.A. (2016). The role of TREX in gene expression and disease. *Biochem. J.*, 473, 2911–2935.

Hellman, L.M. & Fried, M.G. (2007). Electrophoretic mobility shift assay (EMSA) for detecting protein–nucleic acid interactions. *Nat. Protoc.*, 2, 1849–1861.

Hilbert, M., Karow, A.R. & Klostermeier, D. (2009). The mechanism of ATP-dependent RNA unwinding by DEAD box proteins. *Biol. Chem.*, 390.

Hilbert, M., Kebbel, F., Gubaev, A. & Klostermeier, D. (2011). eIF4G stimulates the activity of the DEAD box protein eIF4A by a conformational guidance mechanism. *Nucleic Acids Res.*, 39, 2260–2270.

Hohmann, U., Graf, M., Tirián, L., Pacheco-Fiallos, B., Schellhaas, U., Fin, L., *et al.* (2025). An ATP-gated molecular switch orchestrates human messenger RNA export. *Nature*, 1–3.

Hondele, M., Sachdev, R., Heinrich, S., Wang, J., Vallotton, P., Fontoura, B.M., *et al.* (2019). DEAD-box ATPases are global regulators of phase-separated organelles. *Nature*, 573, 144–148.

Huen, J., Lin, C.-L., Golzarroshan, B., Yi, W.-L., Yang, W.-Z. & Yuan, H.S. (2017). Structural insights into a unique dimeric DEAD-box helicase CshA that promotes RNA decay. *Structure*, 25, 469–481.

Huertas, P. & Aguilera, A. (2003). Cotranscriptionally formed DNA: RNA hybrids mediate transcription elongation impairment and transcription-associated recombination. *Mol. Cell*, 12, 711–721.

Humphreys, I.R., Pei, J., Baek, M., Krishnakumar, A., Anishchenko, I., Ovchinnikov, S., *et al.* (2021). Computed structures of core eukaryotic protein complexes. *Science*, 374, eabm4805.

Hurt, E., Luo, M., Röther, S., Reed, R. & Sträßer, K. (2004). Cotranscriptional recruitment of the serine-arginine-rich (SR)-like proteins Gbp2 and Hrb1 to nascent mRNA via the TREX complex. *Proc. Natl. Acad. Sci.*, 101, 1858–1862.

Iglesias, N., Tutucci, E., Gwizdek, C., Vinciguerra, P., Von Dach, E., Corbett, A.H., *et al.* (2010). Ubiquitin-mediated mRNP dynamics and surveillance prior to budding yeast mRNA export. *Genes Dev.*, 24, 1927–1938.

Iost, I., Dreyfus, M. & Linder, P. (1999). Ded1p, a DEAD-box protein required for translation initiation in Saccharomyces cerevisiae, is an RNA helicase. *J. Biol. Chem.*, 274, 17677–17683.

Iwasaki, S., Floor, S.N. & Ingolia, N.T. (2016). Rocaglates convert DEAD-box protein eIF4A into a sequence-selective translational repressor. *Nature*, 534, 558–561.

Jacobsen, J.O., Allen, M.D., Freund, S.M. & Bycroft, M. (2016). High-resolution NMR structures of the domains of Saccharomyces cerevisiae Tho1. *Acta Crystallogr. Sect. F Struct. Biol. Commun.*, 72, 500–506.

Jarmoskaite, I. & Russell, R. (2011). DEAD-box proteins as RNA helicases and chaperones. *WIREs RNA*, 2, 135–152.

Jeronimo, C., Bataille, A.R. & Robert, F. (2013). The Writers, Readers, and Functions of the RNA Polymerase II C-Terminal Domain Code. *Chem. Rev.*, 113, 8491–8522.

Jeronimo, C., Collin, P. & Robert, F. (2016). The RNA polymerase II CTD: the increasing complexity of a low-complexity protein domain. *J. Mol. Biol.*, 428, 2607–2622.

Jimeno, S., Luna, R., García-Rubio, M. & Aguilera, A. (2006). Tho1, a Novel hnRNP, and Sub2 Provide Alternative Pathways for mRNP Biogenesis in Yeast THO Mutants. *Mol. Cell. Biol.*, 26, 4387–4398.

Jimeno, S., Rond, A. G. & Aguilera, Andrés. (2002). The yeast THO complex and mRNA export factors link RNA metabolism with transcription and genome instability. *EMBO J.*, 21, 3526–3535.

Johnson, S.A., Cubberley, G. & Bentley, D.L. (2009). Cotranscriptional recruitment of the mRNA export factor Yra1 by direct interaction with the 3′ end processing factor Pcf11. *Mol. Cell*, 33, 215–226.

Joiner, J.D., Steinchen, W., Mozer, N., Kronenberger, T., Bange, G., Poso, A., *et al.* (2023). HilE represses the activity of the Salmonella virulence regulator HilD via a mechanism distinct from that of intestinal long-chain fatty acids. *J. Biol. Chem.*, 299.

Kammel, C., Thomaier, M., Sørensen, B.B., Schubert, T., Längst, G., Grasser, M., *et al.* (2013). Arabidopsis DEAD-box RNA helicase UAP56 interacts with both RNA and DNA as well as with mRNA export factors. *PLoS One*, 8, e60644.

Karakasili, E., Burkert-Kautzsch, C., Kieser, A. & Sträßer, K. (2014). Degradation of DNA damage-independently stalled RNA polymerase II is independent of the E3 ligase Elc1. *Nucleic Acids Res.*, 42, 10503–10515.

Katahira, J. (2012). mRNA export and the TREX complex. *Biochim. Biophys. Acta BBA-Gene Regul. Mech.*, 1819, 507–513.

Kelemen, O., Convertini, P., Zhang, Z., Wen, Y., Shen, M., Falaleeva, M., *et al.* (2013). Function of alternative splicing. *Gene*, 514, 1–30.

Kim, M., Ahn, S., Krogan, N.J., Greenblatt, J.F. & Buratowski, S. (2004). Transitions in RNA polymerase II elongation complexes at the 3′ ends of genes. *EMBO J.*, 23, 354–364.

Kim, S.J., Fernandez-Martinez, J., Nudelman, I., Shi, Y., Zhang, W., Raveh, B., *et al.* (2018). Integrative structure and functional anatomy of a nuclear pore complex. *Nature*, 555, 475–482.

Kinoshita, Y., Murakami, R., Muto, N., Kubo, S., Iizuka, R. & Uemura, S. (2021). Heterogeneous dissociation process of truncated RNAs by oligomerized Vasa helicase. *Commun. Biol.*, 4, 1386.

Klostermeier, D. & Rudolph, M.G. (2009). A novel dimerization motif in the C-terminal domain of the Thermus thermophilus DEAD box helicase Hera confers substantial flexibility. *Nucleic Acids Res.*, 37, 421–430.

Kossen, K., Karginov, F.V. & Uhlenbeck, O.C. (2002). The carboxy-terminal domain of the DExDH protein YxiN is sufficient to confer specificity for 23 S rRNA. *J. Mol. Biol.*, 324, 625–636.

Kozlowski, L.P. (2021). IPC 2.0: prediction of isoelectric point and p K a dissociation constants. *Nucleic Acids Res.*, 49, W285–W292.

Lee, Y.J., Jung, J.-H., Chang, D.-Y., Kim, M.G., Bashyal, N., Hwang, W.S., *et al.* (2023). THOC2 expression and its impact on 5-fluorouracil resistance in glioblastoma multiforme. *Am. J. Cancer Res.*, 13, 2410.

Li, Y., Huang, J., Zhu, J., Bao, L., Wang, H., Jiang, Y., *et al.* (2022). Targeted protein degradation reveals RNA Pol II heterogeneity and functional diversity. *Mol. Cell*, 82, 3943–3959.

Li, Y., Lin, A.W., Zhang, X., Wang, Y., Wang, X. & Goodrich, D.W. (2007). Cancer cells and normal cells differ in their requirements for Thoc1. *Cancer Res.*, 67, 6657–6664.

Libri, D., Dower, K., Boulay, J., Thomsen, R., Rosbash, M. & Jensen, T.H. (2002). Interactions between mRNA Export Commitment, 3′-End Quality Control, and Nuclear Degradation. *Mol. Cell. Biol.*, 22, 8254–8266.

Libri, D., Graziani, N., Saguez, C. & Boulay, J. (2001). Multiple roles for the yeast SUB2/yUAP56 gene in splicing. *Genes Dev.*, 15, 36–41.

Lin, D.H. & Hoelz, A. (2019). The Structure of the Nuclear Pore Complex (An Update). *Annu. Rev. Biochem.*, 88, 725–783.

Lin, D.H., Stuwe, T., Schilbach, S., Rundlet, E.J., Perriches, T., Mobbs, G., *et al.* (2016). Architecture of the symmetric core of the nuclear pore. *Science*, 352, aaf1015.

Linden, M.H., Hartmann, R.K. & Klostermeier, D. (2008). The putative RNase P motif in the DEAD box helicase Hera is dispensable for efficient interaction with RNA and helicase activity. *Nucleic Acids Res.*, 36, 5800–5811.

Linder, P. & Jankowsky, E. (2011). From unwinding to clamping—the DEAD box RNA helicase family. *Nat. Rev. Mol. Cell Biol.*, 12, 505–516.

Linder, P., Lasko, P.F., Ashburner, M., Leroy, P., NIELSEN, P.J., NISHI, K., *et al.* (1989). Birth of the DEAD box. *Nature*, 337, 121–122.

Liu, F., Putnam, A.A. & Jankowsky, E. (2014). DEAD-Box Helicases Form Nucleotide-Dependent, Long-Lived Complexes with RNA. *Biochemistry*, 53, 423–433.

Luna, R., Jimeno, S., Marín, M., Huertas, P., García-Rubio, M. & Aguilera, A. (2005). Interdependence between transcription and mRNP processing and export, and its impact on genetic stability. *Mol. Cell*, 18, 711–722.

Lund, M.K. & Guthrie, C. (2005). The DEAD-box protein Dbp5p is required to dissociate Mex67p from exported mRNPs at the nuclear rim. *Mol. Cell*, 20, 645–651.

Ma, W.K., Cloutier, S.C. & Tran, E.J. (2013). The DEAD-box protein Dbp2 functions with the RNA-binding protein Yra1 to promote mRNP assembly. *J. Mol. Biol.*, 425, 3824–3838.

Marcaida, M.J., Kauzlaric, A., Duperrex, A., Sülzle, J., Moncrieffe, M.C., Adebajo, D., *et al.* (2020). The human RNA helicase DDX21 presents a dimerization interface necessary for helicase activity. *Iscience*, 23.

Meinel, D.M., Burkert-Kautzsch, C., Kieser, A., O'Duibhir, E., Siebert, M., Mayer, A., *et al.* (2013). Recruitment of TREX to the transcription machinery by its direct binding to the phospho-CTD of RNA polymerase II. *PLoS Genet.*, 9, e1003914.

Meinel, D.M. & Sträßer, K. (2015). Co-transcriptional mRNP formation is coordinated within a molecular mRNP packaging station in *S. cerevisiae*. *BioEssays*, 37, 666–677.

Mekhail, K. & Moazed, D. (2010). The nuclear envelope in genome organization, expression and stability. *Nat. Rev. Mol. Cell Biol.*, 11, 317–328.

Minocha, R., Popova, V., Kopytova, D., Misiak, D., Hüttelmaier, S., Georgieva, S., *et al.* (2018). Mud2 functions in transcription by recruiting the Prp19 and TREX complexes to transcribed genes. *Nucleic Acids Res.*, 46, 9749–9763.

Miosga, M. (2022). Function of the RNA helicase Sub2 from Saccharomyces cerevisiae and its regulation by Tho1. PhD Thesis. Justus-Liebig-Universität Gießen.

Müller-McNicoll, M. & Neugebauer, K.M. (2014). Good cap/bad cap: how the cap-binding complex determines RNA fate. *Nat. Struct. Mol. Biol.*, 21, 9–12.

Oeffinger, M., Wei, K.E., Rogers, R., DeGrasse, J.A., Chait, B.T., Aitchison, J.D., *et al.* (2007). Comprehensive analysis of diverse ribonucleoprotein complexes. *Nat. Methods*, 4, 951–956.

Ordabayev, Y., Nguyen, B., Niedziela-Majka, A. & Lohman, T. (2018). Regulation of UvrD helicase activity by MutL. *Biophys. J.*, 114, 444a.

Pacheco-Fiallos, B., Vorländer, M.K., Riabov-Bassat, D., Fin, L., O'Reilly, F.J., Ayala, F.I., *et al.* (2023). mRNA recognition and packaging by the human transcription–export complex. *Nature*, 616, 828–835.

Paine, P.L., Moore, L.C. & Horowitz, S.B. (1975). Nuclear envelope permeability. *Nature*, 254, 109–114.

Passmore, L.A. & Coller, J. (2022). Roles of mRNA poly (A) tails in regulation of eukaryotic gene expression. *Nat. Rev. Mol. Cell Biol.*, 23, 93–106.

Patrick, E.M., Yadav, R., Senanayake, K., Cotter, K., Putnam, A.A., Jankowsky, E., *et al.* (2025). High-resolution fleezers reveal duplex opening and stepwise assembly by an oligomer of the DEAD-box helicase Ded1p. *Nat. Commun.*, 16, 1015.

Peña, Á., Gewartowski, K., Mroczek, S., Cuéllar, J., Szykowska, A., Prokop, A., *et al.* (2012). Architecture and nucleic acids recognition mechanism of the THO complex, an mRNP assembly factor. *EMBO J.*, 31, 1605–1616.

Pérez-Calero, C., Bayona-Feliu, A., Xue, X., Barroso, S.I., Muñoz, S., González-Basallote, V.M., *et al.* (2020). UAP56/DDX39B is a major cotranscriptional RNA–DNA helicase that unwinds harmful R loops genome-wide. *Genes Dev.*, 34, 898–912.

Pfaff, C., Ehrnsberger, H.F., Flores-Tornero, M., Sørensen, B.B., Schubert, T., Längst, G., *et al.* (2018). ALY RNA-binding proteins are required for nucleocytosolic mRNA transport and modulate plant growth and development. *Plant Physiol.*, 177, 226–240.

Piruat, J.I. (1998). A novel yeast gene, THO2, is involved in RNA pol II transcription and provides new evidence for transcriptional elongation-associated recombination. *EMBO J.*, 17, 4859–4872.

Piruat, J.I. & Aguilera, A. (1998). A novel yeast gene, THO2, is involved in RNA pol II transcription and provides new evidence for transcriptional elongation-associated recombination. *EMBO J.*, 17, 4859–4872.

Pühringer, T., Hohmann, U., Fin, L., Pacheco-Fiallos, B., Schellhaas, U., Brennecke, J., *et al.* (2020). Structure of the human core transcription-export complex reveals a hub for multivalent interactions. *elife*, 9, e61503.

Putnam, A.A., Gao, Z., Liu, F., Jia, H., Yang, Q. & Jankowsky, E. (2015). Division of labor in an oligomer of the DEAD-box RNA helicase Ded1p. *Mol. Cell*, 59, 541–552.

Putnam, A.A. & Jankowsky, E. (2013). AMP sensing by DEAD-box RNA helicases. *J. Mol. Biol.*, 425, 3839–3845.

Pyle, A.M. (2008). Translocation and Unwinding Mechanisms of RNA and DNA Helicases. *Annu. Rev. Biophys.*, 37, 317–336.

Ramanathan, A., Robb, G.B. & Chan, S.-H. (2016). mRNA capping: biological functions and applications. *Nucleic Acids Res.*, 44, 7511–7526.

Rambout, X. & Maquat, L.E. (2020). The nuclear cap-binding complex as choreographer of gene transcription and pre-mRNA processing. *Genes Dev.*, 34, 1113–1127.

Ren, Y., Schmiege, P. & Blobel, G. (2017). Structural and biochemical analyses of the DEAD-box ATPase Sub2 in association with THO or Yra1. *Elife*, 6, e20070.

Rödel, A., Weig, I., Tiedemann, S., Schwartz, U., Längst, G., Moehle, C., *et al.* (2024). *Arabidopsis* mRNA export factor MOS11 : molecular interactions and role in abiotic stress responses. *New Phytol.*, 243, 180–194.

Rodríguez-Molina, J.B. & Turtola, M. (2023). Birth of a poly(A) tail: mechanisms and control of mRNA polyadenylation. *FEBS Open Bio*, 13, 1140–1153.

Rodríguez-Molina, J.B., West, S. & Passmore, L.A. (2023). Knowing when to stop: Transcription termination on protein-coding genes by eukaryotic RNAPII. *Mol. Cell*, 83, 404–415.

Rogers, G.W., Lima, W.F. & Merrick, W.C. (2001). Further characterization of the helicase activity of eIF4A: substrate specificity. *J. Biol. Chem.*, 276, 12598–12608.

Rougemaille, M., Dieppois, G., Kisseleva-Romanova, E., Gudipati, R.K., Lemoine, S., Blugeon, C., *et al.* (2008). THO/Sub2p functions to coordinate 3′-end processing with gene-nuclear pore association. *Cell*, 135, 308–321.

Rougemaille, M., Gudipati, R.K., Olesen, J.R., Thomsen, R., Seraphin, B., Libri, D., *et al.* (2007). Dissecting mechanisms of nuclear mRNA surveillance in THO/sub2 complex mutants. *EMBO J.*, 26, 2317–2326.

Rozen, F., Edery, I., Meerovitch, K., Dever, T.E., Merrick, W.C. & Sonenberg, N. (1990). Bidirectional RNA Helicase Activity of Eucaryotic Translation Initiation Factors 4A and 4F. *Mol. Cell. Biol.*, 10, 1134–1144.

Rudolph, M.G. & Klostermeier, D. (2009). The Thermus thermophilus DEAD box helicase Hera contains a modified RNA recognition motif domain loosely connected to the helicase core. *RNA*, 15, 1993–2001.

Saguez, C., Gonzales, F.A., Schmid, M., Bøggild, A., Latrick, C.M., Malagon, F., *et al.* (2013). Mutational analysis of the yeast RNA helicase Sub2p reveals conserved domains required for growth, mRNA export, and genomic stability. *Rna*, 19, 1363–1371.

Saguez, C., Schmid, M., Olesen, J.R., Ghazy, M.A.E.-H., Qu, X., Poulsen, M.B., *et al.* (2008). Nuclear mRNA surveillance in THO/sub2 mutants is triggered by inefficient polyadenylation. *Mol. Cell*, 31, 91–103.

Saito, Y., Kasamatsu, A., Yamamoto, A., Shimizu, T., Yokoe, H., Sakamoto, Y., *et al.* (2013). ALY as a potential contributor to metastasis in human oral squamous cell carcinoma. *J. Cancer Res. Clin. Oncol.*, 139, 585–594.

San Martin-Alonso, M., Soler-Oliva, M.E., García-Rubio, M., García-Muse, T. & Aguilera, A. (2021). Harmful R-loops are prevented via different cell cycle-specific mechanisms. *Nat. Commun.*, 12, 4451.

Sanger, F., Nicklen, S. & Coulson, A.R. (1977). DNA sequencing with chain-terminating inhibitors. *Proc. Natl. Acad. Sci.*, 74, 5463–5467.

Santos-Rosa, H., Moreno, H., Simos, G., Segref, A., Fahrenkrog, B., Panté, N., *et al.* (1998). Nuclear mRNA Export Requires Complex Formation between Mex67p and Mtr2p at the Nuclear Pores. *Mol. Cell. Biol.*, 18, 6826–6838.

Satori, C.P., Henderson, M.M., Krautkramer, E.A., Kostal, V., Distefano, M.M. & Arriaga, E.A. (2013). Bioanalysis of Eukaryotic Organelles. *Chem. Rev.*, 113, 2733–2811.

Schuller, S.K., Schuller, J.M., Prabu, J.R., Baumgärtner, M., Bonneau, F., Basquin, J., *et al.* (2020). Structural insights into the nucleic acid remodeling mechanisms of the yeast THO-Sub2 complex. *eLife*, 9, e61467.

Segref, A. (1997). Mex67p, a novel factor for nuclear mRNA export, binds to both poly(A)+ RNA and nuclear pores. *EMBO J.*, 16, 3256–3271.

Seidler, J.F. & Sträßer, K. (2024). Understanding nuclear mRNA export: Survival under stress. *Mol. Cell*, 84, 3681–3691.

Sen, R., Barman, P., Kaja, A., Ferdoush, J., Lahudkar, S., Roy, A., *et al.* (2019). Distinct Functions of the Cap-Binding Complex in Stimulation of Nuclear mRNA Export. *Mol. Cell. Biol.*, 39, e00540-18.

Sengoku, T., Nureki, O., Nakamura, A., Kobayashi, S. & Yokoyama, S. (2006). Structural basis for RNA unwinding by the DEAD-box protein Drosophila Vasa. *Cell*, 125, 287–300.

Sharma, S., Kapoor, S., Ansari, A. & Tyagi, A.K. (2024). The general transcription factors (GTFs) of RNA polymerase II and their roles in plant development and stress responses. *Crit. Rev. Biochem. Mol. Biol.*, 59, 267–309.

Shen, H., Zheng, X., Shen, J., Zhang, L., Zhao, R. & Green, M.R. (2008). Distinct activities of the DExD/H-box splicing factor hUAP56 facilitate stepwise assembly of the spliceosome. *Genes Dev.*, 22, 1796–1803.

Shen, L. & Pelletier, J. (2020). Selective targeting of the DEAD-box RNA helicase eukaryotic initiation factor (eIF) 4A by natural products. *Nat. Prod. Rep.*, 37, 609–616.

Sherman, F. (1991). [1] Getting started with yeast. In: *Methods in enzymology*. Elsevier, pp. 3–21.

Sikorski, R.S. & Hieter, P. (1989). A system of shuttle vectors and yeast host strains designed for efficient manipulation of DNA in Saccharomyces cerevisiae. *Genetics*, 122, 19–27.

Sims, R.J., Belotserkovskaya, R. & Reinberg, D. (2004). Elongation by RNA polymerase II: the short and long of it. *Genes Dev.*, 18, 2437–2468.

Singh, G., Pratt, G., Yeo, G.W. & Moore, M.J. (2015). The Clothes Make the mRNA: Past and Present Trends in mRNP Fashion. *Annu. Rev. Biochem.*, 84, 325–354.

Sloan, K.E. & Bohnsack, M.T. (2018). Unravelling the mechanisms of RNA helicase regulation. *Trends Biochem. Sci.*, 43, 237–250.

Song, H. & Ji, X. (2019). The mechanism of RNA duplex recognition and unwinding by DEAD-box helicase DDX3X. *Nat. Commun.*, 10, 3085.

Stefanyshena, N. & Sträßer, K. (2026). An elevated level of the mRNA exporter Mex67-Mtr2 in nuclear mRNPs impairs nuclear mRNA export. *Nucleic Acids Res.*, 54, gkag025.

Storozhuk, O., Bruekner, S.R., Paul, A., Lebbink, J.H., Sixma, T.K. & Friedhoff, P. (2024). MutL Activates UvrD by Interaction Between the MutL C-terminal Domain and the UvrD 2B Domain. *J. Mol. Biol.*, 436, 168589.

Sträßer, K. & Hurt, E. (2000). Yra1p, a conserved nuclear RNA-binding protein, interacts directly with Mex67p and is required for mRNA export. *EMBO J.*, 19, 410–420.

Sträßer, K. & Hurt, E. (2001). Splicing factor Sub2p is required for nuclear mRNA export through its interaction with Yra1p. *Nature*, 413, 648–652.

Sträßer, K., Masuda, S., Mason, P., Pfannstiel, J., Oppizzi, M., Rodriguez-Navarro, S., *et al.* (2002). TREX is a conserved complex coupling transcription with messenger RNA export. *Nature*, 417, 304–308.

Sugiura, T., Sakurai, K. & Nagano, Y. (2007). Intracellular characterization of DDX39, a novel growth-associated RNA helicase. *Exp. Cell Res.*, 313, 782–790.

Tabassum, S. & Ghosh, M.K. (2023). DEAD-box RNA helicases with special reference to p68: Unwinding their biology, versatility, and therapeutic opportunity in cancer. *Genes Dis.*, 10, 1220–1241.

Taniguchi, I. & Ohno, M. (2008). ATP-Dependent Recruitment of Export Factor Aly/REF onto Intronless mRNAs by RNA Helicase UAP56. *Mol. Cell. Biol.*, 28, 601–608.

Tarn, W.Y., Hsu, C.H., Huang, K.T., Chen, H.R., Kao, H.Y., Lee, K.R., *et al.* (1994). Functional association of essential splicing factor(s) with PRP19 in a protein complex. *EMBO J.*, 13, 2421–2431.

Taschuk, F. & Cherry, S. (2020). DEAD-box helicases: sensors, regulators, and effectors for antiviral defense. *Viruses*, 12, 181.

Taylor, R.G., Walker, D.C. & McInnes, R.R. (1993). E. coli host strains significantly affect the quality of small scale plasmid DNA preparations used for sequencing. *Nucleic Acids Res.*, 21, 1677.

Theissen, B., Karow, A.R., Köhler, J., Gubaev, A. & Klostermeier, D. (2008). Cooperative binding of ATP and RNA induces a closed conformation in a DEAD box RNA helicase. *Proc. Natl. Acad. Sci.*, 105, 548–553.

Thomas, B.J. & Rothstein, R. (1989). Elevated recombination rates in transcriptionally active DNA. *Cell*, 56, 619–630.

Timney, B.L., Raveh, B., Mironska, R., Trivedi, J.M., Kim, S.J., Russel, D., *et al.* (2016). Simple rules for passive diffusion through the nuclear pore complex. *J. Cell Biol.*, 215, 57–76.

Toyama, Y. & Shimada, I. (2024). NMR characterization of RNA binding property of the DEAD-box RNA helicase DDX3X and its implications for helicase activity. *Nat. Commun.*, 15, 3303.

Vinciauskaite, V. & Masson, G.R. (2023). Fundamentals of hdx-ms. *Essays Biochem.*, 67, 301–314.

Von Moeller, H., Basquin, C. & Conti, E. (2009). The mRNA export protein DBP5 binds RNA and the cytoplasmic nucleoporin NUP214 in a mutually exclusive manner. *Nat. Struct. Mol. Biol.*, 16, 247–254.

Waterhouse, A.M., Procter, J.B., Martin, D.M., Clamp, M. & Barton, G.J. (2009). Jalview Version 2—a multiple sequence alignment editor and analysis workbench. *Bioinformatics*, 25, 1189–1191.

Wellinger, R.E., Prado, F. & Aguilera, A. (2006). Replication Fork Progression Is Impaired by Transcription in Hyperrecombinant Yeast Cells Lacking a Functional THO Complex. *Mol. Cell. Biol.*, 26, 3327–3334.

Wende, W., Friedhoff, P. & Sträßer, K. (2019). Mechanism and Regulation of Co-transcriptional mRNP Assembly and Nuclear mRNA Export. In: *The Biology of mRNA: Structure and Function*, Advances in Experimental Medicine and Biology (eds. Oeffinger, M. & Zenklusen, D.). Springer International Publishing, Cham, pp. 1–31.

Werner-Washburne, M., Braun, E.L., Crawford, M.E. & Peck, V.M. (1996). Stationary phase in *Saccharomyces cerevisiae*. *Mol. Microbiol.*, 19, 1159–1166.

Wilkinson, M.E., Charenton, C. & Nagai, K. (2020). RNA Splicing by the Spliceosome. *Annu. Rev. Biochem.*, 89, 359–388.

Winey, M., Yarar, D., Giddings, T.H. & Mastronarde, D.N. (1997). Nuclear Pore Complex Number and Distribution throughout the *Saccharomyces cerevisiae* Cell Cycle by Three-Dimensional Reconstruction from Electron Micrographs of Nuclear Envelopes. *Mol. Biol. Cell*, 8, 2119–2132.

Wood, W.B. (1966). Host specificity of DNA produced by Escherichia coli: bacterial mutations affecting the restriction and modification of DNA. *J. Mol. Biol.*, 16, 118-IN3.

Xie, Y., Clarke, B.P., Xie, D., Mei, M., Bhat, P., Hill, P.S., *et al.* (2025). Structures and mRNP remodeling mechanism of the TREX-2 complex. *Structure*, 33, 566–582.

Xie, Y., Gao, S., Zhang, K., Bhat, P., Clarke, B.P., Batten, K., *et al.* (2023). Structural basis for high-order complex of SARNP and DDX39B to facilitate mRNP assembly. *Cell Rep.*, 42.

Xie, Y. & Ren, Y. (2019). Mechanisms of nuclear mRNA export: A structural perspective. *Traffic*, 20, 829–840.

Xing, Z., Ma, W.K. & Tran, E.J. (2019). The DDX5/Dbp2 subfamily of DEAD-box RNA helicases. *WIREs RNA*, 10, e1519.

Xu, L., Wang, L., Peng, J., Li, F., Wu, L., Zhang, B., *et al.* (2017). Insights into the structure of dimeric RNA helicase CsdA and indispensable role of its C-terminal regions. *Structure*, 25, 1795–1808.

Yahia, Y., Pigeot, A., El Aabidine, A.Z., Shah, N., Karasu, N., Forné, I., *et al.* (2023). RNA polymerase II CTD is dispensable for transcription and required for termination in human cells. *EMBO Rep.*, 24, e56150.

Yang, Q. & Jankowsky, E. (2006). The DEAD-box protein Ded1 unwinds RNA duplexes by a mode distinct from translocating helicases. *Nat. Struct. Mol. Biol.*, 13, 981–986.

Zarnack, K., Balasubramanian, S., Gantier, M.P., Kunetsky, V., Kracht, M., Schmitz, M.L., *et al.* (2020). Dynamic mRNP remodeling in response to internal and external stimuli. *Biomolecules*, 10, 1310.

Zenklusen, D., Vinciguerra, P., Wyss, J.-C. & Stutz, F. (2002). Stable mRNP Formation and Export Require Cotranscriptional Recruitment of the mRNA Export Factors Yra1p and Sub2p by Hpr1p. *Mol. Cell. Biol.*, 22, 8241–8253.

Zhan, Y., Grabbe, F., Oberbeckmann, E., Dienemann, C. & Cramer, P. (2024). Three-step mechanism of promoter escape by RNA polymerase II. *Mol. Cell*, 84, 1699–1710.

Zhang, H., He, C., Guo, X., Fang, Y., Lai, Q., Wang, X., *et al.* (2022). DDX39B contributes to the proliferation of colorectal cancer through direct binding to CDK6/CCND1. *Cell Death Discov.*, 8, 30.

Danksagung

Ich möchte an dieser Stelle allen voran Apl. Prof. Dr. Peter Friedhoff für die Möglichkeit danken, meine Doktorarbeit unter seiner Betreuung durchzuführen. Für seine kontinuierliche Unterstützung und seinen scheinbar unerschöpflichen Ideenreichtum bin ich ihm sehr dankbar. Seine wissenschaftliche Anleitung und die Zusammenarbeit mit ihm waren für mich von unschätzbarem Wert und grundlegend für diese Arbeit.
Mein Dank gilt zudem Prof. Dr. John Ziebuhr, der das Zweitgutachten dieser Dissertation übernommen hat. Darüber hinaus danke ich ihm und Prof. Dr. Katharina Höfer herzlich für ihr hilfreiches Feedback während meiner TAC-Meetings und für ihre Bereitschaft, Mitglieder meiner Prüfungskommission zu sein. Apl. Prof. Dr. Elena Evguenieva-Hackenberg danke ich ebenso für ihre Unterstützung als weiteres Mitglied meiner Prüfungskommission.
Prof. Dr. Katja Sträßer danke ich für die herzliche Aufnahme im Institut.
Ein weiterer Dank gilt meinen Kooperationspartner*innen für ihre wertvollen Beiträge zu dieser Arbeit: Dr. Cornelia Kilchert und Prof. Dr. Karl-Heinz Kogel für die Bereitstellung von DNA, Dr. Uwe Linne und Tina Krieg für die Massenspektrometrie sowie Dr. Wieland Steinchen für die Durchführung und Auswertung der HDX-Messungen und Hilfe bei Strukturfragen. Dr. Vera Bettenworth danke ich herzlich für ihre tatkräftige Unterstützung beim Verfassen unserer Publikation und beim Korrekturlesen dieser Arbeit sowie für ihre ausgezeichnete Organisation des Graduiertenkollegs und nicht zuletzt für ihr stets offenes Ohr.
Matthias danke ich für seine Hilfe und die hervorragende Einarbeitung in das Projekt. Ich danke Minhaz und meinen Bachelorstudent*innen Karin, Giuseppina, Berengar, Jan und Amelie für ihre engagierte Mitarbeit am Projekt. Besonders möchte ich Maren danken, die mich während ihrer Bachelorarbeit und darüber hinaus als Hiwi lange begleitet und unterstützt hat und mit der jeder Labortag ein Stück schöner war.
Ein riesiger Dank geht an die gesamte Arbeitsgruppe für die Unterstützung und die schöne gemeinsame Zeit im und außerhalb des Labors.
Meinen Freundinnen und Freunden danke ich für die vielen schönen Jahre mit zahlreichen gemeinsamen Unternehmungen und Urlauben. Elena, Isabelle und Shiksha danke ich zudem für das Korrekturlesen dieser Arbeit. Ein besonderer Dank gilt Heiko für seinen Rückhalt, seine Geduld und seinen grenzenlosen Optimismus.
Meiner Familie danke ich von ganzem Herzen für ihre bedingungslose Unterstützung – insbesondere meinen Eltern, die mir stets mit Rat und Tat zur Seite standen.

Diese Arbeit entstand im Rahmen des DFG-Graduiertenkollegs RTG 2355 (GRK 2355) und wurde durch die Deutsche Forschungsgemeinschaft (DFG) im Rahmen dieses Graduiertenkollegs gefördert.

Appendix

Supplementary Figures

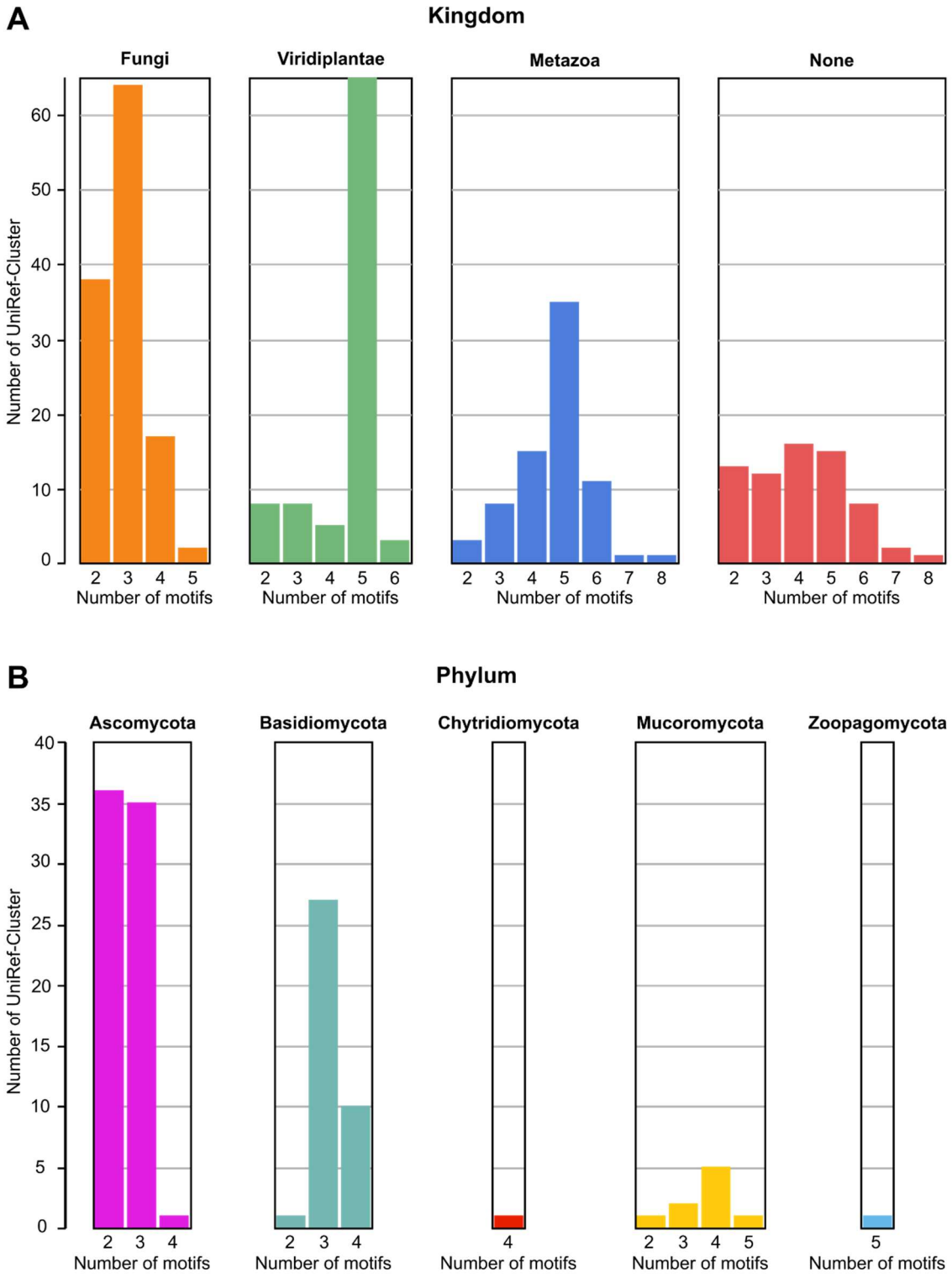

Supplementary Figure S1: Variation in the number of helical motifs among Tho1 orthologs. Distribution of predicted helical motifs in Tho1 orthologs across **(A)** different kingdoms or **(B)** fungal phyla. Histograms show the frequency of proteins with the indicated number of helical motifs. The analysis was performed by Apl. Prof. Dr. Peter Friedhoff using Python (v.3.11). The workflow is described in the Supplementary Methods on page 148.

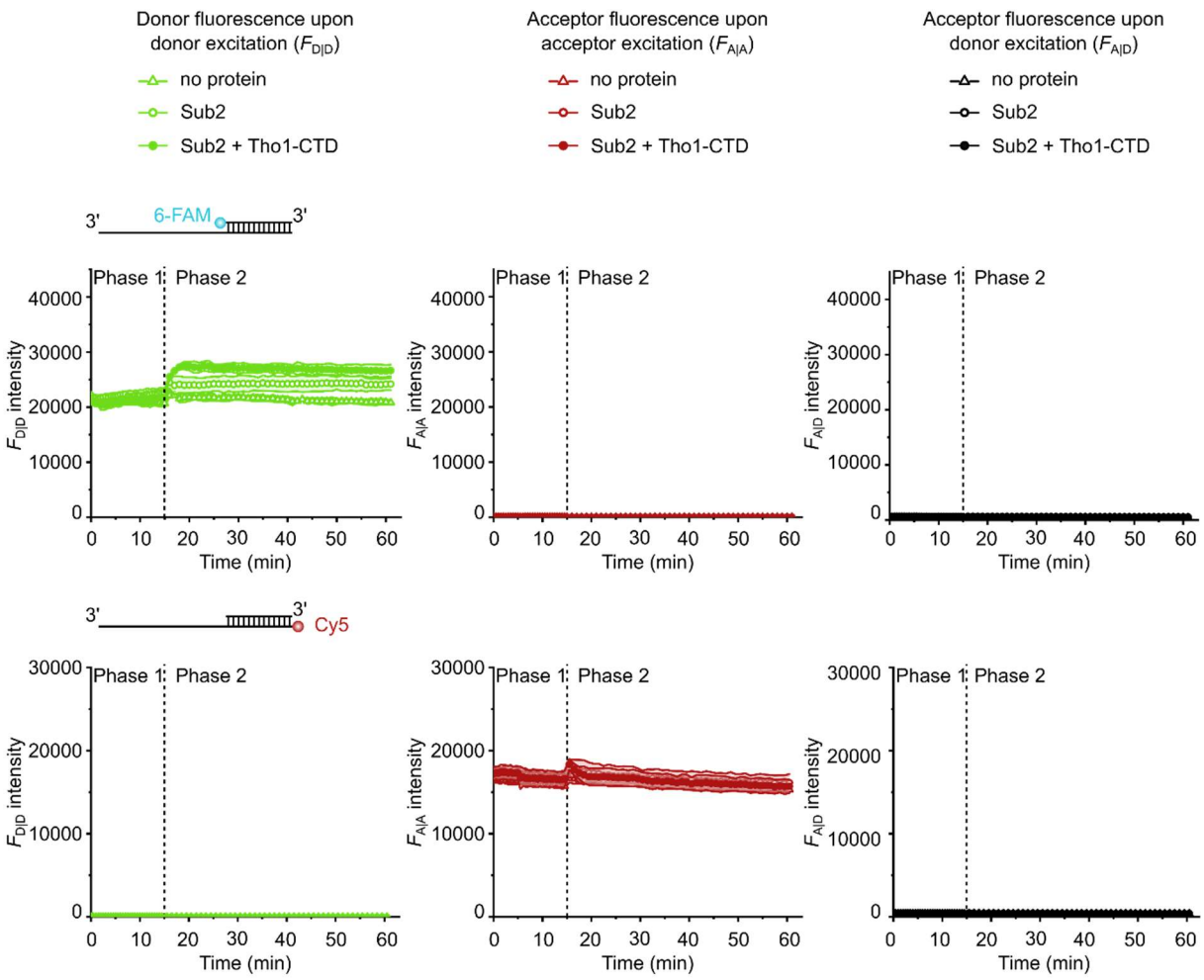

Supplementary Figure S2: Unwinding assays using singly labelled RNA substrates. Real-time unwinding kinetics were measured with pdRNA substrates labelled with a single fluorophore, either 6-FAM (donor) or Cy5 (acceptor). Reactions were performed with or without 1 µM Sub2 during phase 1. In phase 2, either gel filtration buffer or 2 µM Tho1-CTD was added. Fluorescence emission was monitored in three channels: donor (6-FAM) fluorescence after donor excitation ($F_{D|D}$, green), acceptor (Cy5) fluorescence after donor excitation ($F_{A|D}$, black), and acceptor fluorescence after acceptor excitation ($F_{A|A}$, red). For donor-labelled pdRNA, addition of buffer or the Tho1-CTD in phase 2 resulted in an increase in the $F_{D|D}$ signal. Sub2 alone in phase 1 caused only a minor effect. The $F_{A|A}$ signals for the acceptor-labelled pdRNA remained unchanged upon protein addition. No signals were detected for the donor in the $F_{A|A}$ channel or for the acceptor in the $F_{D|D}$ channel. Data represent mean ± SD of n = 3 experiments. These results were used to calculate the crosstalk factors described in the Materials and Methods section on page 46.

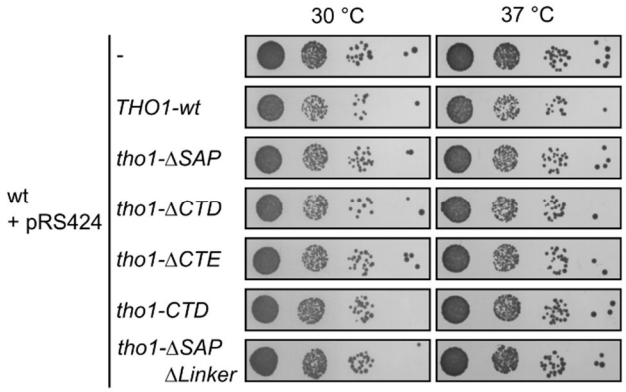

Supplementary Figure S3: Overexpression of Tho1 mutants from plasmids does not influence cell growth in wild-type cells. Dot spot assay of wild-type (W303) cells overexpressing *THO1* or the indicated *tho1* mutant. Tenfold serial dilutions of cells were spotted onto SDC (-Trp) plates and grown at 30°C for two days or 37°C for three days. Representative result of three biological replicates. Wild-type cells transformed with an empty vector served as positive control.

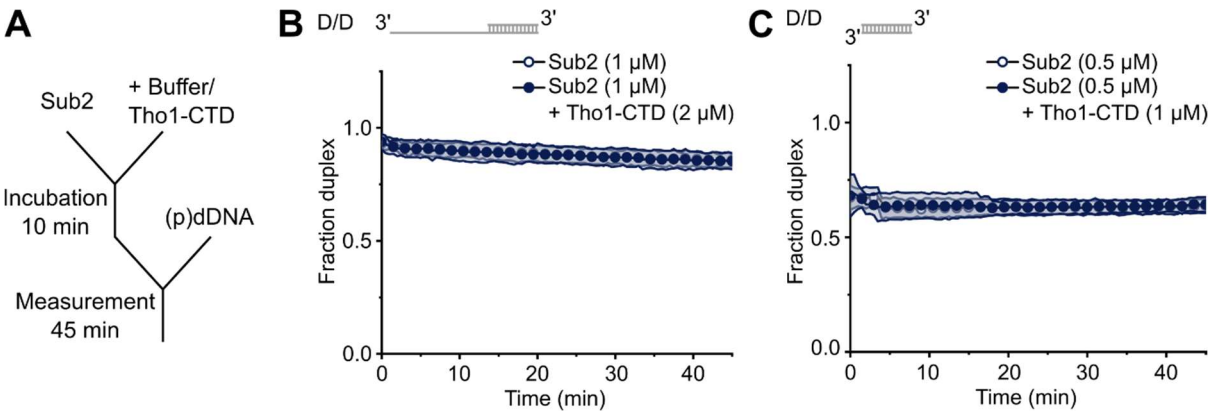

Supplementary Figure S4: Sub2 does not unwind DNA duplexes. (A) Scheme of the unwinding assay. **(B+C)** Unwinding assays of Sub2 (1 µM) with or without 2 µM Tho1-CTD using DNA substrates consisting of (B) a 13/38 pdDNA with a 3′ ssDNA overhang or (C) a 13 bp blunt-end duplex. The fraction duplex is shown as mean ± SD of *n* = 3 experiments. Sub2 did not unwind either DNA substrate, and the presence of the Tho1-CTD had no stimulatory effect.

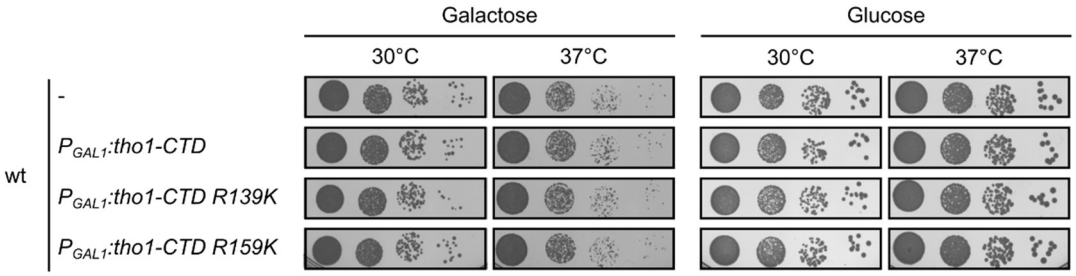

Supplementary Figure S5: Overexpression of Tho1-CTD mutants after genomic integration does not influence cell growth in wild-type cells. Dot spot assay of wild-type (W303) cells overexpressing *THO1* or the indicated *tho1*-CTD mutant. Tenfold serial dilutions of cells were spotted onto plates containing galactose (YPG) or glucose (YPD) and grown at 30°C or 37°C for two days. Representative result of two biological replicates. Wild-type cells served as a positive control.

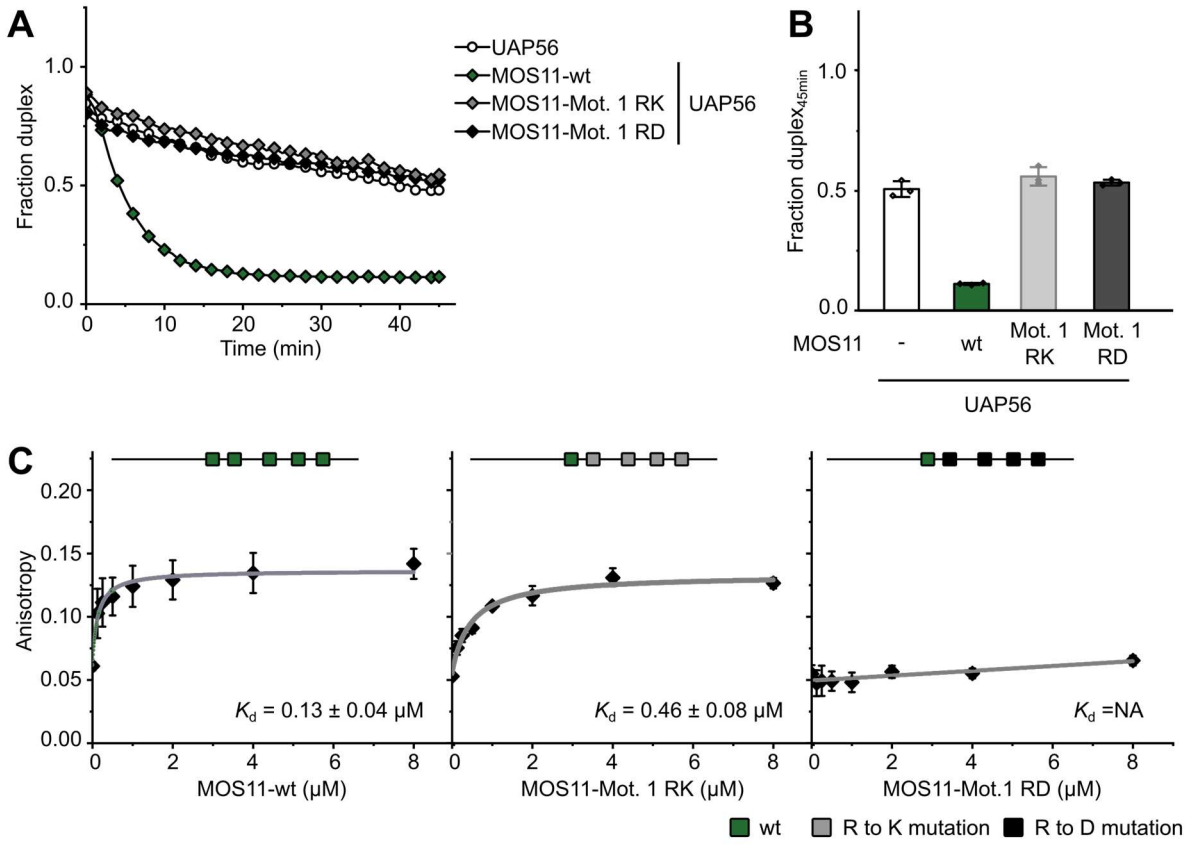

Supplementary Figure S6: R to D mutations in MOS11 impair RNA binding. **(A)** Representative kinetics of 13/38 pdRNA unwinding by 1 µM UAP56 in the absence or presence of 2 µM MOS11 wild-type or the indicated MOS11 mutant. **(B)** Comparison of the fraction duplex remaining after 45 min is shown as mean ± SD of $n = 3$ experiments. **(C)** Fluorescence anisotropy equilibrium titrations (t = 10 min) of wild-type MOS11 and mutants using 6-FAM-labeled 13 nt RNA. Schematic representations indicate intact motifs in green. Mutants contain either R to K (RK, grey) or R to D (RD, black) substitutions in helical motifs 2-5. Data represent mean ± SD of $n = 3$ experiments. All experiments were performed by Amelie Müller as part of her bachelor's thesis (2024).

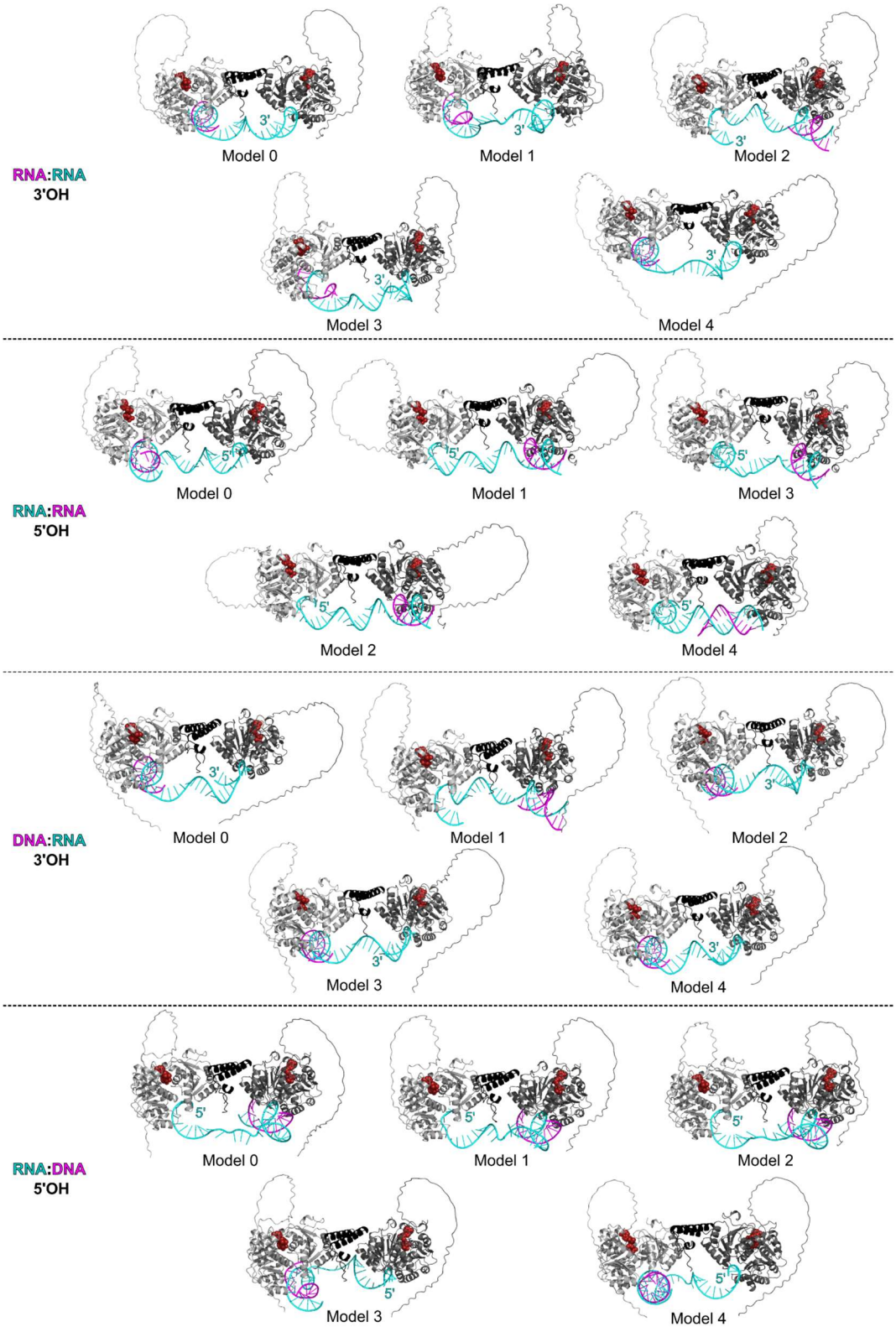

Supplementary Figure S7: Influence of overhang orientation on 2:1 Sub2-Tho1-CTD complexes. Zoomed-out views of AlphaFold 3 predictions of 2:1 complexes formed by Sub2 (grey) and the Tho1-CTD (black) on the indicated partial duplex substrates, corresponding to the close-up views shown in Figure 47. The substrates contain either 3′ or 5′ ssRNA overhangs. The 13 nt top strands are shown in pink and the 38 nt bottom strands in cyan, allowing discrimination between the two strands and identification of the strand bound by Sub2.

Supplementary Methods

Computational analysis of helical motif numbers across Tho1 orthologs

Analysis of helical motif numbers in Tho1 and its orthologs shown in Supplementary Figure S1 was performed by Apl. Prof. Dr. Peter Friedhoff using the following workflow: Primary protein sequences and meta data were retrieved from the UniProt Knowledgebase (UniProtKB), focusing on UniRef50 clusters to reduce sequence redundancy. Taxonomic information, including kingdom and phylum classifications, was mapped to each entry using NCBI Taxonomy IDs. To ensure data quality, entries previously identified as potential outliers (e.g. specific KOG database entries) or misclassifications were filtered out prior to downstream analysis. Secondary structure elements were assigned to protein sequences using AlphaFold 2-predicted structures. Dictionary of Protein Secondary Structure (DSSP) assignments were processed to identify helical regions. The number of helices per protein was calculated by parsing DSSP strings and identifying contiguous segments assigned as α-helices. To identify conserved protein motifs, Hidden Markov Models (HMMs) for the target protein family (PF18592) were searched against the sequence dataset using pyhmmer, a Python wrapper for HMMER3. Motifs were defined based on HMMER hit positions, and only those meeting a predefined bitscore threshold (default = 25) were considered significant. The total number of motifs per entry was appended to the master dataset. To analyse the relationship between taxonomic origin and protein architecture, a specialised plotting data frame was constructed. The dataset was grouped by kingdom, phylum, number of helical motifs, and number of helices. For each unique combination of these variables, the total number of protein entries was calculated. Statistical visualizations were performed using the Altair and Seaborn libraries in Python.

Charge profiles of Tho1 and Tho1 orthologs

The charge profiles shown in Figures 8 and 44 were generated by Apl. Prof. Dr. Peter Friedhoff using the following workflow: Protein sequences and associated metadata were obtained from UniProtKB. For comparative analysis, representative entries for *S. cerevisiae* (P40040), *S. pombe* (O74871), *A. thaliana* (Q9LZ08), and *H. sapiens* (P82979) were selected. The local net charge along each protein sequence was calculated using a sliding window approach with a window size of 21 residues. The charge at each position was determined using the Henderson-Hasselbalch equation and the Isoelectric Point Calculator (IPC) pKa dataset (Kozlowski 2021). This

computational workflow was implemented via a custom Python utility (util/charge.py), adapted from the chargeCalculations.R script in the idpr Bioconductor package. Secondary structure elements, specifically α-helices, were derived from the AlphaFold Protein Structure Database (AlphaFold DB) predictions, with structural data parsed from the DSSP assignments. In the resulting visualizations, α-helices are presented as black blocks positioned along the sequence axis. Conserved helical motifs were identified using the HMMER3 software suite (specifically the phmmer algorithm) via the pyhmmer Python wrapper, searching with the PF18592 profile HMM. Motifs are displayed as horizontal bars.

Computational analysis of the MOS11-UAP56 complexes predicted by AlphaFold 3

Analysis of the MOS11-UAP56 complexes shown in Supplementary Table 1, was done by Apl. Prof. Dr. Peter Friedhoff using the following workflow: The prediction inputs consisted of a single MOS11 molecule (MOS11_ARATH, chain A), two UAP56 molecules (RH15_ARATH, chains B and C), one RNA oligonucleotide (5′-AGCACCGUAAAGA-3′) together with its complementary RNA(5'-UCUUUACGGUGCU-3') or DNA strand (5'-TCTTTACGGTGCT-3'). In addition, two ATP molecules and two Mg^{2+} ions were included. Protein chains were modelled using a template-based approach. The resulting models were processed in a Jupyter notebook environment using custom Python scripts in combination with PyMOL to evaluate the spatial relationship between defined MOS11 motifs and the UAP56 protomers. Structural comparisons were performed using the DDX39B-Tho1-CTD crystal structure (PDB: 8ENK) (Xie *et al.* 2023) as a reference. UAP56-1 chains B (UAP56-1) and C (UAP56-2) from the predicted complex were individually aligned to MOS11 (chain A) of the 8ENK structure. Proximity analysis involved calculating the root mean square deviation (RMSD) between Cα atoms of five selected MOS11 motifs and the Cα atoms of helix 1 of the Tho1-CTD (residues 131-144, chain E in 8ENK). MOS11 motifs exhibiting an RMSD below 0.5 nm were classified as being in close spatial proximity to the reference helix and were subsequently examined for their relative positioning with respect to UAP56-1 or -2 in the AlphaFold model. The analysis pipeline was fully automated and incorporated Biopython for sequence alignment and residue mapping, NumPy for coordinate-based calculations, and pandas DataFrames for data organization and export.

Supplementary Table

Supplementary Table S1: Analysis of UAP56 protomer interactions with MOS11 helical motifs and nucleic acids in AlphaFold 3-predicted complexes.

MOS11 mutant	Model	Chain H	Chain I	Mot 1	Mot 2	Mot 3	Mot 4	Mot 5	UAP56-1 interacts with chain	UAP56-2 interacts with chain	Strands bound by UAP56 protomers
wt	0	DNA	RNA			X		X	H	I	different
wt	1	DNA	RNA	X			X		I	H	different
wt	2	DNA	RNA			X		X	I	H	different
wt	3	DNA	RNA		X		X		I	H	different
wt	4	DNA	RNA			X		X	H	I	different
wt	0	RNA	RNA		X	X			I	H	different
wt	1	RNA	RNA	X				X	I	H	different
wt	2	RNA	RNA		X			X	I	H	different
wt	3	RNA	RNA			X		X	H	I	different
wt	4	RNA	RNA		X		X		I		one
Mot.1-4	0	DNA	RNA		X		X		H	I	different
Mot.1-4	1	DNA	RNA	X		X			I	H	different
Mot.1-4	2	DNA	RNA		X	X			H	I	different

Mot.1-4	3	DNA	RNA			X	X		I	H	different
Mot.1-4	4	DNA	RNA	X	X		X		H	I	different
Mot.1-4	0	RNA	RNA		X		X		I	H	different
Mot.1-4	1	RNA	RNA	X			X		H	I	different
Mot.1-4	2	RNA	RNA		X	X			H	I	different
Mot.1-4	3	RNA	RNA		X	X	X		I	H	different
Mot.1-4	4	RNA	RNA			X	X		H	I	different
Mot.1-3	0	DNA	RNA	X	X				I		one
Mot.1-3	1	DNA	RNA	X		X			H	I	different
Mot.1-3	2	DNA	RNA		X		X		I		one
Mot.1-3	3	DNA	RNA	X	X				I		one
Mot.1-3	4	DNA	RNA		X	X			I	H	different
Mot.1-3	0	RNA	RNA		X	X			H	I	different
Mot.1-3	1	RNA	RNA		X			X	H	I	different
Mot.1-3	2	RNA	RNA		X			X	I	H	different
Mot.1-3	3	RNA	RNA			X		X	H	I	different

Mot.1-3	4	RNA	RNA	X					I	H	different
Mot.1+2	0	DNA	RNA	X	X				I		one
Mot.1+2	1	DNA	RNA	X	X					I	one
Mot.1+2	2	DNA	RNA	X	X				I		one
Mot.1+2	3	DNA	RNA	X	X				I		one
Mot.1+2	4	DNA	RNA	X	X				I	H	different
Mot.1+2	0	RNA	RNA	X	X				I		one
Mot.1+2	1	RNA	RNA	X	X					I	one
Mot.1+2	2	RNA	RNA	X	X					I	one
Mot.1+2	3	RNA	RNA	X	X				I		one
Mot.1+2	4	RNA	RNA	X			X		H	I	different
Mot.1+3	0	DNA	RNA	X		X			H	I	different
Mot.1+3	1	DNA	RNA	X		X			I	H	different
Mot.1+3	2	DNA	RNA	X		X			I	H	different
Mot.1+3	3	DNA	RNA	X		X			I	H	different
Mot.1+3	4	DNA	RNA	X		X			I	H	different

Mot.1+3	0	RNA	RNA	X		X			I	H	different
Mot.1+3	1	RNA	RNA	X				X	H	I	different
Mot.1+3	2	RNA	RNA	X		X			I	H	different
Mot.1+3	3	RNA	RNA	X		X			I	H	different
Mot.1+3	4	RNA	RNA	X		X			H	I	different
Mot.1+4	0	DNA	RNA	X			X		H	I	different
Mot.1+4	1	DNA	RNA	X			X		H	I	different
Mot.1+4	2	DNA	RNA	X			X		I	H	different
Mot.1+4	3	DNA	RNA	X			X		I	H	different
Mot.1+4	4	DNA	RNA	X			X		I	H	different
Mot.1+4	0	RNA	RNA		X		X		H	I	different
Mot.1+4	1	RNA	RNA	X			X		I	H	different
Mot.1+4	2	RNA	RNA	X			X		I	H	different
Mot.1+4	3	RNA	RNA	X			X			I	one
Mot.1+4	4	RNA	RNA		X		X		I	H	different
Mot.1+5	0	DNA	RNA	X				X	I	H	different

Mot.1+5	1	DNA	RNA	X				X	I	H	different
Mot.1+5	2	DNA	RNA	X				X	I	H	different
Mot.1+5	3	DNA	RNA	X				X	H	I	different
Mot.1+5	4	DNA	RNA	X		X			H	I	different
Mot.1+5	0	RNA	RNA	X				X	I	H	different
Mot.1+5	1	RNA	RNA	X				X	I		one
Mot.1+5	2	RNA	RNA	X				X	I	H	different
Mot.1+5	3	RNA	RNA	X				X	H	I	different
Mot.1+5	4	RNA	RNA	X				X	H	I	different

Eigenständigkeitserklärung

„Ich erkläre: Ich habe die vorgelegte Dissertation selbstständig und ohne unerlaubte fremde Hilfe und nur mit den Hilfen angefertigt, die ich in der Dissertation angegeben habe. Alle Textstellen, die wörtlich oder sinngemäß aus veröffentlichten Schriften entnommen sind, und alle Angaben, die auf mündlichen Auskünften beruhen, sind als solche kenntlich gemacht. Ich stimme einer evtl. Überprüfung meiner Dissertation durch eine Antiplagiat-Software zu. Bei den von mir durchgeführten und in der Dissertation erwähnten Untersuchungen habe ich die Grundsätze guter wissenschaftlicher Praxis, wie sie in der „Satzung der Justus-Liebig-Universität Gießen zur Sicherung guter wissenschaftlicher Praxis“ niedergelegt sind, eingehalten.“

Angaben zu auf künstlicher Intelligenz (KI) basierender Hilfen wie ChatGPT oder SchulKI von OpenAI oder Gemini von Google zur Erstellung meiner Dissertation (Zutreffendes angekreuzt):

☐ Ich habe bei der Erstellung dieses Textes kein KI-Tool verwendet.

☒ Ich habe ein KI-Tool in den folgenden Bereichen eingesetzt (Mehrfachnennungen möglich):

☐ Ideen finden, meine Kreativität anregen

☐ Verstehen von Konzepten, Recherche von Fakten und Definitionen

☒ Optimierung eines von mir verfassten Textes

☐ Erstellen ganzer Textpassagen nach meinen Vorgaben

Folgende KI-Tools habe ich verwendet, damit aufgeführte Teile meines Textes von dem Tool wie folgt profitiert haben:

Die sprachliche Überarbeitung aller Texte wurde mit Unterstützung der im Folgenden genannten KI-Werkzeuge durchgeführt.

ChatGPT (OpenAI)

Claude (Anthropic)

DeepL Write (DeepL SE)

Datum: _____ Unterschrift: _____